



HAL
open science

Time resolved measurements in a mesoscopic conductor

Grégoire Rousely

► **To cite this version:**

Grégoire Rousely. Time resolved measurements in a mesoscopic conductor. Condensed Matter [cond-mat]. Université Grenoble Alpes, 2016. English. NNT : 2016GREAY013 . tel-01453263

HAL Id: tel-01453263

<https://theses.hal.science/tel-01453263>

Submitted on 2 Feb 2017

HAL is a multi-disciplinary open access archive for the deposit and dissemination of scientific research documents, whether they are published or not. The documents may come from teaching and research institutions in France or abroad, or from public or private research centers.

L'archive ouverte pluridisciplinaire **HAL**, est destinée au dépôt et à la diffusion de documents scientifiques de niveau recherche, publiés ou non, émanant des établissements d'enseignement et de recherche français ou étrangers, des laboratoires publics ou privés.

THÈSE

Pour obtenir le grade de

**DOCTEUR DE la Communauté UNIVERSITÉ
GRENOBLE ALPES**

Spécialité : **Physique de la matière condensée et du rayonnement**

Arrêté ministériel : 7 Août 2006

Présentée par

Grégoire Roussely

Thèse dirigée par **Christopher Bäuerle**

préparée au sein de l'Institut Néel - CNRS
et de l'École doctorale de Physique

Time resolved measurements in a mesoscopic conductor

Thèse soutenue publiquement le **7 Juillet 2016**,
devant le jury composé de :

Ulf Gennser

Directeur de recherche, LPN-CNRS, Rapporteur

Christian Glattli

Directeur de recherche, IRAMIS-CEA Saclay, Rapporteur

Frank Hekking

Professeur, LPMMC-CNRS/UJF, Président

Xavier Waintal

Chercheur, SPSMS-CEA Grenoble, Invité

Christopher Bäuerle

Directeur de recherche, Institut Néel-CNRS, Directeur de thèse



Remerciements

Ces 3 années ou plutôt 4 années au bâtiment M de l'institut Néel ont été une sacrée expérience. Je me rappelle de mes discussions avec les anciens thésards au début de ce parcours initiatique qui se punctuaient inlassablement par un « tu verras... ». En effet tant qu'on ne l'a pas fait, difficile de se rendre compte de ce que représente une thèse : les longues périodes de galère puis les instants ou tout s'éclaire !

Je tiens en premier lieu à remercier mon directeur de thèse, Christopher Bauerle. Merci d'avoir cru en moi et de m'avoir poussé quand tout foutait le camp. Tu as su (en tout cas essayé de) me transmettre ta rigueur scientifique et ton optimisme même si ce n'était pas gagné !

Je tiens également à remercier Tristan Meunier pour ses éclairages toujours pertinents sur la physique et pour m'avoir enseigné l'art délicat du masqueur. Merci aussi d'avoir pris le temps de m'écouter dans les moments de doute.

La recherche permet de faire de belles rencontres. Il y a quelqu'un à qui je dois beaucoup et qui est devenu un ami, Shintaro Takada. Thank you my friend for your support and your perpetual good mood ! It was a great pleasure to work with such a talented person. Bien sûr je remercie mes compagnons de route : Guigui, pour les soirées détentes autour d'une bière et les soirées moins détentes à Espace Vertical. Benoit, compagnon de course à pied suivi de Pierre André et Candice qui nous ont rejoint dans nos pauses midi/running. Merci à Mathias, Vivien, Hanno, Tobias et ceux que j'oublie, je m'en excuse, pour les bons moments passés ensembles.

Nous avons la chance de bénéficier d'un support technique exceptionnel à l'institut Néel. Sans l'aide de Pierre Perrier (notre ingé cryo attitré), Christophe Hoarau (qui m'a en gros tout appris sur les hautes fréquences), de toute l'équipe de Nanofab' et du Liquef', ce travail de thèse n'aurait tout simplement pas été possible.

J'ai eu l'honneur d'avoir des personnalités de la physique mésoscopique dans mon Jury de thèse. Merci à Christian Glattli et Ulf Gennser, tous deux rapporteurs, pour leurs corrections perspicaces sur ce travail. Merci à Frank Hekking et Xavier Waintal, respectivement président du jury et invité, d'une part pour leur présence à ma soutenance mais surtout pour leur aide inestimable à l'interprétation théorique des résultats. Frank et Xavier ont ce talent de faire comprendre par des images simples les concepts les plus subtils.

Enfin, j'aimerais remercier ma famille pour m'avoir amené jusque là, mes parents et mon grand frère. Merci à ceux qui me sont le plus précieux : Hélène et notre petit bout qui a accepté d'attendre que son papa finisse sa thèse pour arriver.

Contents

1	Introduction	1
2	Background	5
2.1	Quantum transport in 2DEG	6
2.2	The flying qubit	10
2.3	Single electrons sources	13
2.3.1	Tunnel junctions based sources	14
2.3.2	Quantum dot based sources	17
2.3.3	On demand coherent single electron source	19
2.3.4	Surface acoustic waves	20
2.3.5	Lorentzian voltage pulses	22
2.4	Dynamical engineering of interference pattern using fast voltage pulses	24
2.4.1	Principle	24
2.4.2	The Mach-Zehnder interferometer as a probe	26
2.5	Our approach: the tunnel coupled wires	29
2.5.1	Analytical description of the tunnel coupled wires	29
2.5.2	The TCW as a two path interferometer	33
2.5.3	Strategy	34
3	Experimental set-up and technical development	35
3.1	DC connections	38
3.1.1	DC lines	38
3.1.2	Cold finger	40
3.1.3	Temperature performance	41
3.2	RF connections	42
3.2.1	RF line	43
3.2.2	Thermalisation of RF lines	43
3.2.3	Measurement of the temperature of the inner conductor	45
3.2.4	Characterization of the transmission	47
3.2.5	Design of the chip carrier	47
3.2.6	Low resistance ohmic contacts	49
3.2.7	Design and fabrication of the sample	53

3.2.8 Pulse sources	54
Arbitrary Waveform Generator	54
Homemade pulse source	55
3.3 Electronics	59
3.3.1 Control of the electrostatic gates	59
3.3.2 Low noise detection	59
3.4 Conclusion	62
4 Study of the propagation of a voltage pulse	63
4.1 Time resolved measurement of the voltage pulse	64
4.1.1 Principle	64
4.1.2 Comparison between the expected convolution and the in-situ measurement	66
4.1.3 Dependence on the pulse amplitude	68
4.2 Determination of the velocity of the voltage pulse	72
4.3 Plasmonic excitations	74
4.4 Effect of confinement	79
4.4.1 Discussion on the origin of the oscillations	84
4.5 Theoretical approach of the effect of confinement	86
4.6 Conclusion	94
5 Investigation of the tunnel coupled wires	95
5.1 DC regime	96
5.1.1 Observation of antisymmetric oscillations of conductance	96
5.1.2 Temperature dependence of the oscillations	99
5.1.3 Comparison to previous experiment	102
5.2 Short voltage pulses	103
5.2.1 Temperature dependence	105
5.3 Coulomb blockade	107
5.4 Preliminary experiment on the mapping of the tunneling	113
5.4.1 Transfer of the wave-packet between the wires	114
5.4.2 Comparison to the calculated convolution	115
5.5 Confirmation of the velocity	117
5.6 Conclusion	118
6 Conclusion and perspectives	119
Appendix	123
A Delay due to the attenuators	123
B Effect of the confinement	125
C Simulation of the electrostatic potential for a low V_{tunnel}	127

D Intrinsic delay of the RF line connected to the tunnel gate	129
---	-----

Bibliography	131
--------------	-----

CHAPTER 1

Introduction

In the early 80's, the progress in micro-fabrication techniques have made possible the realization of devices whose typical dimensions were smaller than the coherence length of the electrons when placed at very low temperatures. Whereas such devices are composed of billions of atoms, the electronic transport in these devices exhibits quantum effects which are usually associated to the «microscopic» world. This particular scale at the interface of the macroscopic world and the microscopic world is the kingdom of mesoscopic physics. The first success of mesoscopic physics were obtained using metallic structures which enabled to identify the signature of electronic quantum interferences. In 1981, Sharvin and Sharvin observed oscillations of the resistance of a magnesium cylinder depending on the magnetic field applied parallel to the cylinder [Sha81]. Few years later, the observation of universal conductance fluctuations in narrow metallic wires [Umb84] and Aharonov-Bohm oscillations [Web85] in micrometer sized gold rings definitely laid the foundations of mesoscopic physics.

A major boost in the field came from the availability of high quality two dimensional electron gas (2DEG) formed in the GaAs/AlGaAs heterostructure. In these 2D systems, the movement of the electrons is ballistic (without any collisions) over several micrometers. Moreover, the electron gas can be shaped at will using metallic gates deposited at the surface of the material. This opened the way to the realization of remarkable experiments such as the observation of quantized conductance steps in a quantum point contact [Van88; Wha88]. Rapidly, this 2D system has been envisaged to realize quantum electron optics experiments. The purpose of this field is to transpose the concepts of quantum optics using electrons instead of photons. The interest of such experiments are numerous: from a fundamental point of view, it paves the way to new schemes that are not possible with photons because electrons obey to Fermi statistics and they are charged particles, therefore they interact strongly contrary to photons. The basic bricks needed to perform quantum optics experiments with electrons such as beam splitters, phase shifters and electronic «optical fibers» already exist. Using these elements, several groups have been able to perform the counterparts of quantum optic experiments such as the realization of an electronic two path interferometer [Ji03; Rou08b] or Hanbury-Brown and Twiss [Ned07] experiments. Quantum electron optics can also be used to build the fundamental element of a quantum

computer, a qubit. The operation of a qubit based on this approach, the so-called flying qubit, has been demonstrated in [Yam12]. However, all of these pioneering experiments were performed using ensemble measurements. To go a step further in the realization of quantum electron optics experiments as well as the use of flying qubits for quantum information processing, it is of importance to control these systems at the single electron level.

Only recently, few systems have been successfully used to realize on-demand single electron sources into such a ballistic two-dimensional electron system such as an AC driven quantum dot [Fev07], the nonadiabatic single electron pump [Fle13] and surface acoustic wave based source [Her11; McN11]. Among them, the recent single electron source based on short Lorentzian voltage pulses [Dub13] is of particular interest. Besides being very attractive because of its simplicity, such a source could also be used to reveal interesting new physics when coupled to an electronic interferometer. Indeed, our collaborators at CEA Grenoble have shown that when a short voltage pulse is injected in an electronic interferometer, novel interference effects are expected due to the interaction of the pulse with the surrounding Fermi sea [Gau14a]. However, the conditions to observe these effects are quite stringent: the temporal width of the voltage pulse has to be significantly smaller than its time of flight through the two path interferometer: the longer the interferometer, the easier this condition is met. At the same time, the interferometer has to be smaller than the coherence length of the electrons otherwise interference effects are washed out. It is therefore of importance to determine the velocity of the voltage pulse through the interferometer.

A possible architecture for the realization of an electronic interferometer is to engineer a potential landscape to confine the electrons in quasi 1D wires by using electrostatic gates deposited on the surface of the GaAs/AlGaAs heterostructure. Using this approach, a simple electronic two path interferometer, the so-called tunnel coupled wires, can be realized by coupling two 1D wires via a controllable tunnel barrier [Bau14b].

The aim of this PhD work is to address important questions regarding the observation of new quantum interference effects in an electronic two path interferometer. The main objective was to answer basic questions related to the propagation of a short voltage pulse in a quasi 1D wire formed in a two dimensional electron gas: does the propagation through the sample affect the pulse shape ? What is the velocity of the pulse in such a system ? In addition, we have studied a long electronic two path interferometer based on tunnel coupled wires in order to observe coherent tunneling of the electrons.

This manuscript is organized as follows.

In chapter 2, the basic concepts are introduced: the concept of flying qubit is presented and the present state of the art of the single electron sources is given. As mentioned above, combining the single electron source based on short voltage pulses to an electronic two path interferometer leads to novel interference effects. We expose the theoretical work of our collaborators at CEA Grenoble that allows to understand the origin of these striking effects. Finally, a theoretical description of the two path interferometer based on tunnel coupled wires, which is experimentally studied in chapter 5, is presented.

An important effort has been devoted to the realization of an experimental set-up adapted to these «fast quantum electronic» experiments. We have built a set-up that includes a large number of DC lines in order to control the electrostatic gates and high frequency lines compatibles with a cryogenic environment. A particular attention has been given to ensure a proper transmission of high frequency signals from the outside of the cryostat to the heart of the sample. This work is detailed in chapter 3.

In chapter 4, we present the results on the study of the propagation of a short voltage pulse (< 100 ps) injected in a quasi 1D wire defined by electrostatic gates. Using a specific technique that allows time resolved measurements of the voltage pulse directly at the sample level, we have been able to determine its velocity. Our measurements indicate that the voltage pulse propagates much faster than the Fermi velocity. The measured velocity is in very good agreement with the plasmon velocity for a gated two-dimensional electron gas. We show that this velocity can be controlled by modifying the confinement potential due to the electrostatic gates. We have developed a theoretical approach of the effect of the confinement based on the work of Matveev et Glazman [Mat93] which shows a good agreement with our results.

We then investigated the possibility to observe coherent tunneling in $40\ \mu\text{m}$ long tunnel coupled wires. We observe oscillations of the conductance as a function of barrier height between the two tunnel coupled wires. These features have been observed for DC measurements as well as for short voltage pulses and could be attributed to coherent tunneling. However, further measurements need to be realized to corroborate our findings and the interpretation of these results. Finally, we present preliminary experiments on the time resolved mapping of the tunneling of the electrons excited by the voltage pulse in the tunnel coupled wires. These results are presented and discussed in chapter 5.

CHAPTER 2

Background

The recent developments in mesoscopic physics have opened the way to perform experiments similar to the ones of quantum optic but using electrons instead of photons. The basic bricks needed to perform quantum optic like experiments such as single photon sources and detectors, beam splitters, phase shifters and even optical fibers have now their electronic counterparts. In the first part of this chapter, we present a system which is at the origin of many breakthroughs in the field of mesoscopic physics, the AlGaAs/GaAs heterostructure inside which a two dimensional electron gas (2DEG) is formed. The electrons of this gas can propagate over several μm without any scattering. Combined with the nano-fabrication, it is then possible to build electronic systems where the behavior of the electrons is governed by the rules of quantum mechanic. The high control over the electrons forming the 2DEG have made possible the first experiments of «electronic quantum optic».

We then introduce the concept of flying qubit, a particular architecture of qubit based on the same tools needed for quantum optic like experiments. We present two different experimental realizations of flying qubit that are the electronic analogs of the well known Mach-Zehnder interferometer.

The ultimate electronic quantum optics as well as the process of quantum information using flying qubits require to be done at the single electron level. In the third part, we review the different single electron sources built over the past years. Single electron sources are not only interesting from a fundamental point of view but also for the definition of a current standard. Many different approaches have been implemented exploiting a variety of physical phenomena. Very recently, an elegant approach based on voltage pulses have been realized. This required the use of fast voltage pulses with a time width < 100 ps. This timescale is similar to the internal timescale which characterizes the dynamical aspects of the quantum behavior of the electrons in a mesoscopic system.

In the last part, we present a recent theoretical work of our collaborators at CEA Grenoble on this emerging field of fast quantum electronics. They showed that the interaction of a fast voltage pulse with the surrounding Fermi sea allows to engineer striking effects that can be revealed using electronic interferometers. It also introduces a new way to manipulate quantum information by simply controlling the characteristics of the voltage pulse.

2.1 Quantum transport in 2DEG

The progress of mesoscopic physics during the last 30 years is largely based on the AlGaAs/GaAs heterostructure where a two dimensional electron gas (2DEG) is formed at the junction between a n-doped Aluminum-Gallium-Arsenide (n-AlGaAs) layer and Gallium-Arsenide (GaAs) layer. When these two semiconductor materials are brought in contact, the higher Fermi energy of the wide band-gap n-AlGaAs (2.19 eV) equilibrates with the one of the narrow band-gap GaAs (1.42 eV). The electrons migrate from the n-AlGaAs layer to the GaAs layer resulting in a local positively charged layer of donors, in this case silicon (Si). This induces an electric field which bends the bands and a triangular potential well is formed. At low temperature, only the first quantized level is occupied forming the two dimensional electron gas (see fig. 2.1).

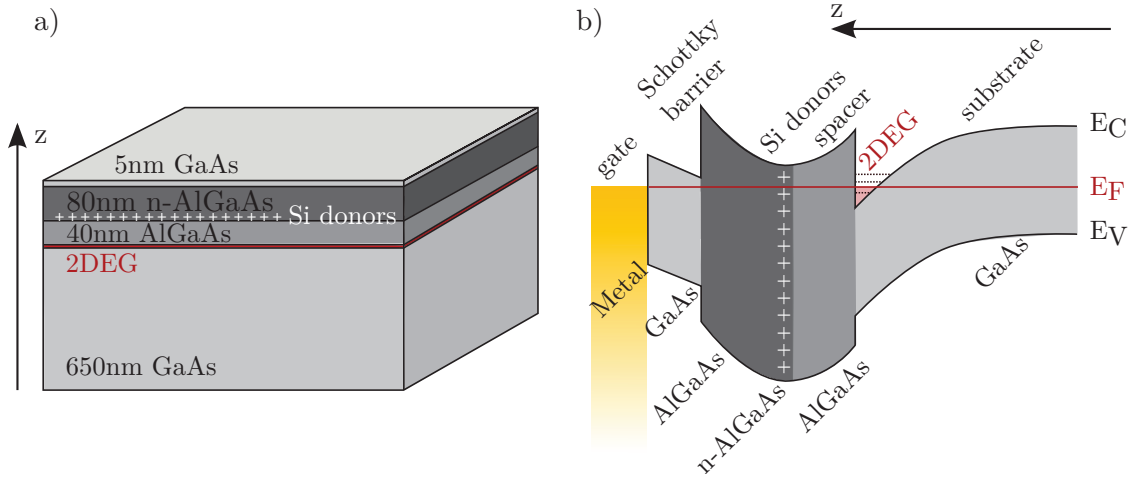


Figure 2.1: a) AlGaAs/GaAs heterostructure, the growth is realized by MBE from bottom to top. b) Due their different band gap, a triangular quantum well is formed at the interface between the GaAs and the AlGaAs. The 2DEG is formed by the electrons which are confined and occupy only the first energy level.

The scattering of the electrons is mostly due to the potential landscape formed by the ionized donors. By putting this layer of donors far away from the junction (in our case ~ 40 nm), the scattering rate is strongly reduced allowing to reach a high mobility. For the envisaged experiments, it is important to dispose of a very high quality 2DEG. Such a high quality 2DEG can be realized by molecular beam epitaxy (MBE) growth allowing to reach a nearly atomically clean structure. The high-mobility GaAs/AlGaAs heterostructure used during my thesis has been provided by our collaborator Prof. Andreas Wieck from the University of Bochum.

The 2DEG has a mobility $\mu = 1.89 \times 10^6 \text{ cm}^2\text{V}^{-1}\text{s}^{-1}$ and a density $n_s = 2.11 \times 10^{11} \text{ cm}^{-2}$. From these quantities, we can estimate the mean free path of the electrons:

$$l_e = \sqrt{2\pi n_s} \frac{\hbar \mu}{e} = 14 \mu\text{m}, \quad (2.1)$$

which means that in average, the distance between two successive collisions of an electron on a scatterer is $14\ \mu\text{m}$. Over this characteristic distance, the movement of the electrons is ballistic. The combination of this long mean free path and nano-fabrication allows to build devices in which the electrons can propagate without any collision. The other important characteristic length is the coherence length l_ϕ . It corresponds to the length over which the phase of the electron wave function stays well defined. At very low temperature, it can reach several tens of μm . To study interference phenomena due to the wave like behavior of the electrons, it is primordial that the size of device is smaller than l_ϕ .

By depositing metallic gates on the surface of the heterostructure one can engineer an electrostatic potential to control the electrons forming the 2DEG. The Schottky barrier formed at the metal-semiconductor interface allows to apply a negative voltage on a gate without any current flowing to the 2DEG. For a sufficiently large negative gate voltage, the electrons below the gate are pushed away and the 2DEG is locally depleted as illustrated in fig. 2.2. Using several gates, one can engineer a particular confinement potential allowing to isolate some portions of the 2DEG from the rest of the gas and to create for instance a channel to guide the electrons. The low density and hence the large Fermi wavelength λ_F of the electrons, typically $\lambda_F \simeq 55\ \text{nm}$ in our case, allows to realize nano-patterned structures whose dimensions can be on the order of λ_F and therefore to control the electrons at the single electron level. Electrical connections with the 2DEG are realized with ohmic contacts. These contacts are made of an alloy of several materials (Nickel/Gold/Germanium) which diffuses from the surface to the 2DEG when annealed at high temperature.

These high quality 2DEGs are formidable tools to investigate mesoscopic physics. A lot of striking experiments have been performed in this system. A famous realization is the quantum point contact (QPC). In 1988, van Wees et al. in Delft as well as Wharam et al. in Cambridge have shown that the conductance of a small constriction separating two wide areas of 2DEG was quantized [Van88; Wha88]. The QPC was formed by two electrostatic gates separated by a few hundred of nanometers. When a negative voltage is applied on the gates, the 2DEG is depleted and only a small channel remains between the two gates (see fig. 2.2). Applying a more and more negative voltage on the gates results in a continuous reduction of the channel width but the conduction changes in discrete steps. The constriction has a dimension on the order of the Fermi wavelength λ_F and act as an electron waveguide. The current through the constriction is carried by a discrete number of electronic modes. For a constriction width equal to $\lambda_F/2$, one single mode is transmitted. As the width is increased to λ_F , two modes are transmitted and so on. As a consequence, the conductance increases in steps of $2e^2/h$ as the voltage applied on the gates is made less and less negative as shown in fig. 2.3. To understand this phenomena, it is necessary to use an approach known as the Landauer-Büttiker formalism. We refer the interested reader to [Dat95].

QPC have attracted a lot of interest because they can be used as an electronic beam splitter. Indeed, on each plateau, the electronic modes are transmitted with a probability equal to 1. Between two plateaus, the transmission probability of the mode being added can be tuned from 0 to 1. When the QPC is tuned such that the first mode has a transmission

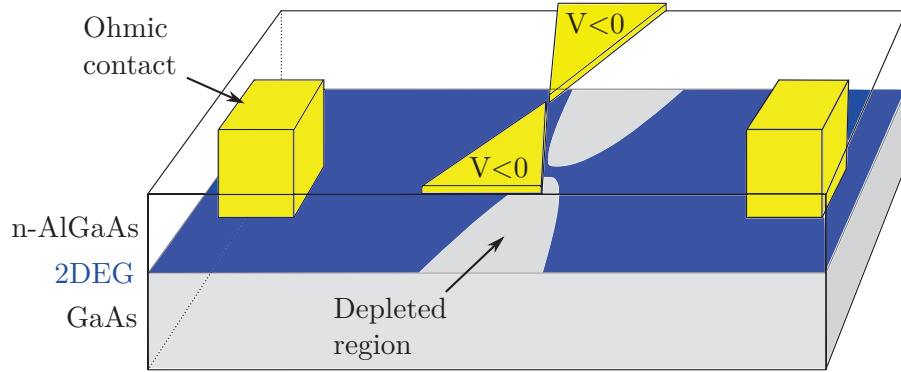


Figure 2.2: Schematic illustrating the depletion of the 2DEG when a negative voltage is applied on the two surface metallic gates. Ohmic contacts allow the electrical connections to the 2DEG. Such a geometry with a small constriction between two wide areas of 2DEG is a so-called quantum point contact.

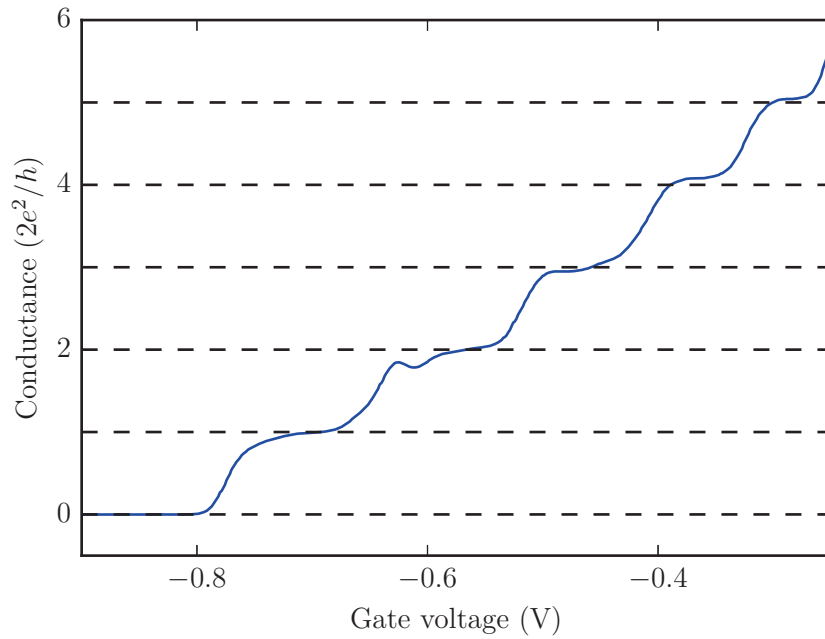


Figure 2.3: Quantized conductance of a QPC implemented in our sample measured at 20 mK. At large negative voltage, the QPC is fully pinched and current cannot flow. As the voltage applied on the gates is made less and less negative, the constriction width increases and when it reaches $\lambda_F/2$, the first electronic mode is transmitted. Each mode having a conductance equal to $2e^2/h$, each time the QPC width increases by a multiple of $\lambda_F/2$, an additional mode is transmitted and the conductance increases by $2e^2/h$.

probability equal to $1/2$, a coherent superposition of the transmitted and reflected states is

created. This feature allowed to perform pioneering experiments of electron quantum optics such as the realization of first electronic analogue of the Mach–Zehnder interferometer by Ji et al. [Ji03] (see fig. 2.7).

Using appropriated electrostatic gates, one can realize a quantum dot¹ where only a small number of electrons are confined in a controlled potential. This system can be seen as an artificial atom because the confinement of the electrons results in a quantized energy spectrum [Kou01]. The development of quantum dots in 2DEG has triggered an incredible number of experiments allowing to study a broad range of physical phenomena such as Coulomb blockade [Kou97], Kondo effect [Kas98; Wie00], coherent spin manipulation [Kop06; Pet05] to cite but a few examples. These experiments on spin manipulation have shown that quantum dots are also a promising candidate to build a quantum computer based on arrays of quantum dots where the spin states of trapped electrons inside each dot is used as a qubit as proposed by Loss and DiVincenzo [Los98].

In their experiment, Ji et al. also exploited a spectacular effect which takes place in a 2DEG when it is submitted to a strong perpendicular magnetic field, the quantum Hall effect². For a detailed description of the quantum Hall effect, we refer the reader to [Dat95]. To sum up, under a strong perpendicular magnetic field of a few T, the current is only carried on the edges of the sample by the so-called edge channels. Classically, one can understand this property by the fact that under a magnetic field, the motion of the electrons is circular, this is the cyclotron motion. In the bulk, the electrons trajectories are closed and they do not participate to the transport. On the edges, they are reflected and they propagate by skipping orbits in opposite directions for opposite edges (see schematic in fig. 2.4) because of the chirality imposed by the magnetic field. These edge channels have remarkable properties: because of this chiral transport, the backscattering of the electrons is suppressed [Büt88], these channels are ballistic over several hundreds of μm and the coherence length reaches $\sim 20\mu\text{m}$ [Rou08b]. The number of edge channels is quantized and depends on the amplitude of the magnetic field applied. They can be easily controlled by using electrostatic gates to engineer a potential landscape along which the channels propagate. They are then well suited to transport the electrons in a coherent way for quantum electron optics experiments.

Moreover, the Hall conductance, which is the transverse conductance of the system is quantized and directly related to the number of edge channels. As the magnetic field is increased, the number of channels decreases. Each time a channel is removed, the Hall conductance decreases by step of exactly e^2/h . Actually, the Hall conductance plateaus are so accurate that the quantum Hall effect is used to define a resistance standard.

1 quantum dots can be made in a lot of systems: self-assembled quantum dots, semiconductor lateral or vertical dots, single molecules trapped between electrodes, semiconductor nanowires, carbon nanotubes, etc.

2 The quantum Hall effect was discovered by Klaus von Klitzing in a silicon metal-oxide-semiconductor field-effect transistor [Kli80] containing a two dimensional electron gas at the semiconductor-oxide interface.

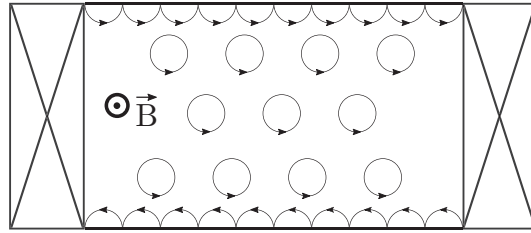


Figure 2.4: Classical picture of the quantum Hall effect. Under a magnetic field B applied perpendicular to the plane, the electrons follow cyclotron orbits. In the bulk, the electrons are localized and do not participate to the transport. On the edges however, the electrons are reflected and propagate forming the so-called edge channels. The electrons propagate in opposite directions for opposite edges because of the chirality imposed by the magnetic field.

2.2 The flying qubit

The implementation of a qubit in a solid state system like a 2DEG using nano-fabricated structures is an appealing approach because of the scalability of these nanometer sized devices. The quantum information can be encoded in the degrees of freedom of the electron either charge [Hay03; Pet10] or spin [Kop06; Pet05]. One possible architecture is to use distant static qubits in between which the quantum information has to be transferred coherently. As mentioned above, quantum dots have already been used as qubits but the connection between distant quantum dots to carry the quantum information is a difficult task. As we will see in the following, one way is to directly transport an electron on which the information is encoded between distant quantum dots using surface acoustic waves. Another approach is to exploit the emission of a single photon by a quantum dot and use this photon to transfer the quantum information [De 12; Gao12].

A different strategy is to combine the transfer and the manipulation of the quantum information. This architecture is the so-called flying qubit: coherent manipulation of the quantum state of a single electron is realized during its propagation in a one dimensional ballistic system [Ber00; Ion99]. Conceptually, a flying qubit is similar to a two-path interferometer [Yam12]. Let's consider the Mach-Zehnder interferometer sketched in fig. 2.5: the source emits a stream of coherent particles which are partitioned between the two arms of the interferometer by the first beam splitter. A phase shifter inserted on one arm allow to control the phase difference between the two paths. The two paths are recombined on the second beam splitter where they interfere and the two detectors measure the two different outputs. In terms of quantum information processing, this system can be seen as a fully controllable qubit. The two eigenstates of the qubit are defined by the pseudo spin states $|\uparrow\rangle$ and $|\downarrow\rangle$ which refer to the presence of a single electron in the associated arm of the interferometer as shown in fig. 2.5. A convenient way to represent a qubit is the Bloch sphere representation where the south and north poles are the eigenstates of the qubit as shown in fig. 2.6. The first beam splitter allows to rotate the qubit state along the y-axis by preparing any arbitrary superposition of state of the electron between the

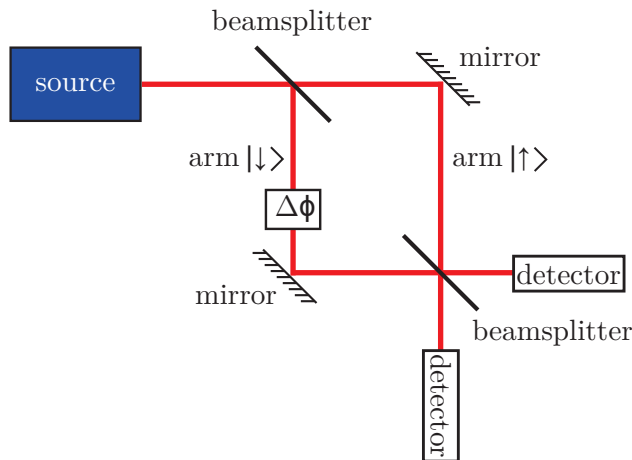


Figure 2.5: Schematic of the Mach-Zehnder interferometer.

$|\uparrow\rangle$ and the $|\downarrow\rangle$ arms. The phase shifter allows to rotate the qubit state along the z-axis. The combination of these two rotations is sufficient to explore all the Bloch sphere and therefore to fully control the qubit state. The second beam splitter projects the state of the qubit on the eigenstates and the two detectors allow to readout the projected qubit state. An important point here is that the size of the interferometer has to be smaller than the coherence length of the electrons otherwise the control over the phase is lost.

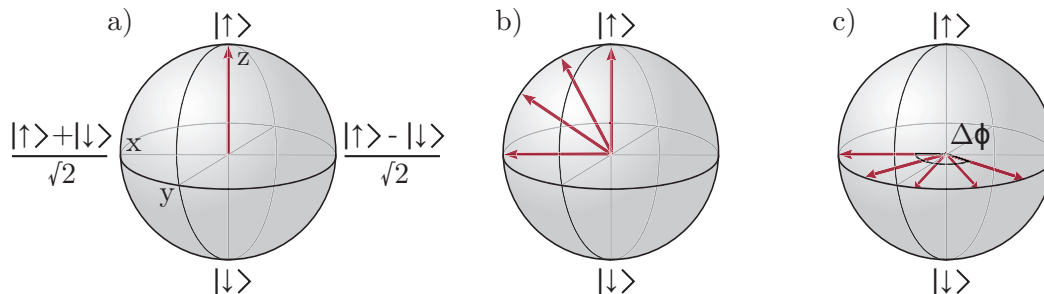


Figure 2.6: a) Bloch sphere representation of the qubit, the state of the qubit is indicated by the arrow. The south and north poles of the sphere are the eigenstates of the qubit. b) Rotation along the y-axis realized by the beam splitter. When the beam splitter is tuned in the 50:50 regime, the qubit is prepared in the so-called symmetric state $\frac{|\uparrow\rangle + |\downarrow\rangle}{\sqrt{2}}$. c) Rotation along the z-axis controlled by the phase shifter. These two rotations can be arbitrarily controlled by changing the ratio of the beam splitter and the phase shift such that one can fully control the state of the qubit.

As discussed previously, an electronic beam splitter can be realized with a QPC and the paths where the electrons propagate by using edge states of the Quantum Hall effect as in the device of Ji et al. Another possibility detailed afterwards is to use a tunnel barrier separating a quantum wire in two distinct channels as a beam splitter [Ala90; Tsu90] and to define the paths where the electron propagate with electrostatic gates.

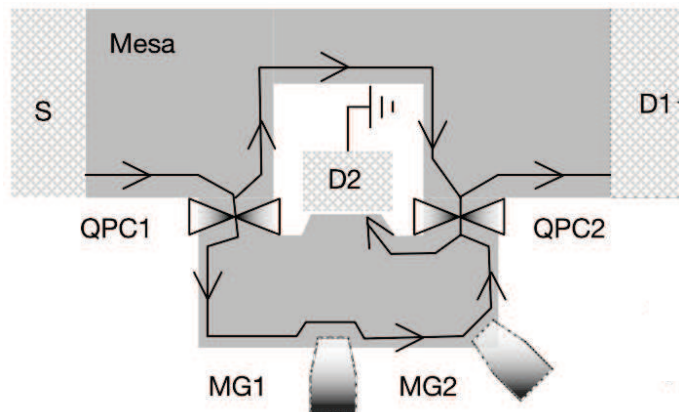


Figure 2.7: Schematic of the electronic two path interferometer realized by Ji et al. extracted from [Ji03]. A strong perpendicular magnetic field is applied such that the electrons propagate in the edge channels of the quantum Hall effect. The QPC 1 splits the electrons coming from the source S into the two arms of the interferometer. Both arms are recombined and interfere on the QPC 2. The phase between the two arms can be modified using the Aharonov-Bohm effect either by varying the magnetic field or by modifying the trajectory of the lower edge channel with the two electrostatic gates MG1 and MG2. D1 and D2 are two ohmic contacts used to measure the two complementary output currents (D2 is actually grounded).

To induce a phase shift between the two arms of the Mach Zehnder interferometer, one can exploit the Aharonov-Bohm effect. The two arms of the interferometer form a closed loop. An applied magnetic field results in a certain magnetic flux enclosed by the loop. One can show that this flux induces a phase difference $\Delta\phi$ between the two paths given by:

$$\Delta\phi = \frac{eBS}{\hbar} \quad (2.2)$$

where e is the electron charge, B the amplitude of the magnetic field and S the surface area of the loop. The phase can be changed by varying the magnetic field or the path length which is easily done with edge channels by changing their trajectory with electrostatic gates. In their device, Ji et al. used these two options to engineer a phase shift. This system is of course interesting from a quantum information point of view but it is also a very nice tool to explore fundamental physics. Similar devices have been used to study the behavior of interfering electrons [Ned06] and decoherence mechanisms [Huy12; Rou08a; Rou09]. The coherence length of edge states was also determined by measuring the visibility of the interference pattern for interferometers of different sizes [Rou08b]. Neder et al. coupled two interferometers to study the interference between two indistinguishable electrons [Ned07]. Another experiment demonstrated the realization of a quantum eraser with two electronic Mach-Zehnder interferometers entangled via Coulomb interaction [Wei14].

Yamamoto et al. built a flying qubit [Yam12] that can be operated without the need of edge channels where the two paths of the interferometer are only defined by electrostatic

gates. A scanning electron microscope (SEM) picture of their device is presented in fig. 2.8. The beam splitters are formed by two tunnel barriers labeled as V_{T1} and V_{T2} , the two paths of the interferometer being the upper channel and the lower channel separated by these tunnel barriers. The control over the phase between the two arms is achieved by means of the Aharonov-Bohm effect. In the center part of the interferometer, the gate V_{T1} is enlarged to well separate the two arms forming a ring. A perpendicular magnetic field is applied such that the enclosed flux induces a phase difference. As we will see in sec. 2.5, a single tunnel barrier is actually sufficient to realize a two path interferometer. Compared to the device of Ji et al. for which the use of edge channels requires a high magnetic field (a few T), this one can be operated at low magnetic field, a few tens of mT. This allowed them to study phenomena that can only be accessed at low magnetic field such as the Kondo effect. By inserting a quantum dot which contains an odd number of electrons and acts as a Kondo impurity in one of the arms, Takada et al. were able to measure the transmission phase shift acquired by the electrons coherently scattered by this Kondo impurity [Tak14].

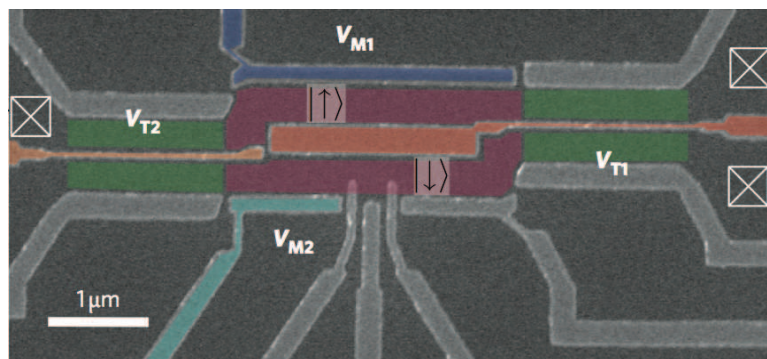


Figure 2.8: SEM picture of the device realized by Yamamoto et al. used as a flying qubit in [Yam12]. An incoming stream of electrons from the upper left contact (white crossed square) is split into two by the tunnel barrier V_{T2} which acts as a beam splitter. The two arms are decoupled by the large middle gate, a magnetic field applied perpendicular to the plane allows to control the phase between the two paths thanks to the Aharonov-Bohm effect. The two paths are recombined on the second tunnel barrier V_{T1} .

2.3 Single electrons sources

To really process quantum information using the systems described previously, it will be necessary to couple several flying qubits and above all to operate them at the single electron level. This will require time controlled single electron sources and single electron detectors. The development of single electron sources is well advanced and several systems are now available. The quest for a single electron source is also motivated for metrological purposes. The easiest way to define the ampere would be to measure the current generated by a well defined number of electrons. An ideal system would be a source emitting exactly N electrons and repeat this emission at a given frequency f . To fulfill the metrological needs,

the current produced $I = Ne f$ should be on the order of several of pico-amperes and the relative error $\delta I/I$ lower than 10^{-8} [Pek13]. This system would be the third branch of the quantum metrological triangle, one being the Josephson voltage standard and the second the quantum Hall resistance standard [Kel08].

2.3.1 Tunnel junctions based sources

The progress of nano-fabrication in the 90's allowed to build the first solid state devices in which single electron transport was observed and then controlled. This was first made possible with tunnel junctions, a device consisting of two metallic electrodes separated by a very thin insulating layer. A tunnel junction can be modeled as a capacitance in parallel with a very large resistance. Applying a voltage V across a tunnel junction results in the random tunneling of electrons across the insulating layer. It is not possible to control the number of transferred charges with a single junction because of this randomness. To control precisely the number of flowing electrons, it is necessary to build an array of tunnel junctions. The other key ingredient to control single electrons is the Coulomb blockade. In between two junctions, a metallic island is formed. When an electron tunnels onto the island, the energy configuration of the island is modified. If the charging energy e^2/C to pay to add one extra electron where e is the electron charge and C the junction capacitance onto the island becomes greater than the thermal fluctuations $k_B T$, no other electron can tunnel onto the island which leads to the so-called Coulomb blockade.

The first observation of this Coulomb blockade was reported by Fulton and Dolan in 1987 [Ful87], confirming theoretical predictions [Ave86]. They used aluminum/aluminum oxide/aluminum junctions having a typical size of ~ 100 nm and a capacitance on the order of 100 fF such that at a temperature of 1 K, $e^2/C > 10k_B T$. In fact they implemented the first single electron transistor (SET), a device with two tunnel junctions (see schematic in fig. 2.9). The electrostatic potential of the island is controlled by a capacitively coupled voltage source U . In this case, the charging energy is given by $E_C = e^2/C_\Sigma$ where $C_\Sigma = C + C' + C_G$. C and C' are the junctions capacitances and C_G is the capacitance between the island and the voltage source. The number of electrons on the island is given by $n = N - N'$. Under a small bias ($V \ll e^2/C$), the flow of electrons through the island can be switched on and off by varying U . Each time U is $\sim ne/2C_G$, the energy configurations of the island with n and $(n+1)$ electrons are equivalent. The system oscillates between these two states and electrons can flow. In between, Coulomb blockade occurs and no electron can flow.

This SET is an ultra sensitive electrometer because a variation of only a fraction of the electron charge on C_G can switch on and off a current on the order of 10^9 electrons per second [Dev92]. However, the charges flowing through the island cannot be controlled at the single electron level. It is not possible to keep an electron on the island for a certain time and then release it at will because when one electron tunnels onto the island, it is energetically favorable for another electron to leave the island. The realization of a controlled single electron source requires at least three junctions.

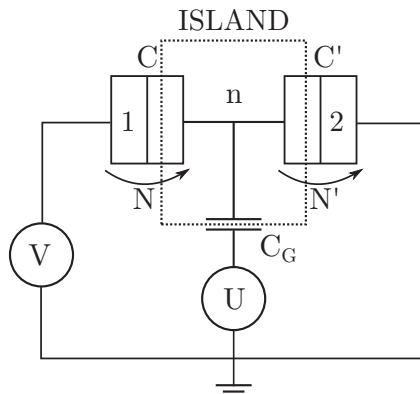


Figure 2.9: Schematic of a SET. A metallic island is formed between two tunnel junctions (labeled 1 and 2). The number of electrons n on the island is the difference between the number of electrons N entering in the island and the number N' leaving the island. The voltage U , by modifying the island potential, authorizes or blocks the passage of the current due to the small bias V across the island.

Single electron pump and turnstile

Almost at the same time, two types of single electron sources based on an array of tunnel junctions have been realized: the electron turnstile developed by Geerlings et al. [Gee90] and the electron pump developed by Pothier et al. [Pot91].

The simplest device is the electron pump (see schematic in fig. 2.10). It consists of a series of three junctions. Two metallic islands are formed and their potentials are controlled by independent voltages U_1 and U_2 . If the left island is tuned to let tunnel an electron but the right island not, then one electron is trapped. To operate the pump, U_1 and U_2 are controlled such that they describe the circle around the point P in the stability diagram of the pump as shown in fig. 2.10. Inside each hexagon of the diagram, the numbers correspond to the couple (n_1, n_2) for which the charging state of the left and right islands is stable. During this cycle, single electrons tunnel sequentially first from the left lead onto the left island, then onto the right island and finally to the right lead such that a single charge has been transmitted in a controlled way. It is done by driving U_1 and U_2 with sinusoidal excitations phase shifted by $\pi/2$. The cycle is repeated at a clock frequency f , producing a current $I = ef$. This electron pump is reversible: depending on the sign of phase shift between U_1 and U_2 , current can flow without any source-drain voltage from left to right or right to left. The current produced is independent of the bias V applied over a large range and the system can even «pump» electrons from low potential to high potential.

The electron turnstile allow to trigger the transfer of a single electron with only one driving voltage but at least four junctions are needed [Gee90]. It is a SET with two additional junctions on each sides forming two intermediate islands (see fig. 2.11). The potential barriers created by these two islands block the tunneling of the electrons through the SET

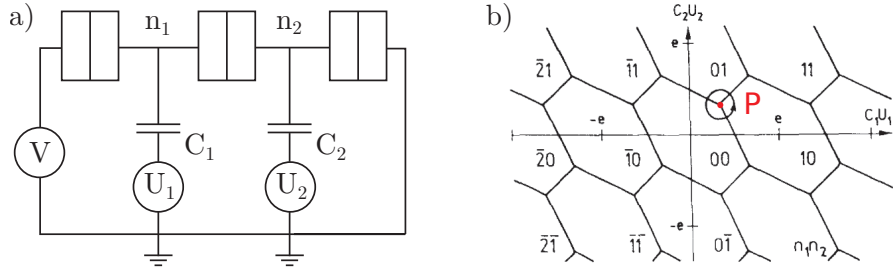


Figure 2.10: a) Schematic of the electron pump. b) Stability diagram of the electron pump extracted from [Dev92].

occurring for $U \sim e/2C$. When U is increased above a certain value, a charge is transferred from one lead onto the central island and when it is decreased one charge can leave the central island. The sign of the current (the transfer direction) is imposed by the sign of the source drain voltage, repeating this modulation at a frequency f generates a current $I = ef$. Contrary to the electron pump, this system is irreversible.

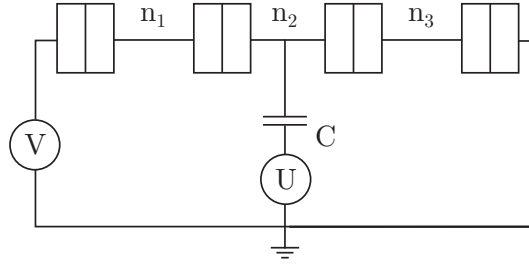


Figure 2.11: Schematic of the electron turnstile.

The relative precision of both sources is on the order of a few percents, far away from metrological needs. The main source of error is the co-tunneling (two electrons tunnel simultaneously). By increasing the number of junctions, these fluctuations can be reduced. An electron pump with seven junctions realized by Keller et al. has allowed to reach a relative error of $15 \cdot 10^{-8}$ [Kel96]. However, the operation frequency is limited to a few MHz by the intrinsic RC time of the junctions and hence the current produced to ~ 1 pA limiting the interest for a metrological application.

Besides this metallic tunnel junctions, single electrons turnstile have also been implemented using normal metal/superconductor junctions by Pekola et al. [Pek08]. They used two devices which are basically a SET, one with superconducting leads and metallic island and one exactly the opposite. As mentioned before, a SET in principle cannot be used as a single electron source. In this case, the combination of the superconducting gap Δ and the Coulomb blockade suppresses tunneling in an energy range determined by Δ . When the junction is biased with a voltage $V \sim \Delta/e$ and the gate capacitively coupled to the

island is driven with the proper amplitude at a frequency f , a current $I = ef$ is produced. Latest generations show an accuracy of $\sim 10^{-6}$ but the current in these devices is presently limited to a few tens of picoamperes [Pek10].

It is important to mention that the devices described above could be used to study coherent phenomena with single electrons but their utilization for quantum information is limited by the nature of the tunneling process because there is no real control on the injection time of the electrons.

2.3.2 Quantum dot based sources

In 1991, Kouwenhoven et al. built a quantum dot turnstile [Kou91]. Compared to the devices describe above, the metallic island is replaced by a quantum dot in a semiconductor heterostructure and the high tunability of tunnel barriers in such a system is exploited. A SEM picture of the sample is shown in fig. 2.12. A quantum dot is formed by means of four electrostatic gates: 1, 2, C and F (3 and 4 are grounded). Tunnel barriers are controlled by the voltage applied on gates 1 and 2. By modulating gates 1 and 2 with a periodic radio-frequency signal, the signal on gate 2 being phase shifted by π , the cycle presented in fig. 2.12 is realized. The left tunnel barrier is lowered such that a single electron can tunnel onto the dot. At the same time, the right barrier is increased making any tunneling from the dot to the right lead impossible. Tunneling of a second electron into the dot is prevented by Coulomb blockade. The right barrier is then lowered and this excess electron is transferred into the right lead. Under a small bias, when this cycle is repeated at a driving frequency f a current $I = ef$ is produced. When gates 1 and 2 are driven with different RF excitation amplitude, a current is produced without any source drain bias. This pump was operated at a frequency of ~ 10 MHz. In this regime, the change of the dot potential is slow compared to the characteristic energy relaxation time of the electrons, the pump is hence operated in the adiabatic regime. In this regime, it necessary to drive the two gates to produce a net flowing current [Mos02].

This kind of system can also be driven in the non adiabatic regime. Blumenthal et al. used a double modulated barriers pump driven at \sim GHz frequency, they produced a quantized current of several hundreds of pico-amperes [Blu07]. In this non adiabatic regime, driving a single gate is sufficient to produce a directional current. As schematized in fig. 2.13, a few electrons are trapped into the dot, the potential of the dot is then tuned to keep only a single electron and a strong voltage applied on one of the side gate of the dot ejects the electron. Such single gate pumps have been implemented using silicon nanowire [Fuj08] and etched AlGaAs/GaAs nanowire [Kae08]. By using the design of etched AlGaAs/GaAs nanowire (see b in fig. 2.13) and applying a strong perpendicular magnetic field of 14 T which enhances the confinement of the electron captured in the dot, Giblin et al. improved the quantization accuracy. They generated a quantized current up to 150 pA with an accuracy better than 1.2 parts per million (ppm) [Gib12]. Up to now, this system is one of the most promising candidates to define a quantum standard of current.

Recently, such sources have been used to investigate the property of the single electron emitted [Fle13]: the electron is actually emitted with a high energy, ~ 150 meV above the

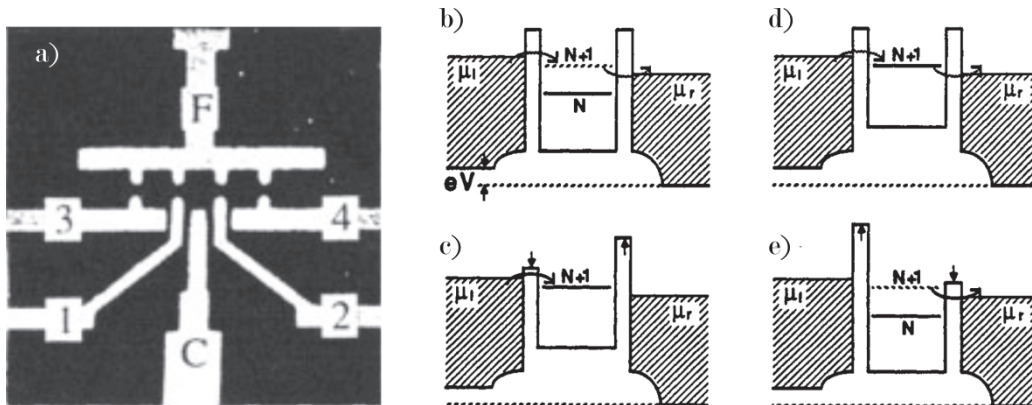


Figure 2.12: a) SEM picture of the sample used by Kouwenhoven et al. as a quantum dot turnstile. b) to e) Potential of the dot when gate 1 and 2 are modulated by a radio-frequency signal leading to the transfer of an electron. μ_1 and μ_2 are the electrochemical potentials of the left and right reservoirs and V the bias voltage. Figures are extracted from [Kou91].

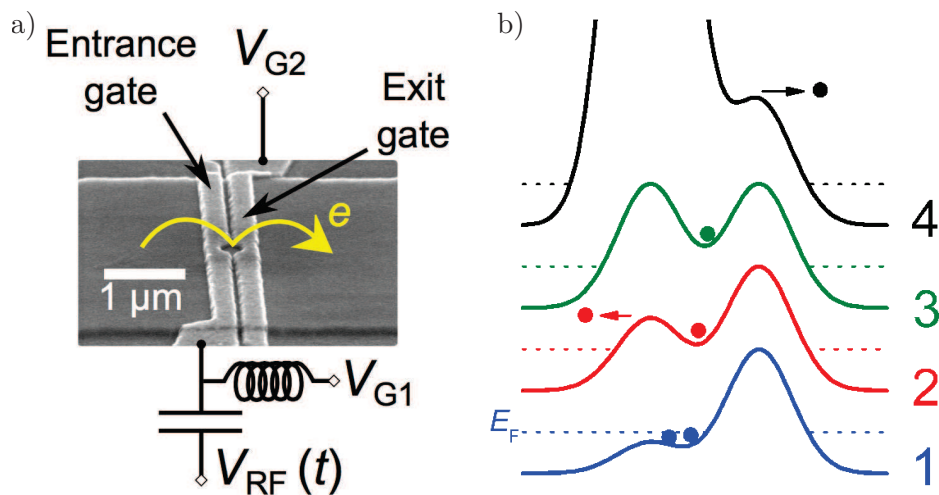


Figure 2.13: a) SEM picture of the sample used by Giblin et al.. Two metallic gates defining the dot are deposited on an etched AlGaAs/GaAs nanowire. b) Schematic of the functioning of the non adiabatic electron pump. The dot is filled with few electrons (1), the potential is tuned to raise the energy level above the Fermi energy and to empty the dot until only one single electron remains (2 and 3) and finally a large voltage is applied on the left gate to expel this electron. Figures are extracted from [Gib12].

Fermi energy and the wave packet has a width of ~ 80 ps. Finally, a similar device was used to generate on demand electron pairs sent on a beam splitter to realize a source of entangled electrons [Ubb14].

2.3.3 On demand coherent single electron source

The first on-demand single electron source has been realized in 2007 by Feve et al. [Fev07] in the group of D.C. Glattli. It is based on a mesoscopic quantum RC circuit that was first studied by Gabelli et al. [Gab06b] to answer theoretical predictions of M. Büttiker on dynamical coherent transport in such a circuit [Büt93].

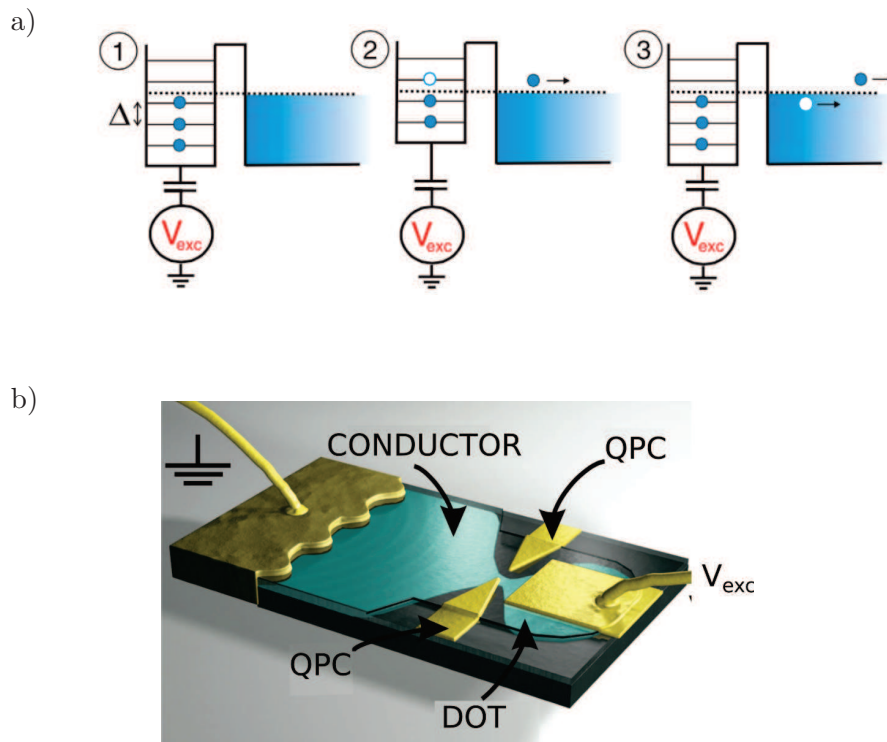


Figure 2.14: a) Functioning of the source: the dot is tuned such that the Fermi energy falls exactly between two energy levels. The potential of the dot is driven by a periodic voltage step resulting in the emission of an electron followed by the emission of a hole. b) Schematic of the sample used by Feve et al. as an on demand single electron source. Figures are extracted from [Fev07] and [Fèv].

The principle is very simple: a quantum dot is coupled to a conductor through a QPC. Electrons are confined in the dot and occupy discrete energy levels. A capacitively coupled gate above the dot is driven by a radio-frequency voltage excitation such that the charging energy is compensated and the electron occupying the highest energy level of the dot is emitted as shown in fig. 2.14. The energy separation between the levels is the sum of the charging energy e^2/C where C is the capacitance between the top gate and the dot and the energy level spacing Δ due to confinement. Usually, the charging energy is larger than Δ . Here, the top gate is very large hence C is big leading to very small charging energy, comparable to Δ .

This source is not exactly a single electron source since during each cycle of voltage

excitation, one electron is emitted followed by the emission of one hole but these two particles are well separated in time. The emitted particles are well defined in energy, the time extension τ of the wave packet is controlled and given by the escape rate $\tau^{-1} = D\Delta/h$, where Δ/h is the frequency attempt and D the QPC transmission.

This source was used recently to perform quantum optics like experiments at the single electron level. First, by coupling the source to a QPC used as a beam splitter, Boquillon et al. realized a Hanbury Brown and Twiss (HBT) experiment [Boc12]. Following this work, they used two independent sources to implement an electronic analog of the Hong-Ou-Mandel experiment [Boc13].

2.3.4 Surface acoustic waves

Surface acoustic waves (SAWs) have been first used by Shilton and Talyanskii et al. to carry electrons one by one through a 1D channel [Shi96; Tal97]. The idea is to use a piezo-electric material such that a propagating mechanical wave is accompanied by a moving electrostatic potential. The AlGaAs/GaAs heterostructure is well suited to implement such a source since this material is piezo-electric and 1D channels can be formed in the 2DEG by using electrostatic gates. The SAW is generated using interdigital transducers (IDT). An IDT consists of interleaved metallic fingers deposited on the surface of the piezo-electric material. These fingers are alternatively connected to two separated electrodes which are connected to a RF signal generator. Applying a RF signal on the IDT results in the generation of a SAW thanks to piezo-electric effect. The spacing between the fingers connected to the same electrode defines the SAW wavelength λ . The applied frequency must match the resonant frequency given by the ratio between the propagating speed c_{SAW} of the SAW (for GaAs, $c_{SAW} \sim 2900 \text{ m.s}^{-1}$) and the wavelength λ .

To generate a quantized current with SAWs, two portions of 2DEG are separated by a fully depleted 1D channel (see fig. 2.15). For a sufficient SAW amplitude, the electrons trapped in the minima of the SAW are dragged over the potential hill formed by the pinched channel. In the channel, the electrons are confined by SAW and by the potential due to the electrostatic gates. This results in the formation of moving quantum dots (QD). Depending on the SAW power and the tuning of the 1D channel, a SAW induced quantized current can be generated showing steps at each multiple of ef where f is the SAW frequency.

The advantage of this source is it can be driven at high frequency, for $\lambda = 1 \mu\text{m}$, the resonant frequency is $f = 2886 \text{ MHz}$. When the system is tuned in the single electron regime, the delivered current is close to 500 pA . In these early experiments, the accuracy of the quantized current was limited to $\sim 0.3\%$. Later on, an accuracy of 200 ppm was reported by Janssen et al. [Jan00], this is still the best value reported for SAW. Different approaches have been used to improve this accuracy: reducing the width of the 1D channel but it required to increase the RF power leading to an overheating of the sample and a degradation of the plateau flatness [Jan01]. Another cause of error is the unwanted tunneling of the electrons out of the moving QD [Ebb03]. Experiment have been performed to overcome this limitation but the obtained accuracy was still on the order of $\sim 10^{-3}$ [Ebb04].

Although being not suitable for metrology at the present time, SAW are very promising for

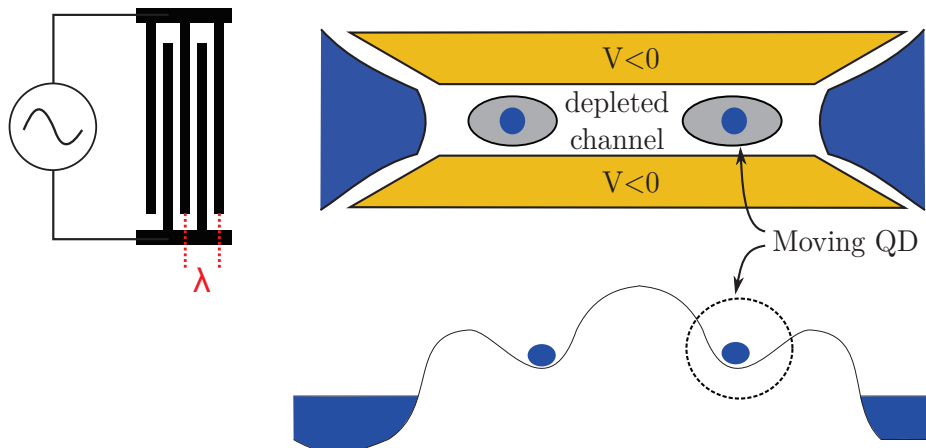


Figure 2.15: Schematic of the process during which SAW induced quantized current is produced. An IDT fed with a RF signal generates the SAW. The depleted 1D channel is formed by applying sufficiently negative voltages on the two electrostatic gates (in yellow). The blue parts represent the two portions of 2DEG and the blue circles represent single electrons. The incoming SAW traps electrons and carries them over the potential hill induced by the gates. When the SAW power and the gate voltage are properly tuned, exactly n electrons are transferred inside each moving QD resulting in a quantized current $I = nef$.

coherent transport of single carriers such as electrons, excitons [Sto05] or single phonons [Gus12]. In 2011, an experiment carried out in our group by Hermelin et al. [Her11] and a similar one by McNeil et al. in Cambridge [McN11] have shown that it is possible to transport a single electron over several μm between two distant QD. As shown in fig. 2.16, the sample used for this experiment by our group is composed of two QDs separated by a $3\ \mu\text{m}$ long 1D channel defined by split gates. Two QPCs, one for each dot, are used as electrometers to detect the presence of a single electron inside a QD [Fie93]. The advantage of this system compared to the others is the fact that one can detect the electrons single shot. Also, the success rate of the transfer is very high. In the original experiment, the success rate was better than 90% [Her11; McN11] while in a newer experiment, a success rate above 99% have been achieved for distances larger than $20\ \mu\text{m}$. By preparing the electron in a specific spin state, one can use this platform to transfer the spin state in a coherent way. In a recent experiment performed in our group, Bertrand et al. demonstrated the possibility to transfer the spin state of one and two electrons using this device [Ber15]. Such a system is also well suited to build a flying qubit and by extension to perform quantum optics experiments at the single electron level. One straightforward implementation of a flying qubit would be to couple the SAW based source and the device of Yamamoto et al. described previously. One difficulty of this approach resides in the excitation of the trapped electron in a superposition of excited states when the moving quantum dot experiences abrupt changes in the confinement potential [Kat09]. One should overcome this problem with a proper design of the electrostatic gates to get a smooth potential landscape. The first step towards the realization of such a flying qubit is ongoing. An experiment where

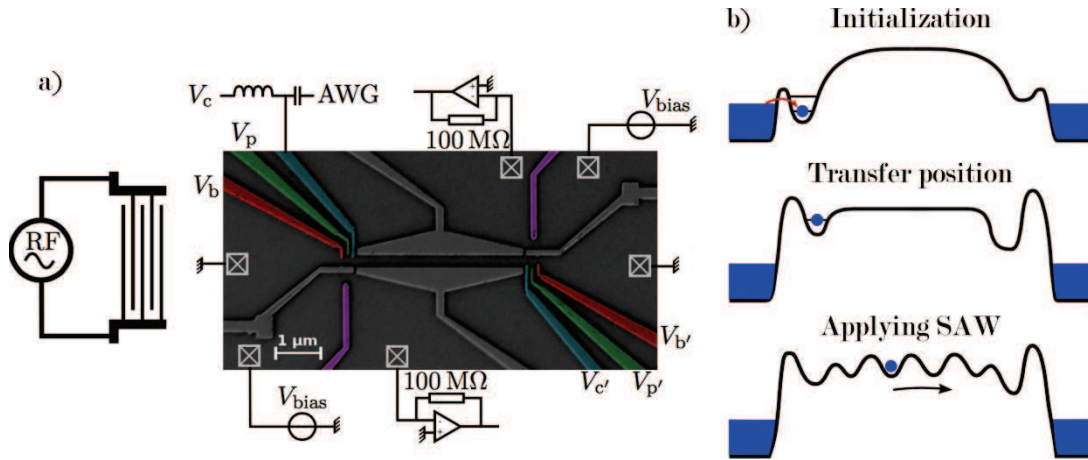


Figure 2.16: a) SEM picture of the sample used by Hermelin et al., the two big triangular gates define the 1D channel. QDs are formed by the 3 colored gates (red, green, blue) and the gray gate. QPCs are formed by the violet gates and also the gray ones. b) Schematic of the single electron transfer protocol. Initialization: a single electron from the Fermi sea is trapped inside a QD. Transfer position: the potential of the dot is raised above the Fermi energy, close to the potential of the pinched 1D channel. Applying SAW: the SAW catches this single electron and carry it up to the second QD where it will stay trapped.

a single electron SAW source coupled to a beam splitter is currently under way. A SEM image of the device is shown in fig. 2.17. The two QDs on the injection side (1 and 2) are used as sources and the two others on the reception side (3 and 4) as detectors. In the center of the structure, a thin electrostatic gate defines the beam splitter.

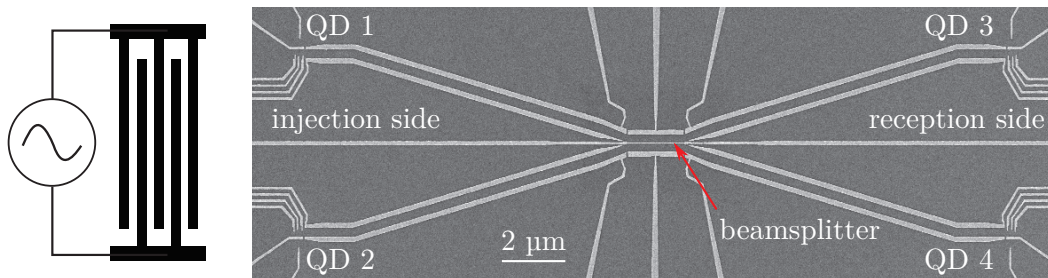


Figure 2.17: SEM picture of the sample combining SAW single electron source coupled to a beam splitter.

2.3.5 Lorentzian voltage pulses

Very recently, a new kind of single electron source has been experimentally realized in the group of D.C. Glattli by Dubois et al. [Dub13]. Based on a proposal of Lesovik and Levitov [Iva97; Kee06; Lev96], the idea is to use a voltage pulse to excite an arbitrary number of electrons. Usually, a voltage pulse affects the entire Fermi sea and excites not

only a certain number of electrons but also a neutral cloud of electron-hole pairs. However, when the voltage pulse $V(t)$ fulfill the two following conditions:

- It has a Lorentzian shape,

$$V(t) = \frac{V_0}{\pi} \frac{W}{(t^2 + W^2)}, \quad (2.3)$$

where V_0 is the amplitude of the voltage pulse and the full width at half maximum is given by $2W$.

- The following quantization condition is fulfilled:

$$\int_{-\infty}^{\infty} eV(t) dt = n\hbar, \quad (2.4)$$

then this source acts as a very clean quasi-particles source. For $n = 1$, only one single electron excitation is created without any additional electron-hole pair excitation. This quasi-particle, the so-called Leviton, can be seen as a well defined wave packet with a time extension $2W$ flying at the surface of the Fermi sea. The remarkable property of these electronic excitations come from their exponential energy distribution (see fig. 2.18) which is the only kind of distribution which does not affect the Fermi sea [Kee06].

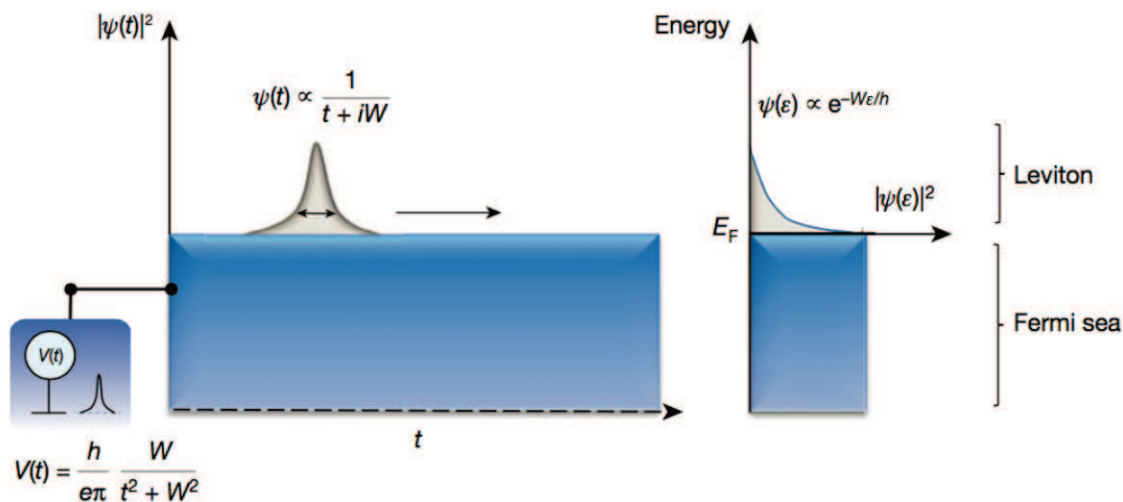


Figure 2.18: Schematic picture of the Leviton wave function in time and energy domains extracted from [Dub13]. The Lorentzian pulse shape in time domain is equivalent to an exponential distribution in energy domain. $|\Psi(\epsilon)|^2$ is the probability to excite an electron with an excess energy ϵ compared to the fermi energy E_F .

To implement such a source, Dubois et al. used a voltage pulses generator allowing to generate Lorentzian shaped pulses. These voltage pulses are injected in a 2DEG through an ohmic contact. A quantum point contact is defined in the middle of the sample by two electrostatic gates, $50 \mu\text{m}$ away of the ohmic contact. A schematic of the sample is presented in fig. 2.19. This QPC is tuned in the single mode regime whose transmission

D is controllable by varying the gates voltage. The number of excitations generated by a pulse is extracted from the shot-noise due to the partitioning of these excitations by the beam splitter formed by the QPC set at a transmission $D < 1$. By comparing Levitons to others excitations generated by square pulses or sinusoidal signals, the authors showed that Levitons effectively minimize the shot noise, the remaining excitations being mostly due to the finite temperature. They also performed shot noise spectroscopy as well as Hong-Ou-Mandel interference that confirmed the energy distribution and time dependence of Levitons [Dub13].

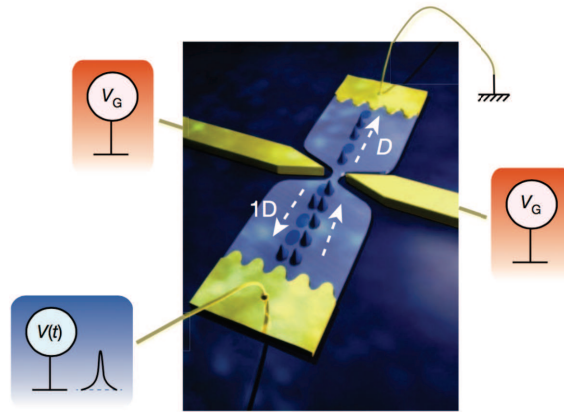


Figure 2.19: Artistic view of the sample used by Dubois et al. extracted from [Dub13].

To observe the fluctuation of the noise, Dubois et al. showed that it is necessary to reach a regime where $k_B T / h\nu$ where ν is the repetition frequency of the pulses must be on the order of 0.1. For an electron temperature of ~ 20 mK, it means that ν should be about 3 GHz. Moreover, the width of the pulse must be small compared to $1/\nu$ which implies that the temporal width of the voltage pulse must be on the order of 60 ps or less [Dub]. This is the typical timescale to which we refer in the following as «fast voltage pulses». This single electron source was then used with success by Jullien et al. to perform the quantum state tomography of a single electron [Jul14].

2.4 Dynamical engineering of interference pattern using fast voltage pulses

2.4.1 Principle

Very recently, our collaborators Xavier Waintal et al. at CEA Grenoble have shown that injecting a fast voltage pulse in an electronic interferometer should allow to observe spectacular effects due to the interaction of the voltage pulse with the surrounding Fermi sea [Gau14a; Gau15]. These findings were made possible thanks to their ability to simulate time resolved quantum transport using their in house algorithm KWANT [Gau14b]. In this section, we expose the results obtained by Gaury et al. [Gau14a].

When a voltage pulse is applied to a conductor it excites a packet of electrons which

propagate through the conductor, the average number of excited electrons being:

$$\bar{n} = \int_{-\infty}^{+\infty} \frac{eV(t)}{h} dt, \quad (2.5)$$

where e is the electron charge and $V(t)$ the function which characterizes the voltage pulse. A very important point is that before applying any voltage pulse to the system, there are already electrons in the conductor which form the Fermi sea. These electrons behave as stationary plane waves. The effect of the voltage pulse is to locally increase the energy of these electrons and therefore to modify the phase of the electronic wave functions as schematized in fig. 2.20. Let us consider a one dimensional conductor, the passage of the pulse is going to modify the electron wave function as:

$$\Psi(x,t) = e^{ikx - iEt/\hbar} \quad \text{before the passage of the pulse,} \quad (2.6)$$

$$\Psi(x,t) = e^{ikx - iEt/\hbar - i\phi(t)} \quad \text{after the passage of the pulse,} \quad (2.7)$$

where $\phi(t)$ is the extra phase due to the pulse:

$$\phi(t) = \int_{-\infty}^t \frac{eV(u)}{\hbar} du. \quad (2.8)$$

The total phase shift due to the pulse is given by $\lim_{t \rightarrow \infty} \phi(t) = 2\pi\bar{n}$. For a voltage pulse of

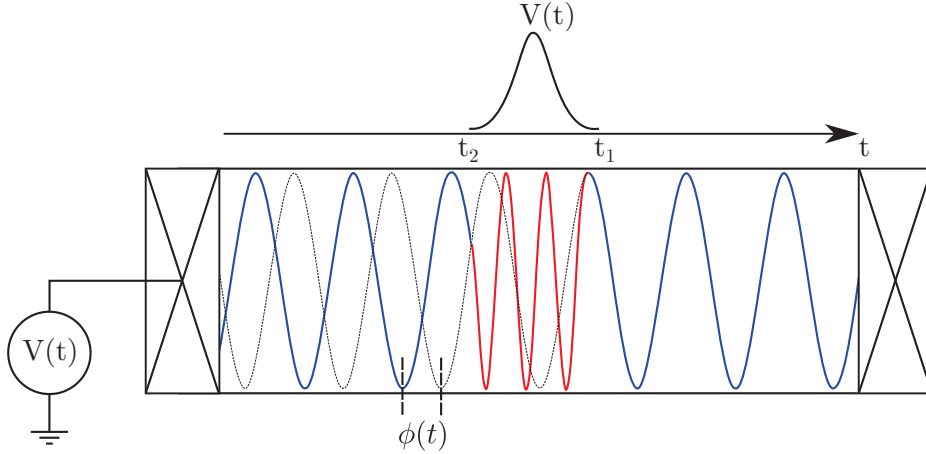


Figure 2.20: Effect of the voltage pulse injected into a one dimensional conductor on the electronic wave function. Before the passage of the pulse ($t > t_1$), the electronic wave function is not modified. The voltage pulse locally increases the energy of the electrons which adds an extra phase $\phi(t)$ to the wave function (the black dotted line corresponds to the unmodified wave function).

amplitude V_p and temporal width τ_p , one finds $2\pi\bar{n} \sim \frac{eV_p\tau_p}{h}$. The control over the phase of the electronic wave function can be done simply by changing V_p (or τ_p). To engineer this dynamical phase shift, it is primordial to be in a regime where τ_p is smaller than the time

of flight of the pulse in the system.

2.4.2 The Mach-Zehnder interferometer as a probe

The two electronic interferometers described previously are very good candidates to probe this dynamical phase. Even though any multi-path interferometer such as Fabry-Perot cavity would be suitable to observe this novel interference effect [Gau14a]. We focus here on the case of the Mach-Zehnder interferometer in the quantum Hall regime because it is conceptually the simplest one to describe. The device is similar to the one realized by Ji et al., with the particularity that one path must be longer than the other as shown in fig. 2.21. The difference of length L between the two arms implies an extra time of flight $\tau_F = L/v_e$ where v_e is the propagating speed of the electrons in an edge state.

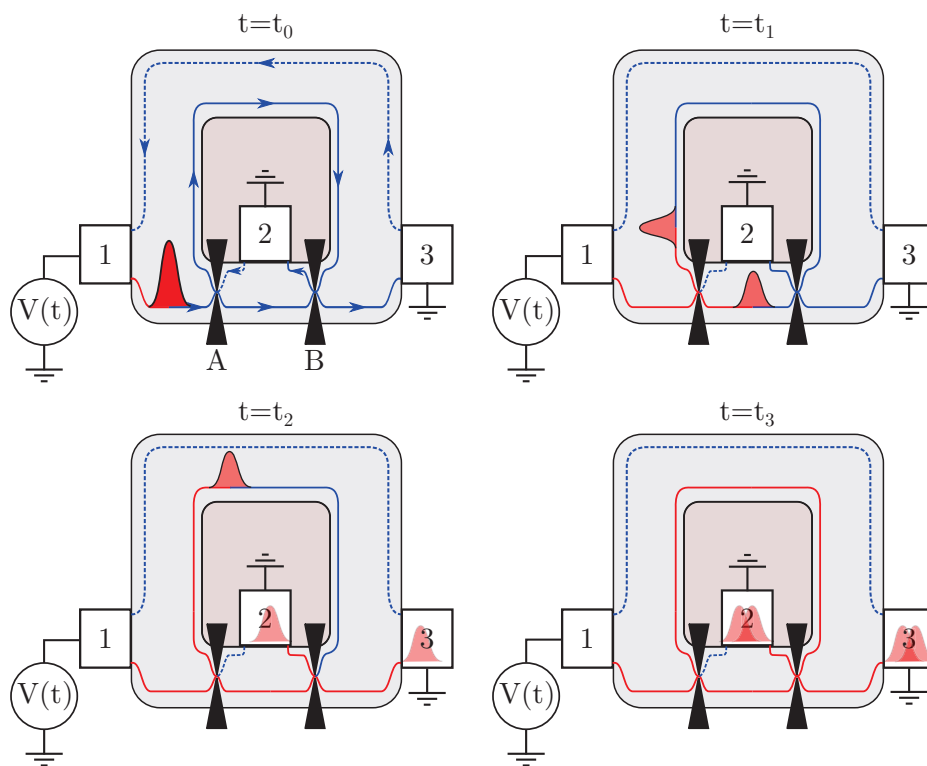


Figure 2.21: Schematic of the propagation of a voltage pulse injected in a Mach-Zehnder interferometer. The stationary wave functions located in the edge states are represented in blue. The dashed blue lines correspond to edges states which are not directly involved in the interference phenomena which takes place during the transient regime. When the voltage pulse propagates in an edge channel, it modifies the phase of the wave functions: the modified wave functions are represented in red.

At equilibrium, there is no net current flowing through the system: the current arriving at a given ohmic contact is exactly compensated by the current leaving this contact. However, when a voltage pulse is applied, this situation is modified. Four regimes can be distinguished (see fig. 2.21):

1. At $t = t_0$, a pulse is injected in an edge channel and propagates up to the first beam splitter (QPC A).
2. At $t = t_1$, the pulse has been split into two, one half of the pulse propagates in the longer arm and the other half in the shorter arm.
3. At $t_2 \leq t \leq t_3$, this is the so-called transient regime. The pulse in the shorter arm has already reached the second beam splitter and again has been split into two, one half being measured at the contact 2 and the other half at the contact 3. However the part of the pulse in the longer arm has not yet reached the second beam splitter. During this transient regime of duration τ_F , the plane waves present in the shorter arm have acquired an additional phase but not the plane waves present in the longer arm. This results in the modification of the interference pattern between these plane waves, therefore the currents arriving at the contact 2 and 3 are different compared to the equilibrium case.
4. At $t = t_3$, the part of the pulse in the longer arm has reached the second beam splitter and subsequently the two output contacts. The plane waves present in both arms of the interferometer have now acquired the same extra phase and the system comes back to its initial state.

The result of the numerical simulation giving the output current at the contact 3 as a function of time is shown in fig. 2.22. The first peak corresponds to the arrival of the pulse which propagates in the shorter arm. The second peak corresponds to the arrival of the pulse which propagates in the longer arm. In between, this is the transient regime: the current is finite and its value depends on the extra phase given by $2\pi\bar{n}$ as we are going to discuss now.

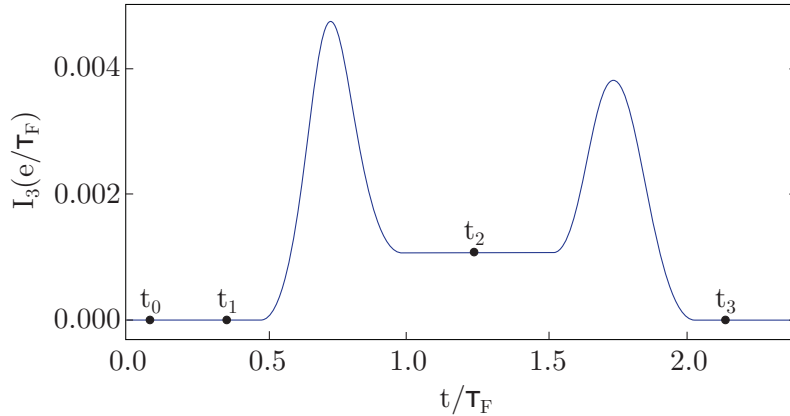


Figure 2.22: Numerical simulation of the output current at the contact 3 as a function of time extracted from [Gau14a]. The four regimes described in the text are indicated by the black dots.

The current arriving at the contact 3 (2) can be determined by calculating the transmission probability from the contact 1 to contact 3 (2). During the transient regime, the state of an electron with an energy E right after the second beam splitter and close to the contact

3 is the sum of the contribution of the two arms of the interferometer:

$$\begin{aligned}\Psi_3(x,t) &= \frac{1}{\sqrt{k}} r_A r_B e^{ikx - iE(t+\tau_F)/\hbar + \phi_0} + \frac{1}{\sqrt{k}} t_A t_B e^{ikx - iEt/\hbar - i\phi(t)} \\ &= \frac{e^{ikx - iEt/\hbar}}{\sqrt{k}} [r_A r_B e^{-iE\tau_F/\hbar + \phi_0} + t_A t_B e^{-i\phi(t)}]\end{aligned}\quad (2.9)$$

where $R_{A,B} = |r_{A,B}|^2$ and $T_{A,B} = |t_{A,B}|^2$ are the reflection and transmission coefficients of the two beam splitters and ϕ_0 the Aharonov Bohm phase. The amplitude of transmission probability from contact 1 to 3 is $d_{31}(t,E) = r_A r_B e^{-iE\tau_F/\hbar} + t_A t_B e^{-i\phi(t)}$. The current arriving at the contact 3 during the transient regime can be calculated using the time dependent generalization of the Landauer formula:

$$I_3(t) = \frac{e}{h} \int |d_{31}(t,E)|^2 f(E) dE \quad (2.10)$$

where $f(E)$ is the Fermi function. In an actual experiment, one would measure the integral over the time of $I_3(t)$ ($I_2(t)$) which is equivalent to measure the number n_3 (n_2) of electrons arriving on the contact 3 (2). After integration, one finds:

$$n_2 = (T_A R_B + R_A T_B) \bar{n} - \frac{2}{\pi} \sqrt{R_A R_B T_A T_B} \sin(\pi \bar{n}) \cos(\phi_0 + \pi \bar{n}) \quad (2.11)$$

$$n_3 = (R_A R_B + T_A T_B) \bar{n} + \frac{2}{\pi} \sqrt{R_A R_B T_A T_B} \sin(\pi \bar{n}) \cos(\phi_0 + \pi \bar{n}) \quad (2.12)$$

The number of transmitted charges oscillates as a function of the average number of injected charges \bar{n} . The graph presented in fig. 2.23 shows the result of the numerical simulation giving the difference $n_3 - n_2$ as a function of \bar{n} as well as the analytical solution using eq. 2.11 and 2.12.

To observe this effect, it is of course primordial to be in a regime where the phase of the electronic wave function is well defined. Therefore the length of the longer arm of the interferometer must be smaller than the coherence length. From the result of [Rou08b], a length of $\sim 20 \mu\text{m}$ can be envisaged. The speed of the electrons in an edge channel has been experimentally measured [Kam10; Kat15] and is on the order of $\sim 10^5 \text{ m.s}^{-1}$. The time needed for the pulse to propagate in the longer arm is then approximately 200 ps. To observe the dynamical change of the interference pattern, the two following conditions must be fulfilled:

1. The temporal width τ_p of the pulse has to be shorter than the time needed to propagate in both arms of the interferometer,
2. The transient regime must be well resolved. In other words, the arrival times of each part of the pulse at the second beam splitter should be separated by at least one τ_p .

Therefore the pulse width τ_p must be on the order of 100 ps. This sets the experimental constraints one has to master: it requires a source able to generate such a fast voltage pulse as well as an adapted experimental set-up to use this type of signal at very low temperatures.

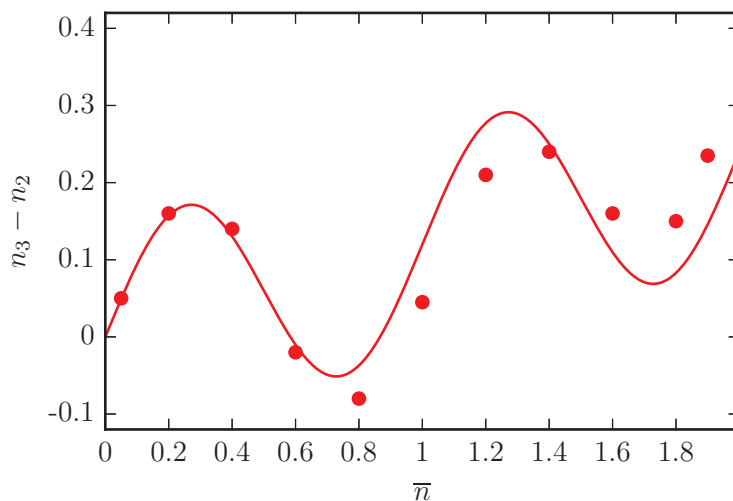


Figure 2.23: Results of the numerical simulation (dots) and the analytical calculation (solid line) giving the difference of the total number of transmitted charges $n_3 - n_2$ as a function of the average number of injected charges \bar{n} . Figure extracted from [Gau14a].

2.5 Our approach: the tunnel coupled wires

Another possible approach to build a two path interferometer is to design a system in which the two paths have the same length but the propagation speed is different in each path. This is possible using two tunnel coupled wires. As we have briefly mentioned in the description of the flying qubit realized by Yamamoto et al. [Yam12], the tunnel coupled wires (TCW) can be formed with a quantum wire which is split into two channels by a tunable tunnel barrier as sketched in fig. 2.24. As we are going to see in the following, the two eigenstates of the TCW are the so-called symmetric and antisymmetric states. These two states have a different energy and therefore a different propagation speed. One advantage of such an architecture over the Mach Zehnder described above relies on the fact that it is possible to reduce the propagation speed of each state by controlling the confinement potential due to the electrostatic gates. Consequently the difference of time of flight between the two states can be made larger. Another point is that a Mach Zehnder interferometer is highly challenging to fabricate. Indeed, to connect the inner ohmic contact (contact 2 in fig. 2.21) as well as the inner gates of the two QPCs, it is necessary to use micrometer sized bridges which requires a delicate lithography process.

2.5.1 Analytical description of the tunnel coupled wires

Let us consider a single electron injected from the contact 1 of the schematic in fig. 2.24. The state of the electron is defined by its position in the wires:

- pseudo-spin $|\uparrow\rangle$ when the electron is present the upper wire,
- pseudo-spin $|\downarrow\rangle$ when it is present in the lower wire.

For $x < 0$, the two wires are completely decoupled and the electron state is $|\uparrow\rangle$. Between $x=0$ and $x=L$, the two wires are coupled and this coupling can be tuned by changing the voltage V_T applied on the tunnel gate. In this region, the electron injected from contact 1 is going to tunnel back and forth between the wires until it reaches the region at $x=L$ where the two wires are separated. The electron is then measured either at contact 3 or contact 4 depending on the number of tunnel oscillations it has experienced. For instance, when the tunnel barrier is tuned in the beam splitter regime (50% $|\uparrow\rangle$, 50% $|\downarrow\rangle$), the electron is in a superposition of states between the two wires and half of the time it will be measured in contact 3 and the other half in contact 4.

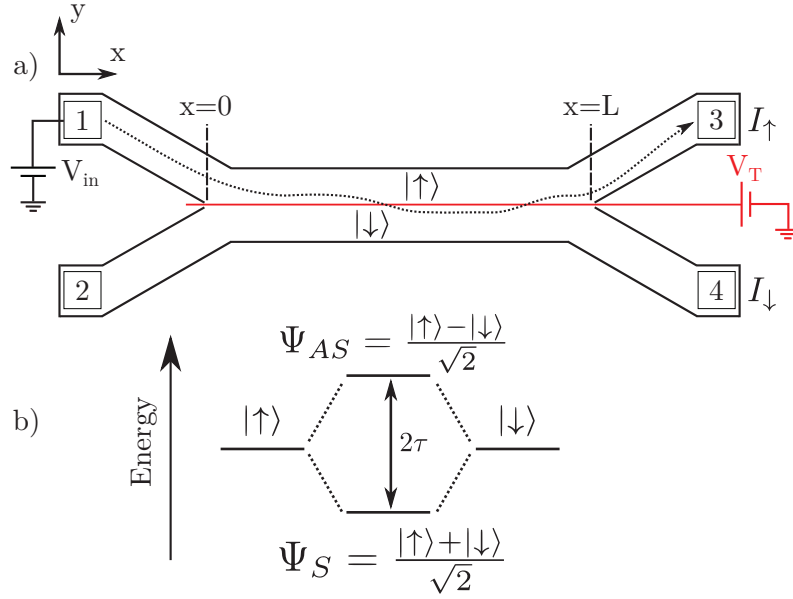


Figure 2.24: Schematic of the tunnel coupled wires, the tunnel gate is represented in red. a) An electron initially injected from contact 1 enters the tunnel coupled region at $x=0$. During its propagation in this region, it can tunnel back and forth between the two wires depending on the tunnel barrier (voltage V_T applied on the tunnel gate). b) The eigenstates of the TCW are the symmetric state Ψ_S and the anti-symmetric state Ψ_{AS} . These two states have different energies and the separation depends on the tunnel coupling τ .

The Hamiltonian of the system is the following:

$$H = H_K + H_T. \quad (2.13)$$

H_K is related to the kinetic energy:

$$H_K = \sum_k \varepsilon_k |k\rangle \langle k| \quad (2.14)$$

$$\text{with } \varepsilon_k = \frac{\hbar^2 k^2}{2m^*}, \quad (2.15)$$

where m^* is the effective mass of the electron. H_T is related the potential energy:

$$H_T = \varepsilon_{\uparrow} |\uparrow\rangle \langle\uparrow| + \varepsilon_{\downarrow} |\downarrow\rangle \langle\downarrow| - \tau(|\downarrow\rangle \langle\uparrow| + |\uparrow\rangle \langle\downarrow|), \quad (2.16)$$

where $\varepsilon_{\uparrow(\downarrow)}$ is the confinement energy associated to the upper (lower) channel and τ is the tunnel coupling energy between the two wires.

Due to the translation invariance along the x direction, we can decompose the wave function of the electron in the TCW as follow:

$$\begin{aligned} |\Psi(x,y)\rangle &= e^{ik_x x} |\Psi(y)\rangle \\ &= \langle x|k\rangle |\Psi(y)\rangle \end{aligned} \quad (2.17)$$

For a symmetric confinement potential, $\varepsilon_{\uparrow} = \varepsilon_{\downarrow} = \varepsilon_0$. Because of the coupling between the two wires, the eigenstates of the system are now the symmetric state $|\Psi_S\rangle = \frac{|\uparrow\rangle + |\downarrow\rangle}{\sqrt{2}}$ and the anti-symmetric state $|\Psi_{AS}\rangle = \frac{|\uparrow\rangle - |\downarrow\rangle}{\sqrt{2}}$. The eigenenergies associated to H_T for these two states are $E_S = \varepsilon_0 - \tau$ and $E_{AS} = \varepsilon_0 + \tau$. The state of an electron in the TCW can then be written as:

$$|\Psi_T\rangle = \alpha \langle x|k_S\rangle |\Psi_S\rangle + \beta \langle x|k_{AS}\rangle |\Psi_{AS}\rangle. \quad (2.18)$$

Before entering in the TCW, the state of the electron is:

$$\begin{aligned} |\Psi_T(x=0)\rangle &= \alpha \langle 0|k_S\rangle |\Psi_S\rangle + \beta \langle 0|k_{AS}\rangle |\Psi_{AS}\rangle \\ &= \alpha \frac{|\uparrow\rangle + |\downarrow\rangle}{\sqrt{2}} + \beta \frac{|\uparrow\rangle - |\downarrow\rangle}{\sqrt{2}}. \end{aligned} \quad (2.19)$$

After its propagation in the TCW, at $x=L$ the state of the electron is:

$$\begin{aligned} |\Psi_T(x=L)\rangle &= \alpha \langle L|k_S\rangle |\Psi_S\rangle + \beta \langle L|k_{AS}\rangle |\Psi_{AS}\rangle \\ &= \alpha e^{ik_S L} |\Psi_S\rangle + \beta e^{ik_{AS} L} |\Psi_{AS}\rangle \\ &= \frac{\alpha e^{ik_S L} + \beta e^{ik_{AS} L}}{\sqrt{2}} |\uparrow\rangle + \frac{\alpha e^{ik_S L} - \beta e^{ik_{AS} L}}{\sqrt{2}} |\downarrow\rangle \end{aligned} \quad (2.20)$$

If the electron is injected from the contact 1, its initial state is $|\uparrow\rangle$ and $\alpha = \beta = \frac{1}{\sqrt{2}}$. In this case:

$$\begin{aligned} |\Psi_T(x=L)\rangle &= \frac{e^{ik_S L} + e^{ik_{AS} L}}{2} |\uparrow\rangle + \frac{e^{ik_S L} - e^{ik_{AS} L}}{2} |\downarrow\rangle \\ &= e^{i\frac{k_S + k_{AS}}{2} L} \left(\cos\left(\frac{k_S - k_{AS}}{2} L\right) |\uparrow\rangle + i \sin\left(\frac{k_S - k_{AS}}{2} L\right) |\downarrow\rangle \right) \end{aligned} \quad (2.21)$$

When the electron is injected from the contact 2, its initial state is $|\downarrow\rangle$, $\alpha = \frac{1}{\sqrt{2}}$ and $\beta = -\frac{1}{\sqrt{2}}$. In this case:

$$\begin{aligned} |\Psi_T(x=L)\rangle &= \frac{e^{ik_S L} - e^{ik_{AS} L}}{2} |\uparrow\rangle + \frac{e^{ik_S L} + e^{ik_{AS} L}}{2} |\downarrow\rangle \\ &= e^{i\frac{k_S + k_{AS}}{2} L} \left(i \sin\left(\frac{k_S - k_{AS}}{2} L\right) |\uparrow\rangle + \cos\left(\frac{k_S - k_{AS}}{2} L\right) |\downarrow\rangle \right) \end{aligned} \quad (2.22)$$

These results can be rewritten as a matrix which is the scattering matrix associated to the tunnel barrier:

$$S_{tcw} = \begin{pmatrix} \cos(\frac{\theta}{2}) & i \sin(\frac{\theta}{2}) \\ i \sin(\frac{\theta}{2}) & \cos(\frac{\theta}{2}) \end{pmatrix} \quad (2.23)$$

where $\theta = (k_S - k_{AS})L$. The current conservation imposes $S_{tcw} S_{tcw}^\dagger = \mathbb{1}$ which is verified. For an electron initially injected from the contact 1, the probability to measure it in the upper contact (3) or in the lower contact (4) after its propagation in the TCW are:

$$|\langle \uparrow | \uparrow \rangle|^2 = \frac{1 + \cos \theta}{2} \quad (2.24)$$

$$|\langle \downarrow | \uparrow \rangle|^2 = \frac{1 - \cos \theta}{2} \quad (2.25)$$

For a stream of electrons injected into the contact 1, the output currents arriving at contacts 3 and 4 oscillate in opposition of phase as a function of $\Delta k = k_S - k_{AS}$ as shown in fig2.25. Δk depends on τ which can be varied by changing the voltage applied on the tunnel gate.

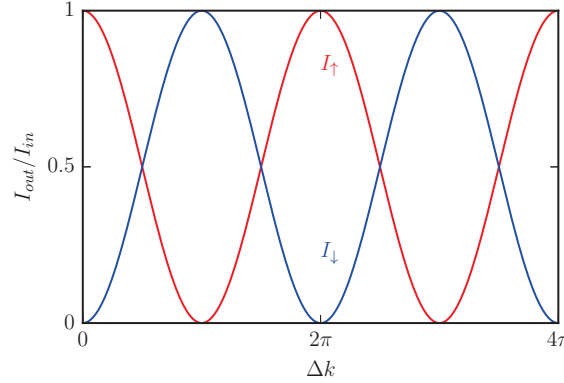


Figure 2.25: Anti-phase oscillation of the output currents arriving at contact 3 (I_\uparrow in red) and contact 4 (I_\downarrow in blue) as a function of Δk when the electrons are initially injected from the contact 1.

2.5.2 The TCW as a two path interferometer

The interpretation of the TCW as a two path interferometer is quite subtle since the two paths are not spatially resolved. In the previous section, we have shown that the propagating modes in the TCW are the symmetric and anti-symmetric states. Before entering in the TCW, there is no tunnel coupling and the states $|\Psi_S\rangle$ and $|\Psi_{AS}\rangle$ are degenerate. However, in the TCW this degeneracy is lifted by the tunnel coupling. The total energy for an electron propagating in the TCW is the sum of its kinetic energy and its potential energy. Since only the electrons having an energy close to the Fermi energy E_F contribute to the transport the following relation must be satisfied:

$$E_S + \frac{\hbar^2 k_S^2}{2m^*} = E_{AS} + \frac{\hbar^2 k_{AS}^2}{2m^*} = E_F, \quad (2.26)$$

we remind that $E_S = \varepsilon_0 - \tau$ and $E_{AS} = \varepsilon_0 + \tau$. From eq. 2.26 we can extract the longitudinal velocities associated with the states $|\Psi_S\rangle$ and $|\Psi_{AS}\rangle$:

$$v_S = \sqrt{\frac{2(E_F - (\varepsilon_0 - \tau))}{m^*}} \quad (2.27)$$

$$v_{AS} = \sqrt{\frac{2(E_F - (\varepsilon_0 + \tau))}{m^*}} \quad (2.28)$$

A voltage pulse injected in the TCW is going to be in a superposition of the states $|\Psi_S\rangle$ and $|\Psi_{AS}\rangle$. The part of the pulse which occupies the state $|\Psi_S\rangle$ propagates faster than the part which occupies the state $|\Psi_{AS}\rangle$. As we have discussed before, prior to the injection of the pulse (at equilibrium) there already exist electrons in the TCW whose states are a superposition of the states $|\Psi_S\rangle$ and $|\Psi_{AS}\rangle$. When a short voltage pulse is injected into the TCW, it is going to modify the phases of the symmetric and antisymmetric states. Since the part of the voltage pulse which affects the phase of the symmetric states propagates faster, there exists a transient regime during which the phases of the symmetric states has been modified but not yet the phase of the antisymmetric states.

Before the passage of the pulse, the state of an electron in the TCW is:

$$|\Psi(x)\rangle = \alpha e^{ik_S x} |\Psi_S\rangle + \beta e^{ik_{AS} x} |\Psi_{AS}\rangle \quad (2.29)$$

During the transient regime, it becomes:

$$|\Psi(x)\rangle = \alpha e^{ik_S x + i\phi_0} |\Psi_S\rangle + \beta e^{ik_{AS} x} |\Psi_{AS}\rangle \quad (2.30)$$

where ϕ_0 is the additional phase due to the voltage pulse. In the case where the electron is injected from the contact 1, its state at $x=L$ is:

$$|\Psi(x=L)\rangle = e^{i\frac{k_S + k_{AS}}{2}L + i\frac{\phi_0}{2}} \left(\cos\left(\frac{k_S - k_{AS}}{2}L + \frac{\phi_0}{2}\right) |\uparrow\rangle + i \sin\left(\frac{k_S - k_{AS}}{2}L + \frac{\phi_0}{2}\right) |\downarrow\rangle \right) \quad (2.31)$$

Therefore, during the transient regime, the probability to detect the electron at the contact 3 or 4 is:

$$|\langle \uparrow | \uparrow \rangle|^2 = \frac{1 + \cos \theta'}{2} \quad (2.32)$$

$$|\langle \downarrow | \uparrow \rangle|^2 = \frac{1 - \cos \theta'}{2} \quad (2.33)$$

where $\theta' = (k_S - k_{AS})L + \phi_0$. It is then possible to modify the repartition of the current between the two contacts by modifying ϕ_0 which can be done by varying the amplitude of the voltage pulse. In an actual experiment, one would set the tunnel coupling at a given value such that $(k_S - k_{AS})L$ would be fixed. Applying voltage pulses on the system would result in anti-phase oscillations of the output currents as a function of the pulse amplitude [Wes16a].

2.5.3 Strategy

As a first experiment, we adopted a conservative approach to design the sample. The pulse source available at the beginning of the project allows to generate voltage pulse having a width τ_p of ~ 100 ps. The time of flight τ_F of the pulse through the sample is set by the speed of propagation of the pulse which in a first approximation should be close to the Fermi velocity. From the density ($n_s = 2.11 \times 10^{11} \text{ cm}^{-2}$) we can estimate the Fermi velocity v_{Fermi} to about $1.95 \times 10^5 \text{ ms}^{-1}$. Reaching the regime where $\tau_p < \tau_F$ requires that τ_F should be on the order of 200 ps. As a consequence, the sample length was set to $v_{Fermi}\tau_F = 40 \mu\text{m}$. Several key points need to be addressed in order to know if it is possible to observe this dynamical effect in a TCW geometry:

1. First, one has to be sure that the temporal width of the voltage pulse (τ_p) is smaller than its time of flight (τ_F) through the sample. Due to several factors such as Coulomb interaction, electrostatic confinement... the velocity of the pulse can in principle differ from the Fermi velocity. It is therefore of importance to determine the velocity in-situ.
2. It should be possible to modulate the velocity by controlling the confinement potential. The lower the velocity, the easier it is to reach the regime where $\tau_p < \tau_F$. It is interesting to evaluate how much the velocity can be affected when the confinement is modified.
3. As said above, the length of the fabricated TCW is $40 \mu\text{m}$. The central question related to this point is then can we still observe coherent oscillations in such a long sample ?

The aim of this PhD work was to address these points which are going to be discussed in chapter 4 and 5. This topic of fast quantum electronic is very new in our group so the first step was to build and characterize an experimental set-up adapted to this work: this is the subject of the following chapter.

CHAPTER 3

Experimental set-up and technical development

Performing an experiment in which one wants to observe quantum phenomena using very fast voltage pulses demands severe constraints on the experimental set-up. The first one is the necessity of very low temperatures, typically a few tens of mK. Indeed, the coherence length of the electrons and hence the visibility of the quantum phenomena depend strongly on the temperature. Typically in our system, above a few hundreds of mK, quantum effects are washed out by temperature.

To work at such a low temperature, the experiment is performed in dilution cryostat which allows to reach a base temperature of ~ 20 mK. For specific details on the functioning of a dilution cryostat, we refer the interested reader to [Pob07]. Reaching this base temperature is a first step, being sure that the sample is at the same temperature is another. To control and perform measurements on the sample, it has to be connected to several electronic equipments outside of the cryostat. In our case, these connections involve low frequency and high frequency lines. Then two main mechanisms can bring heat to the sample: thermal conduction and radiation due to the propagation of photons along the lines. That is why a lot of effort has been devoted to the electrical wiring which connects the sample to the electronic equipments outside of the cryostat. It means a careful choice of the materials used and specific techniques to reduce as much as possible the different sources of heat which could warm-up our sample. This is particularly true for the high frequency part of the set-up. Since we want to work with voltage pulses having a width of ~ 100 ps or even less, we need to implement radio frequency (RF) lines that carry the signal up to the sample without degrading it. However, the wide bandwidth of these lines (DC to few tens of GHz) is not really compatible with very low temperature but we will show that we can circumvent this problem.

As a general trend, samples are becoming more and more complex. For our experiment and for the others experiments performed in the group such as the realization of a beam splitter coupled to SAW single electron sources or spin manipulation in quantum dot arrays, one needs a large number of DC lines to polarize electrostatic gates, connect ohmic contacts as well as RF lines to perform the desired experiments. When we started to develop this new experimental set-up, the idea was to have a versatile tool compatible with various cryostats and the different kinds of experiments performed in our research group.

In this chapter, we will describe the experimental set-up built during this thesis and the technical developments achieved to perform an experiment involving very fast voltage pulses. First we will detail the DC part of the experiment. We have developed a system which combines 42 DC lines and can accept up to 4 RF lines. We will detail the DC wiring composed of two different types of lines compatibles with very low temperature. Finally, we will focus on the RF part of the experiment. This includes the characterization of the RF lines, the fabrication and characterization of low resistance ohmic contacts, the development of a chip carrier adapted to high frequencies and the realization of a very fast voltage pulse source.

The set-up is schematically sketched in fig. 3.1. On top of the cryostat, at 300 K, SMA connectors allow the connection between the electronic equipments and the different lines: the DC or low frequency ones and the RF lines suited for GHz signals. In order to bring the minimum heat possible to the sample, lines are thermally anchored at each stages of the cryostat.

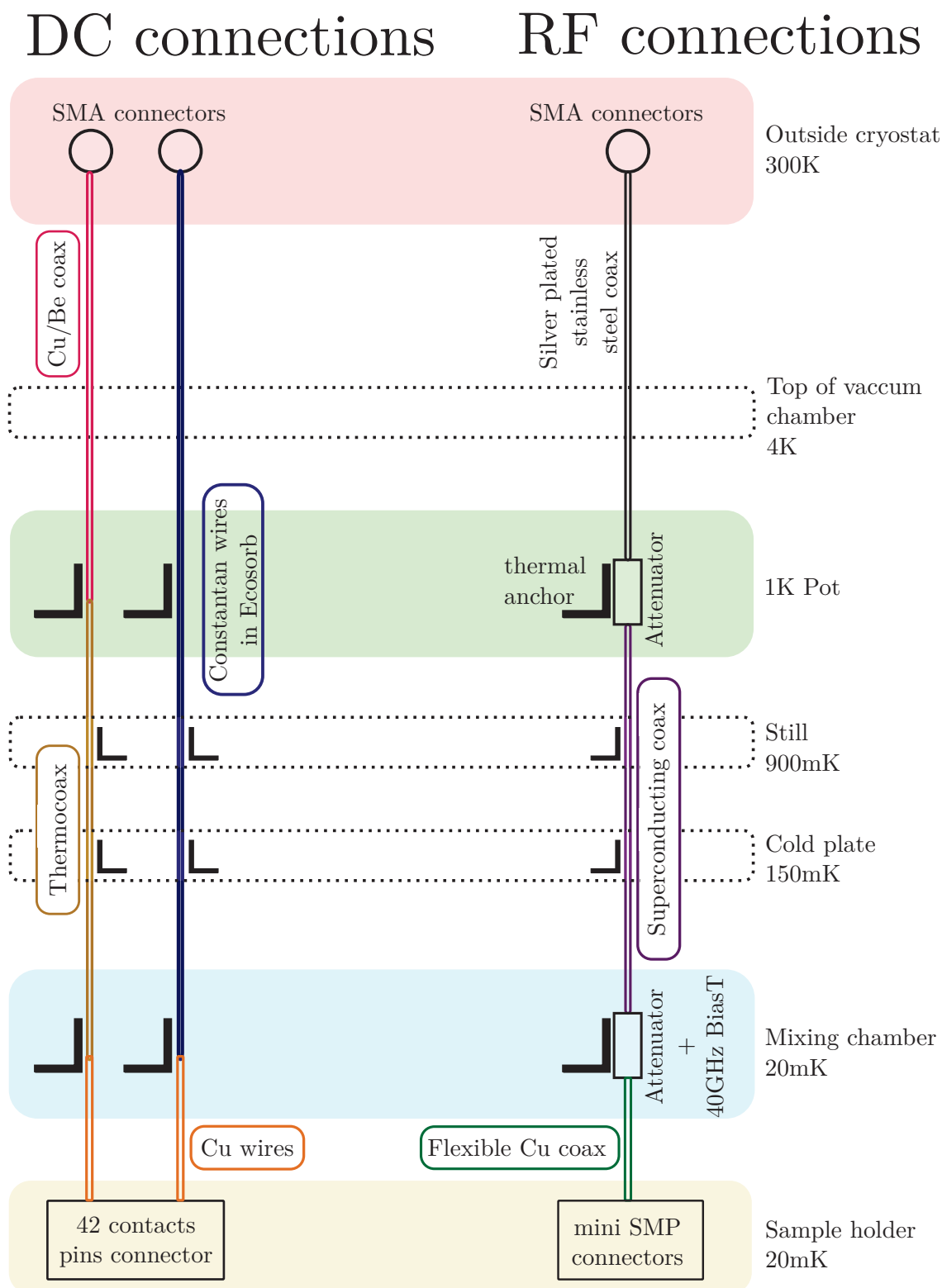


Figure 3.1: Scheme of the experimental set-up.

3.1 DC connections

3.1.1 DC lines

In this section, we will describe in detail the DC part of the experiment. By DC, we mean either real DC or low frequency signal (up to a few tens of kHz). Two types of DC lines are used: coaxial lines as well as Constantan wires. Depending on the purpose, one type will be more adapted than the other. When cross talk between lines has to be avoided, coaxial lines are used, typically to bias the sample, to measure output voltages and to sweep rapidly (MHz) the voltage applied on electrostatic gates. When a large number of lines is needed and cross talk is not a problem, typically to apply static voltages on electrostatic gates, Constantan wires are used. These DC lines have to satisfy the following conditions:

- Coaxial lines and Constantan wires: heat propagating along the lines has to be sufficiently low to not perturb the cryostat functioning and to not increase the electronic temperature of the sample.
- Coaxial lines: since they are used to bias the sample and measure output voltages, Johnson-Nyquist noise due to the resistance of the lines must be smaller than the noise level of our room temperature electronics which is $\sim 0,4 \text{ nV} \cdot \text{Hz}^{-1/2}$.

Coaxial lines

Coaxial lines are divided into two stages. The coaxes used from 300 K to 1 K are made of Copper/Beryllium (Cu/Be) for the inner conductor and Stainless Steel for the outer conductor. Stainless Steel is a poor electrical and so poor thermal conductor. Cu/Be has been chosen due to its relatively small thermal conduction but still reasonable electrical conduction. The resistance of a single line of this Cu/Be coax is 7 ohm (3.5 ohm/m). The amplitude of the Johnson-Nyquist noise for a resistance R at a temperature T is given by:

$$\overline{v^2} = 4k_B T R \Delta f \quad (3.1)$$

where k_B is the Boltzmann constant and Δf the considered bandwidth. By considering the line as separated segments having a defined temperature (30 cm at 300 K and then a linear dependence from 300 K to 1 K), for one Cu/Be coax the noise amplitude is $\sim 0,2 \text{ nV} \cdot \text{Hz}^{-1/2}$. Heat brought by these Cu/Be coaxes on the 1 K pot can be estimated using the Wiedmann-Franz law which relates the thermal conductivity to the electrical one:

$$\dot{Q} = \frac{\pi^2}{3} \left(\frac{k_b}{e} \right)^2 \frac{1}{R} \frac{T_i^2 - T_f^2}{2} [\text{W}] \quad (3.2)$$

where R is the resistance of the wire. Both outer and inner conductor of each Cu/Be coax are thermalised on the 1 K pot. For $R=7 \Omega$, $T_i = 300 \text{ K}$ and $T_f = 1 \text{ K}$, we find $\dot{Q}_{300\text{K} \rightarrow 1\text{K}} = 135 \mu\text{W}$. There are 26 coaxes, the total heat load is $\sim 3.5 \text{ mW}$. The cooling power of the 1 K pot is close to 100 mW so we can safely use this type of coaxes.

For the purpose of RF filtering, Thermocoax™ are employed between the 1 K pot and the mixing chamber. The inner conductor is made of Nickel/Chrome, the outer conductor of Stainless Steel and in between, the dielectric is Magnesium Oxide. Thermocoax™ exhibits a low-pass filter behavior with a cutoff frequency around ~ 20 MHz. For frequencies above 20 GHz the attenuation is more than 200 dB.m^{-1} [Zor95]. In these conditions, we can neglect the heat brought by propagating photons.

For an almost 3 m Thermocoax™, having a resistance of $\sim 150 \Omega$, $\dot{Q}_{1\text{K} \rightarrow 20\text{mK}} = 85 \text{ pW}$. This power is negligible compared to the cooling power of mixing chamber which is close to $10 \mu\text{W}$ at 20 mK and do not perturb the functioning of the cryostat.

The Johnson-Nyquist noise generated by a single Thermocoax™ is $\sim 0.08 \text{ nV.Hz}^{-1/2}$, far below the noise level of electronics. The total noise generated by a coaxial lines is on the order of $\sim 0,22 \text{ nV.Hz}^{-1/2}$, lower than the noise of our room temperature electronic ($\sim 0,4 \text{ nV.Hz}^{-1/2}$).

Besides being difficult to be soldered reliably, one drawback of Thermocoax™ is the fact that it requires quite a lot of space. Indeed, we want to have the possibility to disconnect the part where the sample is installed, the cold finger, from these lines installed in the cryostat. We therefore need connectors between the cold finger and these lines. Each coaxial line needs its own connector. In our set-up, we have 26 coaxial lines terminated by SMC connectors fixed on a copper plate at the mixing chamber for proper thermal anchoring (see the picture in fig. 3.2, the plate is boxed in red). This plate is 15 cm by 10 cm and already occupies half of the space available on the mixing chamber. To increase the number of DC lines, an other approach is needed.

Constantan lines

In order to circumvent these problems we used a technique developed in our group [Man11] which allows to have several tens of DC lines (30 for this set-up) in a very compact manner inside a Copper/Nickel (Cu/Ni) capillary.

Compared to coaxial lines, 30 wires are grouped together in a 3 mm diameter capillary and soldered to a single compact connector. This connector (boxed in blue on the left picture in fig. 3.2) is thermally anchored with a big copper piece attached to the mixing chamber to ensure good thermalisation. This connector only is 4 cm by 1,5 cm (to be compared to the 15 cm by 10 cm copper plate). Below, the second part of the connector allows the connection to the cold finger on which the sample is installed.

These lines are made of Constantan, a Copper/Nickel/Manganese alloy with a ratio close to 58%/40%/2%. Constantan is about 25 times more resistive than copper. We used wires with a diameter of $120 \mu\text{m}$, the resistance is 130Ω for a length of $\sim 2 \text{ m}$.

In order to filter the high frequency signals which could propagate from 300 K to the sample, the Cu/Ni capillary is filled with Ecosorb™. Ecosorb™ is a two part compound heavily loaded with magnetic particles, in this case ferrite and act as a microwave absorber. Ferrite are iron oxides which have a high permittivity and a high permeability. Most of the microwave energy is stored into the material and converted into heat due to the high magnetic and dielectric losses [Eme]. As Thermocoax™, this assembly behaves as a low-pass filter with a cut-off frequency of ~ 10 MHz.

Direct connection from 300 K down to the mixing chamber would result in a heat load of $\dot{Q}_{300\text{K} \rightarrow 20\text{mK}} = 8 \mu\text{W}$ for each wire and even worse for the Cu/Ni capillary. The heat load can actually be strongly reduced by thermally anchoring the Cu/Ni capillary on all stages of the cryostat. By measuring of the temperature of the inner conductor of coaxial lines and Constantan lines, we show that both types of lines are adapted to very low temperatures (see sec. 3.1.3).

3.1.2 Cold finger

To install the sample at low temperature, it is first glued on a chip carrier (see sec. 3.2.5) and this chip carrier is installed inside the cold finger. The cold finger is machined from oxygen free high thermal conductivity (OFHC) copper and gold plated to avoid oxidation. It is divided in two parts: the body and the cap as shown in fig. 3.2. The cap is strongly attached to the mixing chamber for proper thermalisation. Inside the body, a homemade connector is installed. This connector is the interface between the chip carrier on which the sample is glued and the 42 DC lines. It is made of 42 pins on which DC lines are soldered. The head of a pin is actually a small metallic ball mounted on a spring to ensure a good electrical contact with the chip carrier.

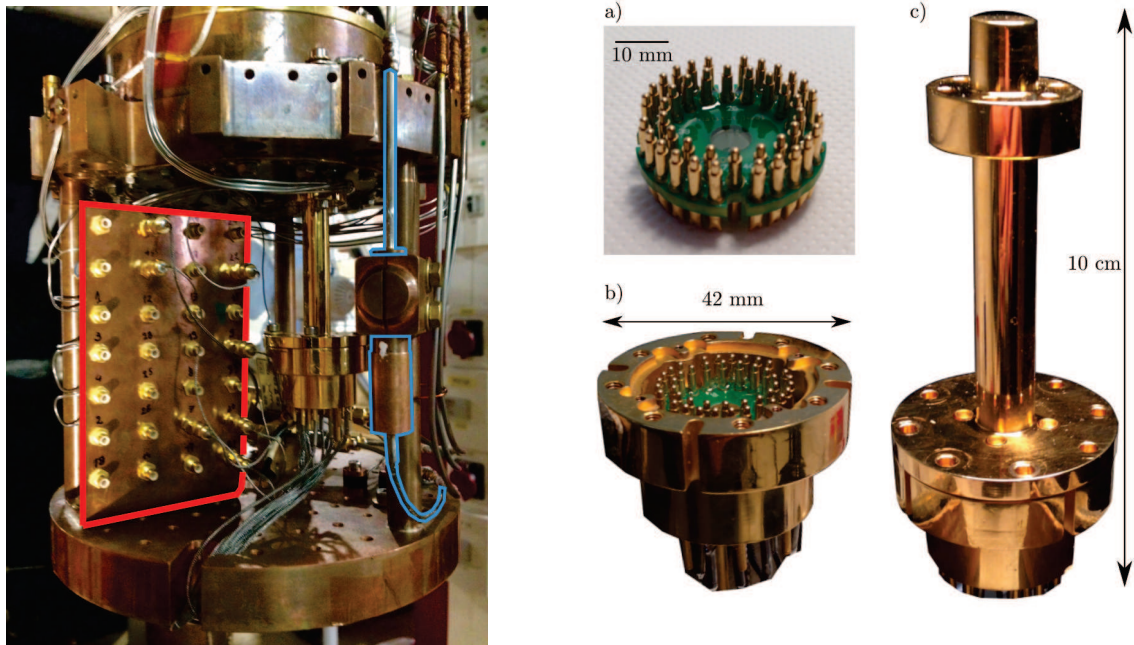


Figure 3.2: **Left:** picture of the mixing chamber of the dilution cryostat on which the new set-up is installed. The 26 ThermocoaxTM are soldered to SMC connectors screwed on the copper plate boxed in red. The capillary which contains the 30 Constantan wires as well as the intermediate connector are boxed in blue. **Right:** a) The 42 pins connector, b) the body of the cold finger with the 42 pins connector installed and c) the body attached to the cap.

3.1.3 Temperature performance

We have mentioned before that it is not at all obvious that the sample is at the same temperature as the base temperature of the cryostat. As the sample is cooled down via the electrical connections (DC lines), it is important to know their actual temperatures. For this purpose, we have mounted two RuO_2 resistances coming from the same batch on a chip carrier. One resistance is connected to four coaxial lines and the other to four Constantan wires in order to perform a four-probe measurement. The electrical connection between the chip carrier and the resistances is made by micro-bonding with gold wires (20 μm diameter). The two resistances are glued on the chip carrier with GE Varnish. A thin sheet of cigarette paper is inserted between the resistances and the chip carrier to avoid electrical shortcut. A picture of the ensemble is shown in fig. 3.3. The chip carrier is then installed in the cold finger which is fixed on the mixing chamber of a dilution fridge with a base temperature of 8 mK.

Results

Starting the measurement from 8 mK the temperature is increased by step up to 800 mK. The observed temperature dependence for both resistances presented are very similar as shown in fig. 3.4. The temperature dependence of the RuO_2 resistance used as a low temperature thermometer for this cryostat is also plotted in fig. 3.4: this is our reference. Below 30 mK, the deviation of both curves compared to the reference indicate that the resistances start to thermally decouple from the cryostat. The resistance connected to Constantan wires reaches a value slightly larger than the one connected to coaxial lines. Since both resistances are connected in the same way and both curves are superimposed up to ~ 20 mK, this seems to indicate that Constantan wires bring less heat to the resistance compared to coaxial lines.

We can estimate the temperature of the internal conductor of both wires. The maximum value of the resistance connected to Constantan wires is 31.4 k Ω . By projecting this value

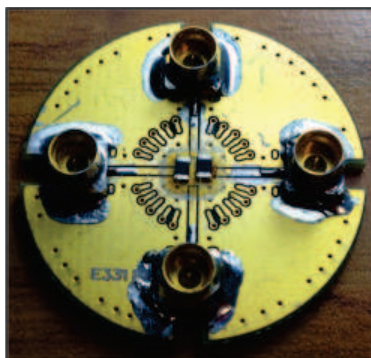


Figure 3.3: The two RuO_2 resistances mounted on a chip carrier. The left one is connected via bonding wires to four coaxial lines and the right one to four Constantan wires. Resistances are microbonded with gold wires.

on the curve of the reference, one finds a temperature $T_1 \simeq 13.8$ mK (see inset in fig. 3.4). The resistance connected to coaxial lines reaches a maximum value of 30.5 k Ω which corresponds to a temperature $T_2 \simeq 14.4$ mK. Both temperatures are very close to the base temperature of the cryostat and hence both sets of DC lines are well suited to work at millikelvin temperatures. Further improvement of our set-up could be achieved by connecting the Constantan wires/coaxial lines to a thermalisation stage installed on the mixing chamber of the cryostat. Such solution is currently tested to evaluate the gain.

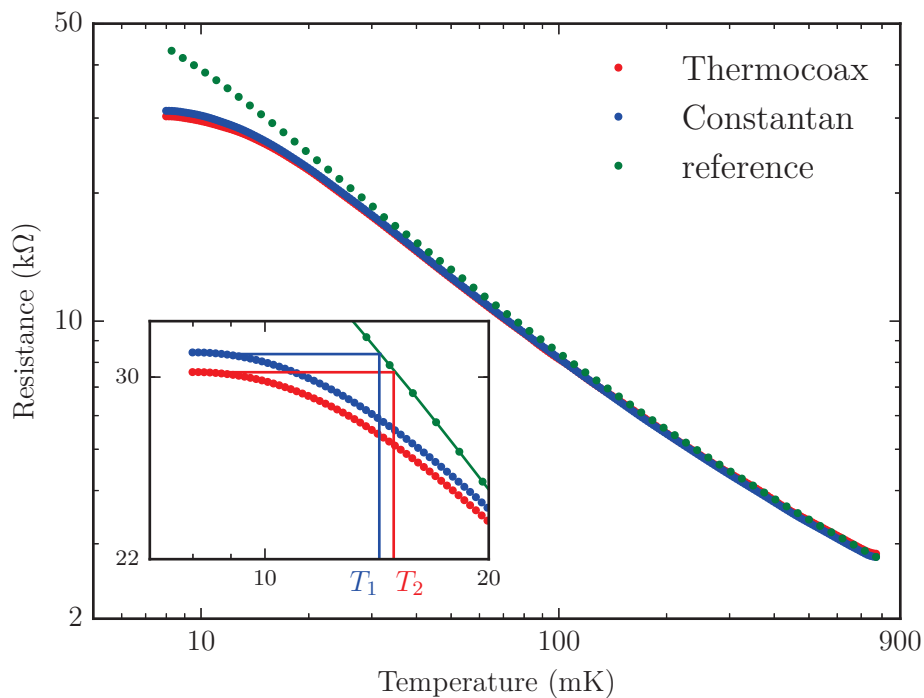


Figure 3.4: Variation of the three RuO₂ resistances with temperature. They exhibit similar behavior up to 30 mK. Below, resistances connected to Thermocoax™ and Constantan wires start to saturate indicating a less efficient cooling. Inset show a zoom on the low temperature range, to estimate the temperature of each resistances, we project the value of the resistance on the curve of the reference. For Constantan wire, we find $T_1 \simeq 13.8$ mK and for Thermocoax™ we find $T_2 \simeq 14.4$ mK.

3.2 RF connections

The DC part of the set-up is well adapted to deal with low frequency signals, however it is not at all suited for high frequency signals. The typical time scale for the fast voltage pulses used is on the order of 30 ps to 100 ps. This requires the use of a transmission line having a bandwidth of at least 20 GHz. This transmission line is composed of several elements including a radio-frequency (RF) line, cryogenic attenuators, bias T, coplanar waveguides on the chip carrier and coplanar waveguides directly patterned on the sample.

3.2.1 RF line

The RF line has to be broadband and hence has to have a low electrical resistance. These are however exactly the two conditions which lead to propagation of thermal radiation and high thermal conduction. To inject voltage pulses in our system, we directly connect the RF line (its inner conductor) to the 2DEG, so the electronic temperature of our sample is strongly linked to the one of the inner conductor. It is then important to properly thermalise this RF line.

3.2.2 Thermalisation of RF lines

Thermal conduction

To limit heat propagation by thermal conduction, we used silver plated stainless steel coax on the stage between 300 K and 1 K. High frequency current flows only in a few skin depths δ of the surface allowing the use of a poor electrical and so poor thermal conductor, stainless steel, clad with a thin layer of a few μm of a good conductor, silver ($\delta = 2 \mu\text{m}$ at $f = 1 \text{ GHz}$ for silver and evolves as $\sim 1/\sqrt{f}$ [M P05]).

The stage from the 1 K pot down to the mixing chamber is made from Niobium (Nb) coax. Nb has a critical temperature of 10 K, so below 1 K, the resistance of the line is basically zero and the number of quasi-particles which could carry heat is close to zero thereby thermal conduction is very low [Ash76].

The thermalisation of the outer conductor of these coaxes is simply done by winding several copper braids around them and attach these braids to the different stages of the cryostat. The thermalisation of the inner conductor is partly due to the attenuators used to attenuate thermal radiation (see next paragraph) and partly due to the dielectric core between the outer and the inner conductor [Gab06a]. Attenuators are crimped in OFHC copper pieces for thermal anchoring. These elements are presented on the scheme in fig. 3.5.

Thermal radiation

To attenuate thermal radiation, cryogenic attenuators (XMATM) are inserted at different stages of the cryostat. We can sketch the situation as depicted in fig. 3.6. A RF line coming from a hot source at a temperature T_{in} is connected via an attenuator having an attenuation of $10 \times \log(D) \text{ dB}$ to a RF line going to a stage at a lower temperature. The attenuator is thermally anchored to a source at a temperature T_B . Under the condition where we consider only photons having a frequency in the range of the RF line bandwidth ($\sim 0 - 40 \text{ GHz}$), one can make a simple analogy: the attenuator act as a beam splitter, hot photons are attenuated by a factor D^2 and photons emitted by the source at a temperature T_B are reflected with a factor $1 - D^2$. T_{in} and T_{out} are simply linked by the following relation:

$$T_{out} = D^2 \times T_{in} + (1 - D^2) \times T_B \quad (3.3)$$

Two attenuators are inserted in the RF line, one of -30 dB at 1 K and one of -30 dB on

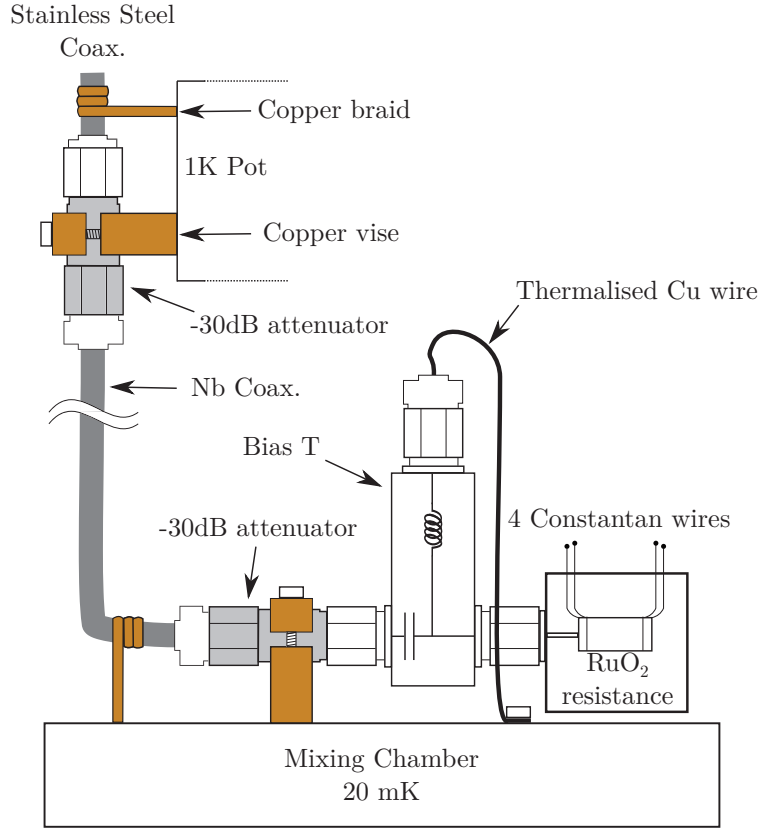


Figure 3.5: Schematic of the RF line including attenuators and the bias T. Thermalisations of the Nb coax on the Still and on the cold plate are not shown. The RuO_2 resistance is used to measure the temperature of the inner conductor right after the bias T.

the mixing chamber at 20 mK. From the measurement of the transmission of this RF line (see fig. 3.8), we know that for frequencies higher than 20 GHz, the RF line has an intrinsic attenuation of at least 5 dB. This attenuation is mainly due the stainless steel coax installed on the stage between 300 K and 1 K. The total attenuation on this stage is then 35 dB. Using eq. 3.3 we calculate the temperature after each attenuator. Results are given in the table 3.1 and show that the contribution of thermal radiation is strongly reduced by using attenuator.

Table 3.1: Temperatures calculated after the attenuators.

T_{in}	300 K	1.1 K
Stage temperature	1 K	20 mK
Attenuation	35 dB	30 dB
T_{out}	1.1 K	21.1 mK

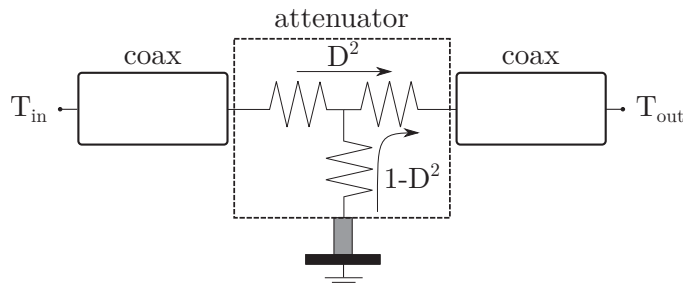


Figure 3.6: Schematic of the attenuation of thermal radiation by an attenuator. The attenuator can be viewed as a beam splitter with a transmission coefficient D^2 and a reflection coefficient $1 - D^2$.

3.2.3 Measurement of the temperature of the inner conductor

Even if the thermalisation of the RF line have been done really carefully, at the mixing chamber level, the temperature of the inner conductor can differ from the cryostat base temperature. For example, the dielectric core made of Teflon has a thermal expansion coefficient almost 10 times higher than stainless steel and Niobium. At low temperature, the contraction of the dielectric core is higher than the one of the outer conductors resulting in a much less efficient thermalisation of the inner conductors. Since the inner conductor is (almost) directly connected to the 2DEG, it is crucial to know its temperature. By almost, we mean that we have to take into account the bias T. In some case, it is needed to superimpose DC voltages to RF signals. This can not be done through the RF line because of the attenuators which act as short to ground for DC signals. A bias T SHF BT 45A compatible with cryogenic temperatures (RF port bandwidth: 20 kHz to 40 GHz) is then inserted at the end of the RF line. The temperature of interest is the temperature of the inner conductor at the output of the bias T.

To measure this temperature, a RuO_2 resistance is installed in a brass box, a SMA connector mounted on this box is screwed onto the bias T. The resistance is directly connected to the inner conductor of this connector. A 4 probe measurement is performed to record the evolution of the resistance as a function of the mixing chamber temperature. The wires used to measure the resistance are thermalised on the mixing chamber so we inserted a stage of Constantan wires to avoid a cooling by these measurement wires. We reproduced the configuration used when the sample is installed, especially the fact that a thermalised copper wire used to bring the DC signal is connected on the DC port of the bias T (see fig. 3.5).

We also measured the temperature of the inner conductor of the RF line without the bias T installed in order to evaluate its contribution to the cooling. Since a thermalised copper wire is connected to the DC port of the bias T, a better thermalisation of the inner conductor may be expected.

Results

The evolution of the temperature of the inner conductor of the RF line as a function of the mixing chamber (MC) temperature with and without the bias T installed are shown in fig. 3.7.

Without the bias T installed, below 200 mK, the temperature of the inner conductor already starts to decouple from the MC temperature. When the base temperature of the cryostat is reached ~ 20 mK, the temperature of the inner conductor is actually much higher, on the order of 110 mK.

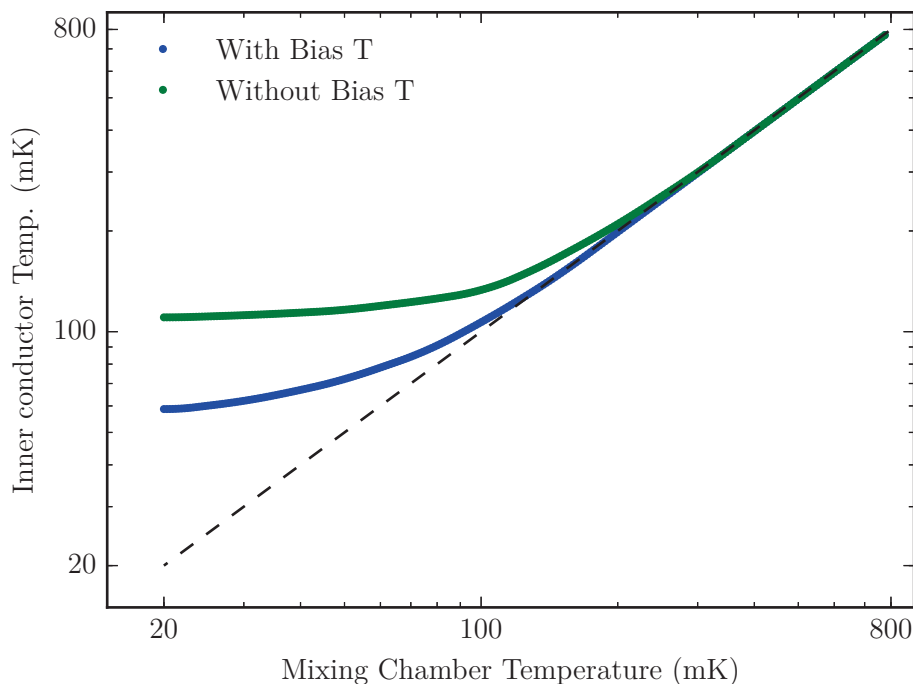


Figure 3.7: Measurement of the temperature of the inner conductor of the RF line with and without the bias T installed as a function of the mixing chamber temperature.

With the bias T is installed, the inner conductor starts to be thermally decoupled from the mixing chamber around 100 mK. At 20 mK, the temperature of the inner conductor of the bias T is ~ 60 mK, lower than without the bias T but still relatively high compared to the base temperature.

For the envisaged experiments, this should not be a problem. This temperature is well below 100 mK so still in the good range to observe quantum phenomena. Moreover, the sample is connected to DC lines having a temperature close to the base temperature (as shown in sec. 3.1). Some part of the sample (ohmic contacts) are also grounded directly on the chip carrier at low temperature and should help for a better thermalisation.

However, to overcome this limitation, additional strategies must be implemented to properly thermalise this inner conductor. Homemade thermalisation devices will be soon tested and

should improve significantly this result.

3.2.4 Characterization of the transmission

The spectrum of a voltage pulse is composed of a large number of frequencies. As the attenuation of a RF line is usually frequency dependent, it is important to characterize this dependence in order to evaluate the effect on the pulse shape. The attenuation in a frequency range of 1 GHz to 20 GHz has been measured using a Vectorial Network Analyzer (VNA). The attenuation measured at 300 K and 20 mK is presented in fig. 3.8. As expected, the attenuation is well reduced at low temperature because Nb coax turns superconducting. At 1 GHz, the attenuation is less than -1 dB. The attenuation is slightly dependent on the frequency and increases to -5.5 dB at 20 GHz. This frequency dependent attenuation will cause a small distortion of the voltage pulses but is still acceptable (see chapter 4 on the experimental results).

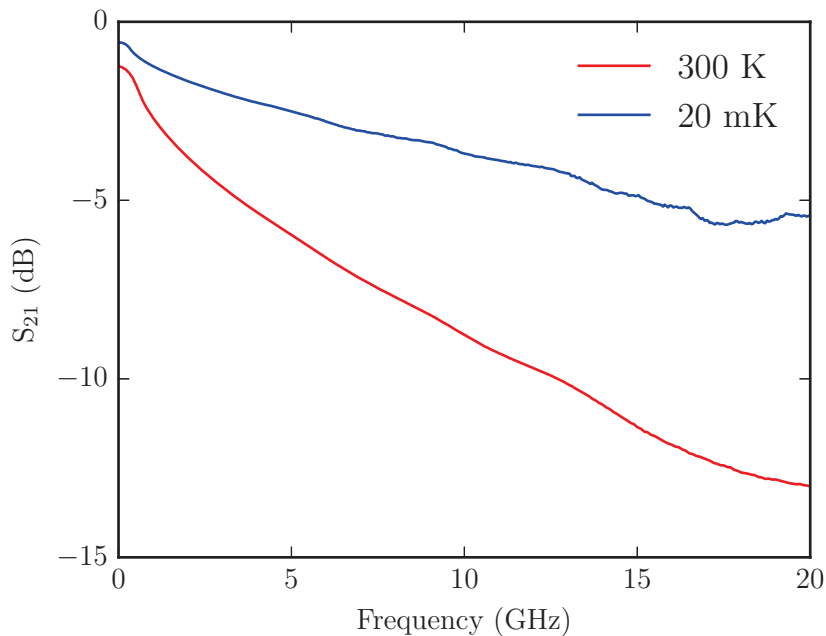


Figure 3.8: Attenuation of the RF line measured at 300 K and 20 mK. At a temperature $T < 10$ K, Niobium becomes superconducting and the attenuation is drastically reduced.

3.2.5 Design of the chip carrier

Connections of RF lines and DC lines to the sample is done by using a chip carrier or PCB (printed circuit board). The PCB is made by piling up metallic and dielectric layers (the substrate). It has been designed to separate DC connections and RF connections to reduce parasitic coupling.

The back side of the PCB (referred to as DC side, see a) in fig. 3.9) is dedicated to the connection to the DC/low frequency lines. This DC side is connected to the 42 pins using a spring-load mechanism (see b) in fig. 3.9). The 24 circular pads allow the connection to 24 DC lines. The choice of using only 24 DC lines and not 42 was guided by two reasons: it was sufficient considering the sample design (number of required electrostatic gates and number of ohmic contacts) and this allowed to improve the design of the RF part of the PCB.

The front side of the PCB (referred to as RF side, see c) in fig. 3.9) is dedicated to the connection to the RF lines and to accommodate the sample.

DC side and RF side are separated by an intermediate metallic layer used as a ground plane to avoid parasitic coupling.

Transmission of RF signals on the PCB up to the sample is ensured by 4 coplanar waveguides (CPWs). The large metalized area defines the ground plane of this CPWs. It is connected using vias to the intermediate ground plane such that all these parts have the same potential. Connection between these CPWs and RF lines is done by 4 RF connectors Rosenberger Mini-SMP having a bandwidth of 40 GHz soldered on the PCB (see d) in fig. 3.9). The PCB is designed to match perfectly the footprint of these connectors to optimize the RF signal transmission. As explained in the following, 4 CPWs are also patterned directly on the sample. The impedance of a CPW is defined by its geometry and the dielectric constant of the substrate. To ensure the continuity between CPWs on the PCB and CPWs on the sample, the substrate used has been chosen to have a dielectric constant as close as possible to the one of GaAs. GaAs has an $\epsilon_r \simeq 12.9$ at low frequency which decreases at high frequency (10 GHz) to $\epsilon_r \simeq 11$. We used the substrate Rogers R03010 having a $\epsilon_r \simeq 10.2$ [Rog]. The design of the CPWs has been done using the transmission line calculator TX-line.

The 24 DC contacts (circular pads) on the DC side are connected using vias to the 24 metallic lines patterned on the RF side (see c) in fig. 3.9). These metallic lines are brought as close as possible to the sample. They are also designed such that SMD (surface mounted device) components can be soldered between two lines of our choice. For instance, as shown on the picture in fig. 3.10, output currents produced by the sample are converted in voltages by resistances directly soldered on the PCB. The goal is to improve the signal to noise ratio. Since these resistances are installed at low temperature, their Johnson noise is very low.

To avoid direct coupling between the different ports of the PCB (between the metallic lines and the CPWs or directly between the CPWs) the internal face of the cap used to close the cold finger has been designed to be as close as possible to the surface of the PCB and to reduce as much as possible free space (see e) in fig. 3.9).

The sample is installed in a window of $3.4 \times 3.4 \text{ mm}^2$ drilled in the center of the RF side over a depth of $700 \mu\text{m}$, such that the surface of the sample is well aligned with the surface of the PCB. This allows to minimize the length of the bonding wires between the CPWs and the sample to about $200 \mu\text{m}$.

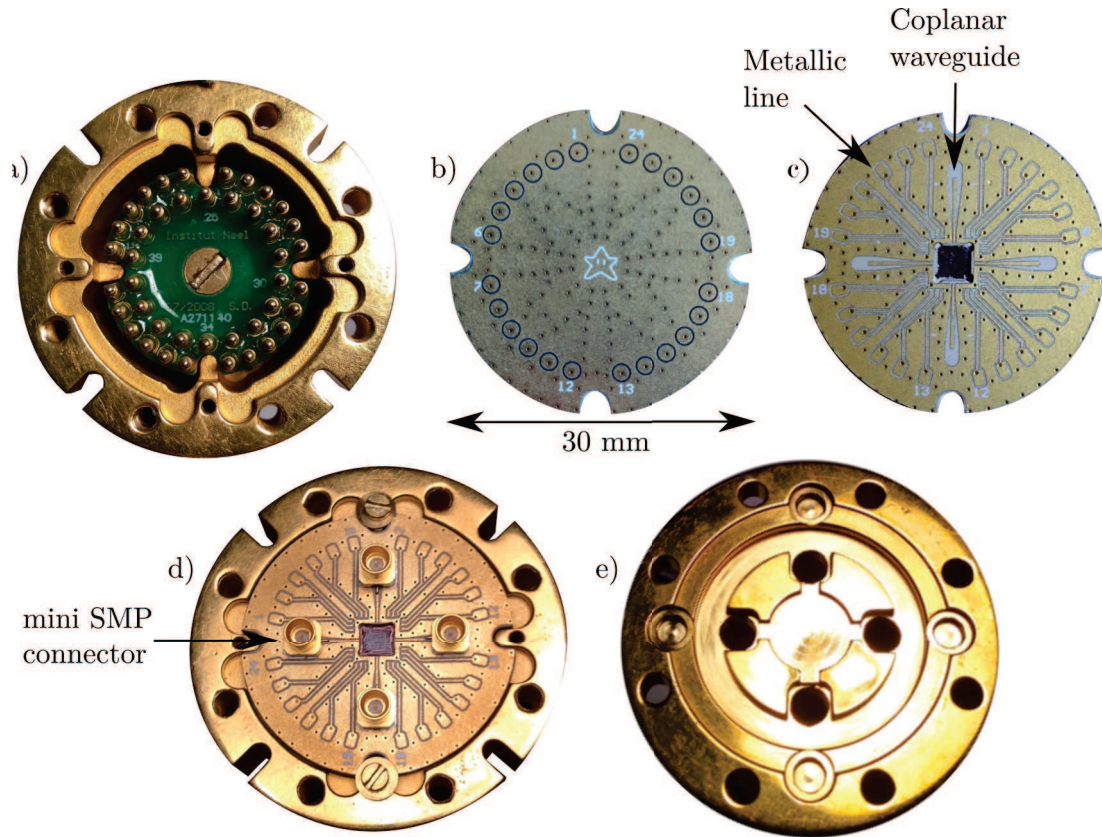


Figure 3.9: a) 42 pins connector on which the DC lines are soldered and onto which the PCB is installed. b) Back side of the PCB. The contact to DC lines is done by the 24 circular pads which sit on the most outer ring of the 42 pins connector. c) Front side of the PCB. The sample is installed in the central window. RF signals are guided up to the sample by 4 CPWs. DC contacts are connected to the 24 metallic lines using vias. d) PCB installed in the cold finger. The 4 RF connectors mini SMP are soldered on the PCB to connect RF lines to the 4 CPWs. e) Internal face of the cold finger's cap. It is designed to reduce maximally the free space.

3.2.6 Low resistance ohmic contacts

The injection of the voltage pulse into the 2DEG is done through an ohmic contact. The resistance of the contact has to be as low as possible to avoid unwanted reflection and dissipation. The fabrication of a reliable and low resistance ohmic contact is not so straightforward, especially for relatively small contacts (on the order of $10\ \mu\text{m} \times 10\ \mu\text{m}$). We therefore have spent some effort to realize and characterize low resistance ohmic contacts. For that purpose, we used the so-called transmission line method described by Goktas et al. in [Gök08]. We compared 2 recipes: the recipe used with success in our group for

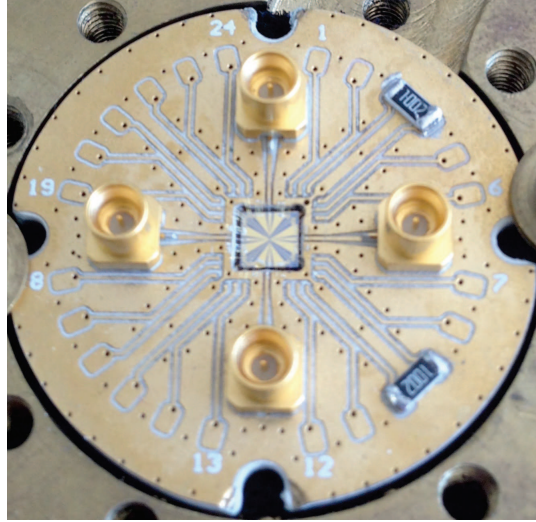


Figure 3.10: Picture of the sample installed on the PCB. The 4 CPWs patterned on the sample appear clearly. We also see the two resistances soldered between different metallic lines to convert output currents into voltages.

relatively large contacts ($\sim 100 \mu\text{m} \times 100 \mu\text{m}$), referred to as recipe 1 and the one proposed by Goktas et al., referred to as recipe 2. The recipe from Goktas et al. should allow to fabricate ohmic contacts having a typical resistance of $\sim 25 \Omega$ for a $10 \mu\text{m} \times 10 \mu\text{m}$ contact. Both recipes are detailed in table 3.2.

Table 3.2: Recipe used in the group (Recipe 1) and proposed by Goktas et al (Recipe 2).

Step	Recipe 1	Recipe 2
O_2 plasma	10 s	10 s
Cleaning in $H_2SO_4 : H_2O$ (1:5) ^a	no	30 s
Cleaning in HCl (30%)	no	5 s
Metal deposition	5 nm Ni 60 nm Ge 120 nm Au 10 nm Ni 100 nm Au	126.7 nm Au 62.4 nm Ge 47.3 nm Ni
Annealing (performed under N_2 atmosphere)	Rapid heat to 450° hold for 60 s Cooling down to room T°	Rapid heat to 370° hold for 120 s 450° for 50 s Cooling down to room T°

^a In the recipe 2 proposed by Goktas et al. , they originally used Semico-Clean™ for 2 minutes to eliminate organic material but we could not get this product. We replaced it by $H_2SO_4 : H_2O$.

The method to determine the contact resistance is the following: we etched a mesa strip

and deposited contacts at several places along this strip (see fig. 3.11). The distances between the left contact and others are: $30\ \mu\text{m}$, $70\ \mu\text{m}$, $120\ \mu\text{m}$, $180\ \mu\text{m}$ and $280\ \mu\text{m}$. We then measured the resistance between the left contact and the others at low temperature (4K). This resistance is the total resistance which is two times the contact resistance ($2 \times R_C$) in series with the mesa resistance. Measuring the total resistance for different lengths gives the curve $Total\ resistance = R_{mesa} + 2R_C$. By extrapolating this curve to a mesa length equal to zero, one obtains the value for $2R_C$ as shown in fig. 3.12.

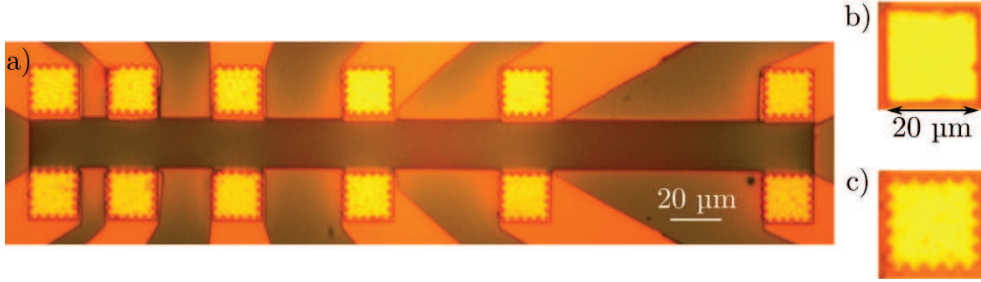


Figure 3.11: a) Sample designed to determine the resistance of the ohmic contacts. On the right, the two types of contacts, b) smooth edges and c) notched edges.

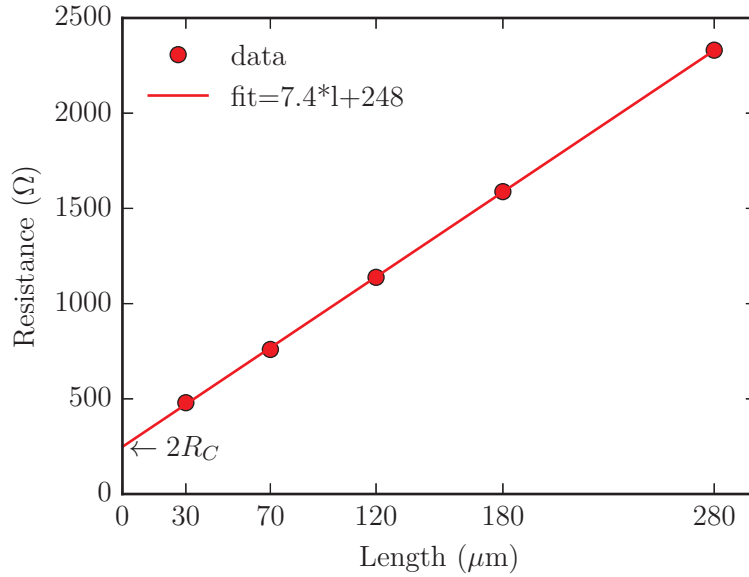


Figure 3.12: Measurement of the variation of the total resistance with the length of the mesa. For this configuration we obtained $2R_C = 248\ \Omega$.

We have characterized 3 different sizes of contacts: $20 \times 20\ \mu\text{m}^2$, $10 \times 10\ \mu\text{m}^2$, $5 \times 5\ \mu\text{m}^2$. Finally, Goktas et al. showed that the contact resistance depends on the alignment of the contact with crystallographic axis. Resistance of the contact is lower (higher) when the border between contact and mesa is perpendicular to $[011]$ ($[0\bar{1}\bar{1}]$) direction. One way to

avoid this dependence is to design contacts with notched edges. To get a complete picture, we characterized contacts aligned with the $[011]$ and $[01\bar{1}]$ directions and with two different designs, a square with smooth edges and one with notched edges (see fig. 3.11).

Table 3.3: Ohmic contact resistances in Ω obtained for the different configurations. The indicated crystallographic axis is the one with which the contact is aligned.

$20 \times 20 \mu\text{m}^2$	Recipe 1	Recipe 2
Configuration	R (Ω)	R (Ω)
Smooth edges/ $[011]$	77	97
Smooth edges/ $[01\bar{1}]$	76	125
Notched edges/ $[011]$	90	97
Notched edges/ $[01\bar{1}]$	61	93

$10 \times 10 \mu\text{m}^2$	Recipe 1	Recipe 2
Configuration	R (Ω)	R (Ω)
Smooth edges/ $[011]$	118	170
Smooth edges/ $[01\bar{1}]$	134	188
Notched edges/ $[011]$	214	127
Notched edges/ $[01\bar{1}]$	140	124

$5 \times 5 \mu\text{m}^2$	Recipe 1	Recipe 2
Configuration	R (Ω)	R (Ω)
Smooth edges/ $[011]$	232	789
Smooth edges/ $[01\bar{1}]$	292	522
Notched edges/ $[011]$	495	224
Notched edges/ $[01\bar{1}]$	243	448

The results of these measurements for all the configurations are presented on table 3.3. Only one $5 \times 5 \mu\text{m}^2$ contact of the recipe 2 was not working, most probably due remaining resist after the lithography (it was close to the edge of the sample where resist thickness vary a lot leading to a bad exposure). Otherwise all the contacts were working, which implies that both recipes allow to get very reliable contacts. These two recipes give similar results for each configurations. Results confirm that the contact resistance depends on the length of the border between the contact and the 2DEG and not on the contact area. Going from $5 \times 5 \mu\text{m}^2$ to $10 \times 10 \mu\text{m}^2$, the contact resistance decreases by a factor of 2 as well as going from $10 \times 10 \mu\text{m}^2$ to $20 \times 20 \mu\text{m}^2$. Resistances for $5 \times 5 \mu\text{m}^2$ contacts show a large spreading, ranging from 224Ω to 789Ω . On the other hand, resistances for contacts of $10 \times 10 \mu\text{m}^2$ and $20 \times 20 \mu\text{m}^2$ are quite reproducible.

Contact resistances obtained with the recipe 2 proposed by Goktas et al. are higher than expected. In their paper, they obtained contact resistances on the order of 25Ω for a border length of $10 \mu\text{m}$ (12.5Ω for $20 \mu\text{m}$ and 50Ω for $5 \mu\text{m}$). Our measurements show a difference of roughly a factor of 5. It is commonly assumed that the contact resistance

is strongly linked to the cleanness of the surface of the mesa. The discrepancy between their results and our measurements may come from the fact that we could not reproduce exactly the cleaning procedure: replacing Semico-CleanTM by $H_2SO_4 : H_2O$ could be at the origin of this difference.

In conclusion, for our purpose, it seems better to not decrease the size below $10 \times 10 \mu\text{m}$. We do not see clear dependence on the crystallographic orientation nor with the edge design. Since our recipe gives similar results and involves less fabrication steps, we used this one for the sample fabrication.

3.2.7 Design and fabrication of the sample

The design of the sample must fulfill several requirements:

- The ohmic contact used to inject the voltage pulse in the 2DEG must be as close as possible to the heart of the sample. Indeed, it is important to reduce as much as possible the unnecessary propagation of the pulse in the 2DEG which would result in a broadening of the pulse. Dimensions of this contact are therefore close to the dimensions of the central part of the sample, typically a few μm . From our results on low resistance ohmic contacts, we decided to use a $10 \times 10 \mu\text{m}^2$ contact.
- To avoid distortion of the pulse, we patterned a CPW from the outer edge of the sample up to this ohmic contact. The dimensions of this CPW at the edge of the sample match the dimensions of the CPW on the PCB. Between the edge of the sample and the ohmic contact, these dimensions have to adapted. The inner conductor is $200\mu\text{m}$ wide at the edge of the sample and has to be reduce to $10\mu\text{m}$ at the ohmic contact level. The tapered design of this CPW ensure the impedance matching while dimensions are changing (see fig. 3.13).
- To perform the different experiments for which particular gates are pulsed on a 100 ps timescale, the same approach as above must be used. Therefore, these gates are also connected to three CPWs. In total, 4 CPWs are patterned onto the sample. One for the ohmic contact and three for pulsed gates. A picture of the sample is shown in fig. 3.13.

I have realized the entire fabrication of the sample has been done at the in-house clean room Nanofab as well as the PTA. The main steps are described in the following:

1. **Mesa:** first the mesa has to be defined. The idea is to remove the 2DEG where it is not necessary allowing to predefine the sample geometry and reduce leakage current between gates and the 2DEG. The part where the 2DEG is left is called the mesa. It is patterned by laser lithography. After development of the lithography, the part which defines the mesa is protected by a layer of resist. The sample is then dipped into a solution of $H_2O : H_2O_2 : H_3PO_4$ for a few tens of second which results in an etching of the first 100 nm of the unprotected surface and hence the suppression of the 2DEG.
2. **Ohmic contacts:** contacts are patterned by laser lithography. As explained in sec. 3.2.6, right after the development, the surface where contacts are going to be

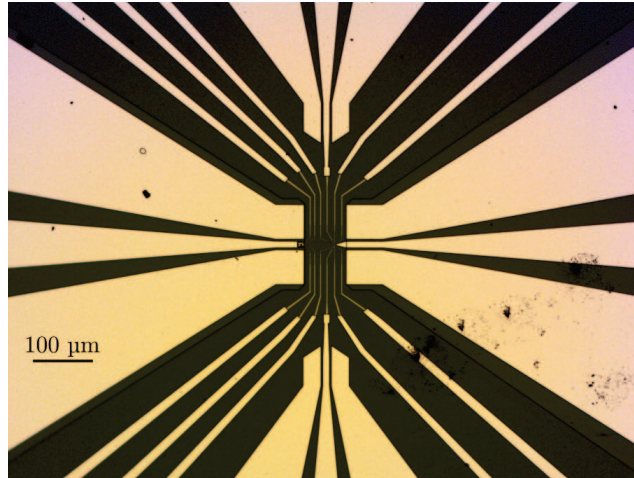


Figure 3.13: Photography of the sample. The tapered design of the 4 CPWs ensure the impedance matching while dimensions are changing. The left CPW is connected to the ohmic contact. The three others CPWs are connected to pulsed gates. In the center, we distinguish the fines gates patterned by e-beam connected to the large gates.

deposited is cleaned by using O_2 plasma. Different metallic layers (Ni/Ge/Au/Ni/Au) are deposited and the annealing process is performed. At the same time, the bonding pads of the electrostatic gates are realized. The structure of the ohmic contacts allows to make very resistant bonding pads and the roughness of the melted metallic surface after annealing help for bonding.

3. **Fines gates:** these gates define the heart of the sample and represent the trickiest part of the sample fabrication. In particular, the gate which control the tunnel coupling between the two wires must be as thin as possible to offer the maximum tunability. These gates are patterned by electronic lithography. We used an e-beam JEOL 6300FS having a resolution of less than 20 nm. The big advantage of such a machine is the high voltage of 100 kV used to accelerate electrons. A high voltage allows a much finer lithography and reduces proximity effect so one can write much more dense patterns (in terms of number of gates and distances between these gates). A picture of the sample is presented in fig. 3.14. The tunnel gate is only 25 nm wide.
4. **Large gates:** these gates are patterned by laser lithography and connect the fines gates to the bonding pads. During this step, we also patterned the 4 CPWs described above.

3.2.8 Pulse sources

Arbitrary Waveform Generator

All the experiments presented in this thesis have been realized with an Arbitrary Waveform Generator (AWG) Tektronix 7122B. To generate a waveform, the AWG simply reads an

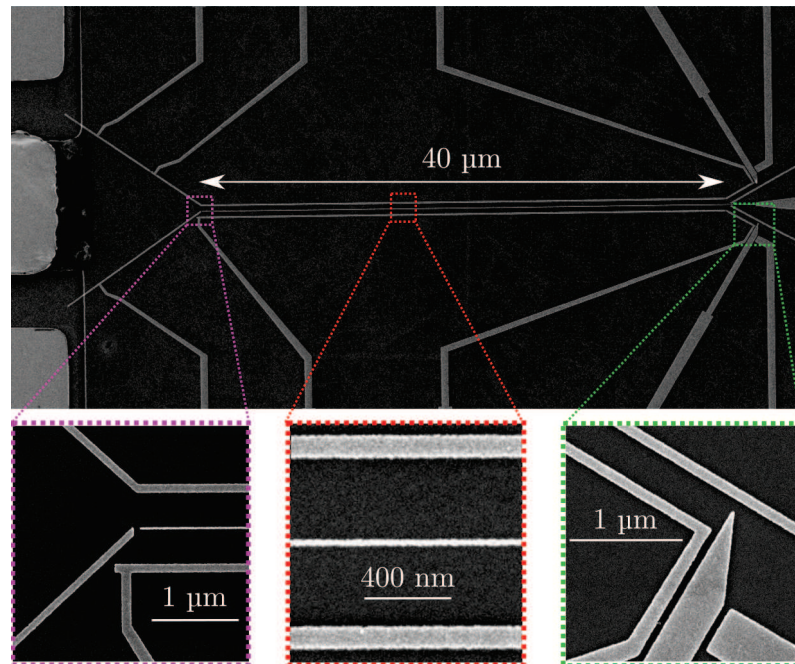


Figure 3.14: a) SEM image of the central part of the sample. These gates are patterned by e-beam lithography. On the left, we can see the end of the CPW (large light gray parts) connected to the ohmic contact (partly hidden dark gray square). b) Zoom on the entrance of the tunnel coupled region. Electrons are injected only in the upper channel. c) Zoom on the tunnel gate and the two side gates, widths are respectively ~ 25 nm for the tunnel gate and 100 nm for side gates. d) Zoom on the QPC used to probe the voltage pulse in-situ.

array of points with a sampling rate of 12 GS.s^{-1} , which means that the time between two points is ~ 83 ps. The shortest pulse one can make with this sampling rate has a FWHM of 85 ps (see fig. 3.15).

The AWG has two output which can generate independent waveforms at this sampling rate with a maximum voltage amplitude of 1 V. It is possible to control the time delay between the two outputs over 200 ps with a resolution of 1 ps. This feature was extensively used in the experiment where we probe the voltage pulse in-situ. The sampling rate can be increased to 24 GS.s^{-1} , in this case only one output is available and the maximum voltage amplitude is 500 mV. With this sampling rate, the pulse FWHM can be reduced to ~ 55 ps (see fig. 3.15).

Homemade pulse source

The AWG describe above is a powerful tool but suffer from two limitations: even when the sampling rate set at 24 GS.s^{-1} , the pulse FWHM is still a bit large and the maximum amplitude available is too low. Indeed, the number of electrons excited by a voltage pulse

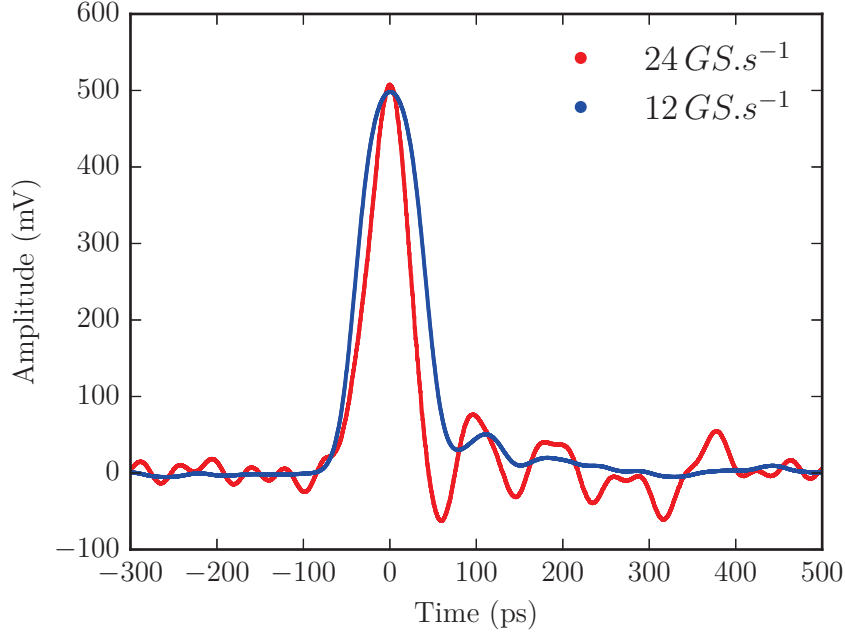


Figure 3.15: Shortest pulses generated by the AWG when the sampling rate is set at 24 GS.s^{-1} and 12 GS.s^{-1} .

is given by:

$$\bar{n} = \int_{-\infty}^{+\infty} \frac{e \times V(t)}{h} dt \quad (3.4)$$

where $V(t)$ is the time dependent voltage pulse, e the charge of an electron and h the Planck constant. The full attenuation on the RF line which guide the pulse from the AWG to the sample is $\sim 66 \text{ dB}$. For a voltage pulse with an FWHM of 55 ps and an amplitude $V_p = 500 \text{ mV}$, the number of excited electrons per pulse is roughly $\bar{n} \simeq 2 - 3$.

To probe the dynamical interference described in the Chapter 1, it would be more comfortable to reach a higher number of electrons per pulse. For these reasons, we built a homemade voltage pulse source which can produce voltage pulses with an FWHM close to 30 ps with a maximum amplitude of $\sim 6 \text{ V}$. Using this source, we can go up to $\bar{n} \simeq 20$. The development of this source is largely inspired from the work of Thibaut Jullien [Jul14]. The principle is quite simple: several harmonics of a 6 GHz sinusoidal source are summed and by controlling the amplitude and the phase of each harmonic, a train of voltage pulses with a FWHM of $\sim 30 \text{ ps}$ and a repetition frequency of the fundamental (6 GHz) is produced. This voltage pulse source is composed by the following elements:

- A 6 GHz source is connected to a power splitter. One output of the splitter is connected to a doubler which produces the 12 GHz harmonic.
- This 12 GHz signal is itself split by a power splitter and one output of this splitter is again connected to a doubler which produces the 24 GHz harmonic.

- Due to the difficulty to get a frequency tripler, an independent source generates the 18 GHz harmonic.
- Voltage controlled phase shifters and attenuators are used to control independently the phase and the amplitude of each harmonic. The amplitude of the 18 GHz harmonic is directly controlled from the source. We do not use a phase shifter for the 24 GHz harmonic since its phase can be fixed and serves as a reference.
- All the harmonics are amplified and recombined together to form a train of pulses with a repetition frequency set by the fundamental: 6 GHz.

The scheme of the set-up as well as typical pulses one can get after a proper tuning of the relative phases and amplitudes of each harmonic are shown in fig. 3.16. The control over the phase and the amplitude of each harmonic allows to fight against the unavoidable distortion of pulses during their propagation from the top of the cryostat up to the sample. The amplitude of each harmonic can be adjusted to compensate exactly the frequency dependent attenuation as well as the relative phases such that the pulse shape is well defined at the sample level: this procedure is called “pulse shaping”.

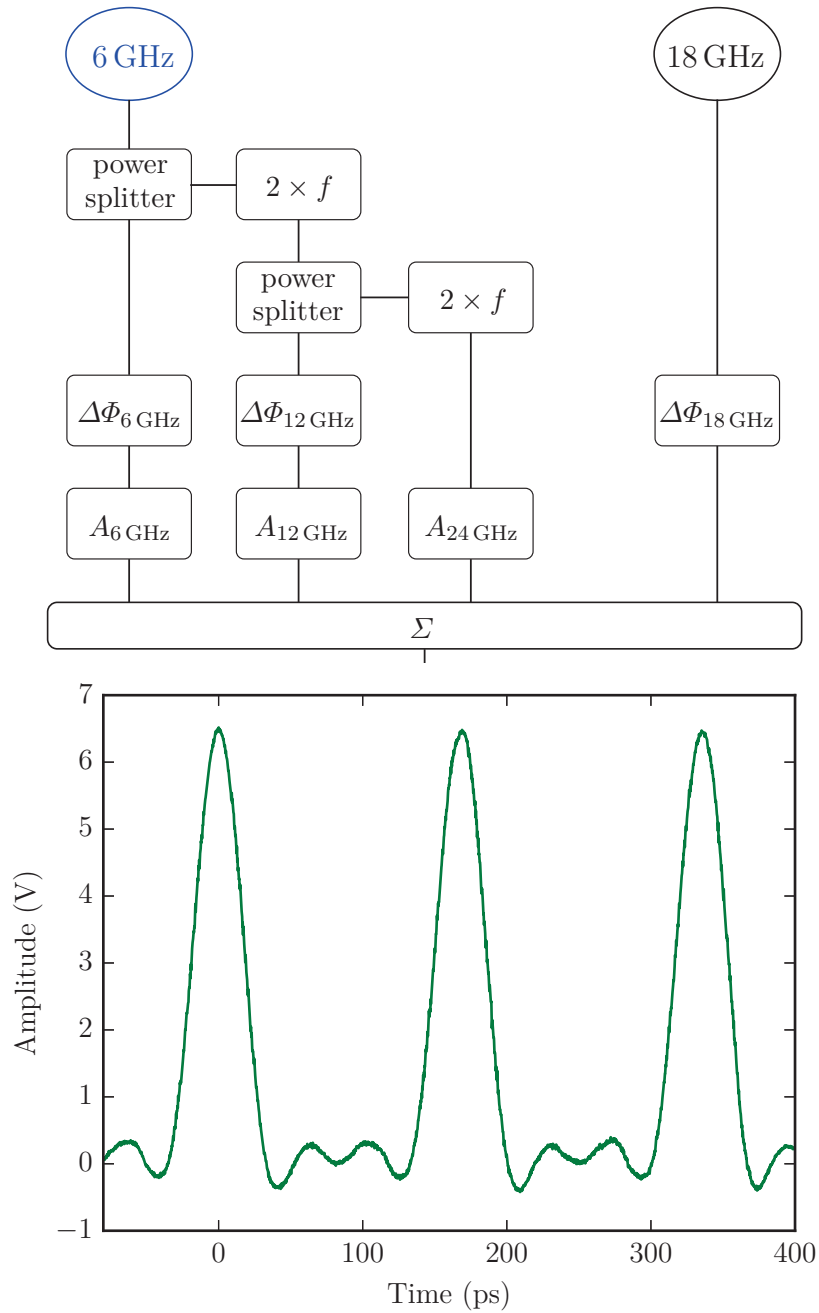


Figure 3.16: Schematic of the set-up used to generate voltage pulses by summing 4 harmonics. One source generates the fundamental at 6 GHz and by means of frequency doublers, the second (12 GHz) and the fourth (24 GHz) harmonics are generated. The third harmonic (18 GHz) is generated by an independent source. The phase of each harmonic can be set by voltage controlled phase shifters, except the phase of 24 GHz which is kept fixed. The amplitudes of the fundamental, the second and the fourth harmonics are adjusted using voltage controlled attenuators (attenuation ranging from 0 to 20 dB). The amplitude of the third harmonic is directly set by the source. All the harmonics are recombined together to form the train of pulses.

3.3 Electronics

3.3.1 Control of the electrostatic gates

The sample is defined by 14 electrostatics gates which need to be independently polarized to tune the sample into a proper configuration. A large number of independent voltage sources is then necessary to control these gates. We used a home made system based on a commercial digital-to-analog converter (DAC) chip (Linear Technology LTC2604). This chip is embedded on an electronic card including low-voltage power-line filtering and a low-noise amplification stage of the output. Optical isolation of the system allows to reduce problems related to ground loops and resulting 50 Hz noise. Each card hosts in the end eight voltage sources.

Each source has a 16 bits resolution for an operating range of -5 V to 5 V resulting in a $153\text{ }\mu\text{V}$ minimal voltage step. The typical noise is $\sim 25\text{ nV}\cdot\text{Hz}^{-1/2}$. A voltage can be changed every $16\text{ }\mu\text{s}$, and the rise time for the voltage is limited to $300\text{ mV}\cdot\mu\text{s}^{-1}$. Each source can be turned into a low frequency voltage source to perform Lock-in detection. The sources have a thermal drift of $0.25\text{ ppm}/\text{C}$, and exhibit a drift smaller than $10\text{ }\mu\text{V}$ in ten hours. Finally, two low-pass filters with cut off frequencies of 120 MHz , and 1.9 MHz have been put at the output of the voltage sources. By considering the present bandwidth (1.9 MHz), the voltage noise due to the source can be estimated to about $35\text{ }\mu\text{V}$.

3.3.2 Low noise detection

The measured signals are relatively small. At a temperature of 20 mK , the bias used must be on the order of the thermal energy $k_B T/e \sim 2\text{ }\mu\text{V}$ to not overheat the sample. The conductance of the sample is close to $10\text{ k}\Omega$ resulting in a current of $\sim 0.2\text{ nA}$. When voltage pulses are used, the current is given by number of electrons excited per pulse multiplied by the repetition frequency. Typically, one electron per pulse is excited at a repetition frequency of 500 MHz which gives a current of $\sim 0.5\text{ nA}$.

All the measurements have been realized by mean of Lock-in detection allowing to reach a very good signal to noise ratio (SNR). In our measurements, the SNR at least is on the order of $1/100$.

The current produced by the sample is actually converted into a voltage across a $10\text{ k}\Omega$ resistance directly soldered on the PCB. One terminal of the resistance is grounded on ground plane of the PCB. The Johnson noise produced by this “cold” resistance is $\sim 0.1\text{ nV}\cdot\text{Hz}^{-1/2}$. Two Coaxial DC lines are connected to the resistance and to a home made room temperature voltage amplifier EPC1b with a gain of 10^4 and a noise level of $0.4\text{ nV}\cdot\text{Hz}^{-1/2}$. The amplified voltage is then measured using a Signal Recovery DSP 7265 Lock-in . Low frequency and DC bias are applied via a coaxial DC line. A $1/1000$ divider is inserted on this line. It is composed of a $100\text{ k}\Omega$ resistor placed at room temperature in parallel with a $100\text{ }\Omega$ resistor placed on the mixing chamber.

As already mentioned before, voltage pulses are sent through a RF line which contains attenuators at several low temperature stages as shown in fig. 3.1. DC/Low frequency and RF lines are connected to a bias T allowing to inject DC as well as RF signals. The set-up is shown in fig. 4.3.

To perform the Lock-in detection when the sample is biased with fast voltage pulses, we modulate the voltage pulses with a low frequency signal. During half of the period of the low frequency signal, pulses are applied and during the other half they are not. With the AWG, this can be done by defining a waveform which already contains this modulation (see fig. 3.18).

With the homemade pulse source, this can be done with a signal mixer (the mixer act as a switch driven by the low frequency signal, see fig. 3.18). It is also possible to trigger the 6 GHz and 18 GHz sources such that they emit signal synchronously with at a given frequency.

The choice of this modulation frequency is a compromise between the bandwidth of the RF port of the bias T and the bandwidth of the voltage amplifier. We have measured the frequency dependence of the output voltage when the sample is biased with modulated voltage pulses produced by the AWG. The optimal modulation frequency extracted from the curve shown in fig. 3.19 is 12 kHz.

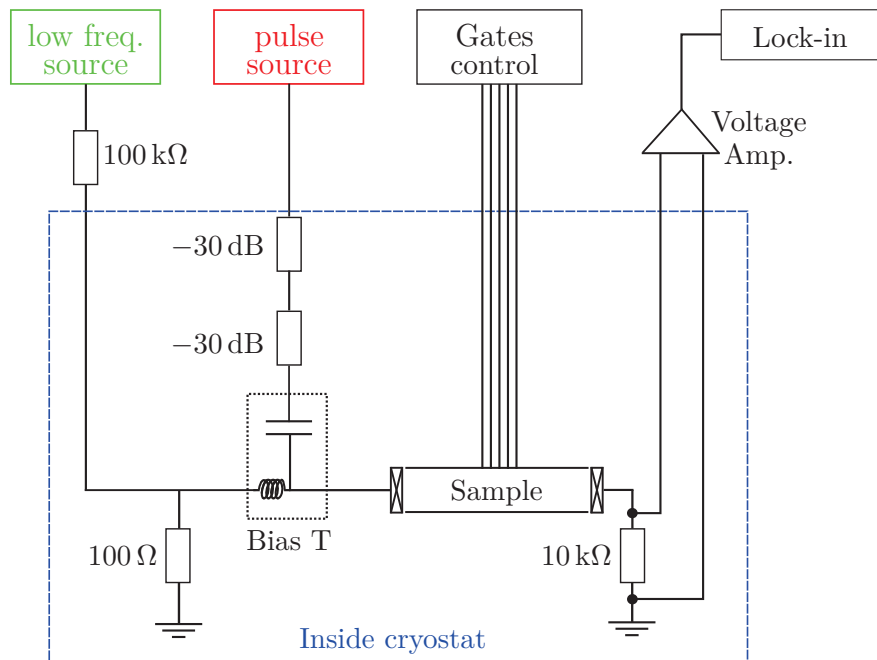


Figure 3.17: Schematic of the set-up used to bias the sample and measure outputs signals.

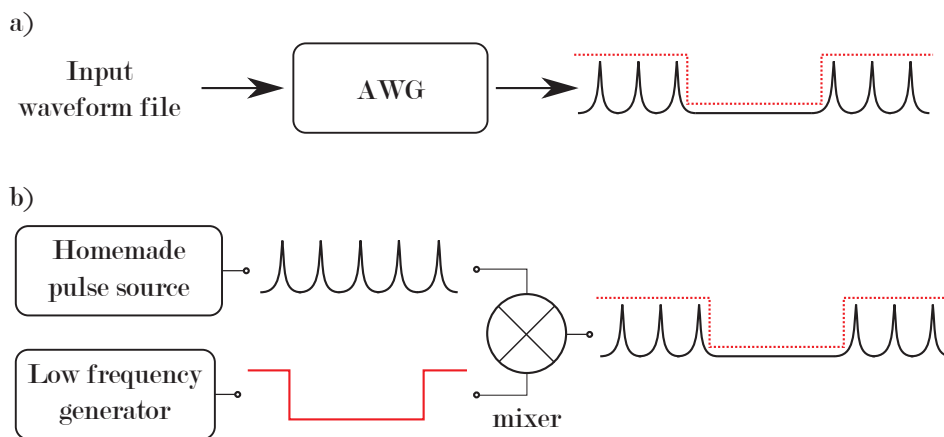


Figure 3.18: Principle of the pulse modulation. a) With the AWG, the low frequency modulation is already contained in the definition of the waveform. b) With the homemade pulse source, this modulation is done by mixing a low frequency signal with the train of pulses.

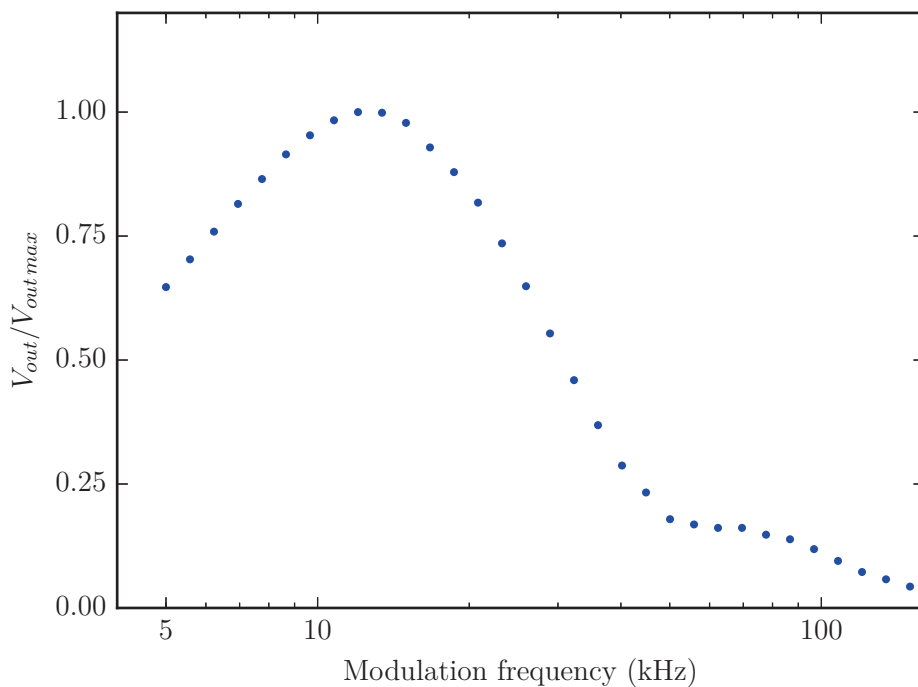


Figure 3.19: Normalized amplitude of the output voltage measured when the sample is biased with modulated voltage pulses as a function of the modulation frequency.

3.4 Conclusion

In this chapter, we have described the experimental set-up developed during my thesis. We have built and characterized a new set-up allowing to perform an experiment with very fast voltage pulses compatible with very low temperatures. It includes a large number of DC/low frequency lines (up to 42) and RF lines (up to 4). Their integration in the cryostat has been done such that the heat brought by thermal conduction and propagation of thermal radiation is reduced as much as possible. Measurements of the temperature of the inner conductors for each type of line show that this requirement is partially fulfilled. There is still room for improvement, especially for the RF lines.

For the envisaged experiments, several key ingredients were needed. Low resistance ohmic contacts have been fabricated, characterized and used with success for the sample fabrication. A chip carrier adapted to high frequencies has been developed. Coplanar waveguides patterned directly on the chip carrier and on the sample ensure the $50\ \Omega$ impedance matching to optimize the pulse propagation up to the heart of the sample. We have implemented a pulse source using harmonics combination to overcome the limitations of the AWG. The measurement set-up is based on a combination of several Lock-in detections. It can be done with a low frequency bias as well as with modulated voltage pulses allowing to reach a very good signal to noise ratio in both cases.

CHAPTER 4

Study of the propagation of a voltage pulse

Our ultimate goal is to reach a regime where the temporal width of the pulse is smaller than its time of flight through the system of interest. It is then highly desirable to know the actual pulse shape inside the sample and to determine the time of flight of the pulse. In this chapter, we present time resolved measurements of the voltage pulse performed at the sample level that allow to access such information. Time resolved measurements of a propagating localized excitation have been pioneered in the quantum Hall regime. The excitation propagating in an edge channel, the so-called edge magneto plasmon (EMP) was generated either by pulsing an electrostatic gate capacitively coupled to a 2DEG [Ash92] or by directly injecting a voltage pulse through an ohmic contact [Suk04; Zhi93]. However, in these experiments, the EMP was not measured locally but at room temperature using a fast sampling scope. Recently, similar experiments have been performed in graphene [Kum13; Kum14; Pet13]. It worth noting that the first experimental evidence of the existence of EMPs was obtained quite earlier by Glattli et al. [Gla85]. The authors measured the spectrum of plasmon modes of electrons confined on a liquid helium surface placed in a normal magnetic field. The first in-situ measurement of an EMP generated by a voltage pulse applied on a ohmic contact was reported by Kamata et al. [Kam09]. The authors used a QPC to probe the time dependent potential due to the traveling EMP. This technique which is going to be detailed in the following was then employed to determine the group velocity of EMPs [Kam10] and to probe the charge fractionalization occurring in a Tomonaga-Luttinger liquid [Kam14]. An equivalent method was applied very recently to characterize a single electron wave packet emitted by a non-adiabatic single electron pump [Fle13; Wall15] and to determine the velocity of the generated wave packet [Kat15]. We have adapted this technique in order to perform a time resolved measurement of a wave packet propagating along a 1D channel defined by electrostatic gates in a 2DEG in zero magnetic field. We show that the voltage pulse propagates much faster than the Fermi velocity. From our measurements we conclude that the propagation velocity agrees very well with the plasmon velocity for a gated two-dimensional electron gas and can be controlled by modifying the confinement potential due to the electrostatic gates. We compare the velocities obtained experimentally to the velocities calculated using a theoretical approach based on the work of Matveev and Glazman [Mat93] and find that both show a good

agreement confirming the plasmonic behavior.

4.1 Time resolved measurement of the voltage pulse

4.1.1 Principle

The idea is to use a QPC as a fast switch. By applying a negative DC voltage on the QPC, the transmission of the QPC is tuned to be close to zero. The QPC is then pulsed with a short positive voltage pulse to increase its transmission during a very short time. When a short voltage pulse is applied on the ohmic contact, the generated electronic wave packet propagates up to the QPC along a 1D channel formed by the electrostatic gates. If the arrival time of the wave packet coincides with the opening of the QPC, the wave packet can pass and be detected, otherwise it is reflected. More formally, the voltage pulse applied on the ohmic contact can be seen as a time dependent change of the source-drain bias $\Delta V_{sd}(t)$. The pulse applied on the QPC results in a time dependent change of the conductance $\Delta G(t)$. The current is then given by $\Delta I(t) \propto \Delta V_{sd}(t) \times \Delta G(t)$. In practice, measuring directly $\Delta I(t)$ is very difficult. However, by adjusting the time delay τ between the pulse applied on the ohmic contact and the pulse applied on the QPC and averaging over a sufficiently long period, one can reconstruct the pulse applied on the ohmic contact as a function of the time delay: $\Delta I(\tau) \propto \langle \Delta V_{sd}(t) \times \Delta G(t - \tau) \rangle$. This expression is similar to the convolution of $\Delta V_{sd}(t)$ and $\Delta G(t)$ as illustrated in fig. 4.1.

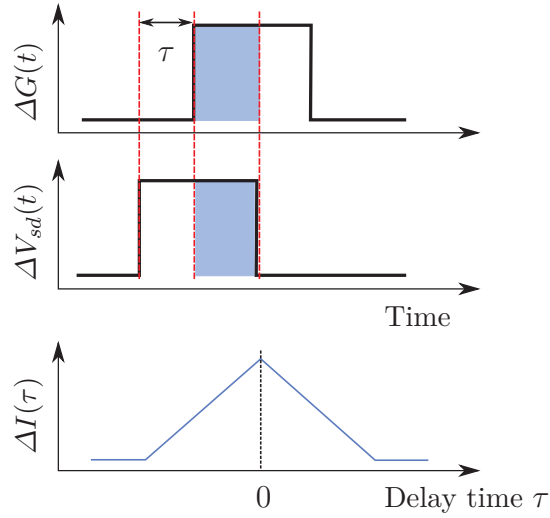


Figure 4.1: Schematic illustrating the principle of the time resolved measurement. The voltage pulse is represented by the square function. The pulse applied on the QPC results in a change of the conductance $\Delta G(t)$ while the pulse applied on the ohmic contact results in a change of the source drain bias $\Delta V_{sd}(t)$. The average output current is given by the overlap between $\Delta G(t)$ and $\Delta V_{sd}(t)$. By varying the time delay τ between the two pulses, one can reconstruct $\Delta I(\tau)$ which is given by the convolution of $\Delta G(t)$ and $\Delta V_{sd}(t)$.

To perform the time resolved measurement of the voltage pulse, the sample is tuned such that a 1D channel is formed by the gates G1 and G2 along which the pulse propagates as shown in fig. 4.2. The lower output of the sample is fully pinched-off by applying a sufficiently strong negative voltage on gates G3 and G4. Therefore, there is only one possible output for the voltage pulse. The QPC used to probe the pulse is situated at the end of the 1D channel. The voltage pulse applied on the ohmic contact and the voltage pulse applied on the QPC are generated by two independent channels of an AWG 7122b. The time delay between these two channels can be controlled with a resolution of one picosecond. Each channel is connected to a high bandwidth RF line terminated by a bias T allowing to superimpose a DC bias to the RF signal. A schematic of the set-up is presented in fig. 4.3.

Initially, the DC voltage applied on the QPC is set such that its transmission is close to zero. A trace of the conductance of the QPC as a function of the applied gate voltage is shown in fig. 4.4. This conductance is actually the total conductance which depends strongly on the $40\ \mu\text{m}$ long 1D channel which separates the ohmic contact from the QPC. This explains why the conductance is much lower than $2e^2/h$. The irregular spacing of the conductance steps is also related to the presence of the 1D channel. Without this 1D channel, the QPC shows the expected behavior of quantized steps of $2e^2/h$ (see sec. 2.1). From this measurement, the DC voltage applied on the QPC was set to $\sim -0.93\ \text{mV}$ (indicated by the black arrow in fig. 4.4). On top of this DC voltage, positive voltage pulses with an amplitude of $\sim 15\ \text{mV}$ at the sample level were added. This amplitude corresponds to the change of gate voltage necessary to cover the steep part of the conductance trace delimited by the rectangle. An example of such a time resolved measurement is presented in fig. 4.5. Voltage pulses of $90\ \text{ps}$ width with a repetition time of $2665.6\ \text{ps}$ were applied on the ohmic contact and on the QPC. The DC output voltage is plotted as a function of the time delay. Two peaks at the delay times of $0\ \text{ps}$ and $2665.6\ \text{ps}$ clearly demonstrate the time resolved measurement of the injected voltage pulse.

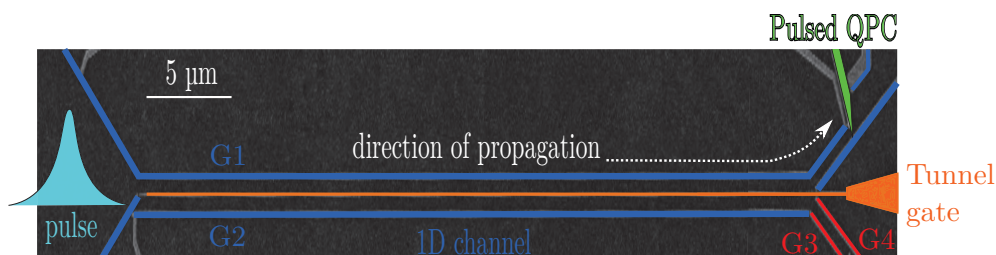


Figure 4.2: SEM picture illustrating how the sample is tuned to perform the time resolved measurement of the voltage pulse in-situ. The electronic wave packet (in light blue) generated at the ohmic contact propagates up to the QPC along a 1D channel formed by the electrostatic gates G1 and G2. The gate G3 and G4 are fully pinched off such that the wave packet can only pass via the upper output where the pulsed QPC is situated.

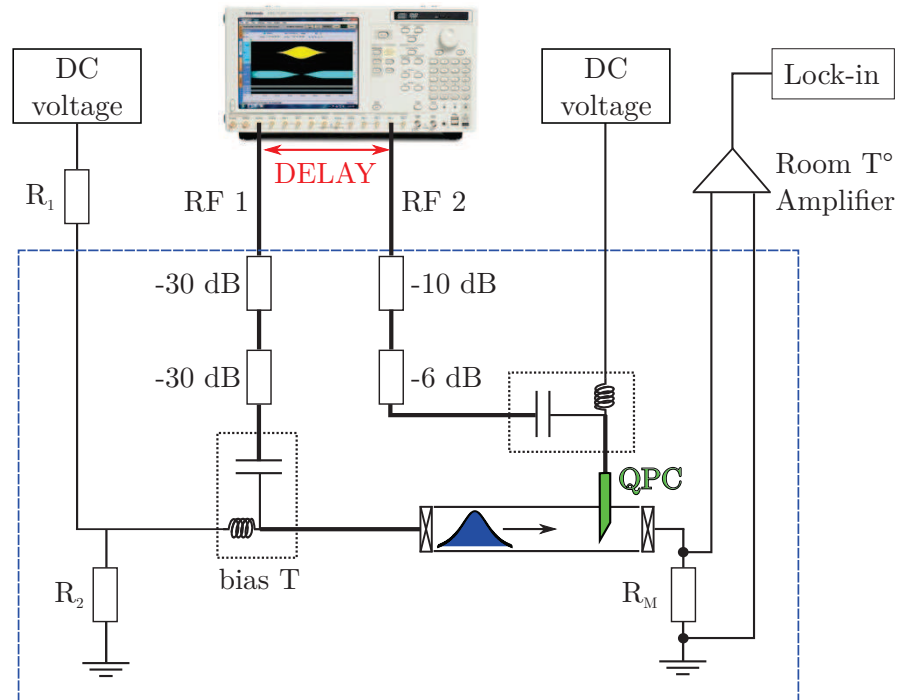


Figure 4.3: Detection scheme used for the time resolved measurement. The pulses applied on the ohmic contact and on the QPC are generated by an AWG and sent through high bandwidth RF lines. The time delay between the two pulses can be controlled with a resolution of one picosecond. Two bias Ts allow to superimpose a DC voltage to the pulses. The current produced by the sample is converted into a voltage through the resistance $R_M = 10 \text{ k}\Omega$ installed at low temperature. This voltage is amplified at room temperature and measured using a Lock-in detection.

4.1.2 Comparison between the expected convolution and the in-situ measurement

Knowing the frequency dependence of the RF line transmission (see sec. 3.2 in chapter 3), it is possible to estimate the pulse shape at the sample level and to calculate the expected convolution by using this pulse shape. For this purpose, we first calculate the Fourier transform of a voltage pulse measured directly at the output of the AWG. The Fourier transform is then weighted with the attenuation of the RF line. By calculating the inverse Fourier transform, one can estimate the pulse shape after the propagation through the RF line. In order to validate this approach, we compare the pulse shape after the propagation through a RF line measured at room temperature and the calculated pulse shape using the attenuation of the RF line also measured at room temperature. The result is presented in fig. 4.6. The measured shape and the calculated shape are in good agreement. There are two main differences between the measured shape and the calculated one. The rising edge of the measured shape is only weakly affected by the RF line whereas the one of the calculated shape is more degraded. The falling edge of the measured shape shows a longer decay time compared to the calculated one. This might be due to the dispersion occurring

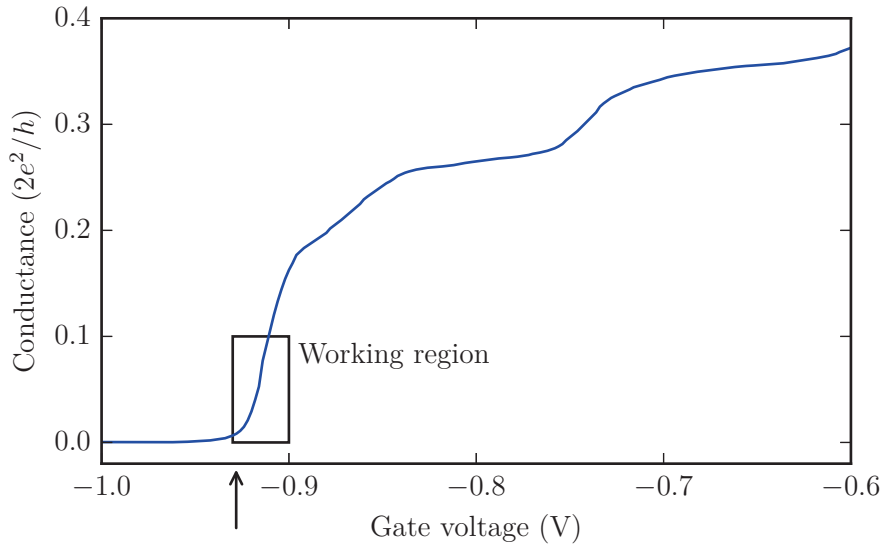


Figure 4.4: Conductance trace of the QPC used to probe the voltage pulse as a function of the applied gate voltage taken at 20 mK. The irregular conductance steps and the fact that the conductance is always lower than $2e^2/h$ are due to the presence of the $40\ \mu\text{m}$ long 1D channel before the QPC. The black arrow indicates the DC voltage applied to the QPC for the time resolved measurement.

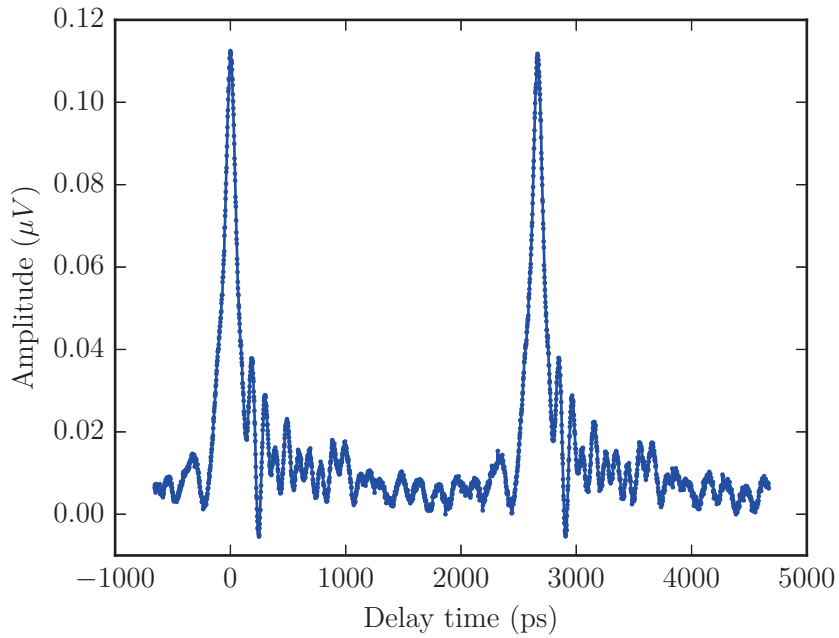


Figure 4.5: Time resolved measurement of the voltage pulse in-situ. Measurement taken at 20 mK, the resolution is 2 ps per point.

along the RF line which can be responsible for the stronger asymmetry of the measured shape. Since the dispersion is not taken into account in the calculation, this can lead to the observed discrepancy. This method was then applied using the attenuation of the RF line measured at 20 mK. The obtained pulse shape is then used to calculate the expected convolution at low temperature. This calculated convolution and the in-situ measurement are presented in fig. 4.7. The convolution of two voltage pulses measured directly at the output of the AWG is also plotted as a reference. By comparing the calculated convolution to the convolution of two voltage pulses measured directly at the output of the AWG, we can estimate the enlargement of the FWHM of the voltage pulse to about 10 ps. This is due to the stronger attenuation of the RF line for higher frequencies which degrades slightly the pulse shape. Except for this enlargement, both convolutions look very similar indicating that the pulse shape is not much affected by the RF line.

Now we compare the calculated convolution and the in-situ measurement. We focus on the main peak, the origin of the additional features appearing after the peak will be discussed afterwards. As expected, the in-situ measurement shows an additional broadening compared to the calculated convolution which can be due to two main contributions affecting mainly the pulse applied to the ohmic contact. The pulse can be affected by the contact itself and by its propagation through the sample up to the QPC. Especially during the propagation, scattering and non-linear dispersion can broaden the pulse and distort it in a complicated way. However, the good agreement between the calculated convolution and the in-situ measurement indicates that the pulse is not very distorted. The main difference lies in the shoulder on the rising edge of the pulse which, as we will see in the following, seems to be related to the oscillations appearing after the main peak.

4.1.3 Dependence on the pulse amplitude

To get important quantitative informations such as the number of injected charges per pulse, it is necessary to determine the effective amplitude of the voltage pulse at the sample level and its shape. The amplitude can be estimated with the total attenuation of the RF line which is on the order of -67 dB: -60 dB due to the attenuators and -7 dB due to the line itself and the other elements encountered by the pulse (additional flexible coax between the RF line and the PCB, connectors...). The effective amplitude of the voltage pulse applied to the 2DEG is then $V_{eff} = V_{in} \times 10^{-67/20}$ where V_{in} is the amplitude of the voltage pulse at the output of the pulse generator. In the previous section, we have seen that the shape of the pulse can be calculated using the weighted FFT, therefore we can estimate the average number of injected charges:

$$\bar{n} = \int \frac{eV_{eff}s(t)}{h} dt \quad (4.1)$$

where $s(t)$ is the function characterizing the shape of the pulse.

In fig. 4.8, the results of the in-situ measurement for amplitudes of the voltage pulse ranging from about 90 μ V to about 450 μ V are presented. The evolution of the main peak amplitude V_{Peak} as a function of V_{eff} is shown in fig. 4.9. The linearity of V_{Peak} with respect to the amplitude of the voltage pulse indicates an ohmic behavior as expected. On

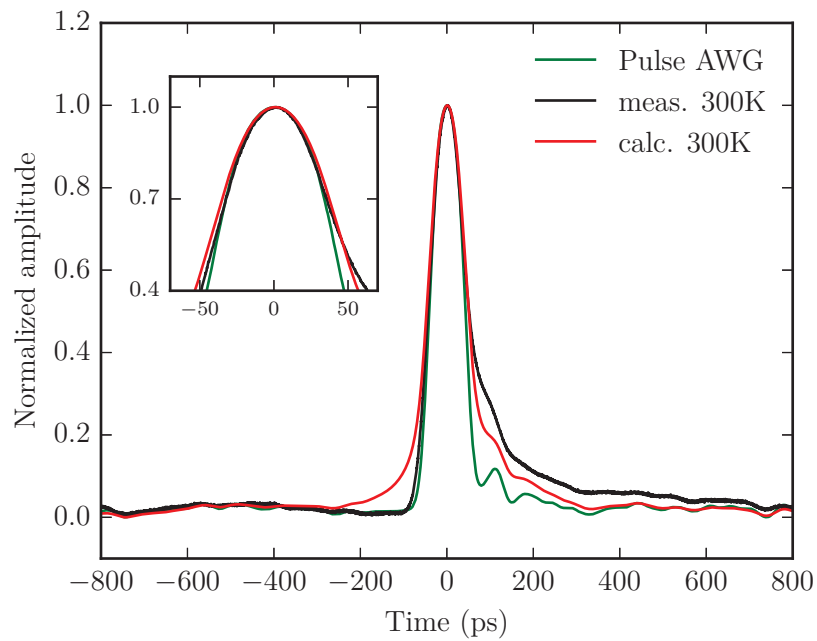


Figure 4.6: Comparison between the pulse shape measured after the propagation through the RF line at room temperature (in black) and the one calculated using the attenuation of the RF line also measured at room temperature (in red). The pulse shape measured directly at the output of the AWG is also presented (in green). The inset shows a zoom on the top part of the pulse shapes.

tab.4.1, the estimated average number of charges injected per pulse as a function of the pulse amplitude is presented.

Table 4.1: Average number of injected charges as a function of the amplitude of the voltage pulse.

Pulse amp. (μV)	89	134	179	223	279	335	381	447
\bar{n}	3.2	4.8	6.4	8	10	12	14	16

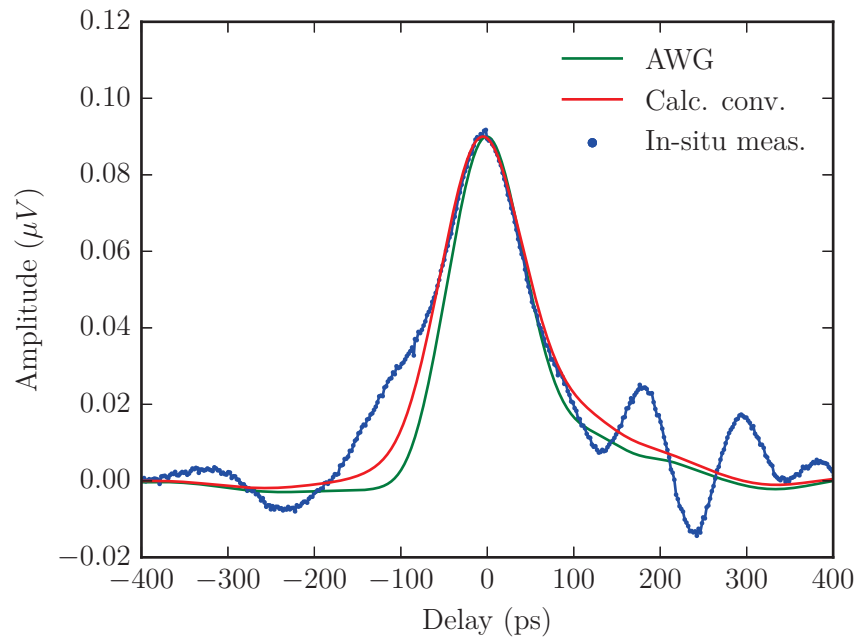


Figure 4.7: Comparison between the calculated convolution of the voltage pulses after their propagation in the RF lines (calculated using the attenuation measured at 20 mK, red solid line) and the in-situ measurement taken at 20 mK (blue dot). The green curve corresponds to the convolution of two voltage pulses measured directly at the output of the AWG (not distorted by their propagation in the RF lines).

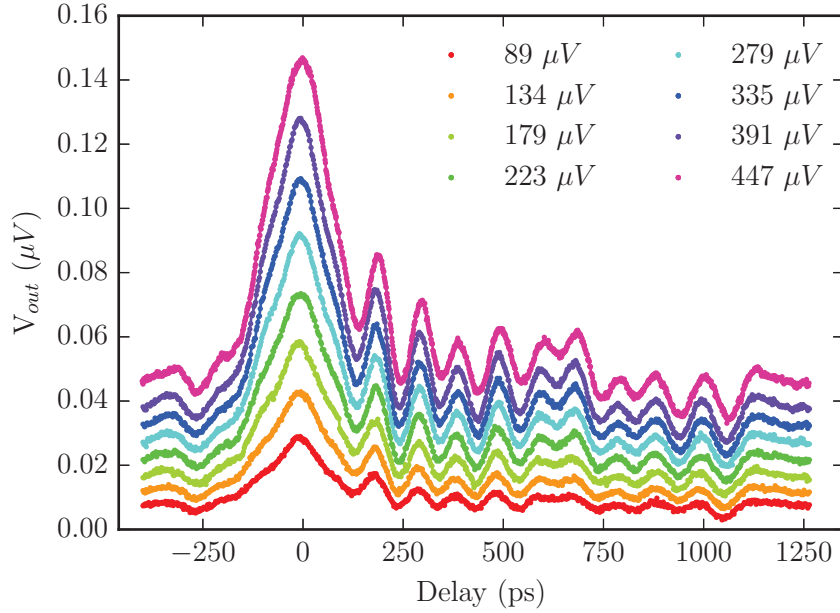


Figure 4.8: Time resolved measurements for different amplitudes of the injected voltage pulse.

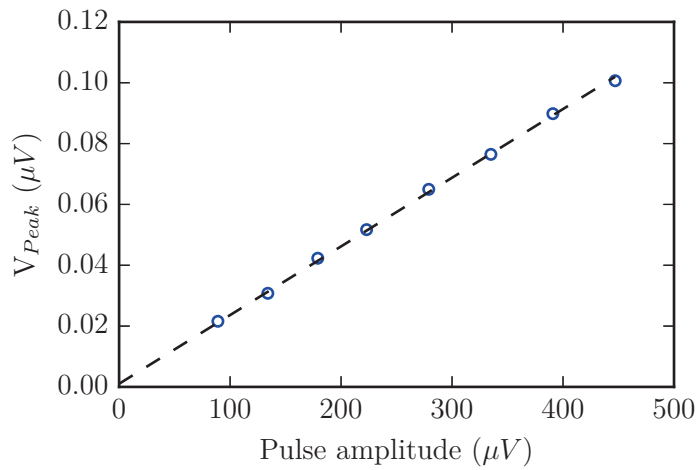


Figure 4.9: Amplitude of the peak as a function of the amplitude of the voltage pulse.

4.2 Determination of the velocity of the voltage pulse

To determine the velocity of the voltage pulse through the sample, we first have to characterize the intrinsic delay between the RF lines due to their difference in length. This was done by using a technique named reflectometry. A pulse generated by the AWG is splitted into two by a power splitter. One output of the power splitter is connected to a RF line and the other output to a sampling scope. The output of the RF line is left open such that the voltage pulse is fully reflected. The pulse travels back to the power splitter and one half of it is sent to the scope. The time delay between the initial pulse and the reflected one is the time needed for the pulse to do one round trip through the RF line (and the power splitter). This technique imposes to remove the attenuators installed on the RF line. The intrinsic delay due to the attenuators has to be measured separately and is presented in appendix A.

The time traces obtained for the RF lines used for the experiment are presented in fig. 4.10. The first big peak is the part of the pulse which is directly sent to the scope. After a certain time, a smaller peak is measured corresponding the pulse reflected at the end of the RF line. The measured delay between the rf line connected to the ohmic contact and the one connected to the QPC accounts to $180/2 = 90$ ps. There is an additional delay of 24 ps due to a length difference of the attenuators (the attenuators inserted in the RF line connected to the ohmic contact are slightly longer). We obtain a total delay of $\sim 114 \pm 10$ ps for the RF line connected to the ohmic contact. The error comes from the distorted shape of the reflected pulse and the limited resolution of 12.5 ps of the oscilloscope used.

The second step is to determine the time delay obtained for the in-situ measurement of the pulse. This time delay is the sum of the delay due to the RF lines, the attenuators and the delay due to the propagation of the voltage pulse from the ohmic contact to the QPC. This time delay is extracted from the measurement presented in fig. 4.11 which represents the output voltage measured as a function of the initial delay time. The initial delay time is defined as the delay between the voltage pulse applied to the ohmic contact and the one applied to the QPC at the output of the AWG. A full sweep of 250 ps with a resolution of 2 ps is repeated four times to take into account the possible drift. The measurement is actually very stable since almost no difference appears between the different traces. The maximum signal is obtained for an initial delay of 162 ± 2 ps. Taking into account the intrinsic delay due to the RF lines and the attenuators, we obtain a time of flight τ_F of the voltage pulse from the ohmic contact to the QPC of:

$$\tau_F = 48 \pm 12 \text{ ps} \quad (4.2)$$

The distance take into account to calculate the velocity of the voltage pulse through the sample is the distance between the interface of the ohmic contact with the 2DEG and the QPC. We consider the ohmic contact to be a fully metallic part up to the 2DEG so that the potential imposed by the voltage pulse is applied instantaneously on the whole contact (with a characteristic time on the order of $\frac{\text{length of the contact}}{\text{speed of light}/\epsilon_0\epsilon_r} \sim 10^{-1}$ ps). The length from the border of the ohmic contact to the QPC is 51 ± 1 μm . The uncertainty on the length is mainly due to the limited precision of the optical lithography used during the

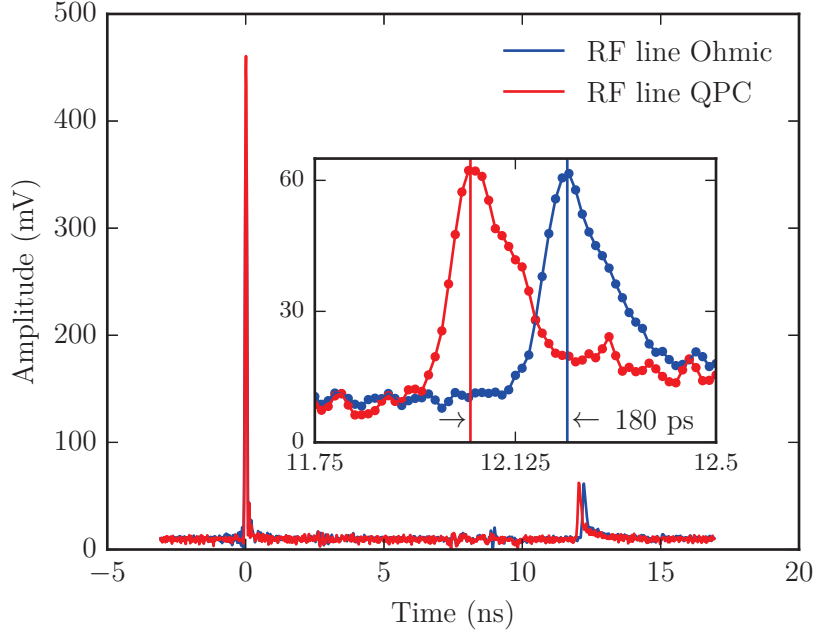


Figure 4.10: Intrinsic delay of the RF lines measured by reflectometry. The measurement for the two RF lines (the one connected to the QPC and the one connected to the ohmic contact) are superimposed. The main peak is the part of the pulse generated by the AWG which is directly sent to the scope after the splitter. The second peak is due to the part of the pulse which is sent into the RF line and reflected at the output of the RF line (left floating). The inset shows a zoom on these peaks. The time difference between these two peaks corresponds to two times the intrinsic delay between the RF lines. The intrinsic delay is then $180/2 = 90 \pm 5$ ps.

fabrication the ohmic contacts. Taking into account this length, the time of flight τ_F and the uncertainties on both values, the velocity v_P of the voltage pulse is estimated to:

$$v_P = 1.06 \pm 0.25 \times 10^6 \text{ m.s}^{-1} \quad (4.3)$$

We emphasize on the fact that for this measurement, the tunnel gate was polarized at -0.3 V. As we will see in the following, this reduces the velocity of the voltage pulse. When the tunnel gate is set to -0.1 V (the minimum possible), v_P is on the order of $1.24 \pm 0.29 \times 10^6 \text{ m.s}^{-1}$. It turns out that this velocity is much higher than the Fermi velocity of the 2DEG. In our case, the Fermi velocity is ($n_s = 2.11 \times 10^{11} \text{ cm}^{-2}$):

$$v_F = \frac{\hbar}{m^*} \sqrt{2\pi n_s} = 2 \times 10^5 \text{ m.s}^{-1}, \quad (4.4)$$

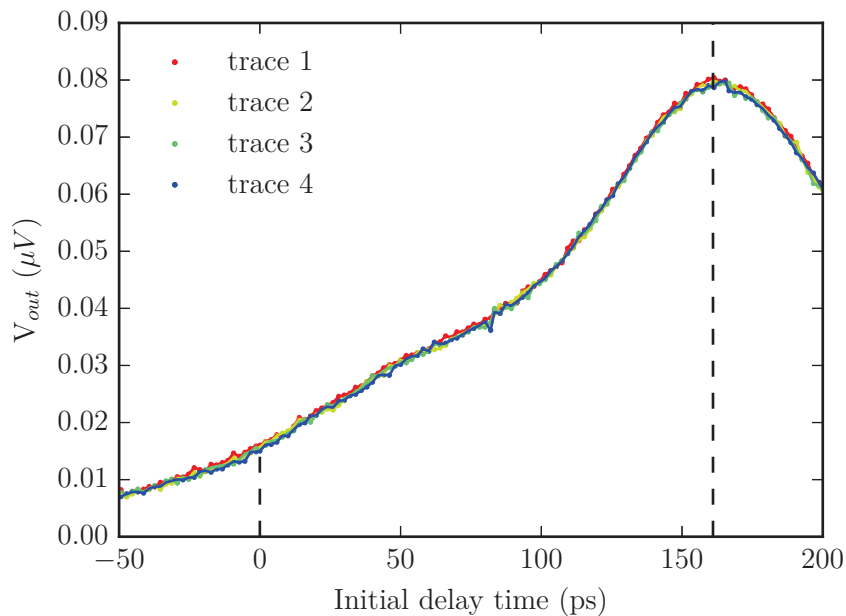


Figure 4.11: Time resolved measurements of the voltage pulse as a function of the initial delay between the voltage pulses applied on the QPC and on the ohmic contact. At an initial delay time of 0 ps, the two voltage pulses are sent synchronously to each RF line. The maximum of signal is obtained for an initial delay time of 162 ± 2 ps which includes the intrinsic delay due to the RF lines and the attenuators as well as the time needed for the pulse to travel from the ohmic contact to the QPC. The measurement is repeated four times to test the reproducibility.

4.3 Plasmonic excitations

The origin of the high velocity determined previously can be understood by considering that the effect of the voltage pulse is to actually create a plasmon. When an excitation such as a voltage pulse is applied to the electrons of a 2DEG, it modifies locally the electron density. This modulation of the density acts on all the surrounding electrons which causes a collective disturbance, a so-called plasmon. Nowadays, plasmons in two-dimensional systems generate a lot of interest as they could be used for terahertz electronics due to their strong sub-wavelength confinement [Yoo14]. Theoretical studies of plasmons in 2D systems on the other hand date back to Stern in the 70's [Ste67]. In this part, we follow the approach of Chaplik who used the Boltzman kinetic equation to derive the properties of plasmons in metal-insulator-semiconductor structures [Cha85]. These calculations which allow us to determine the velocity of plasmons in such a structure have been done in collaboration with Xavier Waintal. In the following development, the bold letters stand for vectors. The first step is to calculate the self-induced electrostatic potential due to the modulation of the electron density. We consider the geometry shown in fig. 4.12 where the 2DEG is located at a distance d_u under the surface covered by a metallic gate and at a distance d_l above a metallic plane (the PCB).

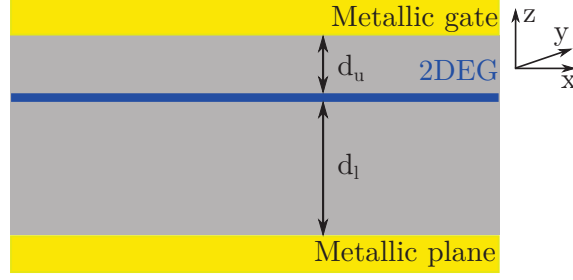


Figure 4.12: Schematic of the geometry considered to calculate the electrostatic potential V at the 2DEG level due to a modulation of the electron density.

Let us suppose that the «perturbed» electron density has the form:

$$n = n_0 + \delta n e^{i\mathbf{q}\cdot\mathbf{r} - i\omega t}, \quad (4.5)$$

where n_0 is the electron density at equilibrium and $\delta n e^{i\mathbf{q}\cdot\mathbf{r} - i\omega t}$ accounts for the modulation. One has to calculate the electrostatic potential V due to this modulation by solving the Poisson equation:

$$\Delta V = \frac{\rho}{\epsilon_r \epsilon_0} \quad (4.6)$$

where $\rho = \delta n e^{i\mathbf{q}\cdot\mathbf{r} - i\omega t} \delta(z)$ describes the modulated charge distribution ($\delta(z)$ ensures the confinement in the z direction). The absence of the minus sign in the Poisson equation is because we define $\rho < 0$ due to the negative charge of the electrons. $\epsilon_r \epsilon_0$ is the dielectric constant of the surrounding material. Therefore, V has the form $V = \bar{V}(x, y) f(z) = \delta V e^{i\mathbf{q}\cdot\mathbf{r} - i\omega t} f(z)$. We have to determine δV and $f(z)$. To determine δV , we can use the fact that the electric field undergoes a discontinuity through the 2DEG:

$$[\mathbf{E}(z = 0^+) - \mathbf{E}(z = 0^-)] \cdot \mathbf{z} = \frac{\delta n}{\epsilon_r \epsilon_0} e^{i\mathbf{q}\cdot\mathbf{r} - i\omega t} \quad (4.7)$$

Since $\mathbf{E} = -\nabla V$:

$$\begin{aligned} \delta V [f'(z = 0^+) - f'(z = 0^-)] &= \frac{\delta n}{\epsilon_r \epsilon_0} \\ \delta V &= \frac{\delta n}{\epsilon_r \epsilon_0} [f'(z = 0^+) - f'(z = 0^-)]^{-1} \end{aligned} \quad (4.8)$$

We have to determine $f(z)$ in order to evaluate $f'(z = 0^+)$ and $f'(z = 0^-)$. Calculating the homogeneous solution of eq.4.6 ($\Delta V = 0$) leads to:

$$f''(z) - q^2 f(z) = 0, \quad (4.9)$$

and therefore:

$$f(z) = A e^{-qz} + B e^{qz}. \quad (4.10)$$

Because of the presence of the metallic gate at $z = d_u$ and the metallic plan at $z = -d_l$, the potential has to be equal to zero at these two positions ($V(z = d_u) = V(z = -d_l) = 0$). These boundary conditions imply:

$$f(z^+) = C_u \sinh(qz - qd_u), \quad (4.11)$$

and

$$f(z^-) = C_d \sinh(qz + qd_l). \quad (4.12)$$

Because of the continuity of the potential through the 2DEG, $V(z = 0^+) = V(z = 0^-)$, therefore $f(z = 0^+) = f(z = 0^-)$. As a consequence:

$$C_u \sinh(-qd_u) = C_d \sinh(qd_l),$$

which leads to:

$$\begin{aligned} C_u &= \frac{1}{\sinh(qd_u)}, \\ C_d &= -\frac{1}{\sinh(qd_l)}. \end{aligned} \quad (4.13)$$

Therefore:

$$\begin{aligned} f(z^+) &= \frac{\sinh(qz - qd_u)}{\sinh(qd_u)} \\ f(z^-) &= -\frac{\sinh(qz + qd_l)}{\sinh(qd_l)} \end{aligned} \quad (4.14)$$

We can now evaluate $f'(z = 0^+)$ and $f'(z = 0^-)$:

$$\begin{aligned} f(0^+) &= q \frac{1}{\tanh(qd_u)}, \\ f(0^-) &= -q \frac{1}{\tanh(qd_l)}, \end{aligned} \quad (4.15)$$

which allows us to determine δV using eq.4.8:

$$\delta V = \frac{\delta n}{\varepsilon_0 \varepsilon_r} \frac{1}{q} \left(\frac{1}{\tanh(qd_u)} + \frac{1}{\tanh(qd_l)} \right)^{-1}. \quad (4.16)$$

The distance d_l is actually very large, on the order of $700 \mu\text{m}$ for our wafer. On the other hand, q (for short pulses) is on the order of $\frac{2\pi}{100 \mu\text{m}}$. Since $\lim_{qd_l > 1} \frac{1}{\tanh(qd_l)} = 1$, the self induced potential seen by the electrons of the 2DEG is:

$$V(x, y, 0) = \frac{\delta n}{\varepsilon_r \varepsilon_0} \frac{1}{q} \frac{1}{(1 + \coth(qd_u))} e^{i\mathbf{q} \cdot \mathbf{r} - i\omega t} \quad (4.17)$$

We can now derive the expression of the electric field (in the following d denotes d_u):

$$\mathbf{E} = -i \frac{\mathbf{q}}{q} \frac{\delta n}{\varepsilon_r \varepsilon_0} \frac{1}{(1 + \coth(qd))} e^{i\mathbf{q}\cdot\mathbf{r} - i\omega t} \quad (4.18)$$

\mathbf{E} is the self induced field created by the modulated electron density. We write it as $\mathbf{E} = \mathbf{E}_0 e^{i\mathbf{q}\cdot\mathbf{r} - i\omega t}$. We define $\mathbf{E}_0 = -i \frac{\mathbf{q}}{q} \frac{\delta n}{\varepsilon_r \varepsilon_0} \chi(q)$ where $\chi(q) = \frac{1}{1 + \coth(qd)}$.

The next step is to inject this self induced field in the Boltzmann kinetic equation. We consider the function $f(\mathbf{r}, \mathbf{k})$ as the electron distribution function such that the charge density is expressed by:

$$n_S(\mathbf{r}) = 2e \int f(\mathbf{r}, \mathbf{k}) \frac{d^2 k}{(2\pi)^2} \quad (4.19)$$

At equilibrium, $f(\mathbf{r}, \mathbf{k})$ is the Fermi-Dirac distribution (which can be approximated by a Heaviside function at low temperature). However, we have just seen that the modulation of the charge density generates an electric field which perturbs the system and drives the distribution function away from equilibrium. Under this condition, $f(\mathbf{r}, \mathbf{k})$ can be written as:

$$f(\mathbf{r}, \mathbf{k}) = \theta[\mu - \varepsilon(k)] + f_1(\mathbf{k}) e^{i\mathbf{q}\cdot\mathbf{r} - i\omega t} \quad (4.20)$$

We can write the Boltzmann kinetic equation:

$$\partial_t f(\mathbf{r}, \mathbf{k}) = -\mathbf{v}_k \cdot \partial_{\mathbf{r}} f(\mathbf{r}, \mathbf{k}) - \frac{e\mathbf{E}}{\hbar} \cdot \partial_{\mathbf{k}} f(\mathbf{r}, \mathbf{k}) \quad (4.21)$$

After derivation, one finds:

$$f_1(\mathbf{k}) = \frac{ie\mathbf{E}_0 \cdot \mathbf{v}_k}{\omega - \mathbf{v}_k \cdot \mathbf{q}} \delta(E_F - \varepsilon(k)) \quad (4.22)$$

We inject $f(\mathbf{r}, \mathbf{k})$ in eq.4.19 which again has the form $n_S(\mathbf{r}) = n_0 + \delta n e^{i\mathbf{q}\cdot\mathbf{r} - i\omega t}$. The important quantity here is δn which is the signature of the plasmon. It is given by $\delta n = 2e \int f_1(\mathbf{k}) \frac{d^2 k}{(2\pi)^2}$. We express it in spherical coordinates:

$$\begin{aligned} \delta n &= \frac{2e}{(2\pi)^2} \int k dk d\theta f_1(k) \\ &= \frac{2e}{(2\pi)^2} k_F \frac{m}{\hbar^2 k_F} \int_0^{2\pi} d\theta f_1(E_F) \\ &= \frac{i2e^2 m v_F \mathbf{E}_0}{(2\pi)^2 \hbar^2} \int_0^{2\pi} d\theta \frac{\cos \theta}{\omega - v_F q \cos \theta} \end{aligned} \quad (4.23)$$

We have to evaluate the term $\int_0^{2\pi} d\theta \frac{\cos \theta}{\omega - v_F q \cos \theta}$:

$$\begin{aligned} \int_0^{2\pi} d\theta \frac{\cos \theta}{\omega - v_F q \cos \theta} &= \frac{1}{\omega} \frac{\omega}{v_F q} \int_0^{2\pi} d\theta \frac{\frac{v_F q}{\omega} \cos \theta}{1 - \frac{v_F q}{\omega} \cos \theta} \\ &= \frac{1}{v_F q} \left[-2\pi + \int_0^{2\pi} \frac{d\theta}{1 - \frac{v_F q}{\omega} \cos \theta} \right] \\ &= \frac{2\pi}{v_F q} \left[\frac{1}{\sqrt{1 - \left(\frac{v_F q}{\omega}\right)^2}} - 1 \right] \end{aligned} \quad (4.24)$$

Therefore, δn is given by:

$$\delta n = \frac{i2e^2 m \mathbf{E}_0}{(2\pi) \hbar^2 q} \left[\frac{1}{\sqrt{1 - \left(\frac{v_F q}{\omega}\right)^2}} - 1 \right] \quad (4.25)$$

Since \mathbf{E}_0 depends on δn , this equation can be simplified:

$$1 = \frac{2e^2 m \chi(q)}{2\pi \hbar^2 q \varepsilon_r \varepsilon_0} \left[\frac{1}{\sqrt{1 - \alpha^2}} - 1 \right] \quad (4.26)$$

which can be written as:

$$\bar{q} = \frac{q a_B}{\chi(q)} \quad (4.27)$$

where we have defined $\alpha = \frac{q v_F}{\omega}$, $a_B = \frac{\pi \varepsilon_0 \varepsilon_r \hbar^2}{e^2 m}$ is an effective Bohr radius and $\bar{q} = \left[\frac{1}{\sqrt{1 - \alpha^2}} - 1 \right]$.

Inverting this last relation leads to $\alpha^2 = \frac{(2 + \bar{q})\bar{q}}{(1 + \bar{q})^2}$ which is equivalent to:

$$\left(\frac{\omega}{v_F q} \right)^2 = \frac{(1 + \bar{q})^2}{(2 + \bar{q})\bar{q}} \quad (4.28)$$

In the case of the strong screening limit, which corresponds to the situation where $qd \ll 1$ (in our case, d the distance between the 2DEG and the surface metallic gates is ~ 100 nm), one finds $\lim_{qd \rightarrow +0} \chi(q) = qd \left(\lim_{x \rightarrow +0} \coth x \simeq \frac{1}{x} \left(1 + \frac{x^2}{3} \right) \right)$, hence $\bar{q} \sim \frac{a_B}{d}$. For our sample, a_B is on the order of 2 nm, about 50 times smaller than d , then $\bar{q} \ll 1$. The eq.4.28 can be simplified:

$$\omega = \sqrt{\frac{d}{2a_B}} v_F q \quad (4.29)$$

This is the plasmon dispersion relation in the case of the strong screening limit. This dispersion relation is linear and we can easily extract the velocity of the plasmon $v_P = \frac{\partial \omega}{\partial q}$:

$$v_P = \sqrt{\frac{d}{2a_B}} v_F \quad (4.30)$$

The numerical application gives $v_P = 5v_F \simeq 1 \times 10^6 \text{ ms}^{-1}$, in very good agreement with the experimentally obtained value of $1.24 \pm 0.29 \times 10^6 \text{ ms}^{-1}$. The small difference could come from the fact that in our structure, the metallic gates do not cover the entire surface. This could result in a larger effective distance d to the gate and hence a higher velocity. It is also interesting to look in more detail into eq.4.28. In fig. 4.13, the ratio $\frac{\omega}{v_F q}$ is plotted as a function of q . Two limits can be distinguished:

- The long wavelength limit (strong screening), when $q < 1/d$ ($\sim 10 \mu\text{m}^{-1}$). The velocity of the plasmon is five times higher than v_F since $\sqrt{d/2a_B} \simeq 5$.
- The short wavelength limit, when $q > 1/a_B$ ($\sim 1000 \mu\text{m}^{-1}$). The dispersion relation is again linear and the plasmon velocity is equal to the Fermi velocity.

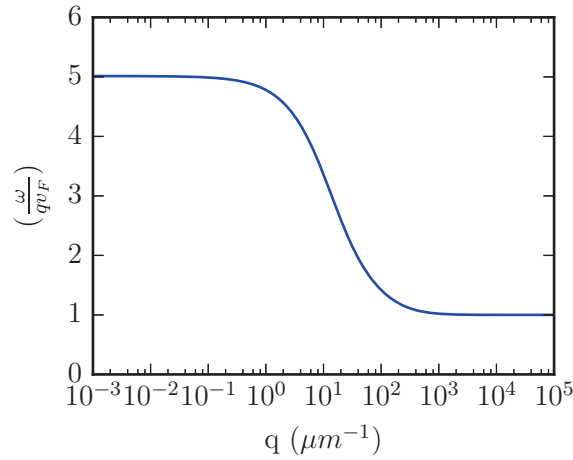


Figure 4.13: Evolution of the ratio $\frac{\omega}{v_F q}$ as a function of q .

It would hence be interesting to be able to pass from one regime to the other. However, it is difficult to reach the short wavelength limit, as it would require to modulate the electron density with a typical wavelength smaller than 100 nm. For a Fermi velocity of about $1 \times 10^5 \text{ m.s}^{-1}$, this would lead to a typical frequency of 1 THz or a typical timescale of 1 ps. Reaching this timescale could be envisaged through the use of particular technology such as pulsed laser coupled to a GaAs photo-conductive switch but it requires a complex implementation to be used in a cryogenic environment.

4.4 Effect of confinement

The electrons excited by the voltage pulse propagate in a 1D channel, therefore it should be possible to reduce their velocity by increasing the confinement potential. Indeed, the energy of the electrons is the sum of their kinetic energy and their potential energy due to the confinement. This energy has to be equal to the Fermi energy since only electrons having an energy close to it contribute to the transport. By increasing the confinement and hence the potential energy, the available kinetic energy is reduced (see fig. 4.14). Therefore,

the velocity of the propagating electrons should decrease.

To control the confinement potential, we have used the tunnel gate. By applying a more and more negative voltage on the tunnel gate, the electrons which initially propagate in the large wire defined by the lateral gates are rapidly forced to propagate in a narrow wire formed by the upper lateral gate and the tunnel gate. As discussed above, the propagating electrons have to pay a higher energy to occupy a conducting channel in a narrow wire and their velocity should be reduced. It is important to mention that the tunnel gate has a strong influence on the nearby QPC used to probe the pulse as shown in fig. 4.15. As a consequence, it is necessary to retune the QPC each time the voltage applied on the tunnel gate is modified.

The time resolved measurements of the voltage pulse as a function of the voltage applied on the tunnel gate V_{tunnel} are presented in fig. 4.16. On the right panel of fig. 4.16, the same data are presented but shifted such that all the maxima are aligned to facilitate the comparison. To extract the peak position, the data are fitted with a Gaussian as it reproduces well the top part of the peak. We emphasize on the fact that the tuning of the QPC is a critical step. For some measurements (especially for $V_{tunnel} = -0.25$ V and -0.5 V) the pulse is slightly distorted, more specifically a shoulder appear on the rising edge. For a reason that we do not understand at present, this shoulder is more pronounced depending on the tuning of the QPC. We focus on the range of voltages applied on the tunnel barrier comprised between -0.1 V and -0.5 V. We have also performed a preliminary experiment with a lower resolution (7 ps between each points) on a larger range (-0.1 V and -0.7 V) showing that the peak position evolves only very slightly once $V_{tunnel} < -0.4$ V. These measurements are presented in the appendix B.

The main peak clearly shifts to longer delay as the voltage applied on the tunnel gate is more and more negative. The corresponding velocities are also presented: one clearly sees that the velocity of the pulse is decreased, from 12.4×10^5 m.s⁻¹ to 9.1×10^5 m.s⁻¹. One observes a continuous evolution of the delay with a saturation at the lowest gate voltage.

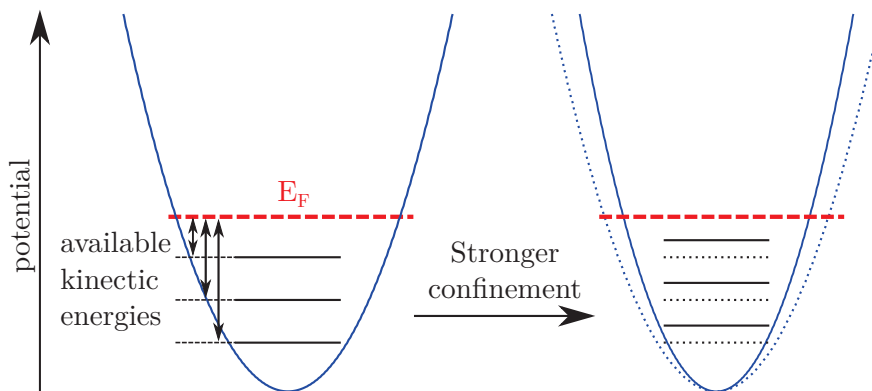


Figure 4.14: Schematic illustrating the effect of the confinement. As the confinement potential is made stronger, the energy levels of the conducting channels are shifted towards the Fermi energy. Therefore, the available kinetic energy is reduced and consequently the velocity.

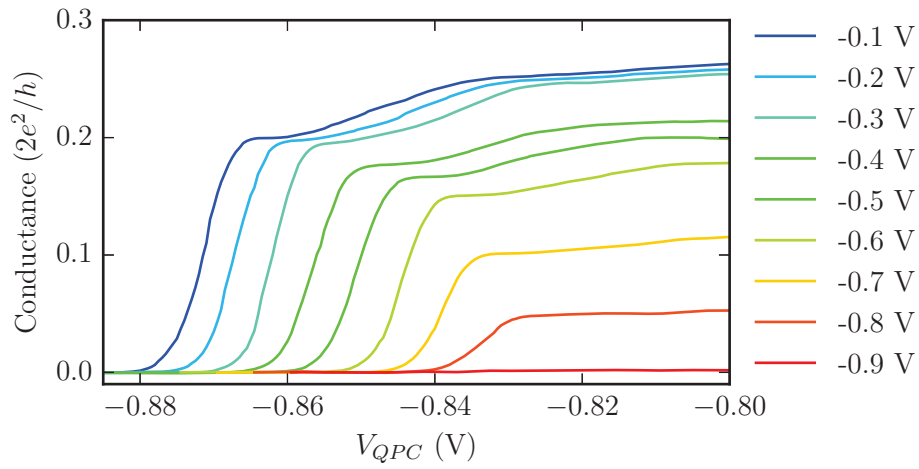


Figure 4.15: Conductance traces of the QPC for different voltages applied on the tunnel gate.

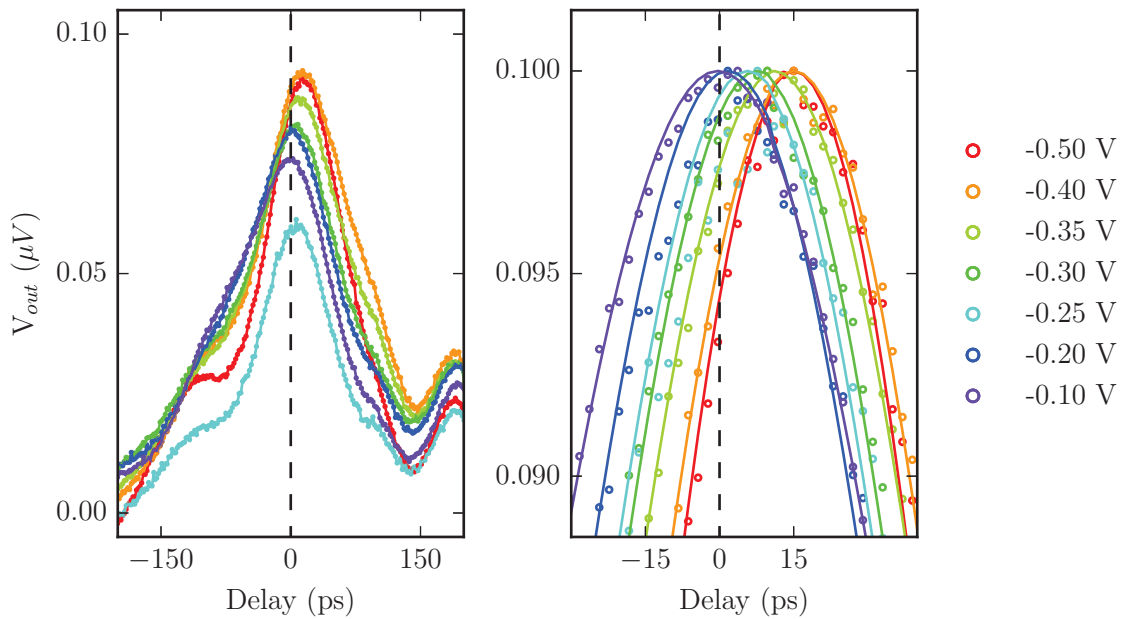


Figure 4.16: Time resolved measurements of the voltage pulse as a function of the voltage applied on the tunnel gate. On the left, the raw data: the peak is moving towards longer delay as the voltage applied on the tunnel gate is made more and more negative. On right, a zoom on the same curves but shifted to facilitate the comparison. The solid lines correspond to a Gaussian fit allowing to extract the peak position.

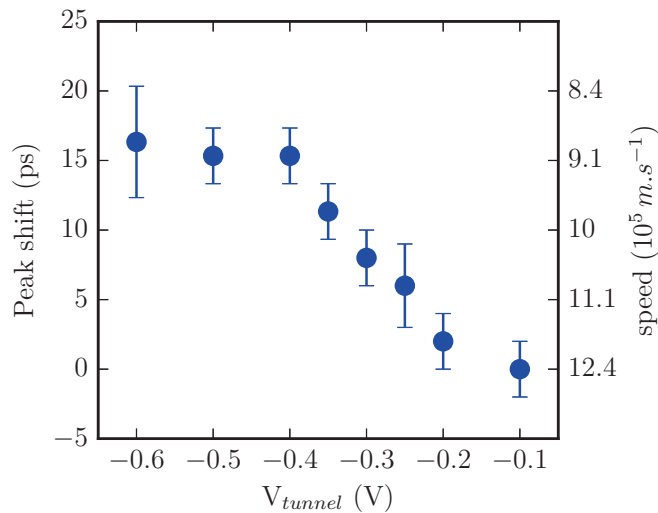


Figure 4.17: Shift of the peak as a function of the voltage applied on the tunnel gate. The point at $V_T = -0.6$ V is extracted from the low resolution measurement presented in the appendix B.

This can be understood by the following: the range of voltages for which the variation is pronounced corresponds to a rapid transition from a wide wire to a narrow wire. This is illustrated by the schematic in fig. 4.18. Indeed, the tunnel barrier allows to split the initial wide wire in two narrower wires (labeled 1 and 2). The electrons which propagate have an energy close to the Fermi energy. As they are initially injected into wire 1, if the tunnel barrier is low enough (typically for $V_{tunnel} = -0.1$ V) they can also populate the wire 2, therefore the two narrow wires act as a single wide wire. On contrary, for $V_{tunnel} < -0.4$ V the barrier potential starts to be high enough such that the electrons are forced to propagate only through the narrow wire 1. The profile of the conductance of the wire 1 and 2 as a function of V_{tunnel} for this range of voltages is presented in fig. 4.19. For small V_{tunnel} (down to -0.4 V, the conductance of both wires is similar as they form a single wide wire. As V_{tunnel} is made more negative, the conductances decreases with a certain rate down to $V_{tunnel} = -0.4$ V. Below this value, the tunnel barrier is high enough such that the wires 1 and 2 start to be separated. The electrons are more and more forced to pass only through the wire 1. The conductance of the wire 1 increases slightly because of this transition from a wide wire to a narrow wire. Except for this increase, between -0.45 V and -0.6 V, the conductance of wire 1 is almost stable. The profile of the conductance agrees well with the evolution of the delay. It is possible in principle to reduce more the velocity by applying a more negative voltage on the tunnel gate. However as we have seen above, this pinches the end of the wire at the QPC level which prevents us to study this regime.

Initially, the present sample has not been designed to measure this effect in detail. In order to investigate this effect in a more controlled way, we have designed a new sample

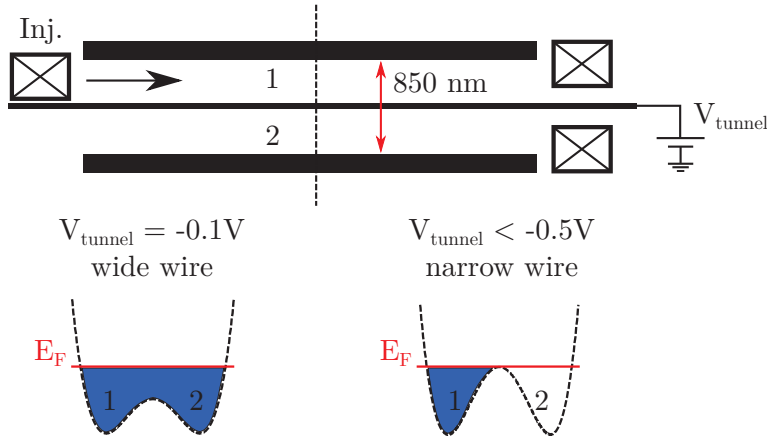


Figure 4.18: Top: schematic of the sample. The tunnel barrier delimits the wire 1 and the wire 2. Initially, the electrons are injected into the wire 1. The dashed line indicates the position of the cross section of the confinement potential. Bottom: schematics of the cross section of confinement potential. For small V_{tunnel} , the electrons see a wide wire formed by the wire 1 and 2. For $V_{\text{tunnel}} < -0.5\text{V}$, the electrons are forced to propagate only through the narrow wire 1.

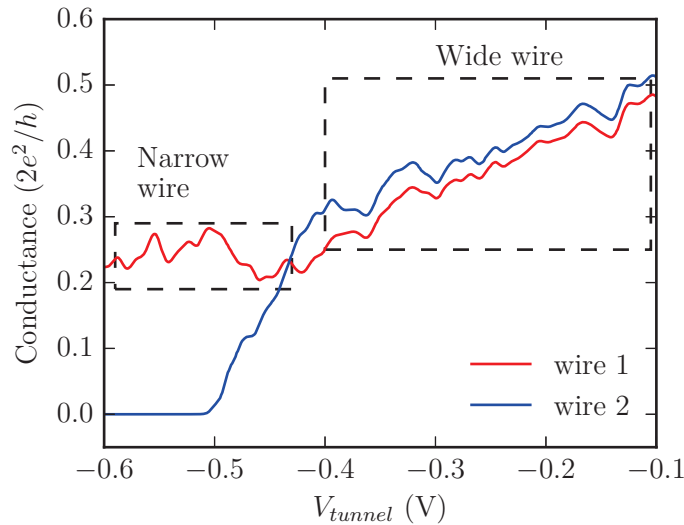


Figure 4.19: Conductance of the sample as a function of the voltage applied on the tunnel gate. The red curve corresponds to the conductance of wire 1 and the blue curve to the conductance of wire 2. For small V_{tunnel} , these two wires form a single wide wire. For $V_{\text{tunnel}} < -0.4\text{V}$, this two wires start to be splitted and the electrons propagate mainly in the wire 1. For $V_{\text{tunnel}} < -0.5\text{V}$, the electrons propagate only through wire 1. The measurement is taken at 20 mK.

(see fig. 4.20) where this can be study in a much larger range. With this new sample, we can also determine the propagation speed over several segments of the 1D channel. These measurements are presently under way.

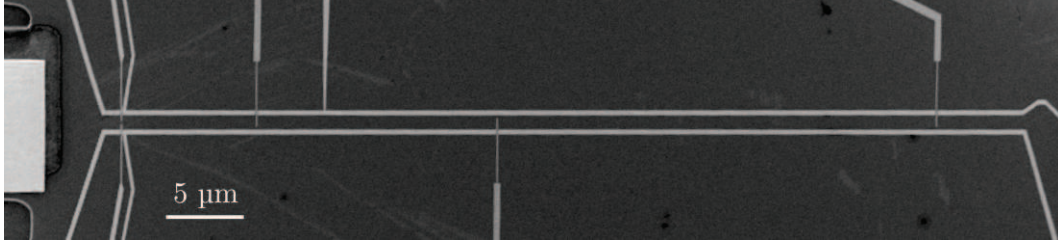


Figure 4.20: SEM picture of the new sample. This design should allow to study the effect of the confinement starting from a wide wire to a fully pinched one.

4.4.1 Discussion on the origin of the oscillations

Let us now turn to the additional oscillations we observe in the in-situ measurements. The Fourier transform of the in-situ measurements clearly reveals two peaks, one around 6 GHz and one at 10 GHz (see fig. 4.21). One possible origin could be some reflections of the pulse inside the sample, for example between the QPC and the ohmic contact. By considering the velocity ($1.24 \pm 0.29 \times 10^6 \text{ ms}^{-1}$) and the length separating these two points ($52 \mu\text{m}$), this would give a frequency of 11.9 GHz so higher than the observed ones. Moreover, contrary to the main peak, this oscillating signal is unaffected by the change of the confinement potential as shown in fig. 4.22 which excludes this possibility. Reflections in the RF line or any element before the ohmic contact (connector, PCB) are also ruled out by this observation since the «reflected» pulses would also be affected by the confinement.

The most probable origin of this oscillation is a standing electromagnetic wave in the cavity formed by the sample holder where the sample is installed. When this standing wave couples to the 2DEG, it results in the generation of «pumped current» which is probed by the pulsed QPC. This parasitic signal may also be at the origin of the shoulder appearing on the rising edge of the main peak in the in-situ measurements. Indeed this oscillation has a period of $\sim 100 \text{ ps}$. As we can see on the left panel of fig. 4.16, the shoulder is located 100 ps before the main peak (it appears clearly for $V_{\text{tunnel}} = -0.5 \text{ V}$). Another shoulder, less visible, appears on the falling edge 100 ps after the main peak. This indicates that this oscillation starts during the rise time of the pulse and is mixed with the signal due to the pulse. To get rid of this parasitic signal is difficult. One possibility would be to cover the internal face of the cap used to close the sample holder with an RF absorber such as Ecosorb™.

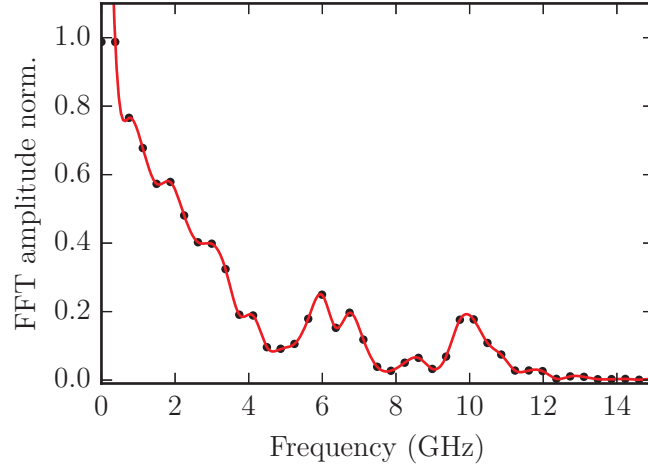


Figure 4.21: Fourier transform of the in-situ measurement. The peaks around 6 GHz and 10 GHz are the signature of the parasitic oscillations appearing in the in-situ measurements.

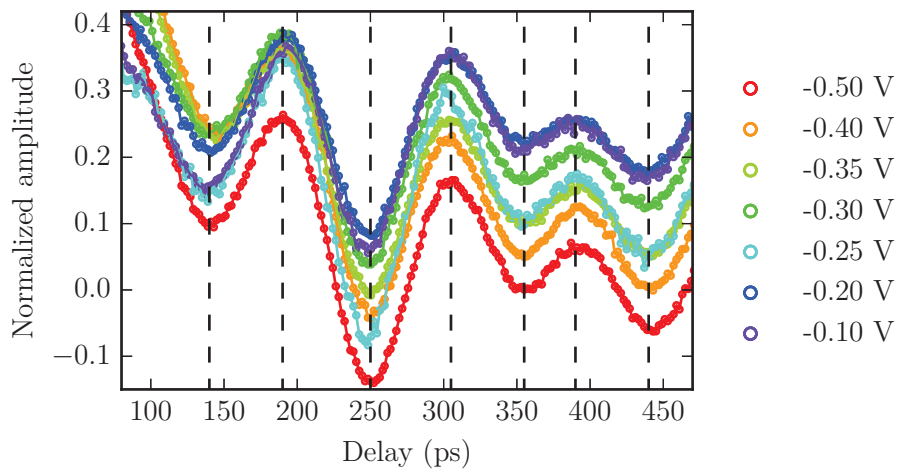


Figure 4.22: Parasitic oscillating signal appearing in the in-situ measurement as a function of the voltage applied on the tunnel gate. This signal is unaffected by the voltage applied on the tunnel contrary to the main peak as we have seen before.

4.5 Theoretical approach of the effect of confinement

The problem of the propagation of electrons in a quantum wire with an arbitrary number of conducting channels has been theoretically investigated by Matveev and Glazman [Mat93]. The authors have shown that the Coulomb interaction between the electrons strongly affect the conductance. Similarly to what we have seen before, it also leads to a modification of the velocity of the electrons due to the Coulomb interaction. In their paper, the authors considered a structure similar to ours where a quasi 1D quantum wire is defined by two electrostatic gates. In this part, we adapt their approach to our structure. These calculations have been done in collaboration with Frank Hekking. Similarly to the approach used to solve the Boltzmann equation, the idea is to consider an electron gas whose density is modulated and has the form $n = n_0 + \delta n$. For a quantum wire containing N modes, the density of the i^{th} mode is $n_{tot,i} = n_i + \delta n_i$ where $\delta n_i = n_i u'_i$. u'_i is the first space derivative of the displacement operator u_i which translates the profile of the electron density in the i^{th} mode at a time t and position x : $u_i = \varepsilon_i e^{ikx - i\omega t}$. The goal is to solve the equation of motion of this interacting electron gas in a quantum wire containing N modes which is given by:

$$\rho_i \ddot{u}_i = \rho_i v_i^2 u_i'' + V_0 \sum_{j=1}^N n_i n_j u_j'' \quad (4.31)$$

where $\rho_i = m^* n_i$ is the mass density of the electrons in the mode i with $m^* = 0.067 m_e$ the effective mass of the electron. \ddot{u}_i is the second time derivative and u_i'' the second space derivative. $n_{i(j)}$ is the electron density of the i^{th} (j^{th}) mode at equilibrium. $v_i = \pi \hbar n_i / m^*$ is the Fermi velocity of i^{th} mode of the non-interacting electrons. V_0 is the zero momentum Fourier component of the Coulomb potential ($V(x) = e^2 / (4\pi \varepsilon_0 \varepsilon_r x)$) screened by the electrostatic gates. The effect of V_0 is to couple the different modes and therefore to induce a collective behavior. For a distance d between the quantum wire and the gate:

$$V_0 \simeq \frac{2e^2}{4\pi \varepsilon_r \varepsilon_0} \ln(k_F d) \quad (4.32)$$

where $\varepsilon_r \varepsilon_0$ is the dielectric constant of GaAs and k_F is the Fermi wave vector. Injecting $u_i = \varepsilon_{il} e^{ik_l x - i\omega_l t}$ into eq.4.31 leads to:

$$-\omega_l^2 \rho_i \varepsilon_{il} = -\rho_i v_i^2 k^2 \varepsilon_{il} - V_0 \sum_{j=1}^N n_i n_j k^2 \varepsilon_{jl} \quad (4.33)$$

We define $s_l = \frac{\omega_l}{k_l}$:

$$s_l^2 \rho_i \varepsilon_{il} = \rho_i v_i^2 \varepsilon_{il} + V_0 \sum_{j=1}^N n_i n_j \varepsilon_{jl} \quad (4.34)$$

Knowing that $\rho_i = m^* n_i$:

$$s_l^2 m^* n_i \varepsilon_{il} = m^* n_i v_i^2 \varepsilon_{il} + V_0 \sum_{j=1}^N n_i n_j \varepsilon_{jl} \quad (4.35)$$

Defining $\gamma_{il} = \sqrt{n_i} \varepsilon_{il}$:

$$s_l^2 \gamma_{il} = \sum_{j=1}^N (v_i^2 \delta_{ij} + \frac{V_0}{m^*} \sqrt{n_i n_j}) \gamma_{jl} \quad (4.36)$$

Using the relation $n_i = \frac{m^* v_i}{\pi \hbar}$:

$$\sum_{j=1}^N (v_i^2 \delta_{ij} + \sqrt{v_i v_j} \frac{V_0}{\pi \hbar}) \gamma_{jl} = s_l^2 \gamma_{il} \quad (4.37)$$

where s_l are the modified velocities due to the Coulomb interaction and δ_{ij} is the Kronecker Delta. $\gamma_{i(j)l}$ is the i^{th} (j^{th}) element of the vectors γ_l which expresses the contribution of the i^{th} (j^{th}) mode to the global charge propagating at the velocity s_l . In eq.4.36, the spin of the electrons has not been explicitly taken into account. Taking into account the spin, eq.4.36 can be expressed in a matrix form $\gamma^{-1} M \gamma = s^2$ where γ is the matrix composed by the vectors γ_l and using $V = V_0/\pi \hbar$:

$$M = \begin{pmatrix} v_{1\uparrow}^2 + v_{1\uparrow} * V & \sqrt{v_{1\uparrow} v_{1\downarrow}} * V & \dots & \sqrt{v_{1\uparrow} v_{N\downarrow}} * V \\ \sqrt{v_{1\downarrow} v_{1\uparrow}} * V & v_{1\downarrow}^2 + v_{1\downarrow} * V & \dots & \dots \\ \sqrt{v_{2\uparrow} v_{1\uparrow}} * V & \sqrt{v_{2\uparrow} v_{1\downarrow}} * V & v_{2\uparrow}^2 + v_{2\uparrow} * V & \dots \\ \dots & \dots & \dots & \dots \\ \sqrt{v_{N\uparrow} v_{1\uparrow}} * V & \dots & \dots & v_{N\downarrow}^2 + v_{N\downarrow} * V \end{pmatrix} \quad (4.38)$$

and

$$s^2 = \begin{pmatrix} s_{1\uparrow}^2 & 0 & \dots & 0 \\ 0 & s_{1\downarrow}^2 & \dots & 0 \\ 0 & 0 & s_{2\uparrow}^2 & \dots \\ \dots & \dots & \dots & \dots \\ 0 & \dots & \dots & s_{N\downarrow}^2 \end{pmatrix} \quad (4.39)$$

M can be simplified since $v_{1\uparrow} = v_{1\downarrow}$, $v_{2\uparrow} = v_{2\downarrow}$ and so on. To determine the velocities s_l and the contribution of each mode (the vectors γ_l), one has to compute the Fermi velocity v_i of each mode and then diagonalize the matrix M.

It is interesting to look at the simple case of a wire with only a single mode which can be easily solved analytically. The electron density of the single mode is $n_1 = n_{1\uparrow} + n_{1\downarrow}$ (with $n_{1\uparrow} = n_{1\downarrow}$). For a wire with a single mode, taking into account the spin, the matrix

M is given by:

$$\begin{pmatrix} v_{1\uparrow}^2 + \sqrt{v_{1\uparrow}v_{1\downarrow}} * V & \sqrt{v_{1\uparrow}v_{1\downarrow}} * V \\ \sqrt{v_{1\downarrow}v_{1\uparrow}} * V & v_{1\downarrow}^2 + \sqrt{v_{1\downarrow}v_{1\uparrow}} * V \end{pmatrix} \quad (4.40)$$

Since $v_{1\uparrow} = v_{1\downarrow} = v_1$, the diagonalization gives two eigenvalues and two eigenvectors:

$$\begin{aligned} s_1 &= \sqrt{v_1^2 + 2v_1V} & \text{with } \gamma_1 &= \frac{1}{\sqrt{2}} \begin{pmatrix} 1 \\ 1 \end{pmatrix} \\ s_2 &= v_1 & \text{with } \gamma_2 &= \frac{1}{\sqrt{2}} \begin{pmatrix} 1 \\ -1 \end{pmatrix} \end{aligned} \quad (4.41)$$

We see that the velocity s_1 is increased by the interaction. The coefficients of the eigenvector γ_1 indicates that $n_{1\uparrow}$ and $n_{1\downarrow}$ contribute with the same weight. This corresponds to the so-called charge mode. On the other hand, the velocity s_2 is unaffected by the interaction. The contribution of $n_{1\uparrow}$ compensates exactly the contribution of $n_{1\downarrow}$, which means that no net charge is propagating with the velocity s_2 . This corresponds to the so-called spin mode. The velocity of the spin mode is not modified because there is no coupling between the spin and the electrostatic potential induced by the modulation of the charge density. Therefore, there is a charge mode propagating at a velocity s_1 higher than the Fermi velocity and a spin mode propagating at the Fermi velocity. This is the famous spin-charge separation which was predicted for a Tomonaga-Luttinger liquid [Lut63; Tom51]. This effect has been observed in several experiments which confirm the existence of a charge mode propagating at a velocity higher than the Fermi velocity and a spin mode propagating at the Fermi velocity [Aus05; Jom09]. We will come back to these observations in the following.

We can now apply this approach to our system. We have seen in sec. 4.4 that it is possible to reduce the velocity of the electrons from $1.24 \times 10^6 \text{ m.s}^{-1}$ to $0.91 \times 10^6 \text{ m.s}^{-1}$ when the voltage applied on the tunnel gate is varied from -0.1 V to -0.5 V . We focus on the case where the tunnel voltage is equal to -0.5 V . The first step is to determine the Fermi velocities of each mode. To do this, it is necessary to know the confinement potential due to the electrostatic gates. A very convenient software has been developed in our group to calculate the potential landscape created by an arbitrary pattern of electrostatic gates [Bau14a]. It is based on the work of Davies et al. [Dav95]. The limitation of this tool lies in the connection between the calculated potential landscape and the real one. Indeed, the electrons of the 2DEG screen the potential due to the gates. This can be taken into account by using an α factor which relates the voltage applied on the gates and the potential seen by the electrons. However, it is not so easy to determine this α factor. In a particular situation, the experiment can help us for its determination. We have seen in sec. 4.4 that when the voltage applied on the tunnel gate is -0.5 V , the electron can not tunnel anymore through the tunnel barrier. It means that the height of the tunnel barrier is on the order of the Fermi energy of the electrons. With this information, we can compute the transverse potential seen by the electrons as shown in fig. 4.23. For this particular gate configuration, the electrons are confined only in the upper narrow wire (defined by gate G1 and the tunnel gate in fig. 4.2). In this case, the potential in which the electrons are

confined is very close to a harmonic potential. It is therefore possible to approximate this potential with a harmonic model:

$$U(y) = \frac{m^* \omega_0^2 y^2}{2} \quad (4.42)$$

The fitting procedure allows us to extract ω_0 . We can then calculate the energy levels of this harmonic potential given by:

$$E_i = E_s + \left((i - 1) + \frac{1}{2} \right) \hbar \omega_0 \quad (4.43)$$

where i labels the mode associated with energy E_i and E_s is the minimum of the potential well (~ 3.7 meV). To determine the number of modes allowed in this potential, we simply have to fill the energy levels while $E_i \leq E_F$. The Fermi energy E_F in our structure is on the order of 7.5 meV. Therefore we have 7 modes which are populated within this potential. Since the energy of each mode is known, we can also calculate the Fermi velocity v_i of the i^{th} mode:

$$v_i = \sqrt{\frac{2(E_F - E_i)}{m^*}} \quad (4.44)$$

It is then easy to calculate the electron density n_i of the i^{th} mode:

$$n_i = \frac{m v_i}{\pi \hbar} \quad (4.45)$$

The energies, Fermi velocities and densities associated with each mode are presented in the tab.4.2.

We now have to compute the value of V ($V = V_0/(\pi \hbar)$) which translates the strength of the interaction expressed as a velocity. For our structure, $k_F = \frac{2\pi}{55 \text{ nm}}$, $d = 100$ nm and

Table 4.2: Calculated energies, Fermi velocities and densities associated with the modes allowed in the harmonic potential.

i	E_i (meV)	v_i (10^5 m.s^{-1})	n_i (10^7 m^{-1})
1	4.1	1.36	2.5
2	4.6	1.26	2.3
3	5.1	1.14	2.1
4	5.6	1.01	1.9
5	6.1	0.86	1.6
6	6.6	0.68	1.3
7	7.1	0.43	0.8

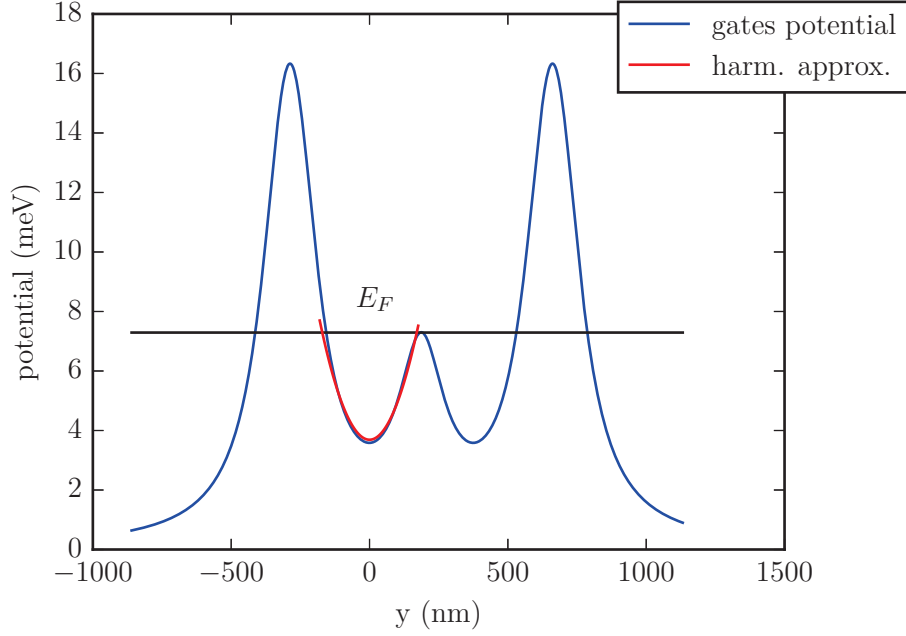


Figure 4.23: Simulation of the transverse electrostatic potential seen by the electron when the voltage applied on the tunnel gate is -0.5 V. The voltage applied on the lateral gates (G1 and G2 in fig. 4.2) is -0.4 V and corresponds to the experimental value.

$\varepsilon_r = 11$ (at high frequencies):

$$V = \frac{1}{\pi\hbar} \frac{2e^2}{4\pi\varepsilon_0\varepsilon_r} \ln\left(\frac{2\pi}{55 \cdot 10^{-9}} \times 100 \cdot 10^{-9}\right) = 3.08 \times 10^5 \text{ m.s}^{-1} \quad (4.46)$$

Knowing the Fermi velocities and V , we can now build the matrix M and diagonalize it in order to extract the new velocities s_l and the associated eigenvectors γ_l . Similarly to the case of the single mode where we obtained two velocities, for 7 modes we obtain 14 velocities: 7 charge mode velocities and 7 spin mode velocities. The components of the vectors γ_l represent the weight of the contribution of each of the 7 conducting modes determined previously. Taking into account the spin, each vector γ_l has 14 components. The velocities s_l of the spin modes and the components of the associated eigenvectors γ_l are presented in tab.4.3. As expected, the velocities of the spin modes are identical to the Fermi velocities. The sum of the contributions of each mode ($\sum \gamma_{jl}$) is always zero, since no charge is carried by a spin mode.

For the charge modes on the other hand, the situation is quite different. As can be seen in tab.4.4, there is one charge mode ($l=1$) whose velocity s_1 is strongly enhanced, reaching $6.6 \times 10^5 \text{ m.s}^{-1}$. All the conducting channels contribute to this charge mode with an almost equal weight (varying from -0.32 to -0.175 , see first column of tab.4.4).

Additionally to this fast charge mode, there are 6 «slow» charge modes with velocities comparable to the Fermi velocities of the non interacting electrons. The contribution of each conducting channel varies strongly. Mainly one or two conducting channels contribute in each case. These slow charge modes represent Fermi-liquid quasiparticles [Mat93]. As can be seen through the values $\sum \gamma_{jl}$, these quasiparticles contribute significantly less than the fast charge mode to the total transport.

We can therefore conclude the transport is mainly ensured by the fast charge mode having a velocity much higher than the Fermi velocity and which corresponds to a plasmon. There is still a fraction of the electrons which propagate with velocities close to the Fermi velocities but they contribute only a little to the transport.

The velocity of the fast charge mode $s_1 = 6.6 \times 10^5 \text{ m.s}^{-1}$ is much higher than the Fermi velocities, in agreement with the experiment. However, it is significantly lower than the experimentally obtained value of $9.1 \times 10^5 \text{ m.s}^{-1}$ (see fig. 4.17 for $V_{tunnel} = -0.5V$). There are several reasons that can explain the difference between the theory and the experiment. Firstly, the Coulomb interaction has been calculated assuming that the metallic gates fully cover the surface of the sample. In reality this is not the case, hence the screening is less effective and which leads to a higher velocity. Second, we have considered that the modulation of the electron density has the form $\varepsilon e^{ikx-i\omega t}$. The modulation caused by the pulse is actually more complex and might change the result of the calculations. Taking into account the effect of the voltage pulse is possible but requires more advanced calculations that are beyond this PhD work.

In principle, it should be possible to see the passage of the slow charge modes in our time

Table 4.3: Calculated spin modes velocities s_l expressed in terms of Fermi velocities v_i and components of the associated eigenvectors.

i	1	2	3	4	5	6	7
l	2	4	6	8	10	12	14
s_l/v_i	1	1	1	1	1	1	1
$\gamma_{1,l} (n_{1\uparrow})$	0.707	0	0	0	0	0	0
$\gamma_{2,l} (n_{1\downarrow})$	-0.707	0	0	0	0	0	0
$\gamma_{3,l} (n_{2\uparrow})$	0	0.707	0	0	0	0	0
$\gamma_{4,l} (n_{2\downarrow})$	0	-0.707	0	0	0	0	0
$\gamma_{5,l} (n_{3\uparrow})$	0	0	0.707	0	0	0	0
$\gamma_{6,l} (n_{3\downarrow})$	0	0	-0.707	0	0	0	0
$\gamma_{7,l} (n_{4\uparrow})$	0	0	0	0.707	0	0	0
$\gamma_{8,l} (n_{4\downarrow})$	0	0	0	-0.707	0	0	0
$\gamma_{9,l} (n_{5\uparrow})$	0	0	0	0	0.707	0	0
$\gamma_{10,l} (n_{5\downarrow})$	0	0	0	0	-0.707	0	0
$\gamma_{11,l} (n_{6\uparrow})$	0	0	0	0	0	0.707	0
$\gamma_{12,l} (n_{6\downarrow})$	0	0	0	0	0	-0.707	0
$\gamma_{13,l} (n_{7\uparrow})$	0	0	0	0	0	0	0.707
$\gamma_{14,l} (n_{7\downarrow})$	0	0	0	0	0	0	-0.707
$\sum \gamma_{jl}$	0	0	0	0	0	0	0

Table 4.4: Calculated charge modes velocities s_l expressed in terms of fermi velocities v_i and components of the associated eigenvectors.

i	1	2	3	4	5	6	7
l	1	3	5	7	9	11	13
s_l/v_i	4.82	1.05	1.05	1.06	1.06	1.07	1.11
$\gamma_{1,l} (n_{1\uparrow})$	-0.322	-0.588	0.177	0.101	-0.07	0.051	-0.036
$\gamma_{2,l} (n_{1\downarrow})$	-0.322	-0.588	0.177	0.101	-0.07	0.051	-0.036
$\gamma_{3,l} (n_{2\uparrow})$	-0.308	0.361	0.487	0.155	-0.092	0.061	-0.041
$\gamma_{4,l} (n_{2\downarrow})$	-0.308	0.361	0.487	0.155	-0.092	0.061	-0.041
$\gamma_{5,l} (n_{3\uparrow})$	-0.291	0.123	-0.448	0.413	-0.141	0.08	-0.049
$\gamma_{6,l} (n_{3\downarrow})$	-0.291	0.123	-0.448	0.413	-0.141	0.08	-0.049
$\gamma_{7,l} (n_{4\uparrow})$	-0.273	0.071	-0.145	-0.517	-0.338	0.119	-0.063
$\gamma_{8,l} (n_{4\downarrow})$	-0.273	0.071	-0.145	-0.517	-0.338	0.119	-0.063
$\gamma_{9,l} (n_{5\uparrow})$	-0.25	0.047	-0.081	-0.143	0.575	0.263	-0.09
$\gamma_{10,l} (n_{5\downarrow})$	-0.25	0.047	-0.081	-0.143	0.575	0.263	-0.09
$\gamma_{11,l} (n_{6\uparrow})$	-0.221	0.033	-0.051	-0.075	0.134	-0.626	-0.177
$\gamma_{12,l} (n_{6\downarrow})$	-0.221	0.033	-0.051	-0.075	0.134	-0.626	-0.177
$\gamma_{13,l} (n_{7\uparrow})$	-0.175	0.022	-0.032	-0.042	0.061	-0.106	0.672
$\gamma_{14,l} (n_{7\downarrow})$	-0.175	0.022	-0.032	-0.042	0.061	-0.106	0.672
$\sum \gamma_{jl}$	-3.68	0.14	-0.185	-0.216	0.259	-0.315	0.43

resolved measurements. However, considering their small amplitude compared to the fast charge mode, there is a high chance that the latter are hidden by the parasitic oscillating signal appearing after the main peak.

We have briefly mentioned that earlier experiments have already allowed to observe the existence of a charge mode propagating at a velocity higher than the Fermi velocity and a spin mode propagating at the Fermi velocity [Aus05; Jom09]. In particular in [Aus05] the authors studied two 1D wires (we refer it to wire 1 and wire 2 in the following) coupled via a tunnel barrier. Because of the coupling between the two wires the situation is similar to having two conducting channels. In their case, they determined the velocity of the charge and spin modes by measuring the tunneling current from wire 1 to wire 2. In principle, they should have observed two charge modes (one fast and one slow) and two spin modes. However, according to the authors, for an unknown reason they did not observe the fast charge mode. Our time resolved measurement allows to observe this fast charge mode and in principle should allow to observe the slow charge mode too.

To conclude this part, we now apply this procedure for several confinement potentials. As we have seen above, when the voltage applied on the tunnel gate is lower than -0.5 V it is possible to approximate the potential seen by the electrons with a harmonic potential allowing to easily calculate the velocities of the non interacting electrons. We therefore have simulated the electrostatic potential for voltages applied on the tunnel gate ranging from -0.6 V to -2.5 V. This latter value corresponds to the case where only one single

channel remains in the narrow wire according to the simulation. We then have calculated the velocity of the fast charge mode for each confinement potential.

On the other hand, when the voltage applied on the tunnel gate is -0.1 V, we have seen that a wide wire is formed. The simulation of the electrostatic potential in this case is shown in the appendix C. As a first approximation, we can also fit this potential with an harmonic model. With this approximation we have calculated the velocity of the fast charge mode for this weak confinement.

Let us now compare the experimentally obtained velocities and the calculated ones. In fig. 4.24 we have plotted the measured velocities determined in sec. 4.4 (blue circles) and the calculated velocities for several confinement potential (green circles). The theoretical data follow nicely the experimentally observed trend. However, the absolute value differs by

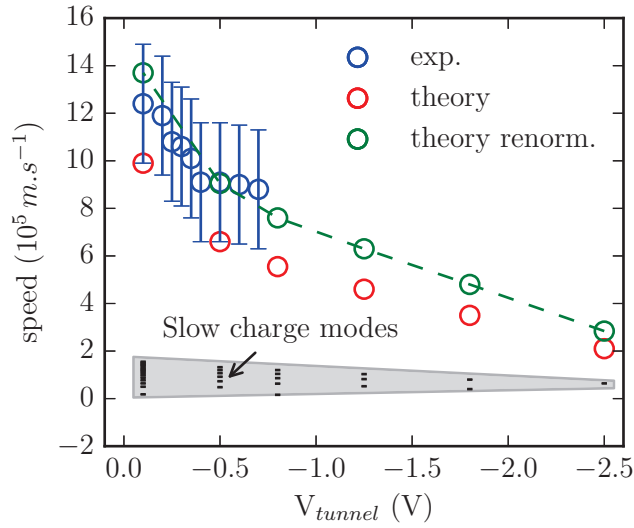


Figure 4.24: Comparison between the measured and calculated propagation velocities as a function of the voltage applied on the tunnel gate. The blue circles are the experimental data, the red circles are the calculated fast charge mode velocities in the case of the non renormalized interaction potential and the green circles are the calculated fast charge mode velocities in the case of the renormalized interaction potential. The black lines delimited by the gray area correspond to the calculated velocities of the slow charge modes.

approximately 30%. In order to overlap the theory with the experiment, we have to «renormalize» by hand the value of the interaction potential $V = \frac{1}{\pi\hbar} \frac{2e^2}{4\pi\epsilon_r\epsilon_0} \ln(k_F d)$. This requires to basically double the value of the interaction strength. Initially $V = 3.1 \times 10^5 \text{ m.s}^{-1}$ expressed in terms of a velocity, the renormalized value is $V = 6 \times 10^5 \text{ m.s}^{-1}$. The calculated velocities using the renormalized potential are represented by the green circles in fig. 4.24. The agreement with the experimental data and the theory in the case of the renormalized potential is extremely good. This suggests that it is necessary to take into account a stronger interaction strength which is certainly due to the weaker screening of our electrostatic gates compared to a metallic gate covering all the surface of the sample.

We also show the calculated velocities of the slow charge modes represented by the black lines delimited by the gray area. We recall that each slow charge mode involves mainly one conducting channel and its velocity is almost equal the Fermi velocity of the channel. In all the case, the velocities of the slow charge modes are well smaller than the fast charge mode velocities.

4.6 Conclusion

In this chapter we have exposed how to perform a time resolved measurement of a voltage pulse in-situ. We have adapted a technique developed by Kamata et al. [Kam09] in which a pulsed QPC is used as a fast switch. It allows to measure the convolution of the pulse applied on the ohmic contact and the pulse applied on the QPC. Knowing the characteristics of the RF lines, we can reconstruct the shape of the pulse after its propagation up the QPC. We have showed that the pulse does undergo only very little distortion over a propagation distance of 51 μm .

We have determined the velocity of the voltage pulse through the sample. Contrary to our initial thought, the measured velocity is much higher than the Fermi velocity: $12.4 \times 10^5 \text{ m.s}^{-1}$ compared to $2 \times 10^5 \text{ m.s}^{-1}$. It turns out that this velocity is in very good agreement with the plasmon velocity which is obtained from the Boltzmann kinetic equation [Cha85]. The Coulomb interaction between the electrons leads to a collective behavior which governs the propagation of the electrons. This velocity depends strongly on the distance between the metallic gates deposited at the surface of the sample and the 2DEG as they screen the Coulomb interaction. The closer the gates, the weaker the interaction and hence the lower the velocity.

Finally we have studied the effect of the confinement on the propagation of the electrons. We have shown that by increasing the confinement, we can reduce the velocity of the electrons by 30% from $12.4 \times 10^5 \text{ m.s}^{-1}$ to $9.1 \times 10^5 \text{ m.s}^{-1}$. With a better design of the sample, it should even be possible to observe a higher variation. A new sample has been designed for the next experiments. It will allow to study in a more controllable way the effect of the confinement. Moreover, it will be possible to measure the velocity of the voltage pulse over several distances. We have developed a theoretical approach of the effect of the confinement based on the work of Matveev and Glazman [Mat93] where the authors studied the propagation of electrons in a quantum wire containing an arbitrary number of modes. This confirms that the transport is mainly governed by the collective behavior of the electrons. The calculated velocities for particular confinements reproducing the experimental conditions are also in good agreement with the experimental values. This approach is very interesting since it allows to study mode by mode the response of the electrons to a fluctuation of the charge density. For the moment we have only considered the simple case of a modulation of the density having a form $\varepsilon e^{ikx-i\omega t}$. It would be very interesting to go a step further and «inject» a voltage pulse into these equations.

CHAPTER 5

Investigation of the tunnel coupled wires

In the preceding chapter, we have investigated the propagation of a short voltage pulse through a quasi 1D electron system and have been able to determine its propagation velocity. In this chapter, we will be interested in the coherent tunneling of a voltage pulse between two quantum wires coupled via a tunnel barrier. As we have seen in chapter 2, the tunnel coupled wires can be seen as a two path interferometer and therefore in principle be used to reveal the dynamical modification of the interference pattern created by a short voltage pulse. To observe this effect, one has to reach a regime where the temporal width of a voltage pulse is much shorter than its time of flight through the interferometer. This is a very stringent requirement because at the same time, the coherence of the propagating electrons excited by the pulse has to be preserved. In our system, we have determined the velocity of the pulse on the order of 10^6 m.s^{-1} . For a voltage pulse of $\sim 100 \text{ ps}$ generated by the AWG, it means that the interferometer should be longer than $\sim 100 \mu\text{m}$. The two path interferometer we have designed taking into account a Fermi velocity of $2 \times 10^5 \text{ m.s}^{-1}$, which is based on tunnel coupled wires, has a length of $40 \mu\text{m}$. Therefore, this regime is at present not accessible. In the near future, the utilization of our homemade voltage pulse source generating voltage pulses having a temporal width of $\sim 30 \text{ ps}$ should allow to reach the good regime. In this case, the length of the interferometer can be reduced to $\sim 30 - 40 \mu\text{m}$ so comparable to the length of our device. However, it is not at all obvious that the coherence is preserved over such a long distance. Several sources of decoherence can destroy the interferences, such as electron-electron interactions [Alt82] or gate voltage fluctuations [See01].

In this chapter, we present preliminarily measurements of coherent tunnel oscillations of the electrons between the tunnel coupled wires. We start with DC measurements that allowed us to characterize the system and to observe oscillations of conductance that could be due to the coherent tunneling of the electrons. These measurements are then compared with measurements using fast voltage pulses of typical width of 100 ps . We will see that another process (the Coulomb blockade) also leads to oscillations of conductance and make the interpretation of the observed oscillation as a coherent tunneling of the electrons more difficult. Finally, we present preliminary results on the time resolved measurement of the tunneling of the voltage pulse between the tunnel coupled wires.

5.1 DC regime

5.1.1 Observation of antisymmetric oscillations of conductance

We briefly recall the main results of the analytical description of the tunnel coupled wires (TCW) obtained in the chapter 2. We define the state of an electron by $|\uparrow\rangle$ if the electron is present in the upper wire (formed by the gate G1 and the tunnel gate, see fig. 5.1) and by $|\downarrow\rangle$ if the electron is present in the lower wire (formed by the gate G2 and the tunnel gate). The eigenstates of the electron in the TCW are the symmetric state $\Psi_S = \frac{|\uparrow\rangle+|\downarrow\rangle}{\sqrt{2}}$ and the antisymmetric state $\Psi_{AS} = \frac{|\uparrow\rangle-|\downarrow\rangle}{\sqrt{2}}$. The sample is designed to inject the electrons in the wire $|\uparrow\rangle$. For an electron initially injected in the wire $|\uparrow\rangle$, the probability to measure it at the output of the wire $|\uparrow\rangle$ or $|\downarrow\rangle$ are respectively:

$$|\langle\uparrow|\uparrow\rangle|^2 = \frac{1 + \cos(\theta)}{2} \quad (5.1)$$

$$|\langle\downarrow|\uparrow\rangle|^2 = \frac{1 - \cos(\theta)}{2} \quad (5.2)$$

where $\theta = (k_S - k_{AS})L$ (L is the length of the TCW). In the case where the kinetic energy is large compared to the tunnel coupling energy, θ can be written as:

$$\theta \simeq \frac{2\tau}{\hbar} \Delta t \quad (5.3)$$

where τ is the tunnel coupling energy and Δt is the time spent by the electron to travel through the TCW. Therefore, θ can be controlled by changing the tunnel coupling energy between the two wires. In practice, this is done by varying the voltage V_T applied on the tunnel gate. As a consequence, the conductances of the wires $|\uparrow\rangle$ and $|\downarrow\rangle$ should oscillate anti-symmetrically as a function of V_T .

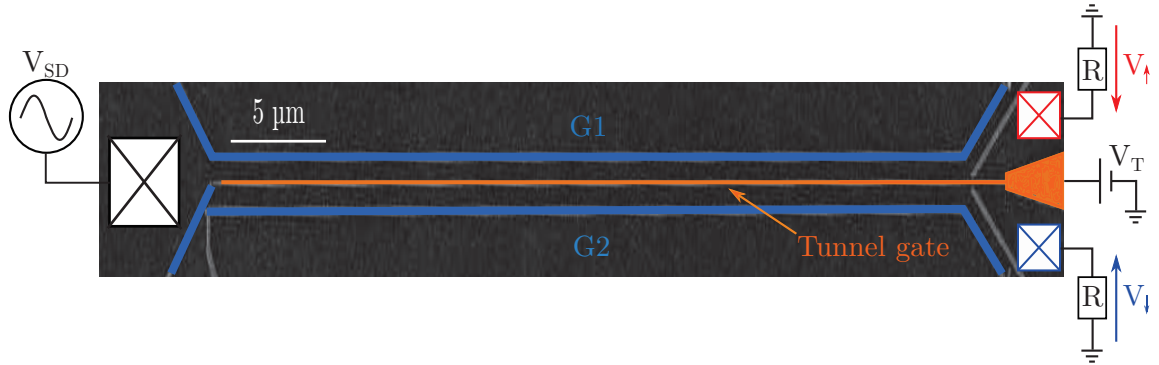


Figure 5.1: SEM picture of the sample illustrating the configuration used to investigate the tunnel oscillations.

To investigate the coherent tunnel oscillations of the electrons, we first started with DC measurements. By DC we mean low frequency Lock in detection (on the order of few

tens of Hz). The sample is biased with a source drain voltage V_{SD} on the order of $10 \mu\text{V}$. The current flowing through the ohmic contacts located at the output of the two wires are converted into voltages through $10 \text{ k}\Omega$ resistances installed at low temperature, which allows us to calculate the conductance of each wires.

Fig. 5.2 shows the conductance of the wires $|\uparrow\rangle$ and $|\downarrow\rangle$ as a function of the voltage V_T applied on the tunnel gate at a temperature of 300 mK . The red curve corresponds to the conductance of the wire $|\uparrow\rangle$ and the blue curve to the wire $|\downarrow\rangle$. Three regimes can be distinguished:

1. for $-0.38 \text{ V} < V_T < -0.3 \text{ V}$, the tunnel barrier is very weak and the two wires form actually a single wide wire. Both conductances are almost identical and evolve symmetrically. Both are decreasing as V_T is made more and more negative because the conductance of the wide wire is decreasing.
2. for $-0.46 \text{ V} < V_T < -0.38 \text{ V}$, the two wires are in the tunnel coupled regime. The wire $|\downarrow\rangle$ is now populated by the electrons tunneling through the tunnel barrier. As V_T is made more negative, the probability for an electron to tunnel in the wire $|\downarrow\rangle$ becomes weaker and weaker and the conductance approaches zero. Hence, the electrons are more and more forced to pass through the wire $|\uparrow\rangle$ and its conductance increases. On top of this general tendency, antisymmetric oscillations of conductance indicated by the dashed lines clearly appear.
3. for $V_T < -0.46 \text{ V}$, the tunnel barrier is so large that electrons cannot tunnel anymore into the wire $|\downarrow\rangle$ and the conductance reaches zero. The conductance of the wire $|\uparrow\rangle$ starts to decrease as the it becomes narrower.

To enhance the visibility of the antisymmetric oscillations of conductance, we extract them by subtracting a background from the raw data. This background is obtained by smoothing the raw data in order to suppress the oscillations. Therefore, by subtracting this background from the raw data, only the oscillating part remains. The antisymmetric oscillations extracted from fig. 5.2 are presented in fig. 5.3. We observe three periods corresponding to a change of θ of 6π .

In order to compare the different experiments performed with DC bias and short pulses and to get quantitative information about the temperature dependence of the oscillations, we calculate the visibility of the oscillations defined as follow: the quantity $\frac{G_{|\uparrow\rangle} - G_{|\downarrow\rangle}}{G_{|\uparrow\rangle} + G_{|\downarrow\rangle}}$ is calculated. Then similarly as described above, a background is obtained by smoothing the quantity $\frac{G_{|\uparrow\rangle} - G_{|\downarrow\rangle}}{G_{|\uparrow\rangle} + G_{|\downarrow\rangle}}$. By subtracting this background, only the oscillating part of $\frac{G_{|\uparrow\rangle} - G_{|\downarrow\rangle}}{G_{|\uparrow\rangle} + G_{|\downarrow\rangle}}$ remains. The result of this procedure is presented in fig. 5.4 (green curve). The extracted signal defined the visibility: it corresponds to the ratio $\delta G/G$ where δG represents the amplitude of the oscillations and G is the total conductance of the two wires. It appears that the amplitude of the oscillations of conductance represents only a fraction of the total conductance, on the order of 7% at maximum for $V_T = -0.445 \text{ V}$ at a temperature of 300 mK . This is due to the fact that only a small fraction of the electrons traveling through the TCW experience a coherent tunneling [Bau14b]. Theoretically, we have considered only a single conducting channel in each wire. In practice, there are several channels in

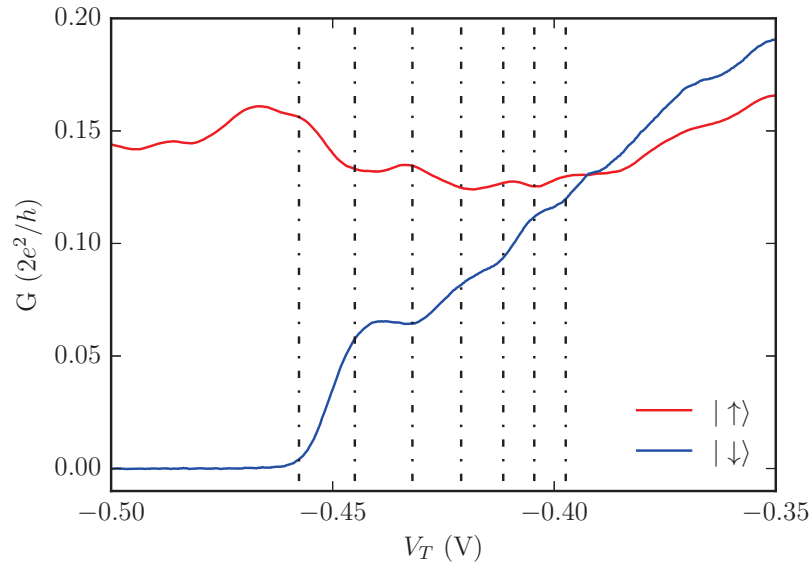


Figure 5.2: Conductance of the wires $|\uparrow\rangle$ and $|\downarrow\rangle$ as a function of the voltage applied on the tunnel gate V_T . A source drain bias of $10\ \mu\text{V}$ and a frequency of $37\ \text{Hz}$ were used. The measurement is taken at a temperature of $300\ \text{mK}$.

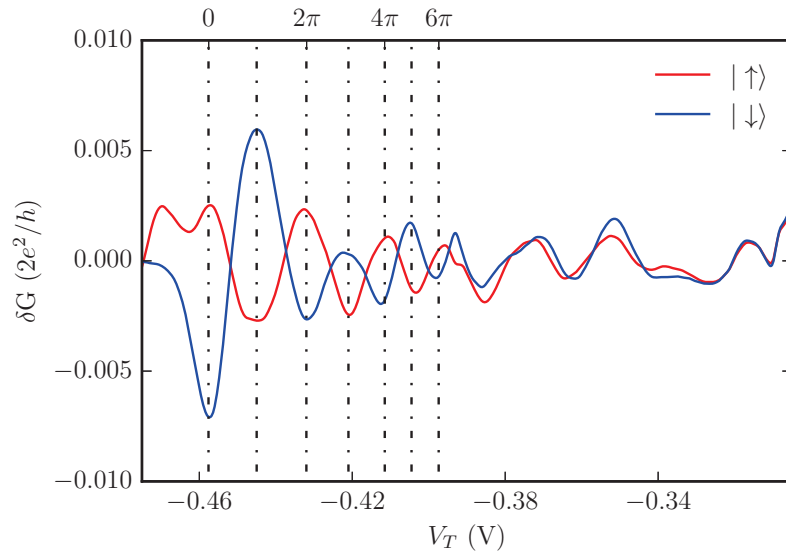


Figure 5.3: Antisymmetric oscillations of conductance of the wires $|\uparrow\rangle$ and $|\downarrow\rangle$ as a function of the voltage applied on the tunnel gate V_T extracted from fig. 5.2. Three periods are observed corresponding to a change of θ of 6π .

each wire (on the order of 6 or 7 see sec. 4.5) but most likely, only two channels (one in each wire) allow tunnel oscillations between them [Wes16b].

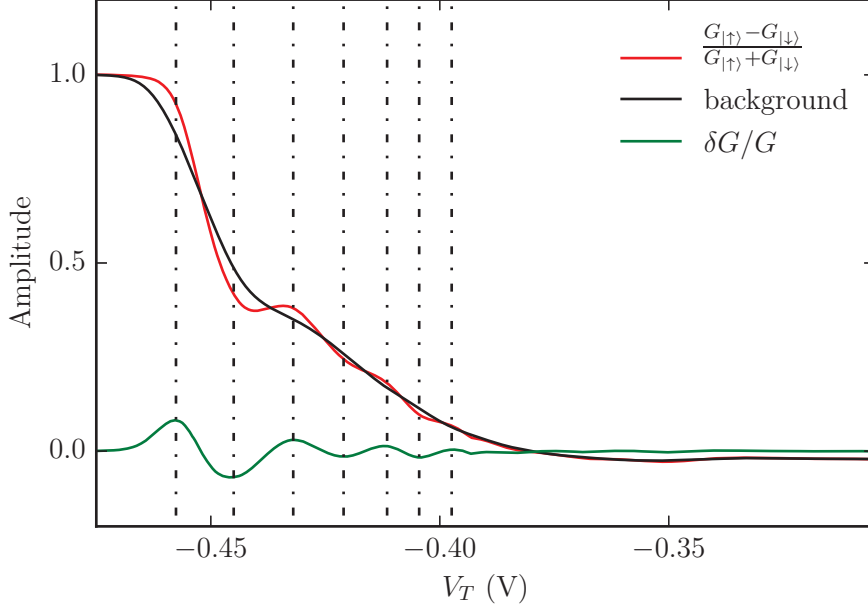


Figure 5.4: Illustration of the procedure used to extract of the visibility $\delta G/G$ of the oscillations. The quantity $\frac{G_{|\uparrow\rangle} - G_{|\downarrow\rangle}}{G_{|\uparrow\rangle} + G_{|\downarrow\rangle}}$ is calculated (red curve). The obtained curve is smoothed to get a background (black curve). By subtracting this background, we obtain the visibility $\delta G/G$ (green curve).

5.1.2 Temperature dependence of the oscillations

The tunnel oscillations of an electron in the TCW is a coherent process. To observe these oscillations, it is therefore necessary that the phase of the electronic wave function stays well defined during the propagation of the electron through the TCW. At low temperature, the coherence length is mainly limited by inelastic collisions between electrons [Alt82]. Increasing the temperature leads to a thermal smearing of the oscillations because the collision rate is increased. Therefore, the visibility of the oscillations should rapidly decrease when the temperature is increased.

We have studied the evolution of the oscillations as a function of temperatures ranging from 20 mK to 800 mK. The bias was adapted to not overheat the sample: $2 \mu\text{V}_{RMS}$ at 20 mK, $4 \mu\text{V}_{RMS}$ at 40 mK and so on. From 200 mK to 400 mK, the bias was kept fixed to $20 \mu\text{V}_{RMS}$ and then $40 \mu\text{V}_{RMS}$ from 500 mK to 800 mK. We emphasize the fact that at very low temperature, the conductance of the wires can be strongly altered. In fig. 5.5, the conductances measured at 20 mK and 200 mK are plotted. The strong variations of the conductance at very low temperature are the signature of impurities located inside the wires. Since our sample is longer than the mean free path ($14 \mu\text{m}$), there is a high

probability to find impurities along the wires. These impurities form potential traps whose characteristics depend on the voltage applied on the tunnel barrier. Such a potential trap can be viewed as a quantum dot. Changing the voltage applied to the tunnel gate changes the size of the dot and therefore the energy level spacing. Each time some energy levels are aligned with the energy levels of a wire, the conductance increases. On the contrary, when the energy levels of the dot are not aligned with the ones of the wire, the conductance decreases. This can affect differently each wire depending on the location of the impurities.

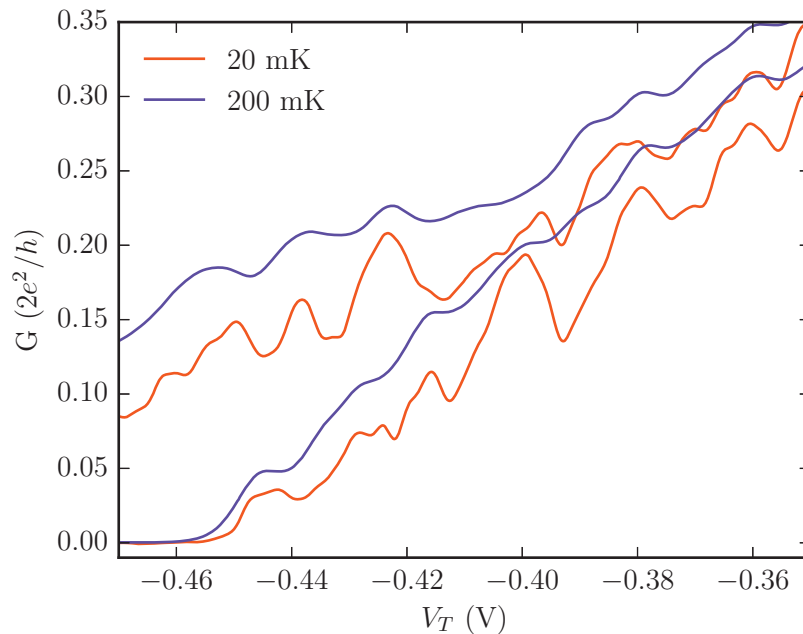


Figure 5.5: Comparison between measurement taken at 20 mK and 200 mK. At 20 mK, the strong variation of the conductance are due to the presence of impurities inside the tunnel coupled wires.

In fig. 5.6, the evolution of the visibility $\delta G/G$ for some temperatures spanning the studied range are shown. As expected, the amplitude of the oscillations clearly decreases as the temperature is increased. The evolution of the visibility $\delta G/G$ of the osc. 1 and the osc. 2 as a function of the temperature is presented in fig. 5.7. The visibility is expected to decrease exponentially with temperature [Han01; Rou08b; Yam12] which is effectively the case. Both show comparable decay with a characteristic evolution $\propto e^{-T/T_0}$ where $T_0 \simeq 260$ mK for the osc. 1 and $T_0 \simeq 210$ mK for the osc. 2. By extrapolating these curves to zero temperature, the visibility would reach a value of about 25 to 30%. This seems to indicate that two pairs of channels are effectively tunnel coupled and the 5 or 6 others pairs are «spectators» leading to a visibility of $2/6$ or $2/7$ therefore about 30%. The temperature dependence allows also to estimate the coherence length of our device at low temperature. The exponential decay of the visibility as a function of the temperature

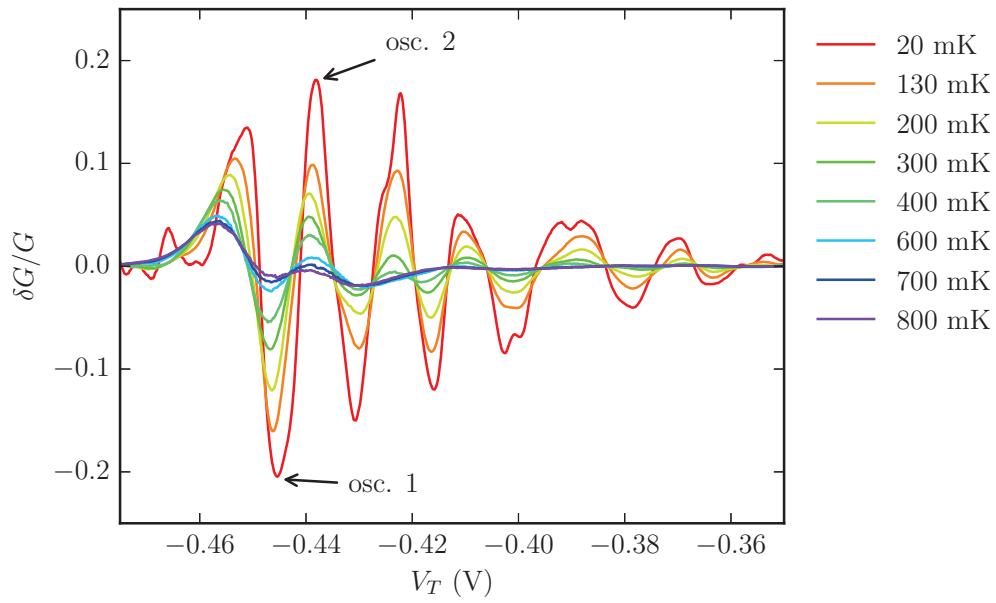


Figure 5.6: Temperature dependence of the visibility $\delta G/G$ for DC measurements.

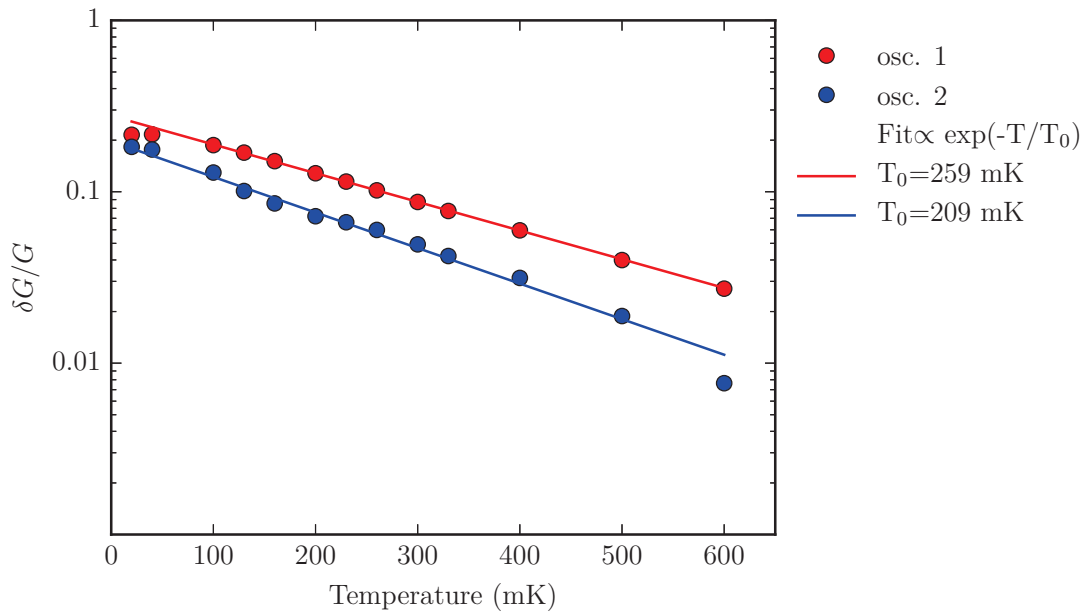


Figure 5.7: Evolution of the visibility of the osc. 1 and 2 extracted from fig. 5.6 as a function of temperature.

indicates the decoherence rate is proportional to $1/T$ which means that $l_\phi \propto 1/T$ [Han01; Rou08b; Yam12]. From this relation, we can calculate the coherence length at any temperature using the relation $\frac{T}{T_0} = \frac{L}{L_\phi(T)}$ where L is the length of our TCW, $40 \mu\text{m}$, and $T_0 = 235 \text{ mK}$ (we take the average of the T_0 extracted for osc. 1 and osc. 2). As can be seen in fig. 5.7, the first two points at 20 mK and 50 mK deviate from the linear behavior. This observation allows us to estimate the electronic temperature of our device to about 60 mK . At a temperature of 60 mK , the coherence length should be on the order of $(40 \mu\text{m}) \times \frac{235}{60} = 156 \mu\text{m}$.

5.1.3 Comparison to previous experiment

We have seen in chapter 2 that our collaborators at university of Tokyo used TCW to operate their flying qubit [Yam12]. In their experiment, they used short TCW of $2 \mu\text{m}$ which they characterized at a temperature of 2.2 K . We briefly present the results they obtained in order to check the consistency of our results. Contrary to our device, they had the possibility to inject the current either in the wire $|\uparrow\rangle$ or in the wire $|\downarrow\rangle$. The currents measured at the output of the TCW as a function of the voltage applied to the tunnel gate in both cases are presented on the left panel in fig. 5.8. Their device shows a behavior similar to ours, with three distinct regimes (single wide wire, tunnel coupled, separated wires) and antisymmetric oscillations of the currents that clearly appear. On the right panel, the oscillations extracted from the raw data are plotted. They are extracted using the procedure described previously by subtracting a background obtained by smoothing the raw data. The amplitude of the oscillations also represents a fraction of the total current. They determined that there were two channels in each wires and one pair effectively tunnel coupled. Therefore, at zero temperature, the expected visibility should be on the order of 50% . However, at such a high temperature the visibility is limited to $\sim 2\%$. They estimated the coherence length of their device at a temperature of 70 mK to about $86 \mu\text{m}$. For our device at 70 mK , the coherence length should be $\sim 134 \mu\text{m}$. The order of magnitude is similar which seems to indicate that our observations are consistent with coherent tunneling of the electrons. It worths noting that they estimated the coherence length of their device by observing the temperature dependence of Aharonov-Bohm (AB) oscillations. Compared to the TCW where the two paths are not physically separated, the two paths of the AB interferometer are on contrary well separated. This device is therefore more sensitive to decoherence phenomena that can affect more one arm than the other such as gate voltage fluctuations [See01] which can lead to a reduction of the coherence length.

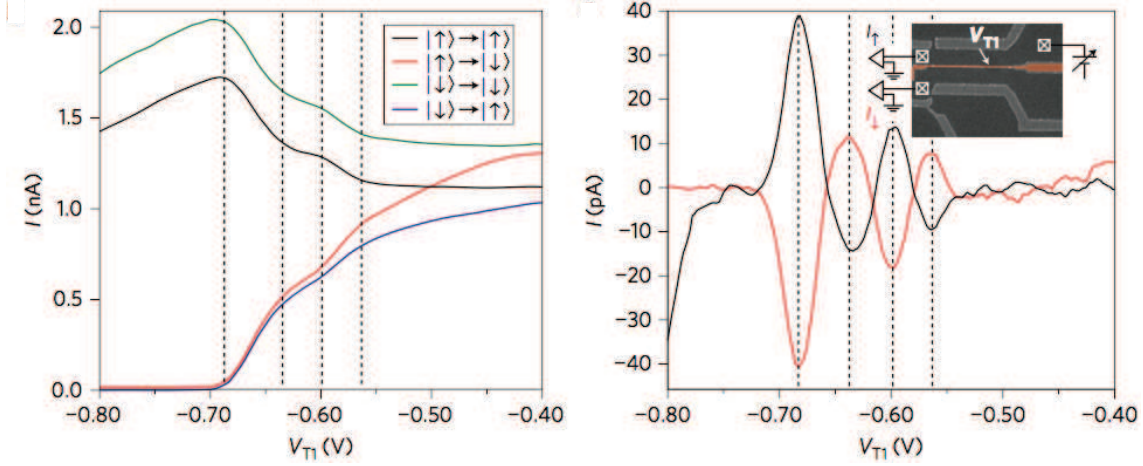


Figure 5.8: Left: measurements of the output current of the TCW used by Yamamoto et al. in [Yam12]. Their device allows to inject current either in the wire $|\uparrow\rangle$ (red and black curves) or in the wire $|\downarrow\rangle$ (green and blue curves). The bias is set at $50\ \mu\text{V}$ and the temperature is $2.2\ \text{K}$. Right: oscillations extracted from the raw data by subtracting a smooth background. The inset show a SEM picture of their device. I

5.2 Short voltage pulses

We now turn to the experiments using short voltage pulses of $100\ \text{ps}$. The pulses are generated by the AWG set at a sampling rate of $12\ \text{GS.s}^{-1}$, the repetition rate of the pulses is set to $6\ \text{GHz}$. We apply the modulation technique described in sec. 3.3.2 in order to perform a Lock-in detection. The amplitude of the pulses at the sample level is $\sim 220\ \mu\text{V}$, corresponding to about 6 electrons excited per pulse. First, let us compare a measurement obtained using short voltage pulses and one obtained using a DC bias of $20\ \mu\text{V}$ (low frequency Lock-in measurement). These two measurements taken at $250\ \text{mK}$ are presented in fig. 5.9. It appears that the visibility of the oscillations of conductance is strongly reduced when short pulses are used.

The reduction of visibility is mainly due to the overheating generated by the pulses. To probe the dynamical modification of the interference pattern, it would be highly desirable to investigate a regime from less than one electron excited per pulse to a few electron as in the present case. Therefore, one has to find a way to reduce this overheating without having to reduce too much the amplitude of the voltage pulse. This can actually be done by using a duty cycle. The duty cycle consists in reducing the repetition rate of the voltage pulses as illustrated in fig. 5.10. The duty cycle reduces the average voltage seen by the sample. Assuming a triangular shape for the voltage pulses, the average voltage \bar{V} is given by:

$$\bar{V} \simeq \frac{1}{4} V_P \times (\text{duty cycle}). \quad (5.4)$$

where V_P is the pulse amplitude. The factor $1/4$ is given by the ratio of the area occupied by the pulse (without duty cycle but with the Lock in modulation) compared to the case of

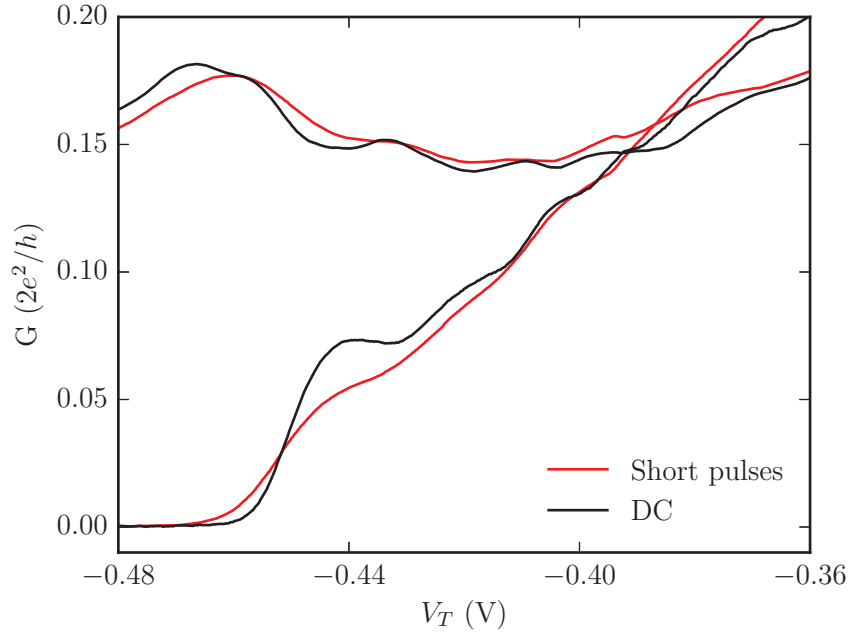


Figure 5.9: Comparison between DC bias (low frequency Lock-in, amplitude $20 \mu\text{V}$) and short voltage pulses (amplitude $220 \mu\text{V}$, repetition rate of 6 GHz). These measurements are taken at 250 mK .

a constant voltage of amplitude V_P . Without duty cycle and for $V_P = 220 \mu\text{V}$, the average voltage seen by the sample is $\bar{V} = 55 \mu\text{V}$. Therefore at 250 mK , $e\bar{V} > k_B T$ leading to a smearing of the oscillations.

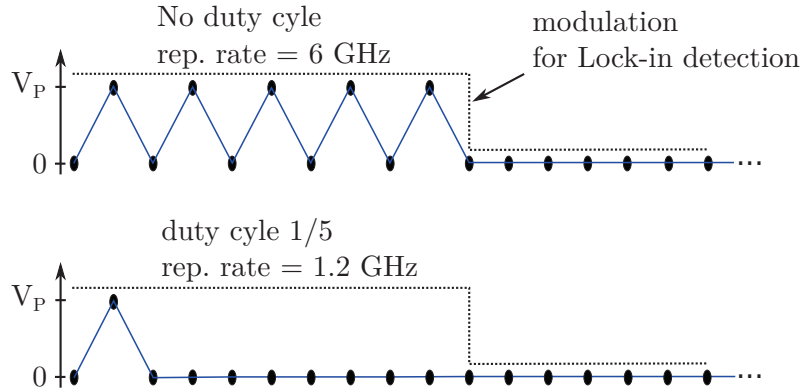


Figure 5.10: Schematics of the waveforms generated by the AWG without duty cycle and with a duty cycle of $1/5$. For a sampling rate of 12 GS.s^{-1} (corresponding to 83.3 ps between each black dots), the repetition rate without duty cycle is 6 GHz .

We have characterized the evolution of the visibility $\delta G/G$ obtained using the same

procedure as for the temperature dependence (see sec. 5.1.2) as a function of the duty cycle. The pulse amplitude was set at $220 \mu\text{V}$ and the measurements performed at a temperature of 250 mK . The result is presented in fig. 5.11. It appears that the visibility is well enhanced by the utilization of a duty cycle and reaches values comparable to the one obtained for DC measurements once the duty cycles reaches about $1/10$, reaching few percents at maximum at a temperature of 250 mK . Afterwards, the visibility does not evolve anymore.

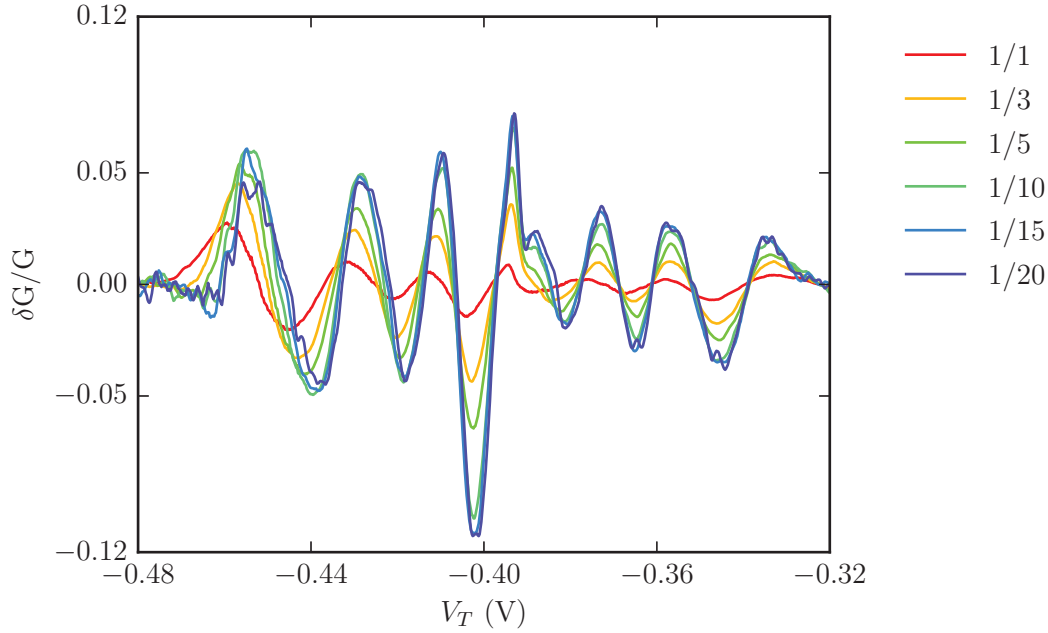


Figure 5.11: Evolution of the visibility $\delta G/G$ as a function of the duty cycle. The pulse amplitude is kept constant at $220 \mu\text{V}$, the data are taken at a temperature of 250 mK . The visibility increases up to a duty cycle of $1/10$ and then does not evolve anymore.

5.2.1 Temperature dependence

We have characterized the temperature dependence of the oscillations when short pulses are used. The configuration of the sample is similar to the one used for the DC experiments except that these results were obtained for a different cool down. We focus on the range 250 mK - 600 mK because the effects of the impurities at lower temperatures prevented the observation of oscillations. Following the discussion on the duty cycle, we have chosen a duty cycle of $1/10$. The amplitude of the voltage pulses was kept fixed at $220 \mu\text{V}$ (at the sample level) which corresponds to an average DC voltage of $5.5 \mu\text{V}$ such that $e\bar{V} < k_B T$. The visibility $\delta G/G$ is extracted using the procedure described in sec. 5.1.2. The evolution of the visibility $\delta G/G$ as a function of the temperature is shown in fig. 5.12. To quantify the decay rate of the visibility, we have plotted in fig. 5.13 the visibility of the first three oscillations as a function of temperature. The evolution of the osc. 1 and 2 obtained for

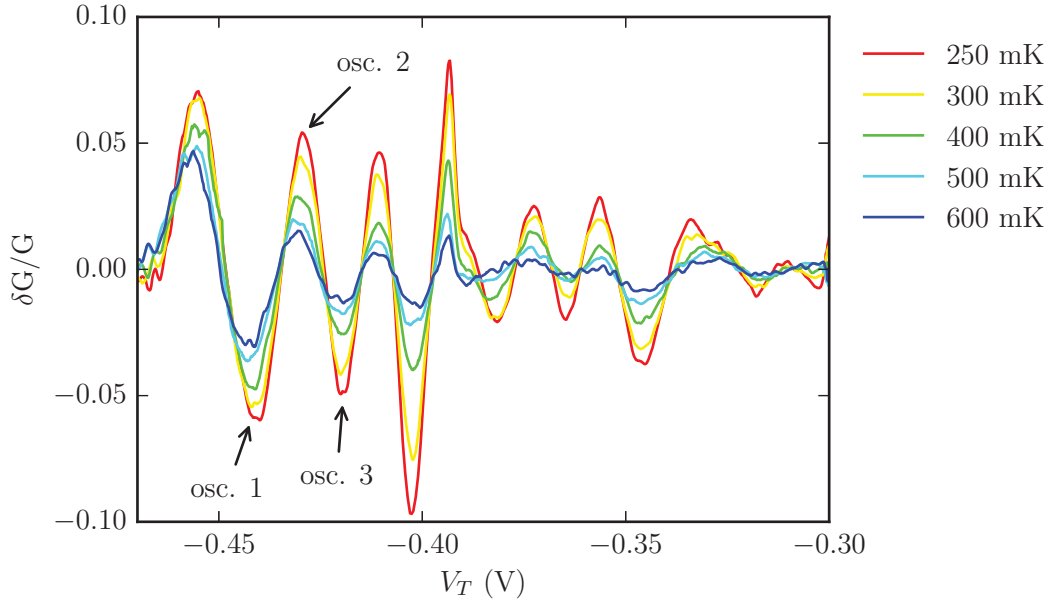


Figure 5.12: Evolution of the visibility $\delta G/G$ as a function of temperature when short pulses are used. The amplitude of the pulses is kept constant at $220 \mu\text{V}$ and the duty cycle is set to $1/10$.

the DC experiment are also plotted in order to facilitate the comparison. We present the first three oscillations because in this case, the behavior of the osc. 1 is significantly different compared to the others. At the present time we do not have a clear explanation for this difference. For the osc. 2 and 3 on the other hand, we find a behavior similar to the DC experiment. The decay rate is equal for both, $\sim 1/0.250 = 4 \text{ K}^{-1}$ and comparable to ones determined during the DC experiment: $1/0.260 = 3.8 \text{ K}^{-1}$ for the osc. 1 and $1/0.210 = 4.8 \text{ K}^{-1}$ for the osc. 2. About the absolute value of the visibility, putting the osc. 1 aside, short pulses and DC give comparable visibility.

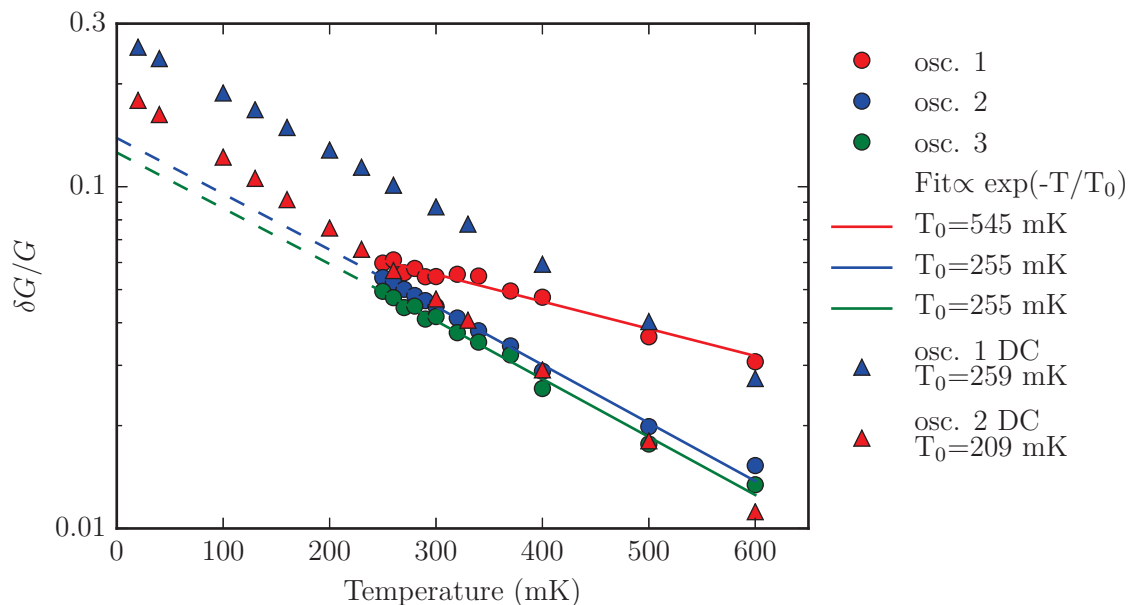


Figure 5.13: Evolution of the visibility of first three oscillations as a function of temperature when short voltage pulses are used (circles). The results obtained for the DC experiment are also shown (triangles).

5.3 Coulomb blockade

We have seen previously in sec. 5.1 that the conductance of the TCW at very low temperature is altered by the presence of impurities. These impurities, which can be seen as quantum dots, modify the conductance of the wires due to Coulomb blockade as illustrated in fig. 5.14. Depending on the location of the impurities and the configuration of the potential formed by the electrostatic gates, the Coulomb blockade can be easily identified through the development of Coulomb peaks at very low temperature. For some cool downs and for a sample configuration similar the one used for the experiments described above, we have identified such Coulomb peaks. It turns out that this Coulomb peaks also leads to anti-phase oscillations of conductance between the two wires. A measurement of conductance taken at 20 mK showing Coulomb peaks is presented in fig. 5.15. Two Coulomb peaks labeled C.P. 1 and C.P. 2 clearly appear on the conductance trace of the wire $|\downarrow\rangle$. Between the two peaks, the conductance almost drops to zero, we identify this region as the valley 1. The conservation of the current leads to oscillations of conductance between the two wires due to this succession of peaks and valleys. The phenomena of Coulomb blockade in quantum conductor has been extensively studied in literature. In particular, it has been shown that the lineshape of a Coulomb is given by well know functions. In the case where the barriers potential defining the trap (l and r in fig. 5.14)

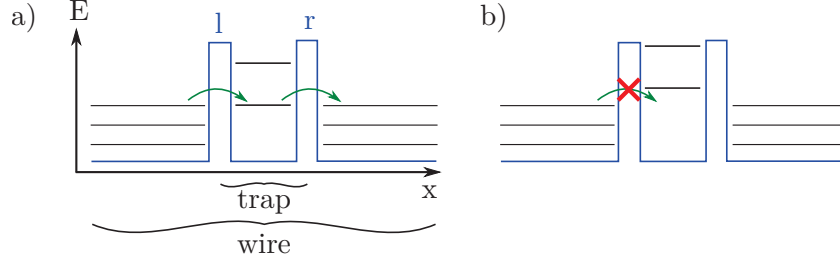


Figure 5.14: Schematic illustrating the Coulomb blockade. Two situations can occur when the electrons which propagate along the wire encounter the potential trap formed by the impurities: a) the energy levels of the trap are aligned with the channels of the wire and the electron can pass. b) The energy level of the trap are not align with the ones of the wire and the electrons can not pass: this is the Coulomb blockade. By varying the voltage applied on the tunnel gate, the characteristic of the trap are modified and the system undergoes a succession of passing and blocked state which results in the formation of Coulomb peaks as the ones shown in fig. 5.15.

have a small conductance: $G_l, G_r \ll e^2/h$, the lineshape is given by [Bee91]¹ :

$$G \propto \frac{\Delta E}{4k_B T} \cosh^{-2} \left(\frac{\delta}{2k_B T} \right) \quad (5.5)$$

where ΔE is the energy level splitting of the trap formed by the impurities and $\delta = e(C_G/C)|V_{T,res} - V_T|$. $C = C_l + C_r + C_G$ is the total capacitance which is the sum of capacitances across the barriers (l and r in fig. 5.14), C_l and C_r , and a capacitance between the dot and the tunnel gate, C_G . In fig. 5.16, we present a zoom on the Coulomb peaks observed on the conductance trace of the wire $|\downarrow\rangle$. These peaks are fitted using eq. 5.5. For the first peak, the agreement between the fit and the data is really good which confirms that this is indeed a Coulomb peak. The second peak is partly hidden but the visible part also agrees well with the fit.

At higher temperature, these Coulomb peaks lead to oscillations of conductance that are very similar to the one described previously. The main difference is the higher visibility of the «Coulomb» oscillations at a given temperature. In fig. 5.17, a measurement of these «Coulomb» oscillations and one of the «Tunnel» oscillations are plotted together. Both measurements are taken at a temperature of 200 mK using a DC bias of 20 μ V.

Let us now apply the same procedure as before to obtain the evolution of the visibility $\delta G/G$ as a function of the temperature of the oscillations of conductance due to Coulomb blockade. We extract the visibility of the first oscillation due to the Coulomb peak 1 (C.P. 1) and the second oscillation due to the valley 1. The results are presented in fig. 5.18, where we also show the evolution of the visibility of the osc. 1 and 2 obtained previously for the DC experiment. First of all, the global behavior is similar in both cases with an exponential decay of the visibility. However the visibility of the Coulomb

¹ In the other limit, the lineshape is given by a Lorentzian [Sto85].

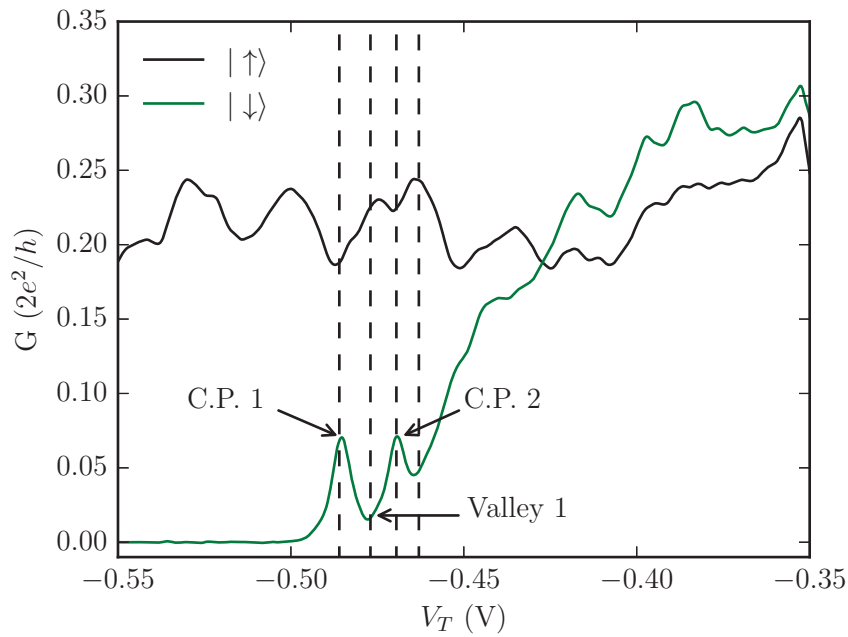


Figure 5.15: Conductance traces of the TCW in presence of Coulomb blockade. Measurements taken at 20 mK.

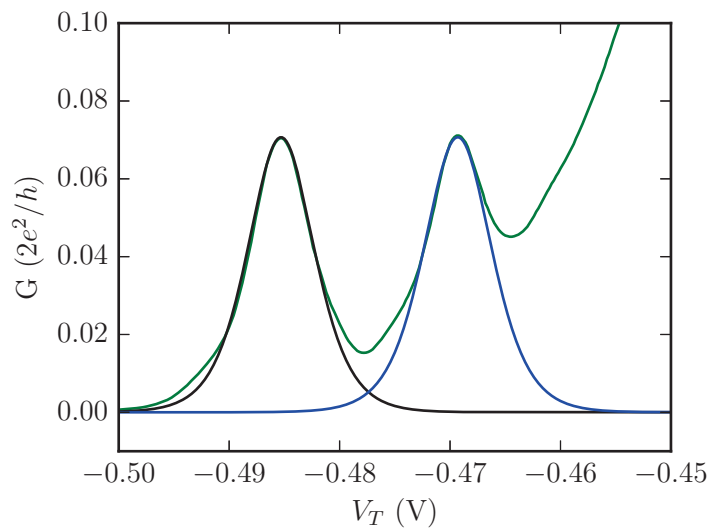


Figure 5.16: Zoom on the Coulomb peaks observed on the conductance trace of the wire $|\downarrow\rangle$. The fit are obtained using eq.5.5.

oscillations saturate well before the visibility of tunnel oscillations. It appears also that the decay rates of the Coulomb oscillations are slower than the tunnel oscillations: about $1/0.300 = 3.3 \text{ K}^{-1}$ for the Coulomb oscillations to be compared to $1/0.250 = 4 \text{ K}^{-1}$ for the first experiments (either with a DC bias or short pulses). However, the orders of magnitude are still comparable.

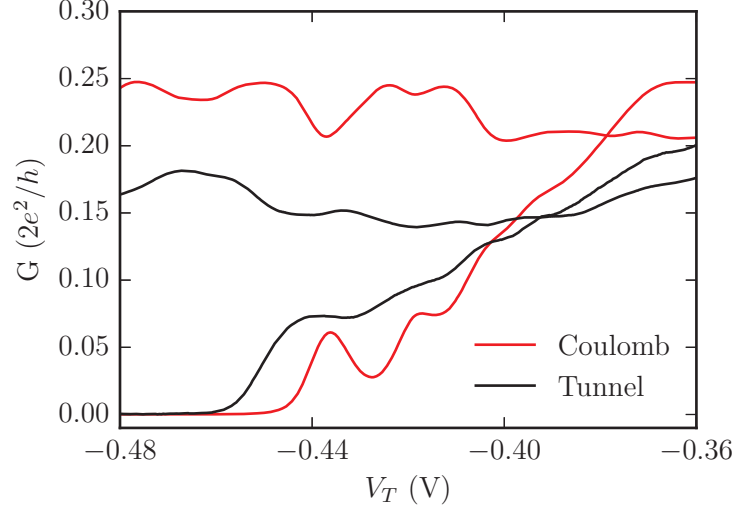


Figure 5.17: Comparison between the first observed oscillations (black curves) of conductance and the Coulomb oscillations (red curves). Both measurements are taken at 200 mK using a DC bias of $20 \mu\text{V}$.

It is clear that both phenomena lead to similar features in the conductance measurements. At present, we cannot exclude that the oscillations observed in our first experiments using DC bias and short voltage pulses are due to Coulomb blockade. On the other hand, the comparison with the results of our colleagues of the University of Tokyo indicates that our observations are consistent with coherent tunnel oscillations, in term of visibility and of coherence length. One way to differentiate the tunnel oscillations from the Coulomb oscillations consists in switching the injection of the current from the wire $|\uparrow\rangle$ to the wire $|\downarrow\rangle$ [Yam12]. If the oscillations are due to coherent tunneling of the electrons, the conductance trace of the wire $|\uparrow\rangle$ ($|\downarrow\rangle$) when the electrons are initially injected into the wire $|\uparrow\rangle$ should be identical to the conductance trace of the wire $|\downarrow\rangle$ ($|\uparrow\rangle$) when the electrons are initially injected into the wire $|\downarrow\rangle$. This is indeed what was observed by our collaborators of university of Tokyo as shown on the left panel in fig. 5.8. On the other hand, if the oscillations are due to Coulomb blockade, this symmetry does not exist. If the conductance trace of the wire $|\uparrow\rangle$ exhibits a Coulomb peak accompanied by a dip on the conductance trace of the wire $|\downarrow\rangle$ when the electrons are initially injected into the wire $|\uparrow\rangle$, it is still the case when the electrons are initially injected into the wire $|\downarrow\rangle$. Therefore, the conductance trace of the wire $|\uparrow\rangle$ ($|\downarrow\rangle$) differs from the conductance trace of the wire $|\downarrow\rangle$ ($|\uparrow\rangle$) when the injection is switched. This check was not possible with our sample since the design

was optimized to create a smooth connection from the ohmic contact to the TCW using a tapered shape allowing to inject the current only in the wire $|\uparrow\rangle$. We are currently working on a new generation of device whose design will allow to switch the injection and also to change the length of the TCW (see fig. 5.19). Therefore we will access the regime where the mean free path is longer than the TCW in order to reduce the probability to find impurities along the wires such that Coulomb blockade should not occur.

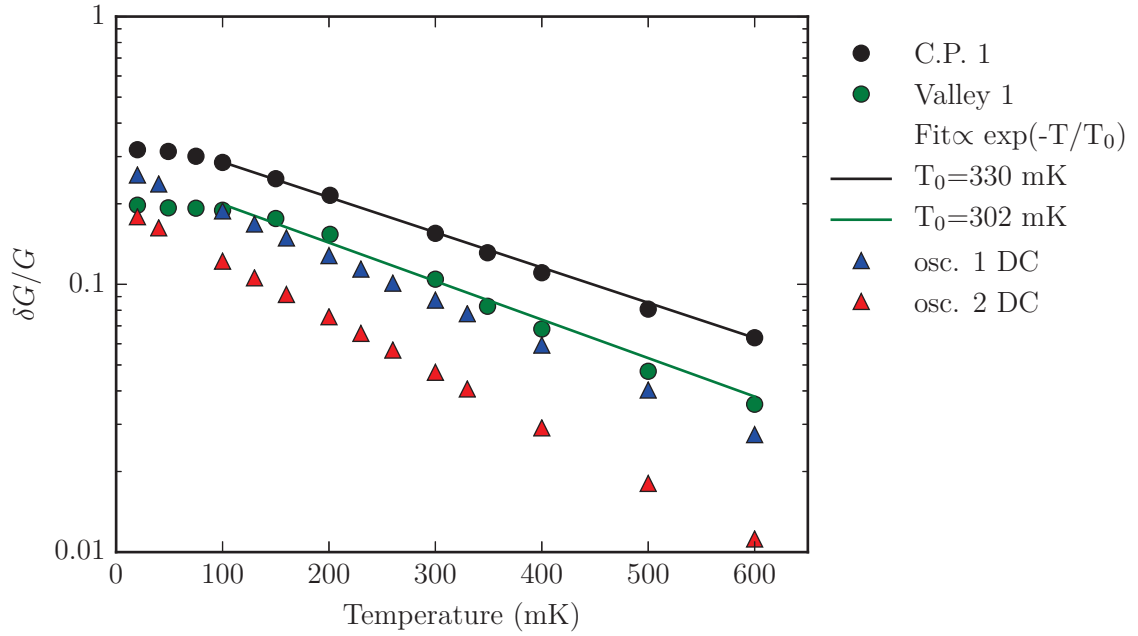


Figure 5.18: Temperature dependence of the visibility of the first oscillation due to the Coulomb peak 1 (C.P. 1) and the second oscillation due to the Valley 1. The evolution of the visibility of the osc. 1 and 2 obtained previously for the DC experiment are also shown.

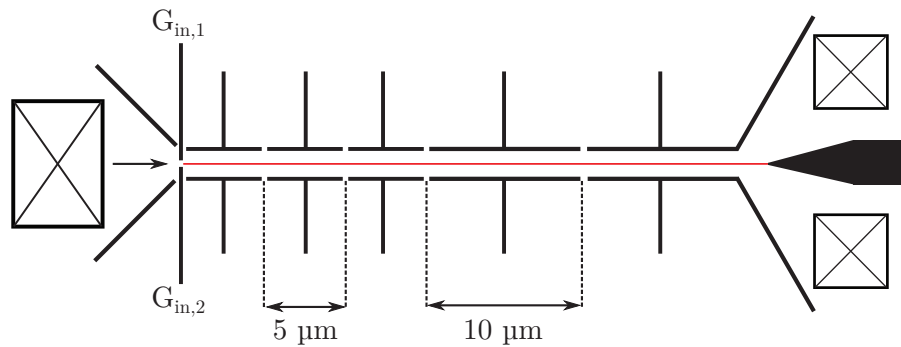


Figure 5.19: Schematic of the new sample allowing to tune the length of the tunnel coupled wires. The length will be adjustable by step of $5 \mu\text{m}$ on the first $15 \mu\text{m}$ and then by two additional steps of $10 \mu\text{m}$. It will be also possible to switch the injection of the electrons between the wires depending on which of the gate $G_{in,1}$ or $G_{in,1}$ is polarized.

5.4 Preliminary experiment on the mapping of the tunneling

One envisaged experiment when we started this project was to map the coherent tunneling of the wave-packet as a function of time. To do so, one would excite a wave-packet by applying a voltage pulse on an ohmic contact, let it propagate in the TCW for a certain amount of time and then pulse the tunnel gate with a negative voltage pulse such that the tunnel barrier becomes high enough to forbid the tunneling. Therefore it should be possible to reconstruct the probability of presence of the wave-packet in each wire of the TCW as a function of time as schematized in fig. 5.20. The success of this experiment relies on the fact that the transition from a certain tunnel coupling to a forbidden tunneling (the change of the voltage applied on the tunnel gate) is fast compare to the time needed by the wave-packet to travel through the TCW. The sample was designed by taking into account a Fermi velocity of $2 \times 10^5 \text{ m.s}^{-1}$, so we estimated the time of flight of the pulse through the TCW of $40 \mu\text{m}$ to 200ps . However, our measurement of the velocity of the pulse definitely shows that this is not case. Even when the velocity is reduced by the confinement, the pulse needs only 45 ps to travel through the TCW. Since the rise time of the AWG 7122b is on the order of 65 ps , this regime is at present not accessible. Nevertheless, preliminary experiments presented in this section allow us to gain important informations for the next generation of experiments. Moreover, it allows us to confirm the high velocity of the voltage pulse.

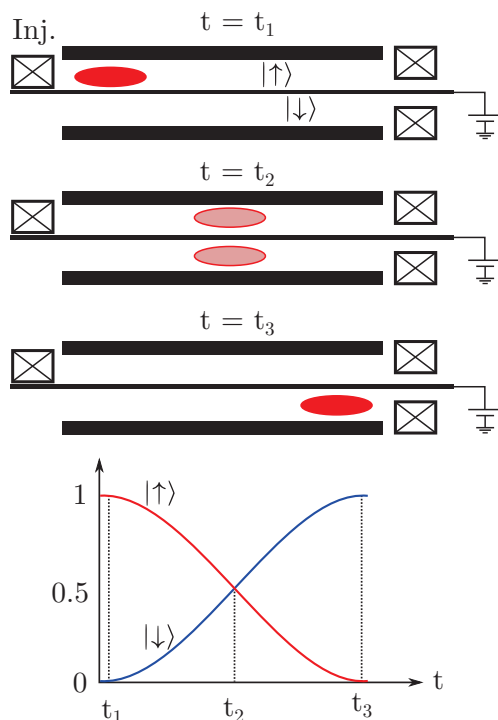


Figure 5.20: Top: schematic of the propagation of the wave packet in the TCW. Bottom: sketch of the evolution of the probability of presence of the wave-packet inside each wire as a function of time.

5.4.1 Transfer of the wave-packet between the wires

As a proof of concept, we show that it is possible to measure in a time resolved manner the transfer of the wave-packet from the wire $|\uparrow\rangle$ to the wire $|\downarrow\rangle$. The principle is similar to the experiment presented in chapter 4 but using the tunnel barrier instead of the QPC. The DC voltage applied on the tunnel gate is set to ~ -0.51 V such that the tunneling from the wire $|\uparrow\rangle$ to the wire $|\downarrow\rangle$ is forbidden as shown in fig. 5.21. A short positive voltage pulse of about 20 mV of amplitude is applied on the tunnel gate to lower the tunnel barrier. This amplitude corresponds to the change of gate voltage necessary to cover the region delimited by the black rectangle in fig. 5.21. If this lowering of the barrier is synchronized with the passage of the wave-packet, then the current measured at the output of the wire $|\uparrow\rangle$ should decrease and the current measured at the output of the wire $|\downarrow\rangle$ should increase from 0 to a given value.

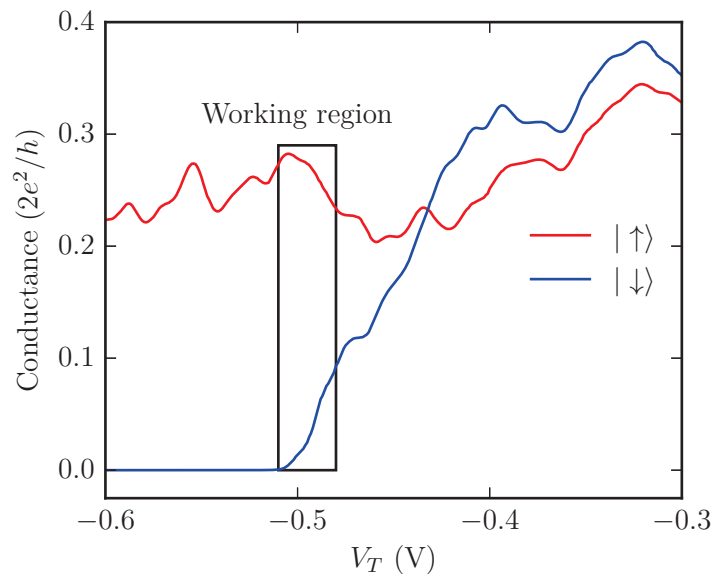


Figure 5.21: Conductance traces of the TCW illustrating the working region allowing to perform time resolved measurements of the transfer of the wave-packet.

The time resolved measurements of the transfer of the wave-packet for several amplitudes of the voltage pulse applied on the ohmic contact ranging from nearly 0 to ~ 450 μ V are presented in fig. 5.22. The measurements of the wire $|\uparrow\rangle$ are shifted such that their baseline coincide to facilitate the comparison. As expected, a peak on the output current of the wire $|\downarrow\rangle$ appears accompanied by a dip on the output current of the wire $|\uparrow\rangle$. The fact that the amplitude of the peak and the dip are different is directly related to the difference of change of conductance of each wire in the working region delimited by the black rectangle in fig. 5.21. The conductance of the wire $|\downarrow\rangle$ changes almost twice as fast as the conductance of the wire $|\uparrow\rangle$ as a function of V_T which is comparable to the difference of amplitude between the peak and the dip.

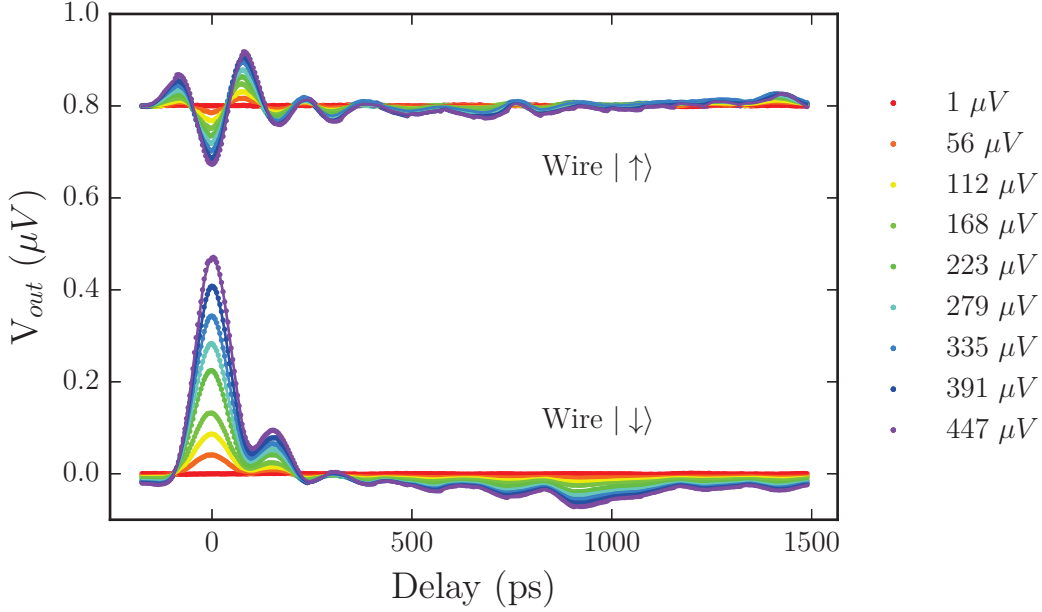


Figure 5.22: Time resolved measurements of the transfer of the wave-packet for different amplitudes of the voltage pulse applied on the ohmic contact. The measurements are taken at 20 mK, the resolution is 4 ps per point.

5.4.2 Comparison to the calculated convolution

Similarly to the previous experiments using the pulsed QPC, the output signals measured as a function of time should give the convolution of the voltage pulse applied on the ohmic contact and the pulse applied on the tunnel gate. In fig. 5.23, the in-situ measurements for each wire using the tunnel gate are plotted together with the calculated convolution (as done in sec. 4.1.2). For the wire $|\downarrow\rangle$, the agreement between the peak and the calculated convolution is very good. For the wire $|\uparrow\rangle$, at a first sight the agreement is not so good. However, as for the measurements using the QPC, an oscillating signal clearly appears. It seems that the peak and the dip are modified by this oscillating signal making them a bit narrower compared to the calculated convolution. Since the dip on the output current of the wire $|\uparrow\rangle$ has a smaller amplitude, it is more affected by this parasitic signal. The Fourier transform of the signal presented in fig. 5.24 reveals a peak centered on ~ 6 GHz as for the QPC experiment. Here again, the parasitic signal mentioned previously could be at origin of this oscillation. Contrary to the QPC experiment, there is no peak centered around 10 GHz. It is possible that this signal is «averaged» due to the long length of the tunnel gate. Indeed, contrary to the QPC whose spatial width is about 300 nm (taking into account the depleted region around the QPC), the tunnel gate is 40 μm long resulting in a spatial averaging which could mask this 10 GHz signal.

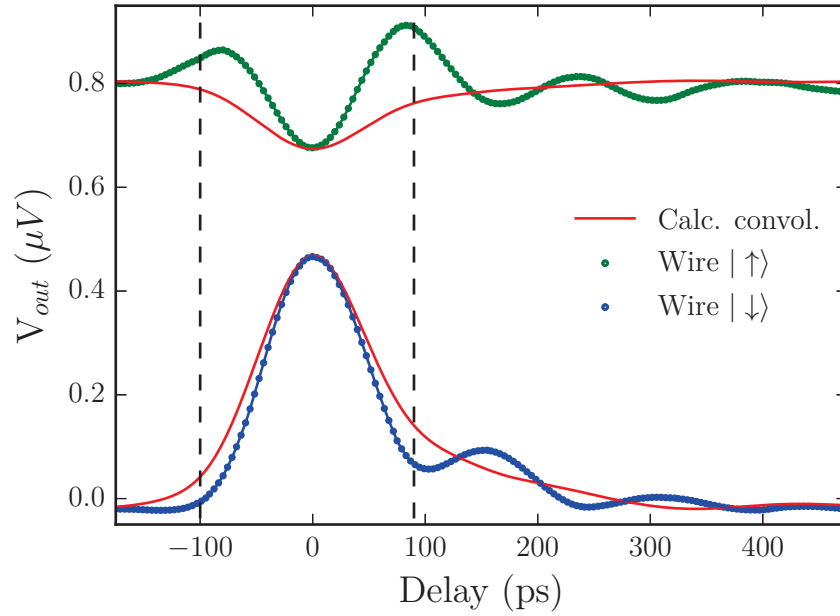


Figure 5.23: Comparison between the in-situ measurement using the tunnel gate and the calculated convolution.

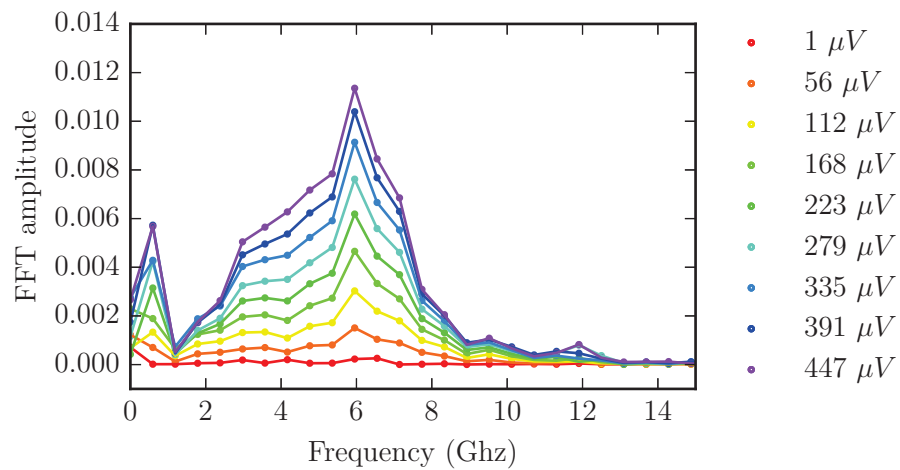


Figure 5.24: Fourier transform of the in-situ measurements of the wire $|\downarrow\rangle$.

5.5 Confirmation of the velocity

The time resolved measurement of the transfer of the wave-packet allows also to determine its velocity. Similarly to the measurement using the QPC, we have characterized the intrinsic delay between the RF line connected to the ohmic contact and the RF line connected to the tunnel gate. Due to the difference in length between the lines (see Appendix D) and the attenuators (see Appendix A), the pulse applied on the ohmic contact is retarded by 70 ± 10 ps. In fig. 5.25, the time resolved measurement of the transfer of the wave-packet is plotted as a function of the initial delay. We remind that an initial delay of 0 ps corresponds to the situation where the pulse applied on the tunnel gate and the pulse applied on the ohmic contact are sent synchronously in their respective RF line. A positive initial delay means that the pulse applied on the tunnel gate is generated after the pulse applied on the ohmic contact. The maximum of signal is obtained for an initial delay of 95 ± 2 ps. It seems reasonable to consider that this maximum of signal is obtained when the pulse (its maximum) is located in the middle of the TCW and coincides with the opening of the tunnel barrier. Therefore, the time of flight of the pulse from the ohmic contact to the middle of the TCW is $\tau_{F2} = 25 \pm 12$ ps. The corresponding distance is $28 \pm 1 \mu\text{m}$. The measured velocity is then:

$$v_P = 1.12 \pm 0.6 \times 10^6 \text{ m.s}^{-1} \quad (5.6)$$

This value is in good agreement with the value determined previously of $0.91 \pm 0.29 \times 10^6 \text{ m s}$ measured previously using the QPC when the tunnel gate is polarized at -0.5 V and hence confirms our finding.

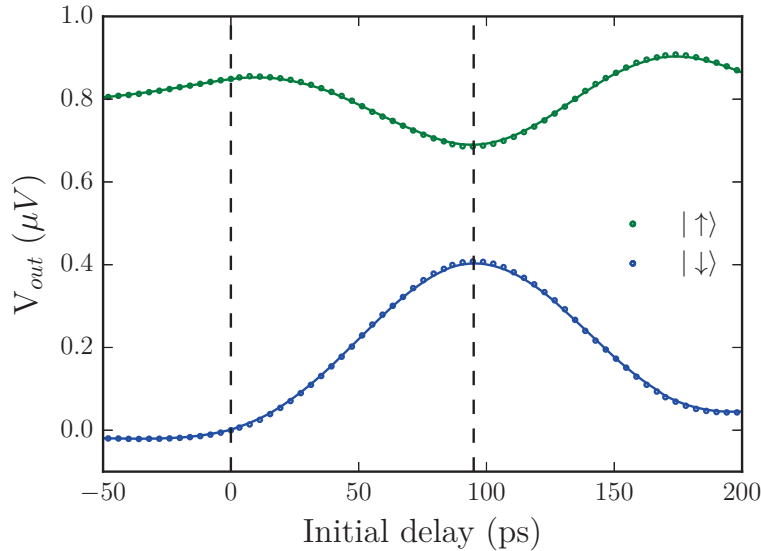


Figure 5.25: Time resolved measurement of the transfer of the wave-packet as a function of the initial delay. The maximum of signal is obtained for an initial delay of 95 ps. The resolution is 4 ps per point.

5.6 Conclusion

In this chapter we have presented the results on the investigation of a 40 μm long electronic two path interferometer based on tunnel coupled wires. We started with DC measurements that allowed us to characterize the device and to observe antisymmetric oscillations of conductance that could be the signature of the coherent tunneling of the electrons between the tunnel coupled wires. We have characterized the temperature dependence of the visibility of the oscillations which shows an exponential decay as expected for this phenomena. By comparing our results to the results of our collaborators from the University of Tokyo, we have shown that the observed oscillations could be indeed tunnel oscillations. We have then compared the results obtained with short pulses of 100 ps to the DC measurements. By using a duty cycle we have reproduced the behavior obtained with the DC bias. The temperature dependence of the oscillations using short pulses is similar to the one using a DC bias except for the first oscillation which remains unclear at the present time.

We have identified another process producing antisymmetric oscillations of conductance: the Coulomb blockade due to the presence of impurities along the TCW. So far, we can not exclude that the oscillations observed in our first measurements using DC bias or short voltage pulses are also due to Coulomb blockade. The temperature dependence of the «Coulomb» oscillations is comparable to one of the «tunnel» oscillations. The main difference lies in the higher visibility of the Coulomb oscillations and slightly slower decay rates. It is necessary to change the design of the device to have the possibility to inject the current in both wires in order to discriminate the Coulomb oscillations from the tunnel oscillations.

Finally we have presented preliminary results on the mapping of the tunneling of the wave packet generated by the voltage pulse. Our result on the velocity of the voltage pulse shows that we are at the moment limited by the performance of the AWG to perform such an experiment. However, we have shown that we can measure in a time resolved manner the transfer of the wave packet between the two wires. It seems challenging to meet the conditions to perform the time resolved measurement of the coherent tunneling of the wave packet. In our case, the wave packet spends only 45 ps in the TCW. Therefore, it would be necessary to change the voltage applied on the tunnel gate with a characteristic time much shorter than 45 ps. This can be done through the use of GaAs photoconductive switch allowing to produce a voltage step with a picosecond rise time [She95]. This preliminary experiment on the transfer of the wave packet also allowed us to confirm the high velocity of the voltage pulse determined previously using the pulsed QPC.

CHAPTER 6

Conclusion and perspectives

During my PhD, I have investigated the propagation of a short voltage pulse in a quasi 1D system formed in a two dimensional electron gas using electrostatic gates. By adapting a technique proposed by Kamata et al. [Kam09] we have been able to perform time resolved measurements of the voltage pulse at the sample level. These measurements allowed us to determine the velocity of the voltage pulse through the sample. The measured velocity is much higher than the bare Fermi velocity contrary to our initial expectation. For our structure, the Fermi velocity should be on the order of $2 \times 10^5 \text{ m.s}^{-1}$. The observed propagating velocity of the voltage pulse is as high as $12 \times 10^5 \text{ m.s}^{-1}$. The origin of this high velocity is due to the fact that the voltage pulse creates a plasmonic excitation. In this case, the Coulomb interaction at the origin of this collective behavior leads to a strong modification of the naive picture of non-interacting electrons. The measured velocity is indeed in very good agreement with the plasmon velocity for a gated two dimensional electron gas calculated using Boltzmann kinetic equation.

We then have shown that it is possible to control the velocity of the pulse by modifying the confinement potential due to the electrostatic gates. We have been able to reduce the velocity of the pulse by 30%. In principle it should be possible to reduce the velocity on a much broader range, but the design of the sample, which was not optimized for such an experiment, prevented us to explore this regime. Our experimental results show a good agreement with a theoretical approach based on the work of Matveev and Glazman [Mat93] which allowed us to calculate the velocities of interacting electrons in a quasi 1D wire containing an arbitrary number of conducting channels. The electron-electron interactions lead to dramatic modifications of the transport properties. More specifically, it leads to the existence of charge modes and spin modes. Among the charge modes, there is one fast charge mode which propagates with the plasmon velocity and involves all the conducting channels. The others charge modes are the so-called «slow» charge modes. Each slow charge mode involves mainly one conducting channel and propagates with a velocity slightly higher than the Fermi velocity of this channel. Finally, each spin mode involves exactly one conducting channel and propagates with the Fermi velocity corresponding to this channel. Previous experiments using momentum-resolved tunneling between a pair of 1D wires [Aus05], or between a 1D wire and a two-dimensional electron gas [Jom09] have successfully

probed the existence of a charge mode and a spin mode. The authors of ref. [Aus05] should have observed a fast charge mode in addition to the slow charge mode but this fast charge mode has stayed elusive. It seems that our time resolved measurement allows for the first time to detect this fast charge mode [Des10]. On the other hand, with our time resolved measurements we have not been able to observe the slow charge modes. In principle, it should be possible to observe these slow charge modes but the presence of a parasitic signal in our measurements probably masked this signal. The spin modes are not detectable using this technique as they do not carry any net charge. These results encouraged us to design a new sample in order to reach the single channel regime and to observe the different charge modes.

We then presented transport measurements on a 40 μm long electronic two path interferometer based on tunnel coupled wires (TCW). The TCW could be used to detect new interference effects when short voltage pulses are injected into it. Our measurement of the velocity of the pulse indicates that at the present time we can not access the required regime as the temporal width of the pulses generated by the AWG is longer than their time of flight through the TCW. Nevertheless, it is important to verify that this system allows to observe coherent tunneling of the injected electrons. By varying the tunnel barrier between the two wires it is possible to control the probability of presence of an electron in each wire. Modifying the tunnel barrier leads to a periodic variation of this probability of presence which gives rise to antisymmetric oscillations of the conductances of the two wires. These antisymmetric oscillations of conductance are the signature of the coherent tunneling of the electrons. We have indeed observed antisymmetric oscillations of conductances that could be due to coherent tunneling. However, we have identified another phenomena, the Coulomb blockade due to impurities present along the wires, which also leads to antisymmetric oscillations of conductance. So far we can not clearly discriminate between these two phenomena. We are planning to realize a new device offering this possibility and allowing to tune the length of the TCW.

Finally, we have exposed preliminary results on the time resolved mapping of the coherent tunneling of a wave packet excited by a short voltage pulse. Here again, due to the high velocity of the pulse, we are limited by the performance of the AWG to really perform such an experiment. This first attempt is encouraging and we are confident that in the near future it should be possible to track in a time resolved manner the coherent tunneling of a wave packet. Thanks to these measurements we have also confirmed the high velocity of the voltage pulse.

This topic of fast quantum electronic is only in its early stages. Important achievements have already been done such as the realization of a single electron source using short Lorentzian voltage pulses. Working in the GHz regime and beyond will allow to study the dynamical aspects of quantum mechanics that were not accessible before. A variety of exciting experiments are now conceivable, from the study of intriguing interference effects, to the realization of new schemes to manipulate single electrons using pulsed gates in the Quantum Hall regime [Gau14c], via time resolved measurements of the coherent evolution of a propagating wave packet in various system. These experiments are very challenging from an experimental point of view, even the latest RF equipments shows their limitations.

Sophisticated opto-electronic devices such as GaAs photo-conductive switches allowing to produce voltage pulses or even voltage steps with characteristic times on the order of few picoseconds should unlock these limits. This solution is currently implemented in our lab and will allow to investigate this emerging physics which definitely sounds very promising.

APPENDIX A

Delay due to the attenuators

The attenuators inserted on the RF lines have different lengths, therefore they contribute to an additional delay. The attenuators installed on the RF line connected to the QPC and to the tunnel gate have the same length. The attenuators inserted on the RF line connected to the ohmic contact are slightly longer. To measure the delay due to the attenuators, first a reference is taken by directly measuring the output of the AWG with a sampling scope. The attenuators are then inserted at the output of the AWG which delay the pulse sent by the AWG. On each RF line, two attenuators are inserted:

- two attenuators of -30 dB on the RF line connected to the ohmic contact.
- two attenuators of -10 dB on the RF line connected to the tunnel gate.
- one attenuator of -10 dB and one of -6 dB on the RF line connected to the tunnel QPC.

Because of their strong attenuation, the attenuators connected to the ohmic contact are measured separately. The measurements are presented on fig.A.1. Each attenuator of -30 dB account for a delay of ~ 90 ps. The attenuators of -10 dB and -6 dB together account for a delay of ~ 156 ps. Therefore, the delay due to the attenuators is $180 - 156 = 24$ ps.

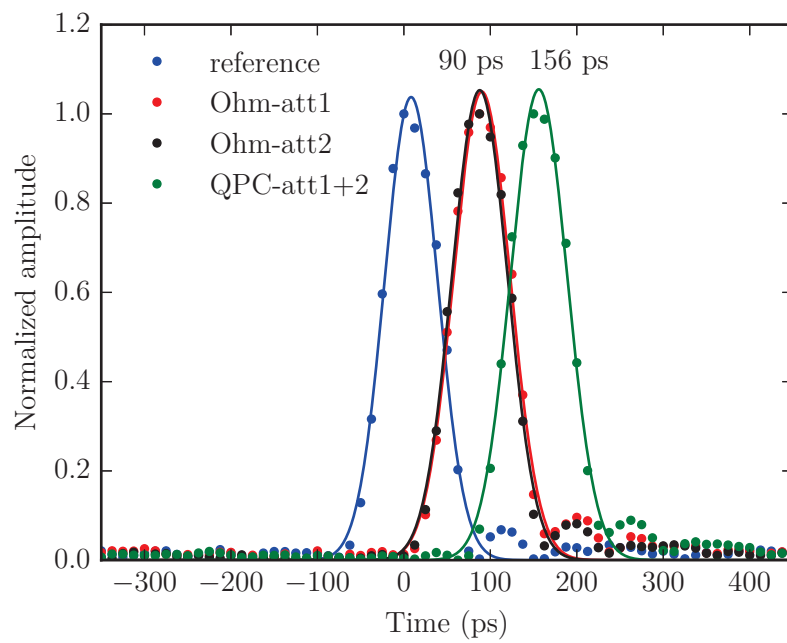


Figure A.1: Measurement of the delay due to the attenuators. The data are fitted with a Gaussian to extract the peak position.

APPENDIX B

Effect of the confinement

Prior to the «high resolution» (2 ps per point) measurements presented in sec.4.4, we have performed a preliminary experiment with a resolution of 7 ps per point. The data are presented on fig.B.1. On the right panel , the same data are presented but shifted such that all the maximum are aligned to facilitate the comparison.

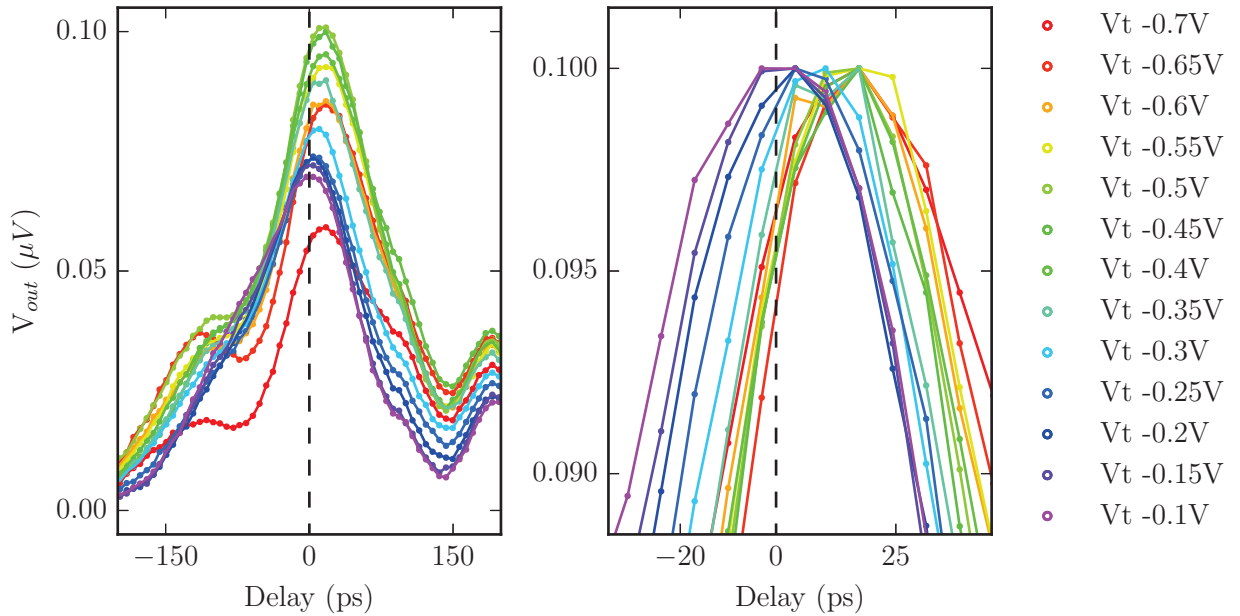


Figure B.1: Time resolved measurements of the voltage pulse as a function of the voltage applied on the tunnel gate. On the left, the raw data: the peak is moving towards longer delay as the voltage applied on the tunnel gate is made more and more negative. On right, a zoom on the same curves but shifted to facilitate the comparison. The resolution is 7 ps per point.

The shift of the peak position as a function of the applied on the tunnel gate is shown on

fig.B.2. Similarly to the high resolution measurements, the peak is shifted by 15 ps when the tunnel gate is varied from -0.1 V to -0.4 V. Then the delay is almost constant.

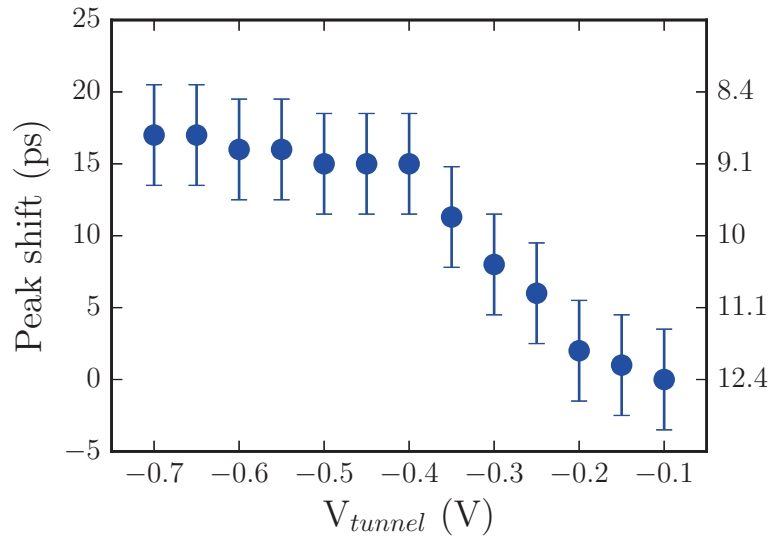


Figure B.2: Shift of the peak as a function of the voltage applied on the tunnel gate.

APPENDIX C

Simulation of the electrostatic potential for a low V_{tunnel}

We have simulated the electrostatic potential seen by the electrons when the voltage applied on the tunnel gate is -0.1 V. As a first approximation, this potential is fitted with an harmonic model to extract the Fermi velocities of the non interacting electrons as done in sec.4.5.

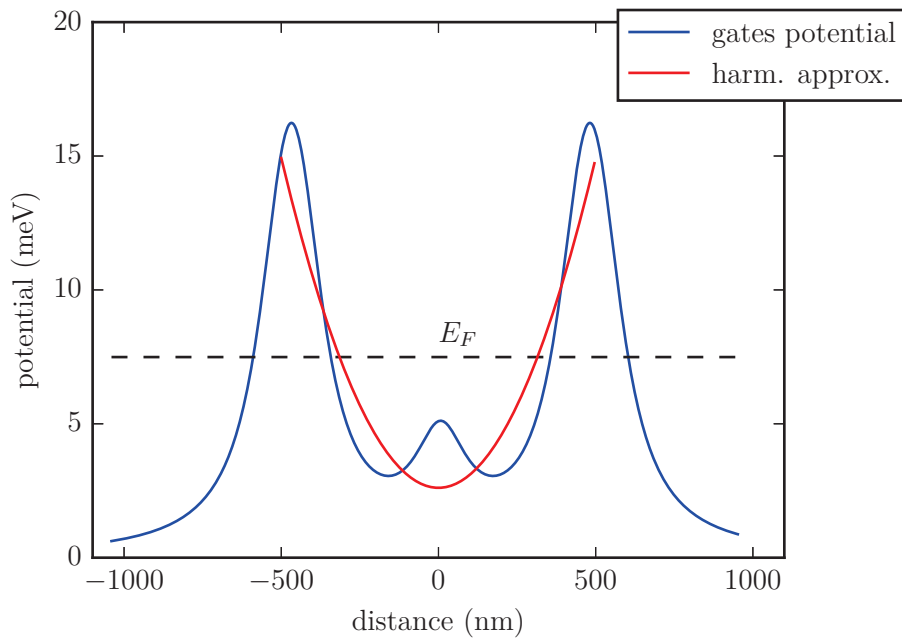


Figure C.1: Simulation of the electrostatic potential for $V_{tunnel} = -0.1$ V.

APPENDIX D

Intrinsic delay of the RF line connected to the tunnel gate

The intrinsic delay between the RF line connected to the ohmic contact and the RF line connected to the ohmic contact has also been measured by reflectometry. For one round trip, the delay between the two lines 92 ps as shown on fig.D.1. Therefore, the intrinsic delay between the lines is $92/2 = 46$ ps.

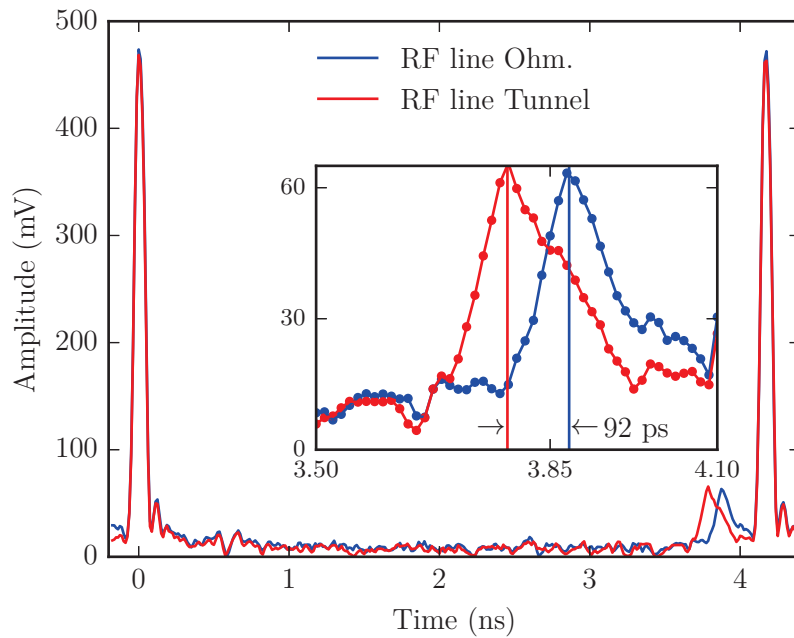


Figure D.1: Intrinsic delay of the RF lines connected to the tunnel gate compared to the RF line connected to the ohmic contact. The intrinsic delay is $92/2 = 46$ ps.

Bibliography

- [Ala90] Jesus A del Alamo and Cristopher C Eugster: ‘Quantum field-effect directional coupler’, *Applied Physics Letters* **56** (1990), 78, DOI: [10.1063/1.102657](https://doi.org/10.1063/1.102657) (see p. 11).
- [Alt82] B L Altshuler, a G Aronov, and D E Khmelnsky: ‘Effects of electron-electron collisions with small energy transfers on quantum localisation’, *Journal of Physics C: Solid State Physics* **15** (1982), 7367–7386, DOI: [10.1088/0022-3719/15/36/018](https://doi.org/10.1088/0022-3719/15/36/018) (see pp. 95, 99).
- [Ash76] Neil. W Ashcroft and N. David Mermin: *Solid state physics*, Brooks Cole, 1976 (see p. 43).
- [Ash92] R. C. Ashoori, H. L. Stormer, L N Pfeiffer, K W Baldwin, and K West: ‘Edge magnetoplasmons in the time domain’, *Physical Review B* **45** (1992), 3894–3897, DOI: [10.1103/PhysRevB.45.3894](https://doi.org/10.1103/PhysRevB.45.3894) (see p. 63).
- [Aus05] O. M. Auslaender: ‘Spin-Charge Separation and Localization in One Dimension’, *Science* **308** (2005), 88–92, DOI: [10.1126/science.1107821](https://doi.org/10.1126/science.1107821) (see pp. 88, 92, 119, 120).
- [Ave86] D. V. Averin and K. K. Likharev: ‘Coulomb blockade of single-electron tunneling, and coherent oscillations in small tunnel junctions’, *Journal of Low Temperature Physics* **62** (1986), 345–373, DOI: [10.1007/BF00683469](https://doi.org/10.1007/BF00683469) (see p. 14).
- [Bau14a] Tobias Bautze: ‘Towards quantum optics experiments with single flying electrons in a solid state system’, PhD thesis, 2014 (see p. 88).
- [Bau14b] Tobias Bautze, Christoph Süssmeier, Shintaro Takada, Christoph Groth, Tristan Meunier, Michihisa Yamamoto, Seigo Tarucha, Xavier Waintal, and Christopher Bäuerle: ‘Theoretical, numerical, and experimental study of a flying qubit electronic interferometer’, *Physical Review B* **89** (2014), 125432, DOI: [10.1103/PhysRevB.89.125432](https://doi.org/10.1103/PhysRevB.89.125432) (see pp. 2, 97).
- [Bee91] C. W J Beenakker: ‘Theory of Coulomb-blockade oscillations in the conductance of a quantum dot’, *Physical Review B* **44** (1991), 1646–1656, DOI: [10.1103/PhysRevB.44.1646](https://doi.org/10.1103/PhysRevB.44.1646) (see p. 108).

- [Ber00] A. Bertoni, P. Bordone, R. Brunetti, C. Jacoboni, and S. Reggiani: ‘Numerical simulation of quantum logic gates based on quantum wires’, *7th International Workshop on Computational Electronics. Book of Abstracts. IWCE (Cat. No.00EX427)*, 2000, 41–42, DOI: [10.1109/IWCE.2000.869912](https://doi.org/10.1109/IWCE.2000.869912) (see p. 10).
- [Ber15] Benoit Bertrand: ‘Long-range transfer of spin information using individual electrons’, PhD thesis, 2015 (see p. 21).
- [Blu07] M. D. Blumenthal, B. Kaestner, L. Li, S. Giblin, T. J. B. M. Janssen, M. Pepper, D. Anderson, G. Jones, and D. A. Ritchie: ‘Gigahertz quantized charge pumping’, *Nature Physics* **3** (2007), 343–347, DOI: [10.1038/nphys582](https://doi.org/10.1038/nphys582) (see p. 17).
- [Boc13] E. Bocquillon, V. Freulon, J.-M. Berroir, P. Degiovanni, B. Placais, A. Cavanna, Y. Jin, and G. Feve: ‘Coherence and Indistinguishability of Single Electrons Emitted by Independent Sources’, *Science* **339** (2013), 1054–1057, DOI: [10.1126/science.1232572](https://doi.org/10.1126/science.1232572) (see p. 20).
- [Boc12] E. Bocquillon, F. D. Parmentier, C. Grenier, J.-M. Berroir, P. Degiovanni, D. C. Glatli, B. Plaçais, A. Cavanna, Y. Jin, and G. Fève: ‘Electron Quantum Optics: Partitioning Electrons One by One’, *Physical Review Letters* **108** (2012), 196803, DOI: [10.1103/PhysRevLett.108.196803](https://doi.org/10.1103/PhysRevLett.108.196803) (see p. 20).
- [Büt88] M. Büttiker: ‘Absence of backscattering in the quantum Hall effect in multiprobe conductors’, *Physical Review B* **38** (1988), 9375–9389, DOI: [10.1103/PhysRevB.38.9375](https://doi.org/10.1103/PhysRevB.38.9375) (see p. 9).
- [Büt93] M. Büttiker, H. Thomas, and A. Prêtre: ‘Mesoscopic capacitors’, *Physics Letters A* **180** (1993), 364–369, DOI: [10.1016/0375-9601\(93\)91193-9](https://doi.org/10.1016/0375-9601(93)91193-9) (see p. 19).
- [Cha85] A.V. Chaplik: ‘Absorption and emission of electromagnetic waves by two-dimensional plasmons’, *Surface Science Reports* **5** (1985), 289–335, DOI: [10.1016/0167-5729\(85\)90010-X](https://doi.org/10.1016/0167-5729(85)90010-X) (see pp. 74, 94).
- [Dat95] Suprio Datta: *Electronic transport in mesoscopic systems*, Cambridge University Press, 1995 (see pp. 7, 9).
- [Dav95] John H. Davies, Ivan A. Larkin, and E. V. Sukhorukov: ‘Modeling the patterned two-dimensional electron gas: Electrostatics’, *Journal of Applied Physics* **77** (1995), 4504, DOI: [10.1063/1.359446](https://doi.org/10.1063/1.359446) (see p. 88).
- [De 12] Kristiaan De Greve, Leo Yu, Peter L McMahan, Jason S Pelc, Chandra M Natarajan, Na Young Kim, Eisuke Abe, Sebastian Maier, Christian Schneider, Martin Kamp, Sven Höfling, Robert H Hadfield, Alfred Forchel, M M Fejer, and Yoshihisa Yamamoto: ‘Quantum-dot spin–photon entanglement via frequency downconversion to telecom wavelength’, *Nature* **491** (2012), 421–425, DOI: [10.1038/nature11577](https://doi.org/10.1038/nature11577) (see p. 10).
- [Des10] Vikram V Deshpande, Marc Bockrath, Leonid I Glazman, and Amir Yacoby: ‘Electron liquids and solids in one dimension’, *Nature* **464** (2010), 209–216, DOI: [10.1038/nature08918](https://doi.org/10.1038/nature08918) (see p. 120).

- [Dev92] Michel H. Devoret, Daniel Esteve, and Cristian Urbina: ‘Single-electron transfer in metallic nanostructures’, *Nature* **360** (1992), 547–553, DOI: [10.1038/360547a0](https://doi.org/10.1038/360547a0) (see pp. 14, 16).
- [Dub] J. Dubois: ‘Towards a n-electron source based on Lorentzian voltage pulses’, PhD thesis (see p. 24).
- [Dub13] J Dubois, T Jullien, F Portier, P Roche, A Cavanna, Y Jin, W Wegscheider, P Roulleau, and D C Glattli: ‘Minimal-excitation states for electron quantum optics using levitons’, *Nature* **502** (2013), 659–663, DOI: [10.1038/nature12713](https://doi.org/10.1038/nature12713) (see pp. 2, 22–24).
- [Ebb04] J. Ebbecke, N. E. Fletcher, T. J. B. M. Janssen, F. J. Ahlers, M. Pepper, H. E. Beere, and D. A. Ritchie: ‘Quantized charge pumping through a quantum dot by surface acoustic waves’, *Applied Physics Letters* **84** (2004), 4319, DOI: [10.1063/1.1757016](https://doi.org/10.1063/1.1757016) (see p. 20).
- [Ebb03] J. Ebbecke, N.E. Fletcher, F.-J. Ahlers, A. Hartland, and T.J.B.M. Janssen: ‘Study of the limitations of the quantized acoustic current technique at pth and npl’, *IEEE Transactions on Instrumentation and Measurement* **52** (2003), 594–598, DOI: [10.1109/TIM.2003.810036](https://doi.org/10.1109/TIM.2003.810036) (see p. 20).
- [Eme] Emerson & Cuming Microwave Products: *Theory and Application of RF/Microwave Absorbers* (see p. 39).
- [Fev07] G. Feve, A. Mahe, J-M Berroir, T Kontos, B. Placais, D C Glattli, A Cavanna, B Etienne, and Y Jin: ‘An On-Demand Coherent Single-Electron Source’, *Science* **316** (2007), 1169–1172, DOI: [10.1126/science.1141243](https://doi.org/10.1126/science.1141243) (see pp. 2, 19).
- [Fèv] Gwendal Fève: ‘Quantification du courant alternatif : la boîte quantique comme source d’électrons uniques subnanoseconde’, PhD thesis (see p. 19).
- [Fie93] M Field, C. G. Smith, M Pepper, D. A. Ritchie, J. E. F. Frost, G. A. C. Jones, and D. G. Hasko: ‘Measurements of Coulomb blockade with a noninvasive voltage probe’, *Physical Review Letters* **70** (1993), 1311–1314, DOI: [10.1103/PhysRevLett.70.1311](https://doi.org/10.1103/PhysRevLett.70.1311) (see p. 21).
- [Fle13] J. D. Fletcher, P. See, H. Howe, M. Pepper, S. P. Giblin, J. P. Griffiths, G. a C Jones, I. Farrer, D. a. Ritchie, T. J B M Janssen, and M. Kataoka: ‘Clock-Controlled Emission of Single-Electron Wave Packets in a Solid-State Circuit’, *Physical Review Letters* **111** (2013), 216807, DOI: [10.1103/PhysRevLett.111.216807](https://doi.org/10.1103/PhysRevLett.111.216807) (see pp. 2, 17, 63).
- [Fuj08] Akira Fujiwara, Katsuhiko Nishiguchi, and Yukinori Ono: ‘Nanoampere charge pump by single-electron ratchet using silicon nanowire metal-oxide-semiconductor field-effect transistor’, *Applied Physics Letters* **92** (2008), 042102, DOI: [10.1063/1.2837544](https://doi.org/10.1063/1.2837544) (see p. 17).
- [Ful87] T. A. Fulton and G. J. Dolan: ‘Observation of single-electron charging effects in small tunnel junctions’, *Physical Review Letters* **59** (1987), 109–112, DOI: [10.1103/PhysRevLett.59.109](https://doi.org/10.1103/PhysRevLett.59.109) (see p. 14).

- [Gab06a] J. Gabelli: ‘Mise en évidence de la cohérence quantique des conducteurs en régime dynamique’, *PhD Thesis, Université Pierre et Marie Curie* (2006) (see p. 43).
- [Gab06b] J Gabelli: ‘Violation of Kirchhoff’s Laws for a Coherent RC Circuit’, *Science* **313** (2006), 499–502, DOI: [10.1126/science.1126940](https://doi.org/10.1126/science.1126940) (see p. 19).
- [Gao12] W. B. Gao, P. Fallahi, E. Togan, J. Miguel-Sanchez, and A. Imamoglu: ‘Observation of entanglement between a quantum dot spin and a single photon’, *Nature* **491** (2012), 426–430, DOI: [10.1038/nature11573](https://doi.org/10.1038/nature11573) (see p. 10).
- [Gau14a] Benoit Gaury and Xavier Waintal: ‘Dynamical control of interference using voltage pulses in the quantum regime’, *Nature Communications* **5** (2014), 1–11, DOI: [10.1038/ncomms4844](https://doi.org/10.1038/ncomms4844) (see pp. 2, 24, 26, 27, 29).
- [Gau14b] Benoit Gaury, Joseph Weston, Matthieu Santin, Manuel Houzet, Christoph Groth, and Xavier Waintal: ‘Numerical simulations of time-resolved quantum electronics’, *Physics Reports* **534** (2014), 1–37, DOI: [10.1016/j.physrep.2013.09.001](https://doi.org/10.1016/j.physrep.2013.09.001) (see p. 24).
- [Gau14c] Benoit Gaury, Joseph Weston, and Xavier Waintal: ‘Stopping electrons with radio-frequency pulses in the quantum Hall regime’, *Physical Review B* **90** (2014), 161305, DOI: [10.1103/PhysRevB.90.161305](https://doi.org/10.1103/PhysRevB.90.161305) (see p. 120).
- [Gau15] Benoit Gaury, Joseph Weston, and Xavier Waintal: ‘The a.c. Josephson effect without superconductivity’, *Nature Communications* **6** (2015), 6524, DOI: [10.1038/ncomms7524](https://doi.org/10.1038/ncomms7524) (see p. 24).
- [Gee90] L. J. Geerligs, V. F. Anderegg, P. A. M. Holweg, J. E. Mooij, H. Pothier, D. Esteve, C. Urbina, and M. H. Devoret: ‘Frequency-locked turnstile device for single electrons’, *Physical Review Letters* **64** (1990), 2691–2694, DOI: [10.1103/PhysRevLett.64.2691](https://doi.org/10.1103/PhysRevLett.64.2691) (see p. 15).
- [Gib12] S.P. Giblin, M Kataoka, J.D. Fletcher, P See, T.J.B.M. Janssen, J.P. Griffiths, G.A.C. Jones, I Farrer, and D.A. Ritchie: ‘Towards a quantum representation of the ampere using single electron pumps’, *Nature Communications* **3** (2012), 930, DOI: [10.1038/ncomms1935](https://doi.org/10.1038/ncomms1935) (see pp. 17, 18).
- [Gla85] D. C. Glatthli, E. Y. Andrei, G. Deville, J. Poitrenaud, and F. I B Williams: ‘Dynamical Hall Effect in a Two-Dimensional Classical Plasma’, *Physical Review Letters* **54** (1985), 1710–1713, DOI: [10.1103/PhysRevLett.54.1710](https://doi.org/10.1103/PhysRevLett.54.1710) (see p. 63).
- [Gök08] Oktay Göktaş, Jochen Weber, Jürgen Weis, and Klaus von Klitzing: ‘Alloyed ohmic contacts to two-dimensional electron system in AlGaAs/GaAs heterostructures down to submicron length scale’, *Physica E: Low-dimensional Systems and Nanostructures* **40** (2008), 1579–1581, DOI: [10.1016/j.physe.2007.09.115](https://doi.org/10.1016/j.physe.2007.09.115) (see p. 49).
- [Gus12] Martin V. Gustafsson, Paulo V. Santos, Göran Johansson, and Per Delsing: ‘Local probing of propagating acoustic waves in a gigahertz echo chamber’, *Nature Physics* **8** (2012), 338–343, DOI: [10.1038/nphys2217](https://doi.org/10.1038/nphys2217) (see p. 21).

- [Han01] A. E. Hansen, A. Kristensen, S. Pedersen, C. B. Sørensen, and P. E. Lindelof: ‘Mesoscopic decoherence in Aharonov-Bohm rings’, *Physical Review B* **64** (2001), 045327, DOI: [10.1103/PhysRevB.64.045327](https://doi.org/10.1103/PhysRevB.64.045327) (see pp. 100, 102).
- [Hay03] T Hayashi, T Fujisawa, H D Cheong, Y H Jeong, and Y Hirayama: ‘Coherent Manipulation of Electronic States in a Double Quantum Dot’, *Physical Review Letters* **91** (2003), 226804, DOI: [10.1103/PhysRevLett.91.226804](https://doi.org/10.1103/PhysRevLett.91.226804) (see p. 10).
- [Her11] Sylvain Hermelin, Shintaro Takada, Michihisa Yamamoto, Seigo Tarucha, Andreas D. Wieck, Laurent Saminadayar, Christopher Bäuerle, and Tristan Meunier: ‘Electrons surfing on a sound wave as a platform for quantum optics with flying electrons’, *Nature* **477** (2011), 435–438, DOI: [10.1038/nature10416](https://doi.org/10.1038/nature10416) (see pp. 2, 21).
- [Huy12] P.-A. Huynh, F. Portier, H. le Sueur, G. Faini, U. Gennser, D. Mailly, F. Pierre, W. Wegscheider, and P. Roche: ‘Quantum Coherence Engineering in the Integer Quantum Hall Regime’, *Physical Review Letters* **108** (2012), 256802, DOI: [10.1103/PhysRevLett.108.256802](https://doi.org/10.1103/PhysRevLett.108.256802) (see p. 12).
- [Ion99] Radu Ionicioiu, Gehan Amaratunga, and Florin Udrea: ‘Ballistic Single-Electron Qputer’, (1999), 1–5 (see p. 10).
- [Iva97] D. A. Ivanov, H. W. Lee, and L. S. Levitov: ‘Coherent states of alternating current’, *Physical Review B* **56** (1997), 6839–6850, DOI: [10.1103/PhysRevB.56.6839](https://doi.org/10.1103/PhysRevB.56.6839) (see p. 22).
- [Jan01] J.-T. Janssen and A. Hartland: ‘Recent measurements of single electron transport of surface acoustic wave devices at the NPL’, *IEEE Transactions on Instrumentation and Measurement* **50** (2001), 227–230, DOI: [10.1109/19.918108](https://doi.org/10.1109/19.918108) (see p. 20).
- [Jan00] T.J.B.M. Janssen and A. Hartland: ‘Accurate measurement of currents generated by single electrons transported in a one-dimensional channel’, *IEE Proceedings - Science, Measurement and Technology* **147** (2000), 174–176, DOI: [10.1049/ip-smt:20000449](https://doi.org/10.1049/ip-smt:20000449) (see p. 20).
- [Ji03] Yang Ji, Yunchul Chung, D Sprinzak, M Heiblum, D Mahalu, and Hadas Shtrikman: ‘An electronic Mach–Zehnder interferometer’, *Nature* **422** (2003), 415–418, DOI: [10.1038/nature01503](https://doi.org/10.1038/nature01503) (see pp. 1, 9, 12).
- [Jom09] Y. Jompol, C. J. B. Ford, J. P. Griffiths, I. Farrer, G. A. C. Jones, D. Anderson, D. A. Ritchie, T. W. Silk, and A. J. Schofield: ‘Probing Spin-Charge Separation in a Tomonaga-Luttinger Liquid’, *Science* **325** (2009), 597–601, DOI: [10.1126/science.1171769](https://doi.org/10.1126/science.1171769) (see pp. 88, 92, 119).
- [Jul14] Thibaut Jullien: ‘Source mésoscopique à quelques électrons par pulses de tension’, PhD thesis, 2014 (see pp. 24, 56).
- [Kae08] B. Kaestner, V. Kashcheyevs, S. Amakawa, M. D. Blumenthal, L. Li, T. J B M Janssen, G. Hein, K. Pierz, T. Weimann, U. Siegner, and H. W. Schumacher: ‘Single-parameter nonadiabatic quantized charge pumping’, *Physical Review B* **77** (2008), 153301, DOI: [10.1103/PhysRevB.77.153301](https://doi.org/10.1103/PhysRevB.77.153301) (see p. 17).

- [Kam14] H Kamata, N Kumada, M Hashisaka, K Muraki, and T Fujisawa: ‘Fractionalized wave packets from an artificial Tomonaga–Luttinger liquid’, *Nature Nanotechnology* **9** (2014), 177–181, DOI: [10.1038/nnano.2013.312](https://doi.org/10.1038/nnano.2013.312) (see p. 63).
- [Kam10] H. Kamata, T. Ota, K. Muraki, and T. Fujisawa: ‘Voltage-controlled group velocity of edge magnetoplasmon in the quantum Hall regime’, *Physical Review B* **81** (2010), 085329, DOI: [10.1103/PhysRevB.81.085329](https://doi.org/10.1103/PhysRevB.81.085329) (see pp. 28, 63).
- [Kam09] Hiroshi Kamata, Takeshi Ota, and Toshimasa Fujisawa: ‘Correlation Measurement of Time-Dependent Potentials in a Semiconductor Quantum Point Contact’, *Japanese Journal of Applied Physics* **48** (2009), 04C149, DOI: [10.1143/JJAP.48.04C149](https://doi.org/10.1143/JJAP.48.04C149) (see pp. 63, 94, 119).
- [Kas98] M. a. Kastner, David Goldhaber-Gordon, Hadas Shtrikman, D. Mahalu, David Abusch-Magder, and U. Meirav: ‘Kondo effect in a single-electron transistor’, *Nature* **391** (1998), 156–159, DOI: [10.1038/34373](https://doi.org/10.1038/34373) (see p. 9).
- [Kat09] M. Kataoka, M. R. Astley, a. L. Thorn, D. K L Oi, C. H W Barnes, C. J B Ford, D. Anderson, G. a C Jones, I. Farrer, D. a. Ritchie, and M. Pepper: ‘Coherent Time Evolution of a Single-Electron Wave Function’, *Physical Review Letters* **102** (2009), 156801, DOI: [10.1103/PhysRevLett.102.156801](https://doi.org/10.1103/PhysRevLett.102.156801) (see p. 21).
- [Kat15] M Kataoka, N Johnson, C Emary, P See, J P Griffiths, G A C Jones, I Farrer, D A Ritchie, M Pepper, and T J B M Janssen: ‘Time-of-Flight Measurements of Single-Electron Wave Packets in Quantum-Hall Edge States’, (2015), 1–5 (see pp. 28, 63).
- [Kee06] J. Keeling, I. Klich, and L. S. Levitov: ‘Minimal Excitation States of Electrons in One-Dimensional Wires’, *Physical Review Letters* **97** (2006), 116403, DOI: [10.1103/PhysRevLett.97.116403](https://doi.org/10.1103/PhysRevLett.97.116403) (see pp. 22, 23).
- [Kel08] Mark W Keller: ‘Current status of the quantum metrology triangle’, *Metrologia* **45** (2008), 102–109, DOI: [10.1088/0026-1394/45/1/014](https://doi.org/10.1088/0026-1394/45/1/014) (see p. 14).
- [Kel96] Mark W Keller, John M Martinis, Neil M Zimmerman, and Andrew H Steinbach: ‘Accuracy of electron counting using a 7-junction electron pump’, *Applied Physics Letters* **69** (1996), 1804, DOI: [10.1063/1.117492](https://doi.org/10.1063/1.117492) (see p. 16).
- [Kli80] K. V. Klitzing, G. Dorda, and M. Pepper: ‘New Method for High-Accuracy Determination of the Fine-Structure Constant Based on Quantized Hall Resistance’, *Physical Review Letters* **45** (1980), 494–497, DOI: [10.1103/PhysRevLett.45.494](https://doi.org/10.1103/PhysRevLett.45.494) (see p. 9).
- [Kop06] F. H. L. Koppens, C. Buizert, K. J. Tielrooij, I. T. Vink, K. C. Nowack, T. Meunier, L. P. Kouwenhoven, and L. M. K. Vandersypen: ‘Driven coherent oscillations of a single electron spin in a quantum dot’, *Nature* **442** (2006), 766–771, DOI: [10.1038/nature05065](https://doi.org/10.1038/nature05065) (see pp. 9, 10).
- [Kou97] L P Kouwenhoven: ‘Excitation Spectra of Circular, Few-Electron Quantum Dots’, *Science* **278** (1997), 1788–1792, DOI: [10.1126/science.278.5344.1788](https://doi.org/10.1126/science.278.5344.1788) (see p. 9).

- [Kou01] L P Kouwenhoven, D G Austing, and S Tarucha: ‘Few-electron quantum dots’, *Reports on Progress in Physics* **64** (2001), 701–736, DOI: [10.1088/0034-4885/64/6/201](https://doi.org/10.1088/0034-4885/64/6/201) (see p. 9).
- [Kou91] L. P. Kouwenhoven, A. T. Johnson, N. C. van der Vaart, C. J. P. M. Harmans, and C. T. Foxon: ‘Quantized current in a quantum-dot turnstile using oscillating tunnel barriers’, *Physical Review Letters* **67** (1991), 1626–1629, DOI: [10.1103/PhysRevLett.67.1626](https://doi.org/10.1103/PhysRevLett.67.1626) (see pp. 17, 18).
- [Kum13] N Kumada, S Tanabe, H Hibino, H Kamata, M Hashisaka, K Muraki, and T Fujisawa: ‘Plasmon transport in graphene investigated by time-resolved electrical measurements’, *Nature Communications* **4** (2013), 1363, DOI: [10.1038/ncomms2353](https://doi.org/10.1038/ncomms2353) (see p. 63).
- [Kum14] N. Kumada, P. Roulleau, B. Roche, M. Hashisaka, H. Hibino, I. Petkovic, and D. C. Glattli: ‘Resonant Edge Magnetoplasmons and Their Decay in Graphene’, *Physical Review Letters* **113** (2014), 266601, DOI: [10.1103/PhysRevLett.113.266601](https://doi.org/10.1103/PhysRevLett.113.266601) (see p. 63).
- [Lev96] Leonid S. Levitov, Hyunwoo Lee, and Gordey B. Lesovik: ‘Electron counting statistics and coherent states of electric current’, *Journal of Mathematical Physics* **37** (1996), 4845, DOI: [10.1063/1.531672](https://doi.org/10.1063/1.531672) (see p. 22).
- [Los98] Daniel Loss and David P. DiVincenzo: ‘Quantum computation with quantum dots’, *Physical Review A* **57** (1998), 120–126, DOI: [10.1103/PhysRevA.57.120](https://doi.org/10.1103/PhysRevA.57.120) (see p. 9).
- [Lut63] J. M. Luttinger: ‘An Exactly Soluble Model of a Many-Fermion System’, *Journal of Mathematical Physics* **4** (1963), 1154, DOI: [10.1063/1.1704046](https://doi.org/10.1063/1.1704046) (see p. 88).
- [M P05] David M Pozar: *Microwave Engineering, 3rd Edition*, 2005, 728, DOI: [10.978.0471/448785](https://doi.org/10.978.0471/448785) (see p. 43).
- [Man11] Soumen Mandal, Tobias Bautze, Rémi Blinder, Tristan Meunier, Laurent Saminadayar, and Christopher Bäuerle: ‘Efficient radio frequency filters for space constrained cryogenic setups’, *Review of Scientific Instruments* **82** (2011), 024704, DOI: [10.1063/1.3543736](https://doi.org/10.1063/1.3543736) (see p. 39).
- [Mat93] K.A. Matveev and L.I. Glazman: ‘Conductance and Coulomb blockade in a multi-mode quantum wire’, *Physica B: Condensed Matter* **189** (1993), 266–274, DOI: [10.1016/0921-4526\(93\)90169-7](https://doi.org/10.1016/0921-4526(93)90169-7) (see pp. 3, 63, 86, 91, 94, 119).
- [McN11] R. P. G. McNeil, M. Kataoka, C. J. B. Ford, C. H. W. Barnes, D. Anderson, G. a. C. Jones, I. Farrer, and D. a. Ritchie: ‘On-demand single-electron transfer between distant quantum dots’, *Nature* **477** (2011), 439–442, DOI: [10.1038/nature10444](https://doi.org/10.1038/nature10444) (see pp. 2, 21).
- [Mos02] M. Moskalets and M. Büttiker: ‘Floquet scattering theory of quantum pumps’, *Physical Review B* **66** (2002), 205320, DOI: [10.1103/PhysRevB.66.205320](https://doi.org/10.1103/PhysRevB.66.205320) (see p. 17).

- [Ned07] I Neder, N Ofek, Y Chung, M Heiblum, D Mahalu, and V Umansky: ‘Interference between two indistinguishable electrons from independent sources’, *Nature* **448** (2007), 333–337, DOI: [10.1038/nature05955](https://doi.org/10.1038/nature05955) (see pp. 1, 12).
- [Ned06] I. Neder, M. Heiblum, Y. Levinson, D. Mahalu, and V. Umansky: ‘Unexpected Behavior in a Two-Path Electron Interferometer’, *Physical Review Letters* **96** (2006), 016804, DOI: [10.1103/PhysRevLett.96.016804](https://doi.org/10.1103/PhysRevLett.96.016804) (see p. 12).
- [Pek10] J. P. Pekola, V. F. Maisi, S. Kafanov, N. Chekurov, A. Kemppinen, Yu. A. Pashkin, O.-P. Saira, M. Möttönen, and J. S. Tsai: ‘Environment-Assisted Tunneling as an Origin of the Dynes Density of States’, *Physical Review Letters* **105** (2010), 026803, DOI: [10.1103/PhysRevLett.105.026803](https://doi.org/10.1103/PhysRevLett.105.026803) (see p. 17).
- [Pek08] Jukka P. Pekola, Juha J. Vartiainen, Mikko Möttönen, Olli-Pentti Saira, Matthias Meschke, and Dmitri V. Averin: ‘Hybrid single-electron transistor as a source of quantized electric current’, *Nature Physics* **4** (2008), 120–124, DOI: [10.1038/nphys808](https://doi.org/10.1038/nphys808) (see p. 16).
- [Pek13] Jukka P. Pekola, Olli-Pentti Saira, Ville F. Maisi, Antti Kemppinen, Mikko Möttönen, Yuri a. Pashkin, and Dmitri V. Averin: ‘Single-electron current sources: Toward a refined definition of the ampere’, *Reviews of Modern Physics* **85** (2013), 1421–1472, DOI: [10.1103/RevModPhys.85.1421](https://doi.org/10.1103/RevModPhys.85.1421) (see p. 14).
- [Pet10] K. D. Petersson, J. R. Petta, H. Lu, and a. C. Gossard: ‘Quantum Coherence in a One-Electron Semiconductor Charge Qubit’, *Physical Review Letters* **105** (2010), 246804, DOI: [10.1103/PhysRevLett.105.246804](https://doi.org/10.1103/PhysRevLett.105.246804) (see p. 10).
- [Pet13] I. Petkovic, F. I B Williams, K. Bennaceur, F. Portier, P. Roche, and D. C. Glattli: ‘Carrier Drift Velocity and Edge Magnetoplasmons in Graphene’, *Physical Review Letters* **110** (2013), 016801, DOI: [10.1103/PhysRevLett.110.016801](https://doi.org/10.1103/PhysRevLett.110.016801) (see p. 63).
- [Pet05] J R Petta: ‘Coherent Manipulation of Coupled Electron Spins in Semiconductor Quantum Dots’, *Science* **309** (2005), 2180–2184, DOI: [10.1126/science.1116955](https://doi.org/10.1126/science.1116955) (see pp. 9, 10).
- [Pob07] Frank Pobell: *Matter and methods at low temperature*, Springer, 2007 (see p. 35).
- [Pot91] H. Pothier, P. Lafarge, P.F. Orfila, C. Urbina, D. Esteve, and M.H. Devoret: ‘Single electron pump fabricated with ultrasmall normal tunnel junctions’, *Physica B: Condensed Matter* **169** (1991), 573–574, DOI: [10.1016/0921-4526\(91\)90332-9](https://doi.org/10.1016/0921-4526(91)90332-9) (see p. 15).
- [Rog] *RO3000 series circuit material* (see p. 48).
- [Rou08a] P. Roulleau, F. Portier, P. Roche, A. Cavanna, G. Faini, U. Gennser, and D. Mailly: ‘Noise Dephasing in Edge States of the Integer Quantum Hall Regime’, *Physical Review Letters* **101** (2008), 186803, DOI: [10.1103/PhysRevLett.101.186803](https://doi.org/10.1103/PhysRevLett.101.186803) (see p. 12).

- [Rou09] P. Roulleau, F. Portier, P. Roche, A. Cavanna, G. Faini, U. Gennser, and D. Maily: ‘Tuning Decoherence with a Voltage Probe’, *Physical Review Letters* **102** (2009), 236802, DOI: [10.1103/PhysRevLett.102.236802](https://doi.org/10.1103/PhysRevLett.102.236802) (see p. 12).
- [Rou08b] Preden Roulleau, F. Portier, P. Roche, A. Cavanna, G. Faini, U. Gennser, and D. Maily: ‘Direct Measurement of the Coherence Length of Edge States in the Integer Quantum Hall Regime’, *Physical Review Letters* **100** (2008), 126802, DOI: [10.1103/PhysRevLett.100.126802](https://doi.org/10.1103/PhysRevLett.100.126802) (see pp. 1, 9, 12, 28, 100, 102).
- [See01] Georg Seelig and Markus Büttiker: ‘Charge-fluctuation-induced dephasing in a gated mesoscopic interferometer’, *Physical Review B* **64** (2001), 245313, DOI: [10.1103/PhysRevB.64.245313](https://doi.org/10.1103/PhysRevB.64.245313) (see pp. 95, 102).
- [Sha81] D. Yu. Sharvin and Yu. V. Sharvin: *Magnetic-flux quantization in cylindrical film of a normal metal*, 1981 (see p. 1).
- [She95] J a Sheridan, D M Bloom, and P M Solomon: ‘System for direct measurement of the step response of electronic devices on the picosecond time scale.’, *Optics letters* **20** (1995), 584–586 (see p. 118).
- [Shi96] J M Shilton, V I Talyanskii, M Pepper, D a Ritchie, J E F Frost, C J B Ford, C G Smith, and G a C Jones: ‘High-frequency single-electron transport in a quasi-one-dimensional GaAs channel induced by surface acoustic waves’, *Journal of Physics: Condensed Matter* **8** (1996), L531–L539, DOI: [10.1088/0953-8984/8/38/001](https://doi.org/10.1088/0953-8984/8/38/001) (see p. 20).
- [Ste67] Frank Stern: ‘Polarizability of a Two-Dimensional Electron Gas’, *Physical Review Letters* **18** (1967), 546–548, DOI: [10.1103/PhysRevLett.18.546](https://doi.org/10.1103/PhysRevLett.18.546) (see p. 74).
- [Sto85] A. Douglas Stone and P. A. Lee: ‘Effect of Inelastic Processes on Resonant Tunneling in One Dimension’, *Physical Review Letters* **54** (1985), 1196–1199, DOI: [10.1103/PhysRevLett.54.1196](https://doi.org/10.1103/PhysRevLett.54.1196) (see p. 108).
- [Sto05] James a H Stotz, Rudolf Hey, Paulo V Santos, and Klaus H Ploog: ‘Coherent spin transport through dynamic quantum dots’, *Nature Materials* **4** (2005), 585–588, DOI: [10.1038/nmat1430](https://doi.org/10.1038/nmat1430) (see p. 21).
- [Suk04] G. Sukhodub, F. Hohls, and R. J. Haug: ‘Observation of an Interedge Magnetoplasmon Mode in a Degenerate Two-Dimensional Electron Gas’, *Physical Review Letters* **93** (2004), 196801, DOI: [10.1103/PhysRevLett.93.196801](https://doi.org/10.1103/PhysRevLett.93.196801) (see p. 63).
- [Tak14] S. Takada, C. Bäuerle, M. Yamamoto, K. Watanabe, S. Hermelin, T. Meunier, A. Alex, A. Weichselbaum, J. von Delft, A. Ludwig, A. D. Wieck, and S. Tarucha: ‘Transmission Phase in the Kondo Regime Revealed in a Two-Path Interferometer’, *Physical Review Letters* **113** (2014), 126601, DOI: [10.1103/PhysRevLett.113.126601](https://doi.org/10.1103/PhysRevLett.113.126601) (see p. 13).

- [Tal97] V. I. Talyanskii, J. M. Shilton, M. Pepper, C. G. Smith, C. J. B. Ford, E. H. Linfield, D. A. Ritchie, and G. A. C. Jones: ‘Single-electron transport in a one-dimensional channel by high-frequency surface acoustic waves’, *Physical Review B* **56** (1997), 15180–15184, DOI: [10.1103/PhysRevB.56.15180](https://doi.org/10.1103/PhysRevB.56.15180) (see p. 20).
- [Tom51] Sin-itiro Tomonaga: *Remarks on Bloch’s Method of Sound Waves applied to Many-Fermion Problems*, 1951, DOI: [10.1143/PTP.5.544](https://doi.org/10.1143/PTP.5.544) (see p. 88).
- [Tsu90] N. Tsukada, a. D. Wieck, and K. Ploog: ‘Proposal of novel electron wave coupled devices’, *Applied Physics Letters* **56** (1990), 2527, DOI: [10.1063/1.102877](https://doi.org/10.1063/1.102877) (see p. 11).
- [Ubb14] Niels Ubbelohde, Frank Hohls, Vyacheslavs Kashcheyevs, Timo Wagner, Lukas Fricke, Bernd Kästner, Klaus Pierz, Hans W. Schumacher, and Rolf J. Haug: ‘Partitioning of on-demand electron pairs’, *Nature Nanotechnology* **10** (2014), 46–49, DOI: [10.1038/nnano.2014.275](https://doi.org/10.1038/nnano.2014.275) (see p. 18).
- [Umb84] C. P. Umbach, S. Washburn, R. B. Laibowitz, and R. A. Webb: ‘Magnetoresistance of small, quasi-one-dimensional, normal-metal rings and lines’, *Physical Review B* **30** (1984), 4048–4051, DOI: [10.1103/PhysRevB.30.4048](https://doi.org/10.1103/PhysRevB.30.4048) (see p. 1).
- [Van88] B. J. Van Wees, H. Van Houten, C. W. J. Beenakker, J. G. Williamson, L. P. Kouwenhoven, D. Van Der Marel, and C. T. Foxon: ‘Quantized conductance of point contacts in a two-dimensional electron gas’, *Physical Review Letters* **60** (1988), 848–850, DOI: [10.1103/PhysRevLett.60.848](https://doi.org/10.1103/PhysRevLett.60.848) (see pp. 1, 7).
- [Wal15] J. Waldie, P. See, V. Kashcheyevs, J. P. Griffiths, I. Farrer, G. A. C. Jones, D. A. Ritchie, T. J. B. M. Janssen, and M. Kataoka: ‘Measurement and control of electron wave packets from a single-electron source’, *Physical Review B* **92** (2015), 125305, DOI: [10.1103/PhysRevB.92.125305](https://doi.org/10.1103/PhysRevB.92.125305) (see p. 63).
- [Web85] R. A. Webb, S. Washburn, C. P. Umbach, and R. B. Laibowitz: ‘Observation of the aharonov-bohm oscillations in normal-metal rings’, *Physical Review Letters* **54** (1985), 2696–2699, DOI: [10.1103/PhysRevLett.54.2696](https://doi.org/10.1103/PhysRevLett.54.2696) (see p. 1).
- [Wei14] E Weisz, H K Choi, I Sivan, M Heiblum, Y Gefen, D Mahalu, and V Umansky: ‘An electronic quantum eraser’, *Science* **344** (2014), 1363–1366, DOI: [10.1126/science.1248459](https://doi.org/10.1126/science.1248459) (see p. 12).
- [Wes16a] Joseph Weston and Xavier Waintal: ‘Towards Realistic Time-Resolved Simulations of Quantum Devices’, (2016), 1–8 (see p. 34).
- [Wes16b] Joseph Weston and Xavier Waintal: ‘Towards Realistic Time-Resolved Simulations of Quantum Devices’, (2016), 1–8 (see p. 99).
- [Wha88] D A Wharam, T J Thornton, R Newbury, M Pepper, H Ahmed, J E F Frost, D G Hasko, D C Peacock, D A Ritchie, and G A C Jones: ‘One-Dimensional Transport and the Quantisation of the Ballistic Resistance.’, *J. Phys. C* **21** (1988), 209–214 (see pp. 1, 7).

- [Wie00] W. G. van der Wiel: ‘The Kondo Effect in the Unitary Limit’, *Science* **289** (2000), 2105–2108, DOI: [10.1126/science.289.5487.2105](https://doi.org/10.1126/science.289.5487.2105) (see p. 9).
- [Yam12] Michihisa Yamamoto, Shintaro Takada, Christopher Bäuerle, Kenta Watanabe, Andreas D. Wieck, and Seigo Tarucha: ‘Electrical control of a solid-state flying qubit’, *Nature Nanotechnology* **7** (2012), 247–251, DOI: [10.1038/nnano.2012.28](https://doi.org/10.1038/nnano.2012.28) (see pp. 2, 10, 12, 13, 29, 100, 102, 103, 110).
- [Yoo14] Hosang Yoon, Kitty Y M Yeung, Philip Kim, and Donhee Ham: ‘Plasmonics with two-dimensional conductors’, *Philosophical Transactions of the Royal Society A: Mathematical, Physical and Engineering Sciences* **372** (2014), 20130104–20130104, DOI: [10.1098/rsta.2013.0104](https://doi.org/10.1098/rsta.2013.0104) (see p. 74).
- [Zhi93] N. B. Zhitenev, R. J. Haug, K. v. Klitzing, and K. Eberl: ‘Time-resolved measurements of transport in edge channels’, *Physical Review Letters* **71** (1993), 2292–2295, DOI: [10.1103/PhysRevLett.71.2292](https://doi.org/10.1103/PhysRevLett.71.2292) (see p. 63).
- [Zor95] A. B. Zorin: ‘The thermocoax cable as the microwave frequency filter for single electron circuits’, *Review of Scientific Instruments* **66** (1995), 4296, DOI: [10.1063/1.1145385](https://doi.org/10.1063/1.1145385) (see p. 39).

List of Figures

2.1	Schematic of the AlGaAs/GaAs heterostructure	6
2.2	Schematic illustrating the depletion of the 2DEG.	8
2.3	Quantized conductance of a QPC measured at low temperature.	8
2.4	Schematic of the classical picture of the QHE	10
2.5	Schematic of the Mach-Zehnder interferometer.	11
2.6	Bloch sphere representation of a qubit.	11
2.7	Schematic of the electronic two path interferometer realized by Ji et al.	12
2.8	Flying-qubit realized by Yamamoto et al.	13
2.9	Schematic of a single electron transistor	15
2.10	Schematic of the single electron pump	16
2.11	Schematic of the electron turnstile	16
2.12	SEM picture of the sample used by Kouwenhoven et al. as a quantum dot turnstile.	18
2.13	SEM picture of the sample used by Giblin et al. as single electron source.	18
2.14	Schematic of the on demand single electron source realized by Feve et al..	19
2.15	Schematic of the process during which SAW induced quantized current is produced	21
2.16	SEM picture of the sample used by Hermelin et al. as a SAW based single electron source.	22
2.17	SEM picture of the sample combining SAW single electron source coupled to a beam splitter.	22
2.18	Schematic picture of the Leviton wave function in time and energy domains.	23
2.19	Artistic view of the sample used by Dubois et al.	24
2.20	Effect of the voltage pulse injected into a one dimensional conductor on the electronic wave function.	25
2.21	Schematic of the propagation of a voltage pulse injected in a Mach Zehnder interferometer	26
2.22	Numerical simulation of the time resolved output current generated when a fast voltage pulse is sent in a Mach Zehnder interferometer.	27
2.23	Results of the numerical simulation and the analytical calculation giving the difference of the total number of transmitted charges as a function of injected number of charge \bar{n} in a Mach-Zehnder interferometer.	29

2.24	Schematic of the tunnel coupled wires.	30
2.25	Theory tcw	32
3.1	Experimental set-up schematics	37
3.2	Set-up installed on the mixing chamber	40
3.3	The two RuO ₂ resistances mounted on a chip carrier used to measure the temperature of the DC lines.	41
3.4	Temperature performance of Constantan wires and Thermocoax TM	42
3.5	Schematic of the RF line including attenuators and the bias T	44
3.6	Schematic of the attenuation of thermal radiation by an attenuator	45
3.7	Measurement of the temperature of the inner conductor of the RF line	46
3.8	Attenuation of the RF line measured at 300 K and 20 mK	47
3.9	Pictures of the PCB	49
3.10	Picture of the sample installed on the PCB	50
3.11	Ohmic bar	51
3.12	Measurement of the variation of the total resistance with the length of the mesa	51
3.13	Photography of the sample	54
3.14	SEM image of the central part of the sample	55
3.15	Pulses generated by the AWG	56
3.16	Schematic of the set-up used to generate voltage pulses by summing 4 harmonics	58
3.17	Schematic of the set-up used to bias the sample and measure outputs signals	61
3.18	Schematic illustrating the principle of the pulse modulation	61
3.19	Normalized output voltage measured as a function of modulation frequency	62
4.1	Schematic illustrating the principle of the time resolved measurement.	64
4.2	SEM picture illustrating how the sample is tuned to perform the time resolved measurement of the voltage pulse in-situ.	65
4.3	Detection scheme used to probe the voltage pulse in-situ.	66
4.4	Conductance trace of the QPC used to probe the voltage pulse as a function of the applied voltage.	67
4.5	Time resolved measurement of the voltage pulse in-situ.	67
4.6	Comparison between the pulse shape measured after the propagation through the RF line at room temperature and the one calculated using the attenuation of the coaxial line.	69
4.7	Calculated convolution of the voltage pulses after their propagation in the RF lines compared to the in-situ measurement.	70
4.8	Time resolved measurements for different amplitudes of the injected voltage pulses	71
4.9	Amplitude of the peak as a function of the amplitude of the voltage pulse	71
4.10	Measurement of the intrinsic delay of the RF lines by reflectometry.	73

4.11	Time resolved measurements of the voltage pulse as a function of the initial delay between the voltage pulses applied on the QPC and on the ohmic contact.	74
4.12	Schematic of the geometry considered to calculate the electrostatic potential	75
4.13	Evolution of the ratio $\frac{\omega}{v_F q}$ as a function of q	79
4.14	Schematic illustrating the effect of the confinement.	80
4.15	Conductance of the QPC for different voltages applied on the tunnel gate. .	81
4.16	Time resolved measurements of the voltage pulse as a function of the voltage applied on the tunnel gate.	81
4.17	Shift of the peak as a function of the voltage applied on the tunnel gate. . .	82
4.18	Schematic of the confinement potential.	83
4.19	Conductance of the sample as a function of the voltage applied on the tunnel gate.	83
4.20	SEM picture of the future sample.	84
4.21	Fourier transform of the in-situ measurement.	85
4.22	Parasitic oscillating signal appearing in the in-situ measurement as a function of the voltage applied on the tunnel gate.	85
4.23	Simulation of the electrostatic potential seen by the electron	90
4.24	Comparison between the measured and calculated propagation velocities. . .	93
5.1	SEM picture of the sample illustrating the configuration used to investigate the tunnel oscillations	96
5.2	Conductance of the wires $ \uparrow\rangle$ and $ \downarrow\rangle$ as a function of the voltage applied on the tunnel gate V_T	98
5.3	Antisymmetric oscillations of conductance of the wires $ \uparrow\rangle$ and $ \downarrow\rangle$ as a function of the voltage applied on the tunnel gate V_T	98
5.4	Illustration of the procedure used to extract of the visibility of the oscillations.	99
5.5	Comparison between measurement taken at 20 mK and 200 mK	100
5.6	Temperature dependence of the visibility $\delta G/G$ for DC measurements . . .	101
5.7	Evolution of the visibility of the oscillations 1 and 2 as a function of temperature	101
5.8	Measurements of the output current of the TCW used by Yamamoto et al.	103
5.9	Comparison between DC and short voltage pulses	104
5.10	Schematics of the waveforms generated by the AWG without duty cycle and with a duty cycle of 1/5	104
5.11	Evolution of the visibility as a function of the duty cycle	105
5.12	Evolution of the visibility $\delta G/G$ as a function of temperature when short pulses are used	106
5.13	Evolution of the visibility of first three oscillations as a function of temperature	107
5.14	Schematic illustrating the Coulomb blockade	108
5.15	Conductance traces of the TCW in presence of Coulomb blockade	109
5.16	Zoom on the Coulomb peaks observed on the conductance trace of the wire $ \downarrow\rangle$	109
5.17	Comparison between the first observed oscillations of conductance and the Coulomb oscillations	110

5.18	Temperature dependence of the visibility of the first oscillation due to the Coulomb peak 1 (C.P. 1) and the second oscillation due to the Valley 1 . . .	112
5.19	Schematic of the new sample allowing to tune the length of the tunnel coupled wires	112
5.20	Schematic of the propagation of the wave packet in the TCW	113
5.21	Conductance traces of the TCW illustrating the working region allowing to perform time resolved measurements of the transfer of the wave-packet . . .	114
5.22	Time resolved measurement of the transfer of the pulse between the wire . .	115
5.23	Comparison between the in-situ measurement using the tunnel gate and the calculated convolution	116
5.24	Fourier transform of the in-situ measurements of the wire $ \downarrow\rangle$	116
5.25	Time resolved measurement of the transfer of the wave-packet as a function of the initial delay	117
A.1	Delay due to the attenuators.	124
B.1	Time resolved measurements of the voltage pulse as a function of the voltage applied on the tunnel gate.	125
B.2	Shift of the peak as a function of the voltage applied on the tunnel gate. . .	126
C.1	Simulation of the electrostatic potential for $V_{tunnel} = -0.1$ V	127
D.1	Intrinsic delay of the RF lines connected to the ohmic contact and the tunnel gate	129

List of Tables

3.1	Temperatures calculated after the attenuators.	44
3.2	Ohmic contact recipes	50
3.3	Ohmic contact resistances	52
4.1	Average number of injected charges as a function of the amplitude of the voltage pulse	69
4.2	Calculated energies, Fermi velocities and densities associated with the modes allowed in the harmonic potential.	89
4.3	Calculated spin modes velocities s_l expressed in terms of Fermi velocities v_i and components of the associated eigenvectors.	91
4.4	Calculated charge modes velocities s_l expressed in terms of fermi velocities v_i and components of the associated eigenvectors.	92

Abstract

Over the past decade, an important effort has been made in the field of low dimensional electronic conductors towards *single electron electronics* with the goal to gain full control of the phase of a single electron in a solid-state system. A particular appealing idea is to use a single *flying* electron itself to carry and manipulate the quantum information, the so-called solid state *flying qubit*. On demand single electron injection into such a ballistic two-dimensional electron system can be realized by employing the recently developed single electron source based on sub-nanosecond lorentzian voltage pulses. Such a source could also be used to reveal interesting new physics. When a short voltage pulse is injected in an electronic interferometer, novel interference effects are expected due to the interference of the pulse with the surrounding Fermi sea. For the realization of such experiments it is important to know with high accuracy the propagation velocity of the electron wave packet created by the pulse.

In this thesis, we present time resolved measurements of a short voltage pulse (<100 ps) injected into a 1D quantum wire formed in a two-dimensional electron gas and determine its propagation speed. We show that the voltage pulse propagates much faster than the Fermi velocity of a non-interacting system. The propagation speed is enhanced due to electron interactions within the quantum wire. For a quantum wire containing a large number of modes, the measured propagation velocity agrees very well with the 2D plasmon velocity for a gated two-dimensional electron gas. Increasing the confinement potential allows to control the strength of the electron interactions and hence the propagation speed. We then have studied an electronic two-path interferometer based on two tunnel-coupled wires. Our preliminary measurements show a signature that can be attributed to the coherent tunneling of the electrons injected into this system. In the near future, this system could be used to reveal these new striking effects due to the interaction of the voltage pulse with the Fermi sea.

Résumé

Au cours de la dernière décennie, un important effort a été fait dans le domaine des conducteurs électroniques de basse dimensionnalité afin de réaliser *une électronique à électrons uniques*. Une idée particulièrement attractive étant de pouvoir contrôler complètement la phase d'un électron unique *volant* pour transporter et manipuler de l'information quantique dans le but de construire un *qubit volant*. L'injection contrôlée d'électrons uniques dans un système électronique bidimensionnel balistique peut être faite grâce à une source d'électrons uniques basée sur des pulses de tensions lorentziens sub-nanosecondes. Une telle source peut aussi être utilisée pour mettre en évidence de nouveaux phénomènes d'interférences électroniques. Lorsqu'un pulse de tension court est injecté dans un interféromètre électronique, de nouveaux effets d'interférences sont attendus du fait de l'interaction du pulse avec les électrons de la mer de Fermi. Pour la réalisation de cette expérience, il est important de connaître avec précision la vitesse de propagation du paquet d'onde électronique créé par le pulse.

Dans cette thèse, nous présentons des mesures résolues en temps d'un pulse de tension court (<100 ps) injecté dans un fil quantique 1D formé dans gaz d'électron bidimensionnel qui nous ont permis de déterminer sa vitesse de propagation. Nous montrons que le pulse se propage bien plus vite que la vitesse de Fermi d'un système sans interaction. La vitesse de propagation est augmentée par les interactions électron-électron. Pour un fil quantique contenant un grand nombre de modes, la vitesse mesurée est en excellent accord avec la vitesse d'un plasmon dans un système 2D en présence de grilles métalliques. En modifiant le potentiel de confinement électrostatique et donc l'intensité des interactions, nous montrons qu'il est possible de contrôler la vitesse de propagation. Nous avons ensuite étudié un interféromètre électronique à deux chemins basé sur deux fils couplés par une barrière tunnel. Nos mesures préliminaires font ressortir une signature qui peut être attribuée à des oscillations tunnel cohérentes des électrons injectés dans ce système. Dans un future proche, cet interféromètre pourrait être utilisé pour mettre en évidence ces nouveaux effets spectaculaires dus à l'interaction du pulse avec les électrons de la mer de Fermi.